Study of Co2MnSi Heusler alloy magnonic crystals

Sarah Mantion

Université Fédérale
Toulouse Midi-Pyrénées

THÈSE

En vue de l'obtention du
DOCTORAT DE L'UNIVERSITÉ DE TOULOUSE
Délivré par l'Université Toulouse 3 - Paul Sabatier

Présentée et soutenue par

Sarah MANTION

Le 7 avril 2023

Étude de cristaux magnoniques reconfigurables à base d'alliages d'Heusler Co2MnSi

Ecole doctorale : **SDM - SCIENCES DE LA MATIERE - Toulouse**

Spécialité : **Nanophysique**

Unité de recherche :
CEMES - Centre d'Elaboration de Matériaux et d'Etudes Structurales

Thèse dirigée par
Nicolas BIZIERE

Jury

M. Grégoire DE LOUBENS, Rapporteur
Mme Catherine GOURDON, Rapporteure
M. Vincent CROS, Examinateur
M. Benjamin LASSAGNE, Examinateur
M. Nicolas BIZIERE, Directeur de thèse
M. Vincent PAILLARD, Président

Remerciements

Enfin est arrivé le moment tant attendu ! Je viens de réaliser un rêve que j'ai depuis le collège : réaliser et présenter une thèse en physique et l'obtenir dans le but de travailler dans la recherche en nanotechnologies (et oui c'était déjà assez précis !).

Ce travail de thèse a nécessité le support et l'apport de plusieurs personnes que je souhaite remercier.

En premier lieu, je remercie vivement l'ensemble des membres de mon jury de thèse : mes rapporteurs Grégoire De Loubens et Catherine Gourdon, mes examinateurs Vincent Cros, Benjamin Lassagne et le président du Jury Vincent Paillard. Merci d'avoir pris le temps d'évaluer mon travail, merci beaucoup pour vos conseils, questions et retours sur le manuscrit.

Ensuite je remercie grandement mon directeur de thèse Nicolas Biziere, pour m'avoir permis de travailler sur un domaine aussi fascinant qu'est la magnonique. Merci pour tout ce que tu m'as appris durant la thèse. Merci beaucoup pour tous tes conseils, ton soutien, ta disponibilité lorsque j'avais le moindre problème ou questionnement. Malgré les (nombreux) soucis d'équipements que nous avons rencontré pendant ma thèse, tu t'es toujours démené pour que je puisse travailler dans les meilleures conditions possibles et je t'en suis énormément reconnaissante. Cette thèse a été de véritables montagnes russes (avec beaucoup beaucoup de loopings !), mais par chance j'aime bien les sensations fortes ! Merci pour toutes nos discussions, ce fut un réel plaisir de travailler avec toi !

Un point clé de ce travail a été d'utiliser la lithographie électronique au CEMES pour réaliser mes échantillons. Je remercie de nouveau Benjamin Lassagne du LPCNO pour m'avoir formée à la lithographie électronique, pour m'avoir conseillée et répondu à toutes mes questions sur cette fabuleuse technique. Mes remerciements vont même remonter à plus loin dans le temps. A l'INSA, tu m'as conseillée et aidée à aménager mon emploi du temps pour ma pratique sportive (vive les SHN !), tu m'as conseillée sur les différents domaines de la physique par rapport à mes affinités, sur le parcours d'étude pour pouvoir faire une thèse, et aujourd'hui j'y suis enfin arrivé ! Merci pour toutes tes recommandations et échanges que l'on a pu avoir !

Ces travaux de thèse ont nécessité l'aide et l'apport de plusieurs personnes au sein du CEMES. Notamment, une très grande part de ces travaux s'est déroulée en salle blanche, je remercie beaucoup Sébastien Pinaud pour tout le support dont j'avais besoin, pour toutes mes questions et ta disponibilité pour le moindre problème. Je remercie également Laure Noé pour m'avoir donnée les bases de lithographie électronique. Ce fut aussi un plaisir de travailler avec vous deux.

Une autre partie de mes travaux concernait le FIB, je remercie beaucoup Robin Cours pour m'avoir formée à cette technique et m'avoir conseillée. Merci beaucoup pour ta gentillesse et ta disponibilité. Concernant le sputtering, je remercie beaucoup Béatrice Pécassou et Sophie Barre pour leur formation et aides. Je remercie également Alain Claverie pour les simulations SRIM pour l'échantillon fait au FIB. Je remercie Nicolas Ratel pour les mesures de caractérisations XRR de certains de nos échantillons. Je remercie Nicolas Renon de Calmip pour la possibilité de faire des simulations OOMMF et

Mumax3 avec les ressources HPC de Calmip.

Je remercie également l'ensemble des membres du groupe MEM.

I would like to thank our collaborators, Silvia Tacchi and Marco Madami, from the Università di Perugia for their micro-BLS measurements on the last sample made in the end of my PhD.

Le bon déroulement de cette thèse a été également supervisé et je tiens à remercier mon parrain de thèse Michel Goiran pour les discussions autour de l'avancée et de l'environnement de ma thèse et tous les conseils apportés. Je remercie l'Ecole Doctorale Sciences de la Matière, en particulier Joël Douin pour ses conseils et aides administratives.

Durant ma thèse, j'ai également eu l'opportunité de faire de l'enseignement. Je remercie Michel Bonnet et le département de Génie Physique de l'INSA Toulouse pour m'avoir permis d'encadrer les TPs de première année en Optique géométrique et Electrocinétique. J'ai beaucoup apprécié cette expérience d'enseignement, qui plus est sur des TPs que j'avais moi-même pratiqué lors de ma première année à l'INSA. Cela fait quelque chose d'être de "l'autre côté" !

Pendant ces trois années de thèse, j'ai rencontré et côtoyé de nombreuses personnes qui ont rendu cette expérience encore plus remarquable.

Elodie, merci pour ta gentillesse, nos diverses discussions sur les animes et tes paroles réconfortantes et motivantes pour la soutenance ! Hâte de voir le résultat en Livaï !

Lionel, le meilleur responsable de master au bureau parfaitement rangé ! Merci pour ta gentillesse et nos fous rires avec Rémi ! Et pour la dernière fois, ce drapeau n'est pas à moi !

Kylian, merci pour tes conseils et ton magnifique placement produit à ta soutenance !

Julien, merci pour ta bonne humeur et pour toutes nos conversations !

Lucas, tu es une personne géniale, merci pour ton humour absurde. Ce fut une superbe rencontre avec Serge. Merci pour ton accueil dans ton magnifique gîte. Sache que j'ai bravé mes peurs pour venir (et celles de Rémi et Benjamin même s'ils ne veulent pas l'avouer). Je te remercie beaucoup pour le petit livre que tu m'as offert, il fut d'un précieux réconfort en fin de rédaction !

Bertrand, merci pour ta gentillesse et ta générosité. Merci pour nos discussions qui me rassuraient et me motivaient. Je suis ravie de t'avoir converti à "Attaque des Titans" !

Paul, alias Bébou, la neutralité à toute épreuve, merci pour tes soirées chez toi ce fut fortement apprécié. Rémi a fait preuve de génie avec cette magnifique photo dossier de toi.

Clément, merci pour ta gentillesse et ta passion pour la musique classique. Comme Cécilia l'a si bien dit, tu es vraiment un rayon de soleil, avec une voix qui traverse les murs et les quartiers.

Cécilia, merci pour tous les bons moments passés ensemble, ta bienveillance et ta générosité.

Rémi, merci pour ton humour et tous nos fous rires. Sache que ce n'est pas bien de rigoler quand quelqu'un se fait torturer dans un film. Merci pour tes propositions de films les plus bizarres !

Ah viens enfin ton tour Benjamin... Sache que j'ai fortement apprécié de t'avoir volé ton grand amour. Heureusement tu peux compter sur Bébou pour compenser en partie cette perte. Pareil, on pourrait écrire un roman sur toi. Tu as tellement égayé ces trois années et demi de thèse ! Je salue ta grande capacité à refaire sur commande des scènes de films avec dialogues complets et jeux d'acteurs (Franck !). Ce qui est drôle c'est que j'ai bien plus de photos dossiers de toi que de Sébastien... Et que dire de nos discussions jeux vidéos (surtout un en particulier), je n'approuve pas tes critiques de ma team, ils sont beaux et forts, c'est tout ce qui compte pour moi !

Martin, ce fut génial de passer ces trois ans avec toi et de partager ce magnifique bureau A226. Tellement bien que visiblement on m'entendait rire dans le couloir, faisant alors apparaître un Rémi furtif à la porte. Ce fut un honneur de faire partie des fondateurs et du bureau de l'association des doctorants au CEMES que nous avons crée, et il est clair que toi et Cécilia en avaient été de grands moteurs ! Désolée pour mes nombreux "je n'ai pas le temps, j'ai salle blanche". Par contre, je ne te remercie pas pour ce montage mixant moi et une tielle, ce n'est pas très respectueux pour cette

superbe spécialité culinaire de ma terre natale.

Aurélien, notre bébé du bureau. J'ai adoré partager ce bureau avec toi aussi. Merci pour ta gentillesse et ton humour timide. J'apprécie très fortement tous tes T-shirts de chats (j'espère que tu en avais un lors de ma soutenance) et ton appétit sans fin (petit trou noir). Prends soin de ma fausse plante carlin que je t'ai légué, elle te portera bonheur.

De manière plus générale, je remercie tous les anciens doctorants, les post-doctorants, permanents Laureen, Toufa, Nicolas, Nicolas, Melvynn, Guillaume, Camille, Rashma, Leifeng, Romain, Mia, Cécile, Florent, Julien, Aurélien, Jimmy et les nouveaux doctorants Anaïs, Marine, Quentin, Simon (encore merci pour ce super gâteau au chocolat pour mon anniversaire !), Loïc, Hassan, Agathe, Elio, Estefania, Liz, Malo, Benoit, Elie, Kedar, Afnan... et je m'excuse si j'en oublie certains.

Je remercie le club de volley Balma Quint-Fonsegrives, en particulier mes coachs Thomas, Guillaume, Olivier pour avoir toléré mes retards ou absences pour pas mal d'entraînements à cause du travail ! Évidemment merci à l'équipe aussi et big up à notre montée en élite !

Pour finir je souhaite remercier les membres de ma famille.

Tout d'abord je remercie ma belle-famille, Florence, Jacques, Emma, Sophie, Pierre et le petit dernier Gaspard (tu es le plus beau, ne le dis pas à Sébastien). Vous m'avez apporté beaucoup de soutien, joie et réconfort tout au long de la thèse. Je remercie fortement tout particulièrement Florence et Jacques qui m'ont chouchouté pendant les quelques mois de rédaction, me permettant d'être dans de très bonnes conditions pour terminer le manuscrit et la soutenance.

Je remercie Lydie pour son soutien, c'était génial Port Aventura.

Je remercie mes grands-parents, Josy et Jean-Louis, Daniel et Antoinette d'avoir suivi mes péripéties de thèse et de m'avoir soutenu dans les moments de doute. Josy, Daniel votre départ fut une étape douloureuse sur mon chemin, j'aurais aimé que vous puissiez en voir le résultat, je sais que vous êtes fiers de moi.

Je remercie mes frères géniaux, Hadrien et Nathan pour leur soutien, amour et nos débats enflammés lors des repas.

J'ai la chance d'avoir des parents extraordinaires, Sabine et Eric. Vous m'avez toujours encouragée, soutenue, donné les moyens pour poursuivre mes différentes passions. Ce fut un temps le volley, et depuis bien plus longtemps la physique. Vous m'avez toujours réconfortée et aidée quand j'étais au plus bas moralement, je vous remercie d'être aussi géniaux et de tout l'amour que vous nous apportez à mes frères et moi-même. Je vous aime. Comme tu le dis si bien Papa, "petit à petit l'oiseau fait son nid".

Enfin je remercie mon compagnon Sébastien, pour tout l'amour et support que tu as pu me donner pendant ces années de thèse (sauf la dernière année où tu as fui en Allemagne !). Tu m'as énormément apporté de joie, d'amour, de soutien, de confiance, tu m'as rassurée dans les moments de doute. Ton don culinaire fut un atout indéniable au bon déroulé de ma thèse. Bientôt ce sera ton tour de rédiger ! (et à moi de cuisiner ?)

Bon Maman, tu as toujours dit que tu aimerais avoir un docteur dans la famille, et bien voilà c'est chose faite !

Contents

Introduction

In a magnetic material, a uniform or localized perturbation of the magnetic order results in the collective or propagative precession of the spin magnetic moments. When the precession of the magnetic moments is not uniform (i.e. not in phase), one speaks of a spin wave (or magnons when treated in the corpuscular case), the concept of which was introduced by Bloch in 1930 [1]. These waves have several special characteristics compared to electromagnetic waves propagating in vacuum, which make them very attractive for miniaturizing high-frequency components (from a few hundred MHz to ten THz) despite the fact that they have slower group velocities compared to photons. First of all, their wavelengths are generally several orders of magnitude lower than those in vacuum and their frequencies can be adjusted via a magnetic field for example. They have a dispersion relation $f(k)$ whose characteristics vary according to the magnetic order (ferro, ferri, anti-ferromagnetic) of the material, the shape of the latter or the amplitude and orientation of an applied magnetic field. Their propagation can thus show an isotropic or anisotropic character.

Magnonics is the topic that focuses on the study of the emission, propagation and detection of these spin waves. This area has been the subject of intense research for about 20 years with the aim of developing new electronic components that are potentially less energy-consuming and more versatile. For example, it has been demonstrated in laboratories that the control of the amplitude and/or the phase of these waves can be used to produce logic components (with the example of the magnon transistor [2]), microwave components (radio frequency filters, phase delay lines, phase shifters, circulators, multiplexers... [3]) or for communication technologies (5G) [4–7]. Magnonics thus embraces a strong potential, whether fundamental or applied, through promises of miniaturization, wide usable frequency band and low energy consumption. It is also to be noted that spin waves carry a "spin current", the magnetic equivalent of a load current but without ohmic loss. By combining magnetic materials with materials with a strong spin-orbit coupling, a new field called "spin-orbitronics" is in full swing and opens up new avenues for developing very low-energy components, while reducing their size and giving them a multifunctional character. All these studies in magnonics and spin-orbitronics are motivated by the need to go beyond CMOS technologies, and as such, spin wave devices were mentioned in 2021 as a credible alternative to CMOS by " the International Roadmap for Devices and Systems (IRDS)" [8]. For example, it should be noted that 50 nm magnonic waveguides have been produced, thus having dimensions close to those of current CMOS transistors [9].

Within the framework of this thesis, we were interested in a particular type of system of magnonics called "magnonic crystal". A magnonic crystal is a magnetic material whose magnetic properties are periodically and artificially modified. The propagation of spin waves in these systems follows the laws established and formalized in 1929 by C. Kittel concerning the propagation of waves in periodic systems and which have since constituted the foundations of solid-state physics [10]. An important property of these structures which makes them unique and attractive is that the propagation of waves in these media can only take place in certain very specific frequency bands. Indeed, for wave vectors corresponding to a multiple of the elementary length of the periodic lattice, the waves are in Bragg conditions. This results in the appearance of stationary modes (therefore non-propagating) with, in

addition, an energy band in which no wave can propagate. Magnonic crystals thus allow the emergence of a multitude of innovative methods to control and modulate spin waves for logic operations or signal processing. These objects are thus the magnetic counterparts of the photonic crystals in optics which were born in 1987 [11, 12] and which made it possible to guide and/or trap light to produce more efficient optical integrated circuits and photovoltaic solar cells [13]. However, although known since the 1970s [14], it was not until the early 2000s that the concept of magnonic crystal reappeared [15, 16], in particular thanks to the mastery of nanofabrication techniques as well as ultra-thin film deposits.

Compared to other artificial crystals, magnonic crystals offer a major advantage: the band structure is not only dependent on the periodicity of the crystal, it can change depending on the magnetic configuration or the application of an external field. This additional degree of freedom strongly distinguishes them from photonic crystals. To go further in band engineering, several strategies, other than the application of a magnetic field, have been explored in the literature, in particular by varying the geometry of the reflective centers of the magnonic crystal such as for example the thickness, the width or the number of magnetic layers [17, 18], the presence of discs [19, 20] or holes [21–23], but also by modulating the magnetic constants through the incorporation of another material [24, 25] or by ion implantation [26] in the magnetic layer

The magnonic crystals thus present a rich diversity of applications. In the work presented in this manuscript, we were particularly interested in their radio frequency (RF) absorption and filtering properties [23, 27, 28]. In particular, our main objective was to obtain a model system operating at zero bias field (i.e. at remanence) but presenting RF absorption bands which could be modified on purpose. This type of components is called reconfigurable. The advantage of having systems operating at remanence is to avoid using permanent magnets to maintain uniform magnetization in the magnetic material and ensure the functionality of the component. Indeed, the majority of magnonic devices and magnonic crystals discussed in the literature operate with a saturated magnetization along a particular direction. No longer using permanent magnets will not only solve the stray field problems associated with magnets which complicate the integration of components, but also respond to the ecological and economic problems linked to the supply of rare earths and whose the market is controlled by only a few countries.

Regarding the reconfigurable aspect, the objective is to obtain components that can have several functionalities, again with the aim of reducing the ecological and energy impact of the components. The reconfigurability of the device is generally obtained by transitioning the system between different remanent magnetic states having different RF responses. Although presenting a strong application potential, there are still relatively few studies in this field. Among the works carried out, we can mention in particular those concerning the use of networks of nanopillars [29, 30], of elliptical nanostructures with two different magnetic materials [31], or of nanowires coupled by dipolar interaction [32–34]. However, most of these works require complex remanent state initialization schemes with large applied field amplitudes. Among the most promising avenues is the use of shape anisotropy in nanostructures of rhombohedral shape and specific dimensions. These structures allow the stabilization of a quasi-uniform magnetic configuration along the long or short axis of the nanostructure [35] via a magnetic pulse of the order of few tens of mT. A frequency shift of the spin wave modes of the order of 400-600 MHz depending on the configurations used [36, 37] was thus obtained. To increase this frequency gap, the authors used the same type of nanostructures but composed of several magnetic layers spaced by a non-magnetic material (for example NiFe/Cr/NiFe), thus allowing frequency shifts in the range 3-15 GHz from 1 GHz up to 5 GHz depending on the number of magnetic and non-magnetic layers and their arrangement [38–40]. In addition, they also demonstrated the possibility of propagating spin waves at remanence through straight or curved waveguides formed by an arrangement of chains of these same nanostructures [41], making it possible to obtain a function of the "spin wave switch" type [41].

In the work presented here, we have sought to achieve a reconfigurable magnonic crystal at re-

manence from a simple and well-known geometry, namely a periodic array of holes in a thin film (or "antidot lattices" in the literature). Over the past ten years, a very large number of publications have focused on the determination of spin wave modes in this type of artificial lattice as well as on the observation of forbidden frequency bands. Beyond applications in magnonics, they have also been studied to produce high-density storage memories [42, 43] or magnetic nanoparticle sensors [44]. To obtain the reconfigurability at remanence of this lattice of holes, we chose to explore a way little followed for the moment in magnonics. This consists in taking advantage of the intrinsic properties of the materials and, in particular for our case, of the cubic magnetocrystalline anisotropy of some. Few research works have explored the intrinsic magnetic properties of the magnetic material in order to produce reconfigurable RF components at remanence. There is the case of thick films of magnetic ferrites like bismuth hexaferrite which have strong magnetic anisotropy [45]. Such devices are currently marketed [46], however, due to their thickness and dimensions (in the order of mm), such magnetic films are difficult to nanostructure, thus limiting the miniaturization of the component. In the case of thin films, most studies in magnonics in general, or on magnonic crystals in particular, have been carried out either with YIG or with permalloy (Py). YIG is a ferrimagnetic insulating material and has the lowest dynamic damping coefficient (3.10^{-5}) [47], which makes it possible to propagate spin waves over distances up to millimeters in the case of thick films (of the order of µm) [7]. Nevertheless, it has a low saturation magnetization (about 0.17 T) which limits the usable RF range (a few hundred MHz close to remanence). All the experimental demonstrations of logical operations mentioned above were carried out with YIG. However, in order to be compatible with existing CMOS technologies, one must be able to grow it in its crystalline form on silicon substrates, which is still quite complex from a technological point of view although great progress has been made in recent years [48]. Permalloy is a metallic ferromagnetic material very widely used in the literature because of its ease of fabrication and nanostructuring [7]. Its saturation magnetization is relatively high (1 T) but its damping coefficient is much higher than the one of YIG (about 6.10^{-3}) [7]). As a result, the attenuation length (proportional to $1/\alpha$) that the spin waves can travel, where their amplitudes are decreased by a factor of $1/e$, is of the order of only a few microns.

Thus, we studied the possibility of fabricating an antidot array from a thin film of the Heusler alloy Co_2MnSi [49, 50]. This material has been studied at CEMES for several years [51–53]. In the context of our work, its main advantage compared to YIG or Py is its cubic anisotropy which can reach a few tens of mT [52, 53]. We will show that this allows i) to stabilize quasi-uniform magnetic states in antidot arrays having the good aspect ratio between the size of the antidots and their spacing and ii) to adjust the number and the frequencies of the reconfigurable spin wave modes depending on the antidots size. It is interesting to note that, to our knowledge, only a few studies on magnonic waveguides based on Heusler alloys have been carried out until now [54–59], and even less on the production of magnonic crystals based on Heusler alloys [49, 50]. Compared to YIG or Py, the Co_2MnSi Heusler alloy also has other advantages. It is ferromagnetic with a saturation magnetization of approximately 1.3 T. This makes it possible to obtain working frequencies at remanence above 1 GHz [52, 53] and, in the case of magnonic crystals, to increase the width of the forbidden frequency bands [60, 61]. It is also half-metallic (spin polarization greater than 90% [62, 63]) which is the cause of a low damping coefficient value ranging from 1.10^{-3} [53, 64] to 4.10^{-4} [54, 65]. Finally, its Curie temperature of around 985K [66] offers a good thermal stability to the components. Thus, it makes it possible to consider the development of devices combining magnonics, spintronics and spin-orbitronics [67, 68]. Its main drawback concerns its fabrication. It is usually deposited on MgO (001) substrates to ensure an epitaxial growth, which could limit its compatibility with existing microelectronic devices. However, a recent research work has proven that it is possible to grow polycrystalline Co_2MnSi on (amorphous) glass substrates without a drastic change in the spin polarization and damping coefficient (on the order of $1.5.10^{-3}$) [64]. Such a result offers the prospect of depositing good quality Co_2MnSi on silicon substrates making the transition to industrial applications compatible.

This manuscript is organized around six chapters. While the first chapter offers a reminder of the

basic mechanisms of spin dynamics in magnetic thin films, the second will address the fundamental concepts and the state of the experimental art concerning magnonic crystals. It will also introduce a description of Heusler alloys, in particular Co_2MnSi. The third chapter will describe the numerical and experimental techniques used during our work. After presenting the main magnetic properties of the Co_2MnSi thin film deposited at the CEMES, the chapter 4 will go into details in one of the main task of this work, namely the micro and nanofabrication processes developed to obtain magnonic crystals from a thin film of Co_2MnSi. In particular we will present the two different strategies that have been explored to realize the antidot arrays, i.e. FIB milling on one side and electron beam (e-beam) lithography followed by Ar^+ ion milling on the other side. The chapter 5 will present a purely numerical study in which we will show the necessary conditions (antidots size and spacing) to obtain reconfigurable spin wave modes at remanence in a square antidot lattice made of Co_2MnSi. We focused our attention on hole dimensions compatible with nanofabrication techniques. We will highlight in particular the contribution of the cubic anisotropy compared to isotropic materials. We will also show how the size of the holes and their spacing modify the number and frequency of reconfigurable modes. We discuss the effect of a finite sample size since the first part of the chapter deals with the case of a quasi-infinite crystal. Finally, we will present the expected performance of this artificial component to go from one quasi-uniform remanent state to another under the effect of a field pulse by following a numerical strategy proposed by other authors. The last chapter will address the characterization by ferromagnetic resonance of spin wave modes in magnonic crystals fabricated either by FIB or by electron beam lithography followed by Ar^+ ion etching. We will show in particular the impact of FIB etching on the modification of the intrinsic properties of the Heusler alloy and consequently on the spectrum of the measurable spin wave modes. The spatial profile of the different measured modes will be discussed according to the evolution under field of the state of magnetic equilibrium. In a last part we will show that despite a relatively degraded quality of our sample which is explained in chapter 4, some reconfigurable spin wave modes could be observed for magnonic crystals made from e-beam lithography and ion beam etching.

Chapter 1

Dynamic magnetism

In this chapter, we recall the fundamentals of dynamic magnetism through the different magnetic interactions, the formalization of uniform precession of magnetization and the concept of spin waves. The concepts of ferromagnetic resonance and spin waves dispersion are described, in particular in the case of magnetic thin films and magnetic stripes with magneto-crystalline anisotropy. Finally, the notions of relaxation and damping of magnetization are briefly approached.

1.1 Micromagnetism

1.1.1 Origin and classification of magnetic materials

To some extent, all materials can be described as magnetic [69]. Magnetism comes from the magnetic moments of the atoms constituting matter. In the same way that a current loop produces a magnetic moment perpendicular to the plane of the loop, the movement of electrons generates a magnetic moment. The atomic nucleus also has a magnetic moment but it is much weaker than the one from the electrons (three orders of magnitude separate them [70]). As a result, the materials magnetism results mainly from electrons. The electron magnetic moment is composed of two contributions. The first contribution is related to the orbital motion of the electron around the atomic nucleus, which generates a magnetic moment normal to the plane of the orbit. The second is associated with an intrinsic property of the electron called spin. One can imagine the spin as the precession of the electron on itself, which produces a magnetic moment parallel to the axis of rotation. In reality, this representation is false as the shape of the electron or the distribution of its charge in its volume are not known. Moreover, the spin has no classical analogue and can only be correctly described in a quantum manner. The magnetic moment thus generated by the orbital magnetic moment $\vec{L}$ and spin magnetic moment $\vec{S}$ can be written as [70] :

$$\vec{m} = -\gamma_e(\vec{L} + \vec{S}) = -\gamma_e \vec{J} \tag{1.1}$$

with $\vec{J}$ the total angular momentum of the electron and $\gamma_e = \frac{g|e|}{2m_e}$ the electronic gyromagnetic factor with g the Landé factor, e the elementary charge of an electron and m_e its elementary mass. The Landé factor g has a value of 2 in the case of a magnetic moment $\vec{m}$ solely comprising the spin moment (case of a free electron) and a value of 1 in the case where the magnetic moment is purely orbital.

The global magnetic moment of materials is then the vector sum of all atomic magnetic moments.

The magnetic moment or magnetic dipole $\vec{m}$ is an elementary quantity of magnetism affiliated to atoms. In micromagnetism, one can nevertheless consider a magnetic system as a continuous mesoscopic medium by freeing oneself from the description of the system at the atomic scale. The notion of magnetic moment per unit volume V or magnetization $\vec{M}$ can be introduced as [71]:

$$\vec{M} = \frac{\sum_V \vec{m}}{V} \tag{1.2}$$

The application of a magnetic field $\vec{H}$ will tend to align the magnetization along the direction of $\vec{H}$. The response of the magnetization $\vec{M}$ to an applied magnetic field $\vec{H}$ is expressed through the magnetic susceptibility $\bar{\chi}$ [72]:

$$\vec{M} = \bar{\chi} \cdot \vec{H} \tag{1.3}$$

Magnetic susceptibility $\bar{\chi}$ is a 3×3 tensor, and in the case of isotropic materials it reduces to a scalar χ.

Depending on the magnetic order, orientation and magnitude of the atomic magnetic moments in a solid, it is possible to group materials into different magnetic classes.

When the electronic layers of atoms or ions are complete, by the Pauli exclusion principle, they do not have permanent magnetic moments. In this case, the material is called diamagnetic or non-magnetic because of its weak response to a magnetic field. When a magnetic field is applied to a diamagnetic material, the orbital motion of the electrons is altered in such a way as to produce an opposite magnetic field, which implies a negative magnetic susceptibility ($\chi < 0$). This diamagnetic behaviour is in fact present in all types of materials, but this effect remains very weak compared to other magnetic responses, which will be discussed below.

When the electronic layers of atoms or ions are incomplete, they have permanent magnetic moments. If the material has no long-range magnetic order, the latter is then paramagnetic. The atomic magnetic moments are randomly oriented due to thermal fluctuations, implying a null total magnetic moment. When a magnetic field is applied, these magnetic moments will partially align with the field inducing a permanent magnetic moment. The magnetic susceptibility is then weakly positive ($\chi > 0$). By removing the magnetic field, the magnetization is not preserved.

Materials with a long-range magnetic order can be ferro-, ferri- or antiferromagnetic. Depending on the relative orientation of the neighbouring atomic magnetic moments, they may have a spontaneous macroscopic magnetic moment, i.e. one that remains in the absence of a magnetic field, or not. Above a certain critical temperature, called the Curie temperature for ferromagnetic and ferrimagnetic materials and the Néel temperature for antiferromagnetic materials, the atomic magnetic moments of these materials orient themselves randomly, becoming paramagnetic. In the case of antiferromagnetic materials, they consist of two sub-arrays of magnetic moments, one oriented spontaneously in one direction and the other oriented in the opposite direction, implying a total magnetic moment of the material of zero ($\chi > 0$). Ferrimagnetic materials also exhibit antiparallel magnetic moments but they are not equivalent in magnitude, thus generating a spontaneous macroscopic magnetic moment. These different amplitudes of antiparallel magnetic moments can be obtained with a material composed of different types of atoms or ions. Finally, ferromagnetic materials have a parallel alignment of their magnetic moments also implying spontaneous magnetization. The magnetic susceptibility of ferro- and ferrimagnetic materials is then positive and very large ($\chi \gg 0$).

In this thesis, we worked with the Heusler alloy $\mathrm{Co_2MnSi}$ (CMS) which is a ferromagnetic material. In the following section we will discuss the magnetic interactions that favor the orientation of magnetic moments.

1.1.2 Magnetic interactions and effective magnetic field

The orientation of magnetic moments in a finite-size sample is not uniform throughout its volume at equilibrium. The latter has magnetic domains, where the magnetization is uniform, resulting from the competition between different magnetic interactions. In this case, the macroscopic magnetization of this magnetic sample is written as [71]:

$$\vec{M} = \frac{\sum_i \vec{M}_i V_i}{\sum_i V_i} \tag{1.4}$$

with $\vec{M}_i$ and V_i the magnetization and the volume of the magnetic domains respectively. The norm of the magnetization is constant in space and varies only with temperature:

$$\|\vec{M}(\vec{r})\| = M_s(T) \tag{1.5}$$

Thus only the direction of the magnetization $\vec{M}(\vec{r})$ varies and its norm is the saturation magnetization M_s. By applying a magnetic field strong enough to saturate the ferromagnetic sample, the magnetic domains disappear to reveal the saturation magnetization M_s.

The predominance of these magnetic interactions governing the magnetic domains depends on the type of material (exchange interaction), its crystal structure (magnetocrystalline anisotropy), its shape (dipole interaction, shape anisotropy) and the presence of external magnetic fields (Zeeman interaction). The distribution of magnetic directions in a material results from the minimization of the total free energy of the magnetic system, which is composed as follows:

$$E_{tot} = E_{ex} + E_K + E_d + E_Z \tag{1.6}$$

The first three energy terms are affiliated with the exchange interaction, the magnetocrystalline anisotropy and the dipolar interaction respectively. These interactions are intrinsic to the magnetic system. The fourth term is the Zeeman interaction which results from an applied external magnetic field. Other interactions exist, such as magnetostriction, but these are weak in the magnetic system studied in this thesis. For this reason they will be neglected.

The different energy terms will be expressed with spherical coordinates with the notations used in Figure 1.1. The magnetization with cartesian coordinates (M_x, M_y, M_z) is expressed with the

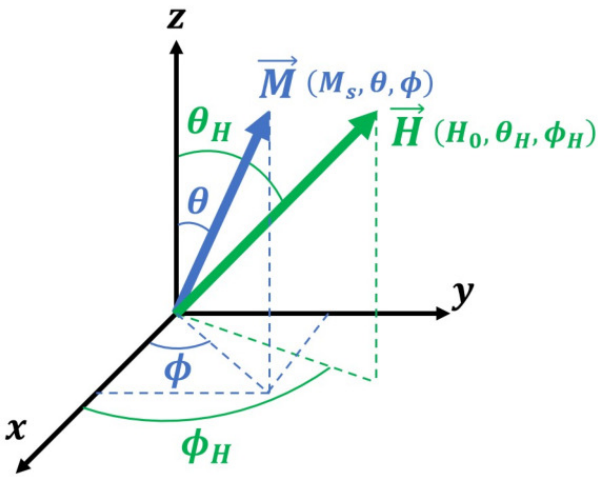

Figure 1.1: Representation of the magnetization $\vec{M}$ and the applied magnetic field $\vec{H}$ in a Cartesian reference frame in spherical coordinates

spherical coordinates (M_s, θ, ϕ) according to:

$$M_x = M_s \sin\theta \cos\phi \qquad M_y = M_s \sin\theta \sin\phi \qquad M_z = M_s \cos\theta \tag{1.7}$$

Exchange interaction

The exchange interaction, introduced in 1928 by Heisenberg [73], is a purely quantum effect and is at the origin of the long-range magnetic order, especially in ferromagnetic materials. Electrons carry magnetic moments and by the Pauli exclusion principle, electrons cannot occupy the same quantum state, i.e. they cannot be in the same position if they have the same spin. Since electrons are indistinguishable fermions, the total wave function of the multi-electron system must be antisymmetric when one electron is exchanged with another. The total wave function of the multi-electron system can be decomposed into a spatial component and a spin component. In a two-electron system, this translates into two possible combinations: the spin component of the total wave function is symmetric (parallel spin alignment) with the spatial component of the total wave function which is then antisymmetric or vice versa. The change of symmetry of the spatial component of the wave function involves different positions of the electrons with respect to each other but also with respect to the atomic nuclei. By Coulomb repulsion and attraction, a preferential symmetry of the spatial component of the wave function will impose on the system, and the spin component of the wave function will adapt its symmetry by favoring an alignment of parallel (ferromagnetic materials) or antiparallel (ferrimagnetic, antiferromagnetic materials) spins. The exchange interaction energy is written as the sum of scalar products of magnetic spin moments weighted by a coupling parameter J_{ij}:

$$E_{ex} = -\sum_{i \neq j}^{N} J_{i,j} \vec{S_i} \cdot \vec{S_j} \tag{1.8}$$

with J_{ij} the exchange integral. This parameter represents the overlap of the orbitals of two electrons i and j and its value depends mainly on their relative distance. In the case where the exchange integral is positive, the exchange energy is lower with a parallel configuration of spins (ferromagnetism), and in the case of a negative exchange integral, an anti-parallel configuration (antiferromagnetism, ferrimagnetism) is favored. As discussed previously, the exchange interaction is limited to small distances (nearest neighbour atoms) due to the necessity of overlapping electronic orbitals. Nevertheless, this interaction allows magnetic order to be established over long distances through indirect exchange interactions, particularly in the case of ferromagnetic metallic materials with the exchange interaction via the conduction electrons. The indirect exchange interactions are reflected in the value of the exchange integral and its dependence on the interatomic distance. This interaction is thus at the origin of spontaneous magnetization in ferromagnetic materials. Furthermore, it can be noted that the exchange interaction does not depend on a particular periodicity of position of the atoms, so it is not necessary to have a crystalline material for it to be ferromagnetic.

In micromagnetism, for a magnetic volume, the exchange energy can then be written as:

$$E_{ex} = \frac{A}{M_S^2} \int (\vec{\nabla} \cdot \vec{M}(\vec{r}))^2 dV \tag{1.9}$$

with $\vec{r}$ the position (x, y, z) in space and A the exchange constant characterizing the intensity of the exchange interaction which is specific to a material (unit $\mathrm{J\,m^{-1}}$). It depends on the spin of the atoms, the atomic number Z of the atoms, the exchange integral and the interatomic distance. The exchange interaction can also be described by an exchange field $\vec{H}_{ex}$ such as:

$$\vec{H}_{ex} = \Lambda_{ex}^2 \vec{\nabla}^2 \vec{M} \tag{1.10}$$

with Λ_{ex} the exchange length which describes the range of the exchange interaction, i.e. the distance below which the exchange interaction predominates over the dipolar interaction which, we will see just after, is a long range interaction. The exchange length is written as:

$$\Lambda_{ex} = \sqrt{\frac{2A}{\mu_0 M_S^2}} \tag{1.11}$$

with μ_0 the vacuum permeability. For ferromagnetic metals, the exchange length is generally in the order of nm. For example for NiFe and Co_2MnSi it is close to 5 nm.

Dipolar interaction

The dipole interaction corresponds to the impact of the magnetic field generated by the magnetic sample on itself. This corresponds to a dipole-dipole interaction of all the magnetic moments of the sample: each magnetic moment generates a dipole field and is subjected to the magnetic field generated by all the other magnetic moments. As all magnetic moments must be taken into account for the calculation of the dipole field, this interaction is long range. Discontinuities of the magnetization at the edges of the sample (component of the magnetization normal to an external or internal surface) produce magnetic poles which induce a dipole field $\vec{H}_d$ opposite to the magnetization. This interaction results from Maxwell's principle which states that there can be no magnetic monopole or divergence of the magnetic field. Consequently, whenever the magnetization is such that $\vec{\nabla} \cdot \vec{M} \neq 0$, a demagnetizing field will appear to recover a zero magnetic field divergence. The dipole field thus also enters in competition with the uniform magnetization resulting from the exchange interaction, which then generates magnetic domains within the sample. The dipole energy E_d, also called magnetostatic energy, is therefore minimized when the magnetic field fluxes are closed and is expressed as follows:

$$E_d = -\frac{\mu_0}{2} \int \vec{M} \cdot \vec{H}_d dV \tag{1.12}$$

To determine the dipole field $\vec{H}_d$, one can use Maxwell's equations in the magnetostatic approximation (absence of electrical charges and currents, the system is considered quasi-static, it is slow compared to the speed of light) [74–76], which will be discussed in more detail later in section 1.3.1:

$$\vec{\nabla} \times \vec{H}_d = 0 \tag{1.13}$$

$$\vec{\nabla} \cdot \vec{B} = \mu_0 \vec{\nabla} \cdot (\vec{H}_d + \vec{M}) = 0 \tag{1.14}$$

With the equation (1.13), a scalar potential Φ_d is associated with the dipole field such that $\vec{H}_d(\vec{r}) = -\vec{\nabla}\Phi_d(\vec{r})$. Using the equation (1.14), the scalar potential can be written [74, 75]:

$$\Phi_d(\vec{r}) = \frac{1}{4\pi} \left[\int_V \frac{\lambda_V(\vec{r'})}{|\vec{r} - \vec{r'}|} d^3\vec{r'} + \int_S \frac{\sigma_S(\vec{r'})}{|\vec{r} - \vec{r'}|} d^2\vec{r'} \right] \tag{1.15}$$

The first term of the sum comprises $\lambda_V = -\vec{\nabla} \cdot \vec{M}$ which corresponds to the magnetic charges of the volume, which will thus generate a dipolar field. The second term with $\sigma_S = \vec{M} \cdot \vec{n}$ corresponds to the magnetic surface charges with $\vec{n}$ the normal to the surface of the magnetic sample pointing outwards. It is in particular this second term that gives rise to the demagnetizing field $\vec{H}_{demag}$ generated by the shape of the magnetic sample. The dipole field being the gradient of the scalar potential, it is expressed as follows [74] :

$$\vec{H}_d(\vec{r}) = \frac{1}{4\pi} \left[-\int_V \vec{\nabla} \cdot \vec{M}(\vec{r'}) \frac{\vec{r} - \vec{r'}}{|\vec{r} - \vec{r'}|^3} d^3\vec{r'} + \int_S \vec{M}(\vec{r'}) \cdot \vec{n}(\vec{r'}) \frac{\vec{r} - \vec{r'}}{|\vec{r} - \vec{r'}|^3} d^2\vec{r'} \right] \tag{1.16}$$

The dipole interaction predominates over the exchange interaction over long distances because of its intensity proportional to $\frac{1}{|\vec{r}-\vec{r'}|^3}$ with $|\vec{r}-\vec{r'}|$ the relative position of the magnetic moments [77].

If the magnetization is uniform in the volume, the first term in the formula (1.16) disappears. As a result, the dipole field is now only conditioned by the geometry of the magnetic system (demagnetizing field), which is also called shape anisotropy. By reducing the shape of a sample to a uniformly magnetized ellipsoid, the dipole or demagnetizing field becomes a linear function of the magnetization and is therefore more easily written as:

$$\vec{H}_{demag} = -\overline{\overline{N}}\vec{M} \tag{1.17}$$

with $\overline{\overline{N}}$ the demagnetizing tensor which will be discussed in more detail in section 1.2.3. Apart from simple geometries, the calculation of the dipole field remains complex such as in the case of magnonic crystals, where there are few or no general analytical formulas (some exist for very particular cases, which are mentioned in section 2.1.2 of chapter 2). In this case, micromagnetic simulations through the spatial discretization of the structures, detailed in section 3.1.1 of chapter 3, represent very useful tools for the calculation of the demagnetizing field in these structures.

In the spherical coordinate system (M_s, θ, ϕ) of Figure 1.1, the energy density of the demagnetizing field in the case of a uniformly magnetized ellipsoid can be written as:

$$e_{demag} = \frac{\mu_0}{2}\vec{M}\cdot\overline{\overline{N}}\vec{M} = \frac{\mu_0}{2}M_s^2\left[N_x\sin^2\theta\cos^2\phi + N_y\sin^2\theta\sin^2\phi + N_z\cos^2\theta\right] \tag{1.18}$$

with N_x, N_y and N_z scalar elements of $\overline{\overline{N}}$ with $N_x + N_y + N_z = 1$.

Magnetocrystalline anisotropy

The orbital magnetic moments of the electrons are influenced by electrostatic forces coming from the atomic sites. These electrostatic interactions are anisotropic with respect to the crystal symmetry of the material and tend to favor particular electron orbitals. By spin-orbit coupling, which corresponds to the coupling between the spin magnetic moment and the orbital magnetic moment, the spin magnetic moments of the electrons are then also influenced by the crystal symmetry and preferentially align along a particular crystallographic direction. On a macroscopic scale, this translates into the presence of easy and difficult axes of magnetization which therefore depend on the crystal structure of the system [78]. An easy axis (hard axis) corresponds to a crystallographic direction for which the magnetic moments will preferentially align (avoid alignment). This results in an anisotropic magnetic energy corresponding to the work required by an applied magnetic field to orient the magnetization out of the axis of easy magnetization. This energy can be written as:

$$E_K = \int e_K dV \tag{1.19}$$

with e_K the magnetocrystalline energy density. Its expression depends on the symmetry of the magnetic crystal system.

The simplest case is uniaxial anisotropy, as it has only one direction of easy magnetization. This type of anisotropy can occur in thin films stressed during growth or naturally in crystalline solids with hexagonal symmetry. The magnetocrystalline energy density is written in this case up to order 2 [69, 70, 74, 76]:

$$e_{K_u} = K_{u1}\sin^2\beta + K_{u2}\sin^4\beta \tag{1.20}$$

$$e_{K_u} = -\frac{K_{u1}}{M_s^2}(\vec{u}\cdot\vec{M})^2 - \frac{K_{u2}}{M_s^4}(\vec{u}\cdot\vec{M})^4 \tag{1.21}$$

with K_{ui} the uniaxial anisotropy constants at order i (1, 2) in $\mathrm{J\,m^{-3}}$ and β the angle between the magnetization $\vec{M}$ and the uniaxial anisotropy axis $\vec{u}$. The expression of e_{K_u} with (1.21) is the formulation

used for micromagnetic simulations. By considering only the first order and when K_{u1} is positive, the magnetocrystalline energy is minimal when $\beta = 0$, and thus the uniaxial anisotropy axis $\vec{u}$ is an axis of easy magnetization, as shown in Figure 1.2 a). When K_{u1} is negative, the energy is minimal when $\beta = 90°$. In this case, we have a plane of easy magnetization which is perpendicular to the uniaxial anisotropy axis (Figure 1.2 b)).

In the spherical coordinate system (M_s, θ, ϕ) of Figure 1.1, the uniaxial anisotropic energy density along the direction of the uniaxial anisotropy axis defined either along the x, y or z axes can be written respectively:

$$\begin{cases} \text{Axis of uniaxial anisotropy along } \vec{x} : e_{K_u} = K_{u1}\left(1 - \sin^2\theta\cos^2\phi\right) \\ \text{Axis of uniaxial anisotropy along } \vec{y} : e_{K_u} = K_{u1}\left(1 - \sin^2\theta\sin^2\phi\right) \\ \text{Axis of uniaxial anisotropy along } \vec{z} : e_{K_u} = K_{u1}\sin^2\theta \end{cases} \tag{1.22}$$

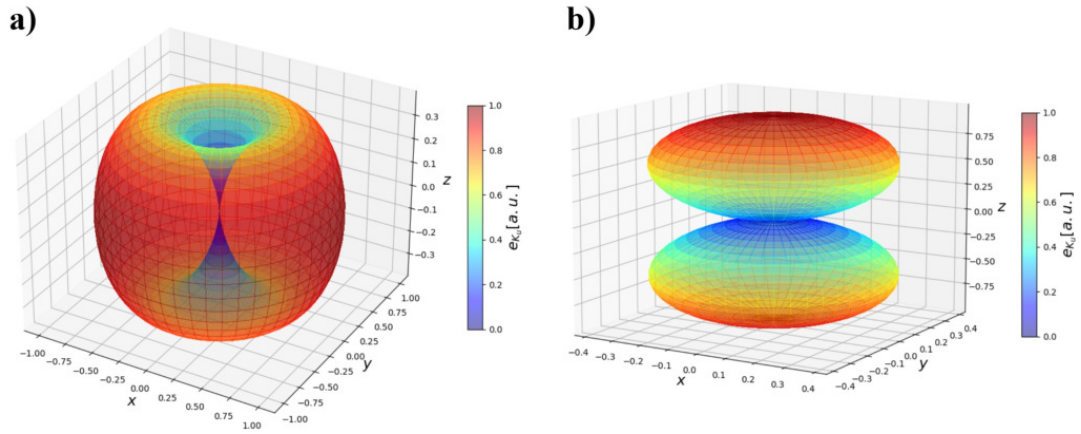

Figure 1.2: Uniaxial magnetocrystalline anisotropy energy density with a) $K_{u_1} > 0$, the $\vec{z}$ axis is the easy magnetization axis, and b) $K_{u_1} < 0$, the (xy) plane is an easy magnetization plane.

The second magnetocrystalline anisotropy which is frequently present and which, in the context of this thesis, is of great importance is the cubic anisotropy. Indeed, as Fe or Ni [71], Co_2MnSi Heusler alloy exhibits a cubic magnetocrystalline anisotropy by having several easy and hard axes. Taking the orthogonal axes of cubic anisotropy $\vec{a}$, $\vec{b}$ and $\vec{c}$, the cubic energy density can be written as [69, 70, 76]:

$$e_{K_c} = K_{c1}(\alpha_1^2\alpha_2^2 + \alpha_2^2\alpha_3^2 + \alpha_3^2\alpha_1^2) + K_{c2}(\alpha_1^2\alpha_2^2\alpha_3^2) \tag{1.23}$$

$$e_{K_c} = \frac{K_{c1}}{M_s^4}\left[(\vec{a}\cdot\vec{M})^2(\vec{b}\cdot\vec{M})^2 + (\vec{b}\cdot\vec{M})^2(\vec{c}\cdot\vec{M})^2 + (\vec{c}\cdot\vec{M})^2(\vec{a}\cdot\vec{M})^2\right] + \frac{K_{c2}}{M_s^6}\left[(\vec{a}\cdot\vec{M})^2(\vec{b}\cdot\vec{M})^2(\vec{c}\cdot\vec{M})^2\right] \tag{1.24}$$

with $\alpha_i = \frac{M_i}{M_s}$ the cosine directions with respect to the axis i of the cubic symmetry and M_i are the components of the magnetization projected on the i axis. The formulation (1.24) of the magnetocrystalline energy density is also the one most commonly used in micromagnetic simulations. By taking the cubic symmetry along the x, y, z axes of the magnetic system, one can express the α_i such that:

$$\alpha_x = \frac{M_x}{M_s} = \sin\theta\cos\phi \qquad \alpha_y = \frac{M_y}{M_s} = \sin\theta\sin\phi \qquad \alpha_z = \frac{M_z}{M_s} = \cos\theta \tag{1.25}$$

By focusing only on the first order and by combining (1.23) and (1.25), the cubic magnetocrystalline energy density is then written :

$$e_{K_c} = K_{c1}\sin^2\theta(\cos^2\theta + \sin^2\theta\cos^2\phi\sin^2\phi) \tag{1.26}$$

Let us consider a magnetic crystal system with a cubic magnetocrystalline anisotropy whose cubic anisotropy axes are $\langle 100\rangle, \langle 010\rangle, \langle 001\rangle$. In the case where the cubic anisotropy constant is positive

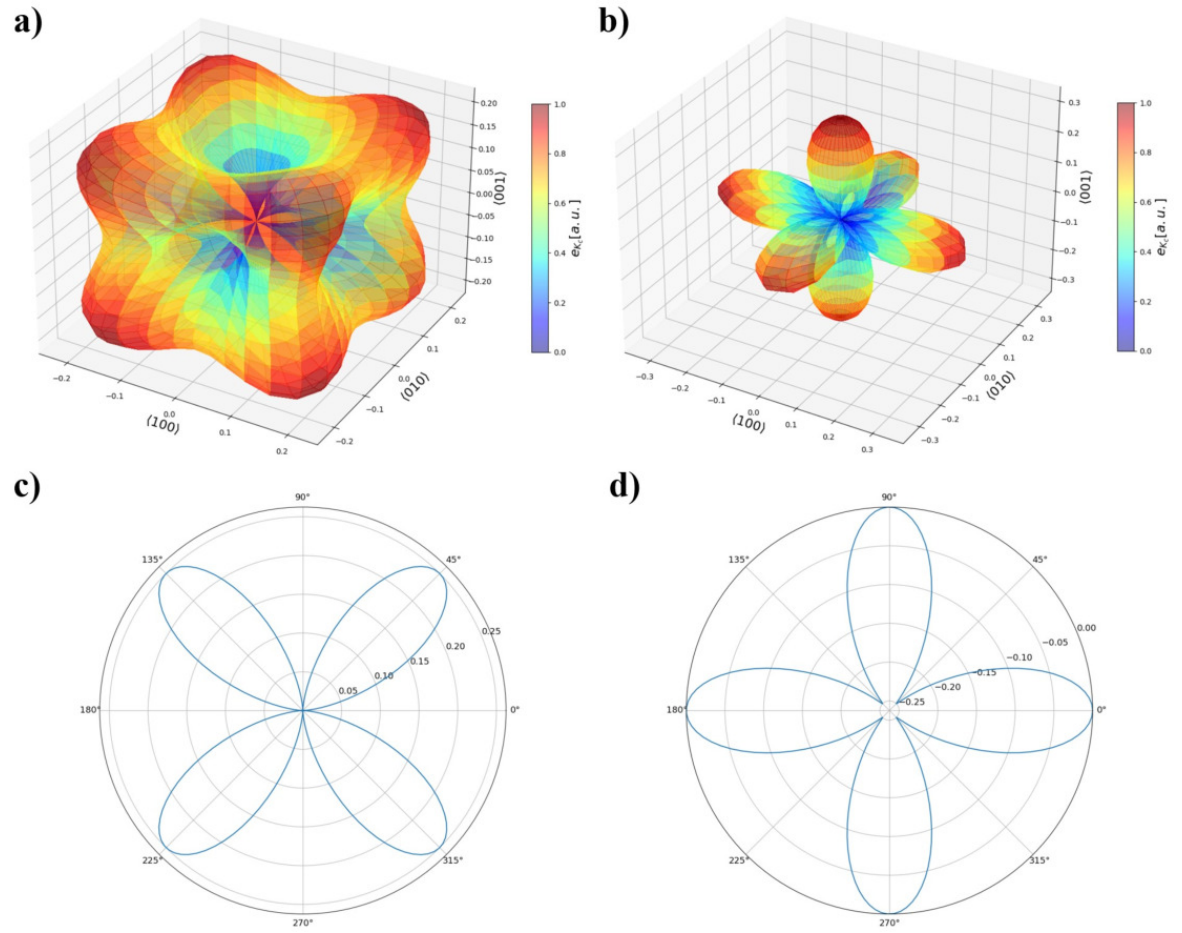

Figure 1.3: Cubic magnetocrystalline energy density in the case of the cubic anisotropy axes $\langle 100\rangle, \langle 010\rangle, \langle 001\rangle$ with a) $K_{c1} > 0$ and b) $K_{c1} < 0$. Angular profile of the cubic magnetocrystalline energy density in the (100) plane for c) $K_{c1} > 0$ and d) $K_{c1} < 0$. 0° corresponds to the axis $\langle 100\rangle$ and 90° to the axis $\langle 010\rangle$.

($K_{c1} > 0$), one can observe on Figure 1.3 a) that the cubic energy density in the $\langle 100\rangle$ direction is lower than those in the $\langle 110\rangle$ and $\langle 111\rangle$ directions. Consequently, the direction $\langle 100\rangle$ is an easy axis and the directions $\langle 110\rangle$ and $\langle 111\rangle$ are hard axes. In the opposite case (Figure 1.3 b)), when $K_{c1} < 0$, we then have $e_{\langle 111\rangle} < e_{\langle 110\rangle} < e_{\langle 100\rangle}$, and thus the directions $\langle 111\rangle$ and $\langle 011\rangle$ constitute easy axes and the direction $\langle 100\rangle$ a hard axis. In the case of magnetic thin films, one can restrict the representation of the energy density to the (100) plane to visualize the easy and hard axes. They are oriented along the directions $\langle 100\rangle$ and $\langle 110\rangle$ respectively in the case of $K_{c1} > 0$ in Figure 1.3 c) and inversely in the case of $K_{c1} < 0$ (Figure 1.3 d)).

It is possible to define a cubic anisotropy field H_K aligned along the easy axes such that [76]:

$$H_K = \frac{2K_{c1}}{\mu_0 M_s} \tag{1.27}$$

It should be noted that this anisotropy field is fictitious, but it allows to account for the action of the magnetocrystalline anisotropy. A more complete formula for the cubic anisotropy field can be found in [70].

Zeeman interaction

The magnetic interactions discussed so far are intrinsic to the ferromagnetic material. In particular, the exchange interaction and the dipole interaction are ubiquitous. The Zeeman interaction arises from the application of an external magnetic field. The energy associated with this interaction tends to be

minimized for an alignment of the magnetization with an applied magnetic field [74]:

$$E_Z = -\mu_0 \int \vec{M} \cdot \vec{H}_{ext} dV \tag{1.28}$$

In the spherical coordinate system (M_s, θ, ϕ), the Zeeman energy density is written:

$$e_Z = -\mu_0 M_s H_0 \left[\sin\theta \sin\theta_H \cos\left(\phi - \phi_H\right) + \cos\theta \cos\theta_H\right] \tag{1.29}$$

with H_0 the magnitude of the applied magnetic field $\vec{H}$, θ_H and ϕ_H the angles respectively between the z axis, the x axis of Figure 1.1 and the applied magnetic field $\vec{H}$.

Effective magnetic field

By minimizing the total free energy E_{tot} locally or globally, one obtains the different magnetization configurations at equilibrium. It is possible to formulate this condition with an effective magnetic field $\vec{H}_{eff}$ such that [75, 77]:

$$\vec{H}_{eff} = -\frac{1}{\mu_0} \vec{\nabla}_{\vec{M}} E_{tot} \tag{1.30}$$

The effective magnetic field can also be expressed as $\vec{H}_{eff} = \vec{H}_{ex} + \vec{H}_K + \vec{H}_d + \vec{H}_Z$.

The use of the effective field allows a simpler approach to the total energy minimization equation. At static equilibrium, the direction of the magnetization must be stable throughout the volume. This translates into the fact that no torque should be exerted on the magnetization, such as:

$$\vec{M} \times \vec{H}_{eff} = 0 \tag{1.31}$$

This equation is known as the Brown equation [77] and will be mainly solved in complex magnetic systems by micromagnetic simulations, as approached in chapter 3 section 3.1.2. Therefore, at equilibrium, the magnetization must be collinear with the effective field throughout the volume of the magnetic sample.

1.2 Uniform precession of magnetization

1.2.1 Equations of magnetization motion: Landau-Lifshitz and Landau-Lifshitz-Gilbert equations

As the magnetization can be averaged over the whole system as seen in section 1.1.1, the dynamics of the magnetic system can be reduced to the description of the dynamics of a macrospin in the case of a uniform magnetization $\vec{M}$. It then becomes possible to solve the evolution of this mean magnetization in a classical way. From a dynamical point of view, if the torque $\vec{M} \times \vec{H}_{eff}$ is non-zero, the magnetization will react in a gyratory manner. The latter will in fact precess around the effective field $\vec{H}_{eff}$. This phenomenon is called Larmor precession. One can then define an average angular momentum $\vec{J}$ of the ferromagnetic material. According to the fundamental principle of dynamics, the time variation of the angular momentum is equal to the torque exerted on it:

$$\frac{d\vec{J}}{dt} = \vec{M} \times \mu_0 \vec{H}_{eff} \tag{1.32}$$

with $\vec{H}_{eff}$ the effective field described previously in 1.1.2 part. In the same way that the angular momentum of electrons is related to the electrons magnetic moment by a proportionality factor, the electron gyromagnetic factor γ_e (1.1), the average angular momentum of the ferromagnetic system is proportional to the average magnetization via the gyromagnetic factor γ. This equation is written as follows and is the Landau-Lifshitz (LL) equation established in 1935 [79]:

$$\frac{d\vec{M}}{dt} = -\gamma\mu_0\vec{M} \times \vec{H}_{eff} \tag{1.33}$$

The Landau-Lifshitz equation is used to describe the phenomenon of Larmor precession but also the response of a ferromagnetic system to a microwave electromagnetic excitation. The gyromagnetic factor γ, characteristic of the collective precession of magnetic moments at the frequency $\omega \approx \gamma H_{eff}$, is a parameter which is not exactly equal to the electronic gyromagnetic factor γ_e ($\gamma \approx \gamma_e$) mentioned earlier in section 1.1.1. This parameter has to be determined experimentally. When the electronic gyromagnetic factor is mainly composed of the spin gyromagnetic factor (case of quenched orbitals), the latter is $28\ \mathrm{GHz\,T^{-1}}$. This involves that the electron has a frequency of precession of $28\ \mathrm{GHz}$ when subjected to a magnetic field of $1\ \mathrm{T}$. Therefore, the precession frequency of the magnetization is rather in the range GHz-THz.

Moreover, the LL equation (1.33) guarantees the conservation of the magnitude of the magnetization [80] discussed earlier in section 1.1.2, since when one carries out a scalar product of the equation (1.33) with the magnetization $\vec{M}$, one obtains:

$$\frac{dM^2}{dt} = 0 \tag{1.34}$$

This equation means that the magnetization performs a precessional motion whose radius is fixed. The trajectory of the magnetization is not necessarily circular and will depend strongly on the magnetic interactions defining the effective field.

If one looks at (1.33) as it is, no energy loss phenomenon is introduced and the magnetization $\vec{M}$ would precess endlessly around the effective magnetic field. In reality, however, a damping process is at work which eventually involves the return at equilibrium of the magnetization $\vec{M}$ along the effective field $\vec{H}_{eff}$. This damping phenomenon can be added in the form of a viscosity term acting on the magnetization and directed towards the effective field. This damping effect is illustrated in Figure 1.4. There are various ways of introducing this damping effect [79, 80]. Often it is simpler to

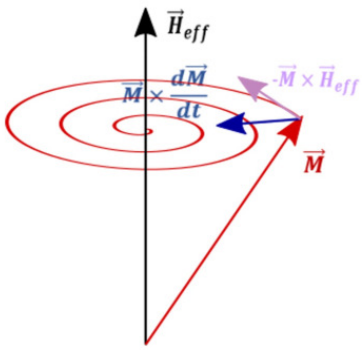

Figure 1.4: Schematic representation of the damped precessional motion of the magnetization described by the LLG equation.

use the notion of a dimensionless phenomenological damping factor α, developed by T. Gilbert [81]. The equation of motion of the magnetization is then described via the Landau-Lifshitz-Gilbert (LLG) equation:

$$\frac{d\vec{M}}{dt} = -\gamma\mu_0\vec{M} \times \vec{H}_{eff} + \frac{\alpha}{M_S}\left(\vec{M} \times \frac{d\vec{M}}{dt}\right) \tag{1.35}$$

The damping coefficient α allows us to take into account the different energy dissipation processes, which will be later discussed in section 1.5. The origin of the dissipative contributions is multiple, however it is possible to extract this parameter experimentally, in particular with measurements of ferromagnetic resonance (FMR), which will be approached later in chapter 3 section 3.3.2.

1.2.2 Solving the Landau-Lifshitz equation: Polder susceptibility tensor and Ferromagnetic Resonance

The LL and LLG equations describing the magnetic response are difficult to solve as they are intrinsically non-linear. Analytical solutions exist for simplified cases, otherwise their resolution requires numerical methods, such as micromagnetic simulations. Nevertheless, it is possible to linearize them if one considers the case where the oscillation amplitudes of the applied magnetic field and of the magnetization are small. In the case of high precession amplitudes, non-linear effects arise [82, 83]. For a start, the damping effects will be neglected here. One considers an effective magnetic field $\vec{H}_{eff}(\vec{r},t)$ which can be decomposed into a static part $\vec{H}_0$ along the direction $\vec{z}$ and a dynamic component $\vec{h}(t)$. The magnetization is decomposed in the same way with $\vec{M}_0$ the equilibrium magnetization and $\vec{m}(t)$ the dynamic component. One considers that the material is saturated and that its equilibrium magnetization is aligned with the applied static field ($\vec{M}_0 \parallel \vec{H}_0$). The effective field and the magnetization can therefore be written as follows:

$$\vec{H}_{eff}(\vec{r},t) = H_0\vec{z} + \vec{h}(t) \tag{1.36}$$

$$\vec{M}(\vec{r},t) = M_s\vec{z} + \vec{m}(t) \tag{1.37}$$

The dynamic components can be expressed as time-harmonic solutions: $\vec{m}(t) = \vec{m}e^{i\omega t}$ and $\vec{h}(t) = \vec{h}e^{i\omega t}$. Since the amplitude of the field and magnetization oscillations are very weak, one has $m(t) << M_s$ and $h(t) << H_0$. With all these assumptions, the LL equation (1.33) reduces to:

$$\frac{d\vec{m}}{dt} = -\gamma\mu_0\left[M_s\vec{z}\times\vec{h}(t) + \vec{m}(t)\times H_0\vec{z}\right] \tag{1.38}$$

By projecting onto the x, y, z axes, one obtains the following system of equations respectively:

$$i\omega m_x = \gamma\mu_0 M_s h_y - \gamma\mu_0 H_0 m_y \tag{1.39}$$

$$i\omega m_y = -\gamma\mu_0 M_s h_x + \gamma\mu_0 H_0 m_x \tag{1.40}$$

$$i\omega m_z = 0 \tag{1.41}$$

By solving this system of equations [80], it is possible to express the relationship between $\vec{m}(t)$ and $\vec{h}(t)$ using a tensor:

$$\vec{m} = \overline{\chi}\cdot\vec{h} \tag{1.42}$$

with $\overline{\chi}$ the Polder susceptibility tensor [80] which is written as:

$$\overline{\chi} = \begin{bmatrix} \chi & i\kappa & 0 \\ -i\kappa & \chi & 0 \\ 0 & 0 & 0 \end{bmatrix} \tag{1.43}$$

where $\chi = \frac{\omega_m\omega_0}{\omega_0^2-\omega^2}$ and $\kappa = \frac{\omega_m\omega}{\omega_0^2-\omega^2}$, with $\omega_m = \gamma\mu_0 M_s$ and $\omega_0 = \gamma\mu_0 H_0$ [84].

Since the non-diagonal components are opposite, the tensor is anti-symmetric, which is consistent with the gyratory response of the magnetization. This tensor is also of order 2 involving a generation

of dynamic magnetization only in the (xy) plane, there is no dynamic longitudinal component of the magnetization.

As the excitation frequency ω approaches the frequency ω_0 ($\omega \to \omega_0$), the elements of the tensor tend to infinity. Therefore, ω_0 is defined as the ferromagnetic resonance frequency. The phenomenon of ferromagnetic resonance (FMR) was established theoretically in 1935 by Landau and Lifshitz [79] and discovered experimentally in 1946 by Griffiths [85]. It consists in the absorption of electromagnetic energy by a ferromagnetic material establishing a uniform and in-phase precession of magnetic moments for an infinite duration. This mathematical anomaly arises from the ideal case of a magnetic system with no energy losses subjected to microwave excitation. The solution of the LLG equation in the case of losses will be dealt with in section 1.5.1.

Finally, due to the anti-symmetry of the tensor, the direction of precession at resonance can only be to the right with respect to the equilibrium direction [70].

This linear response of the magnetization to a microwave magnetic field described above is in the very special case of a non-dissipative magnetic medium of infinite dimensions without exchange interactions and anisotropy. In reality, the shape of the magnetic system as well as the presence of magnetocrystalline anisotropy will strongly influence the resonance frequency of the system.

1.2.3 Kittel formulas

In 1948, Kittel [86] demonstrated that the shape of the magnetic material influences its resonance frequency. This dependence can be calculated via the demagnetizing field $\vec{H}_{demag} = -\overline{\overline{N}}\vec{M}$ introduced earlier in section 1.1.2. The static and dynamic components of the effective field $\vec{H}_{eff}(\vec{r},t)$ are rewritten as follows:

$$\vec{H}_0 = \vec{H}_{e0} - \overline{\overline{N}}\vec{M}_0 \tag{1.44}$$

$$\vec{h}(t) = \vec{h}_e(t) - \overline{\overline{N}}\vec{m}(t) \tag{1.45}$$

with $\vec{H}_{e0}$ and $\vec{h}_e(t)$ the static and dynamic components respectively of the external magnetic field, and $\overline{\overline{N}}$ the demagnetizing tensor. In the case of an ellipsoid, this tensor is diagonal:

$$\overline{\overline{N}} = \begin{bmatrix} N_x & 0 & 0 \\ 0 & N_y & 0 \\ 0 & 0 & N_z \end{bmatrix} \tag{1.46}$$

where N_x, N_y and N_z are the demagnetizing factors. Their values depend on the shape of the system of interest and must obey the following condition: $N_x + N_y + N_z = 1$. The system is magnetically saturated along the $\vec{z}$ axis and is subjected to a transverse dynamic excitation in the (xy) plane. One can therefore write:

$$\begin{cases} \vec{H}_0 = \vec{H}_{e0} - N_z\vec{M}_0 \\ \vec{h}(t) = \vec{h}_e(t) - \overline{\overline{n}}\vec{m}(t) \quad \text{with} \quad \overline{\overline{n}} = \begin{bmatrix} N_x & 0 \\ 0 & N_y \end{bmatrix} \end{cases} \tag{1.47}$$

From the equation (1.42), we can rewrite (1.47):

$$\overline{\overline{\chi}}^{-1}\vec{m} = \overline{\overline{\chi_e}}^{-1}\vec{m} - \overline{\overline{n}}\vec{m} \tag{1.48}$$

with $\overline{\overline{\chi_e}}$ the susceptibility describing the response of the magnetic system to the dynamic excitation.

One can then write the resolution of the LL equation (1.33) in a matrix form:

$$\vec{h}_e = \overline{\overline{\chi}}_e^{-1}\vec{m} = \frac{1}{\omega_m}\begin{bmatrix} \omega_x & i\omega \\ -i\omega & \omega_y \end{bmatrix}\vec{m} \tag{1.49}$$

with $\omega_0 = \gamma\mu_0 (H_{0e} - N_z M_s)$, $\omega_x = \omega_0 + N_x\omega_m$ and $\omega_y = \omega_0 + N_y\omega_m$.

The system is brought to resonance when its response diverges. The condition of resonance results from the non-invertibility of the tensor $\overline{\overline{\chi}}_e$:

$$det\left(\overline{\overline{\chi}}_e^{-1}\right) = \frac{\omega_x\omega_y - \omega^2}{\omega_m^2} = 0 \Rightarrow \omega_{res} = \sqrt{\omega_x\omega_y} \tag{1.50}$$

The Kittel formula for the above resonant frequency is expressed as:

$$\omega_{res} = \gamma\mu_0\sqrt{\left[H_{e0} + M_s (N_y - N_z)\right]\left[H_{e0} + M_s (N_x - N_z)\right]} \tag{1.51}$$

Thus, the resonance pulsation also depends on the saturation magnetization and the demagnetizing tensor. Another special property of the Kittel tensor is that the precession is no longer circular but elliptical.

In the case of a thin magnetic layer, which can be assimilated to a flattened cylinder, where the magnetization is oriented in plane or out of plane of the magnetic layer, the demagnetizing factors are respectively $N_x = N_z = 0, N_y = 1$ and $N_x = N_y = 0, N_z = 1$. The resonance frequencies of a thin film reduce to:

$$\begin{cases} \omega_{res} = \gamma\mu_0\sqrt{H_{e0}\left(H_{e0} + M_s\right)} & \vec{M}//\text{Plane} \\ \omega_{res} = \gamma\mu_0\left(H_{e0} - M_s\right) & \vec{M}\perp\text{Plane} \end{cases} \tag{1.52}$$

1.2.4 Kittel formulas with magnetocrystalline anisotropy

The material under study in this thesis has a cubic magnetocrystalline anisotropy. Therefore in this section we will discuss the Kittel formulas in the case of a thin film with magnetocrystalline anisotropy. First, we will discuss the calculation of the ferromagnetic resonance in the case of an anisotropic ferromagnetic material through two methods: the method of spherical coordinates and the method of effective demagnetization factors [80]. We will then apply one of these two methods on one of the two different kinds of anisotropy previously discussed. The ferromagnetic resonance in the case of uniaxial anisotropy will be determined by using the method of spherical coordinates and the one in the case of a cubic anisotropy by using the method of effective demagnetization factors.

Spherical coordinates method

The spherical coordinates method was developed by Smit and Beljers [87] and by Suhl [88]. By replacing the Cartesian components of the magnetization (M_x, M_y, M_z) by their spherical components (M_s, θ, ϕ) and by solving the equation (1.35), it then becomes possible to derive the expression of the resonance frequency with $\alpha = 0$, called the Smit-Suhl formula such that [80]:

$$\omega_{res} = \frac{\gamma}{M_s \sin\theta_{eq}}\sqrt{E_{\theta\theta}E_{\phi\phi} - E_{\theta\phi}^2} \tag{1.53}$$

with $E_{\theta\theta} = \frac{\partial^2 E}{\partial\theta^2}$, $E_{\phi\phi} = \frac{\partial^2 E}{\partial\phi^2}$, $E_{\theta\phi} = \frac{\partial^2 E}{\partial\theta\partial\phi}$ and E the total free energy density. The partial derivatives are calculated at equilibrium with the equilibrium angles $\theta = \theta_{eq}$ and $\phi = \phi_{eq}$ that can be determined via:

$$(E_\theta)_{\theta=\theta_{eq},\phi=\phi_{eq}} = \left(\frac{\partial E}{\partial\theta}\right)_{\theta=\theta_{eq},\phi=\phi_{eq}} = 0 \qquad (E_\phi)_{\theta=\theta_{eq},\phi=\phi_{eq}} = \left(\frac{\partial E}{\partial\phi}\right)_{\theta=\theta_{eq},\phi=\phi_{eq}} = 0 \tag{1.54}$$

If one now takes into account the energy dissipation ($\alpha \neq 0$), the resonance frequency becomes complex. The real part corresponds to the expression (1.53) and the imaginary part is:

$$\omega'' = \frac{1}{2}\frac{\alpha\gamma}{M_s}\left(E_{\theta\theta} + \frac{1}{\sin^2\theta_{eq}}E_{\phi\phi}\right) \tag{1.55}$$

The Smit-Suhl formula nevertheless presents a divergence when the magnetization is normal to the (xy) plane ($\theta = 0$). To avoid this problem, it is possible to use the formula proposed by Baselgia et al [89]:

$$\omega_{res} = \frac{\gamma}{M_s}\sqrt{E_{\theta\theta}\left[\frac{E_{\phi\phi}}{\sin^2\theta} + \frac{\cos\theta}{\sin\theta}E_\theta\right] - \left[\frac{E_{\theta\phi}}{\sin\theta} - \frac{\cos\theta}{\sin\theta}\frac{E_\phi}{\sin\theta}\right]^2} \tag{1.56}$$

Effective demagnetization factor method

The method of effective demagnetization factors was introduced by Kittel [86] and developed by MacDonald [90]. The interest of this method is to write the effective field $\vec{H}_{eff}$ in the same way as the demagnetizing field (1.17) in the case of weak magnetization oscillations ($m \ll M_s$):

$$\vec{H}_{eff} = -\overline{\overline{N}}_{eff}\vec{M} \tag{1.57}$$

with $\overline{\overline{N}}_{eff}$ the effective demagnetizing tensor. The advantage of expressing the effective field in such a way to take account of the magnetocrystalline anisotropy is that one can use the Kittel formulas previously developed in section 1.2.3 by substituting the tensor $\overline{\overline{N}}$ by $\overline{\overline{N}}_{eff} = \overline{\overline{N}} + \overline{\overline{N}}_a$. $\overline{\overline{N}}_a$ is the demagnetizing tensor of magnetocrystalline anisotropy such that $\vec{H}_a = -\overline{\overline{N}}_a\vec{M}$ (in the case of uniform magnetization).

Thin film with uniaxial anisotropy

One considers the case of a thin film whose infinitely thin thickness is perpendicular to the z axis and therefore the plane of the thin film corresponds to the (xy) plane. The coordinate system is the same as in Figure 1.1. The uniaxial anisotropy axis is along the x axis. The magnetization makes an angle θ with the z axis and an angle β with the uniaxial anisotropy direction. A magnetic field $\vec{H}_0$ of amplitude H_0 is applied and is sufficiently strong so that the magnetization is uniform and collinear with this field ($\theta_H = \theta$)

In order to determine the resonance frequency of a thin magnetic layer with uniaxial anisotropy, it is possible to use the spherical coordinates method using the Baselgia formula (1.56). The free energy density of this magnetic system is:

$$E_{tot} = E_Z + E_{demag} + E_{K_u} \tag{1.58}$$

with E_Z the energy density of the Zeeman interaction, E_{demag} the energy density of the demagnetizing field and E_{K_u} the energy density of the uniaxial anisotropy. By calculating the partial derivatives of (1.54) with the formulas for the different energy densities, respectively via (1.29), (1.18), (1.22), the resonance frequencies when the magnetization is in the plane of the thin film ($\theta = \frac{\pi}{2}$), parallel to the uniaxial anisotropy axis ($\phi = 0$) or perpendicular to the anisotropy axis ($\phi = \frac{\pi}{2}$) are expressed:

$$\omega_{res} = \gamma\mu_0\sqrt{\left(H_0 + M_s + \frac{2K_{u1}}{\mu_0 M_s}\right)\left(H_0 + \frac{2K_{u1}}{\mu_0 M_s}\right)} \quad \| \text{ plane and } \phi = 0 \tag{1.59}$$

$$\omega_{res} = \gamma\mu_0\sqrt{(H_0 + M_s)\left(H_0 - \frac{2K_{u1}}{\mu_0 M_s}\right)} \quad \| \text{ plane and } \phi = \frac{\pi}{2} \tag{1.60}$$

Thin film with cubic anisotropy

We will now deal with the case of a thin magnetized layer with a cubic magnetocrystalline anisotropy, in the coordinate system schematized in Figure 1.5 a). Figure 1.5 a) is almost identical to that of Figure 1.1, except that the (x, y, z) coordinate system of Figure 1.1 is replaced by the crystallographic directions $[100]$, $[010]$ and $[001]$. Another coordinate system (x, y, z) is used for simplicity in Figure 1.5 such that the magnetization is collinear with the z axis. One also introduces ϕ_M the angle between the magnetization and the crystallographic axis $\langle 100 \rangle$ in the plane of the thin film.

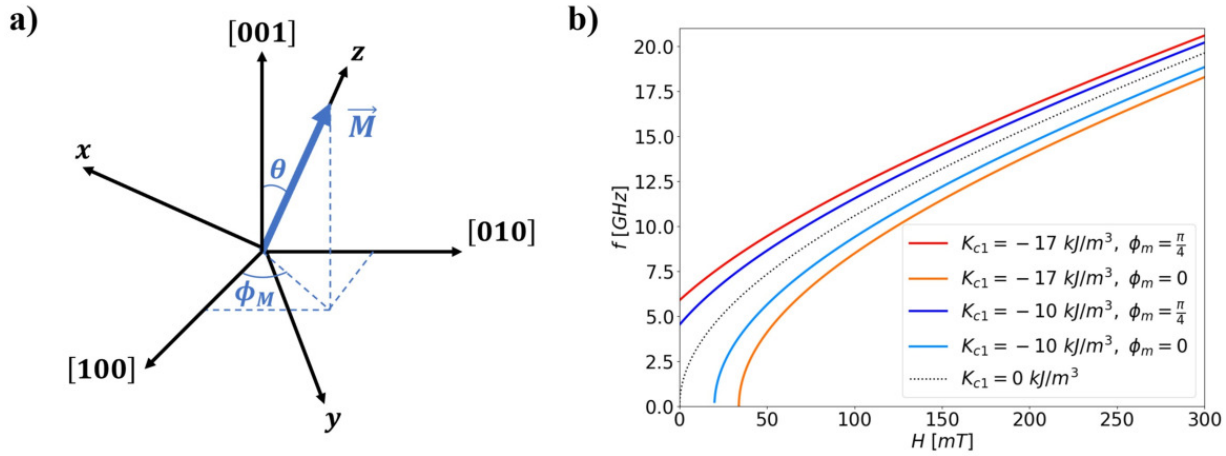

Figure 1.5: a) Schematic representation of the coordinate system in the case of cubic anisotropy. b) Calculation of the resonance frequency of a thin film with cubic anisotropy in the $\{100\}$ plane magnetized in the plane of the layer ($\theta = \frac{\pi}{2}$) with the magnetic parameters: $M_s = 1.26$ mT, $\gamma = 28.7$ GHz T^{-1}, $A = 18.10^{-12}$ J m^{-1}. $K_{c1} = -17$ kJ m^{-3} for the red and orange curves corresponding respectively to the $\phi_M = \frac{\pi}{4}$ and $\phi_M = 0$. $K_{c1} = -10$ kJ m^{-3} for the dark blue and light blue curves corresponding respectively to the cases $\phi_M = \frac{\pi}{4}$ and $\phi_M = 0$. The dashed black curve corresponds to the case without cubic anisotropy ($K_{c1} = 0$).

As seen previously, it is possible to apply the method of spherical coordinates to determine the resonance frequency of a thin film with cubic anisotropy, this time with the total energy density $E_{tot} = E_z + E_{demag} + E_{K_c}$. It is also possible to apply the method of effective demagnetization factors, and we will also see its use in section 1.4.3. Depending on the crystallographic orientation of the thin film plane ($\{100\}$, $\{110\}$ or $\{111\}$) and on the orientation of the magnetization with respect to the film plane (parallel or perpendicular), there are different expressions for the anisotropic demagnetizing factors. The CMS thin films deposited during this thesis are oriented $\{100\}$, the cubic anisotropy demagnetizing factors are written in this case [91]:

- When the magnetization $\vec{M}$ is in the plane of the thin film ($\theta = \frac{\pi}{2}$):

$$\begin{cases} N_{xx}^a = N_{xy}^a = 0 \\ N_{yy}^a = \frac{3H^A}{2M_s}\left(\cos\left(4\phi_M\right) - 1\right) \\ N_{zz}^a = -\frac{H^A}{2M_s}\left(\cos\left(4\phi_M\right) + 3\right) \end{cases} \tag{1.61}$$

- When the magnetization $\vec{M}$ is normal to the plane of the thin film ($\theta = 0$):

$$\begin{cases} N_{xx}^a = N_{yy}^a = N_{xy}^a = 0 \\ N_{zz}^a = -\frac{2H^A}{M_s} \end{cases} \tag{1.62}$$

with $H^A = \frac{K_{c1}}{\mu_0 M_s}$. In order to determine the resonance frequencies in the different configurations (parallel, perpendicular magnetization to the film plane), it is then sufficient to replace the demagnetizing factors of (1.51) by $N_x + N_{xx}^a$, $N_y + N_{yy}^a$ and $N_z + N_{zz}^a$:

- When the magnetization is in the plane of the layer ($\theta = \frac{\pi}{2}$, $N_x = 1$, $N_y = N_z = 0$) and is parallel to the crystallographic axis $\langle 100 \rangle$ ($\phi_M = 0$):

$$\omega_{res} = \gamma\mu_0 \sqrt{\left(H_0 + \frac{2K_{c1}}{\mu_0 M_s}\right)\left(H_0 + \frac{2K_{c1}}{\mu_0 M_s} + M_s\right)} \qquad (\theta = \frac{\pi}{2}, \phi_M = 0) \tag{1.63}$$

- When the magnetization is in the plane of the layer ($\theta = \frac{\pi}{2}$, $N_x = 1$, $N_y = N_z = 0$) and is parallel to the crystallographic axis $\langle 110 \rangle$ ($\phi_M = \frac{\pi}{4}$):

$$\omega_{res} = \gamma\mu_0 \sqrt{\left(H_0 - \frac{2K_{c1}}{\mu_0 M_s}\right)\left(H_0 + \frac{K_{c1}}{\mu_0 M_s} + M_s\right)} \qquad (\theta = \frac{\pi}{2}, \phi_M = \frac{\pi}{4}) \tag{1.64}$$

- When the magnetization is perpendicular to the plane of the layer ($\theta = 0$, $N_x = N_y = 0$, $N_z = 1$):

$$\omega_{res} = \gamma\mu_0 \left(H_0 - M_s + \frac{2K_{c1}}{\mu_0 M_s}\right) \qquad (\theta = 0) \tag{1.65}$$

In Figure 1.5 b) is plotted the ferromagnetic resonance curves as a function of the applied field $f(H_0)$ in the case of a thin film magnetized in the plane ($\theta = \frac{\pi}{2}$) with a cubic magnetocrystalline anisotropy for negative anisotropy constants $K_{c1} = -17$ kJ m^{-3} and $K_{c1} = -10$ kJ m^{-3}. The resonance frequencies were calculated when the magnetization is aligned along the crystallographic axis $\langle 100 \rangle$ ($\phi_M = 0$) (hard axis when $K_{c1} < 0$) and along the crystallographic axis $\langle 110 \rangle$ ($\phi_M = \frac{\pi}{4}$) (easy axis when $K_{c1} < 0$). The presence of the cubic anisotropy and its intensity will shift the $f(H)$ curve towards weaker field values when the magnetization is aligned with an easy axis, and conversely towards stronger fields in the case of the magnetization aligned with a hard axis.

1.3 Magnetostatic spin waves in a thin film

So far, we focused on the uniform precession of the magnetization, i.e. the FMR mode (of wavevector $k = 0$), by the application of a microwave field on the whole magnetic system. If a microwave magnetic field is applied locally, it will then be possible to locally excite a precession of the magnetic moments of the sample. By dipole and exchange interactions, this precessional motion will be communicated from one magnetic moment to an other ($k \neq 0$). The propagation of this precessional motion is called a spin wave. This corresponds to a precession of the magnetic moments at the same frequency but out of phase with each other, as illustrated in Figure 1.6.

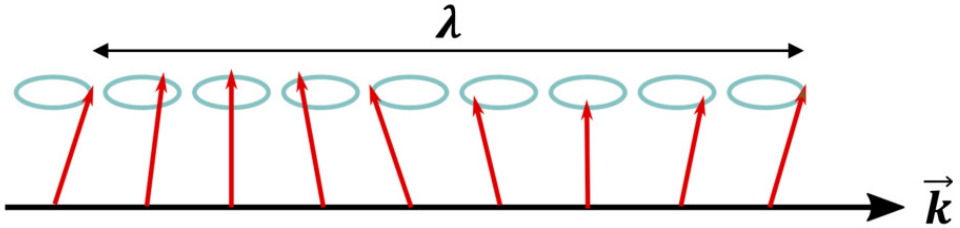

Figure 1.6: Illustration of a spin wave.

Firstly, we will consider the case of magnetostatic waves whose wavelengths are longer than the exchange length in the case of an infinite magnetic volume. In this case, the phase difference between

neighbouring magnetic moments is weak. This corresponds to the spin waves regime dominated by dipolar interaction. In a second step, we will detail the different types of spin waves that can propagate in magnetic thin films, the classification of which is based on the orientation of the saturated magnetization with respect to the direction of propagation. Then, we will deal with the propagation of spin waves in the dipole-exchange regime, where the exchange interaction can no longer be neglected. Also the magnetocrystalline anisotropy interaction will be taken into account in the dispersion relation. Finally, the dispersion of spin waves in anisotropic magnetic waveguides will be detailed in particular.

1.3.1 Magnetostatic approximation and Walker equation

In the microwave range, the wavelength of spin waves is shorter than that of electromagnetic waves through vacuum ($k \gg \frac{\omega}{c}$ with c the speed of light). This corresponds to the case of slow waves and one can then describe the propagation of spin waves in the magnetostatic limit [70, 80]. For the moment, neither the exchange interaction nor the magnetocrystalline anisotropy interaction are considered here. Therefore, these excitations are called dipolar spin waves (nonexchange magnetostatic waves), magneto-quasi-static waves or more generally magnetostatic waves, where their wavevectors are weak, involving that the exchange interaction is negligible compared to the dipolar interaction ($\Lambda \gg \Lambda_{ex}$). In this approximation, the magnetic and electric components of a magnetostatic wave are decoupled and Maxwell's equations are written as follows:

$$\vec{\nabla} \times \vec{h} = 0 \tag{1.66}$$

$$\vec{\nabla} \cdot \vec{b} = 0 \tag{1.67}$$

where $\vec{h}$ is the magnetic field of the wave, $\vec{b} = \mu_0(\overline{I} + \overline{\chi})\vec{h}$ is the induction, with $\overline{I}$ the identity matrix. From the equation (1.66), one can calculate a scalar potential ψ allowing to write:

$$\vec{h} = -\vec{\nabla}\psi \tag{1.68}$$

By substituting the equation (1.68) into the equation (1.67), one then obtains the propagation equation of a spin wave, also called Walker Equation [92]:

$$\vec{\nabla} \cdot [\mu_0(\overline{I} + \overline{\chi}) \cdot \vec{\nabla}\psi] = 0 \tag{1.69}$$

The resolution of this equation allows the determination of the magnetostatic modes of spin waves and their dispersions in a magnetic homogeneous medium. In the case of the propagation of a plane wave in an infinite ferromagnetic medium (bulk), the magnetostatic potential can be expressed as $\psi(\vec{r}, t) = \psi_0 e^{i(\omega t - \vec{k}.\vec{r})}$. Since the z axis coincides with the direction of the magnetization at equilibrium as in Figure 1.5, the equation (1.69) then becomes:

$$(1 + \chi)(k_x^2 + k_y^2) + k_z^2 = 0 \tag{1.70}$$

with k_i the components of the spin wave wavevector. By introducing θ_k as the angle between $\vec{k}$ and $\vec{M}$, and by replacing χ by its expression in the equation (1.43), the dispersion relation for magnetostatic spin waves is [70]:

$$\omega = \sqrt{\omega_0(\omega_0 + \omega_m \sin^2\theta_k)} \tag{1.71}$$

One can notice that the dispersion relation does not depend on the amplitude of the wavevector but only on its direction. This involves that the group velocity ($v_g = \frac{d\omega}{dk}$) is zero and that these magnetostatic waves do not propagate (stationary feature). There are in fact several possibilities that allow

magnetostatic waves to have a non-zero group velocity, and therefore to propagate. First of all, this concerns the influence of the exchange interaction, which we will discuss in section 1.4, but also the influence of the edge conditions. In particular, we will deal with the case of the thin film in section 1.4.4.

Via the equation (1.71), the frequencies of magnetostatic waves in an infinite ferromagnetic medium are in the range: $\omega_0 \leq \omega \leq \sqrt{\omega_0(\omega_0 + \omega_m)}$. Moreover, this system is degenerate as for one frequency there are several possible wavelengths. This degeneracy can be removed again by including the exchange interaction or by considering a finite dimensional system.

1.3.2 Typology of spin waves in a magnetic thin film

In this section, we will deal with the solutions of the Walker equation (1.69) in the case of a thin film of thickness t. The equilibrium magnetization $\vec{M}$ is oriented along the z direction as schematized in Figure 1.7. As seen previously, the spin wave modes which are solutions of the Walker equation depend on the relative orientation of their propagation direction $\vec{k}$ with the magnetization $\vec{M}$. Generally, three configurations of spin waves in magnetic thin films are mainly studied in the literature and will be detailed below. In order to better represent these three cases of spin waves propagation, they can be schematized by dividing the thin film into quarter-wave domains as illustrated in Figure 1.7. The red arrows in these domains represent the dynamic magnetization $\vec{m}(t)$ which is perpendicular to the direction of the equilibrium magnetization $\vec{M}$, in the limit of small precession angles. The presence of this dynamic magnetization generates magnetic "charges" on the faces of the thin film and/or in the wave planes in the plane of the thin film. The accumulation of these charges then manifests itself as a dynamic dipolar field (green arrows in Figure 1.7) involving the propagation of a spin wave.

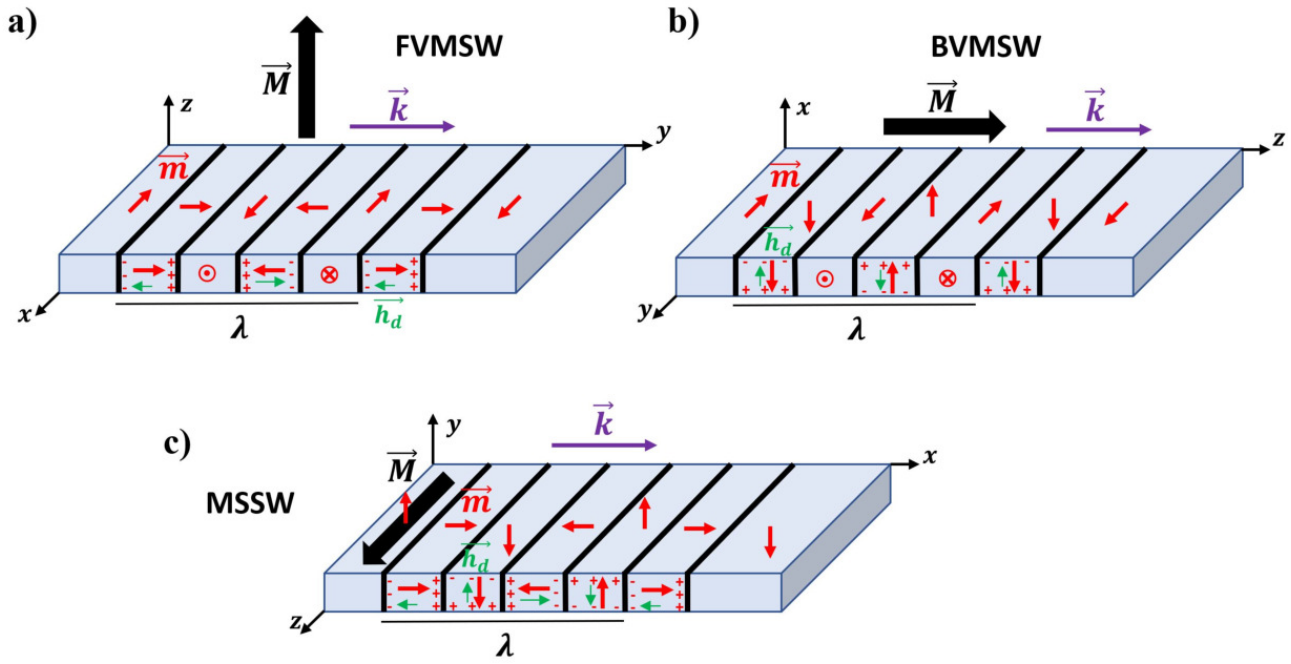

Figure 1.7: Schematics of the three main propagating spin wave modes in magnetic thin films: a) Forward Volume Magnetostatic Spin Waves (FVMSW), b) Backward Volume Magnetostatic Spin Waves (BVMSW) and c) MagnetoStatic Surface Spin Waves (MSSW). The z axis is always oriented along the direction of the magnetization $\vec{M}$. The magnetic thin film is divided into quarter-wave domains, where the red arrows represent the dynamic magnetization $\vec{m}(t)$ and the green arrows represent the generated dynamic dipolar field $\vec{h}_d(t)$.

Forward Magnetostatic Volume Spin Waves (FVMSW)

When the equilibrium magnetization of the thin film is normal to the plane of the layer and the spin wave wavevector $\vec{k}$ is perpendicular to $\vec{M}$, the magnetostatic waves propagating in this configuration are called Forward Volume Magnetostatic Spin Waves (FVMSW) [93]. By solving the Walker equation in this configuration, Kalinikos [70, 94] established an approximation of the dispersion relation of FVMSW for the first mode in thickness (the magnetization is uniform along the thickness) which is written:

$$\omega^2 = \omega_0 \left[\omega_0 + \omega_m \left(1 - \frac{1 - e^{-k_\parallel t}}{k_\parallel t} \right) \right] \tag{1.72}$$

with $k_\parallel = \sqrt{k_x^2 + k_y^2}$ the wavevector component in the plane of the thin film. From this formula, the dispersion of FVMSW is not dependent on the direction of the wavevector in the plane of the film $\vec{k_\parallel}$ but only on its amplitude. As a result, this involves an isotropic propagation of the wave. Nevertheless, the presence of magnetocrystalline anisotropy (not taken into account in the dispersion relation above) can induce an anisotropy in the propagation of FVMSW in the plane of the film. An example of the dipersion of FVMSW is plotted in Figure 1.8 b) (green dashed line). In this graph, the frequency increases with the wavevector which involves a positive group velocity $v_g = \frac{d\omega}{dk} > 0$ and in the same direction as the phase velocity $v_\phi = \frac{\omega}{k}$, explaining the name of "forward". The amplitude of the dynamic magnetic components is sinusoidally distributed in the thickness of the thin film, explaining their characteristic as a volume wave. Finally, FVMSW have a quasi-circular precession of the dynamic components of the magnetization (m_x, m_y) due to a similarity of the dynamic dipole fields (h_x, h_y) since they are in the plane of the thin film.

Backward Volume Magnetostatic Spin Waves (BVMSW)

Damon and Eschbach described in the 1960s two particular types of in-plane magnetostatic waves in thin films [95]. When the propagation of the wave is parallel to the direction of the magnetization ($\vec{k} \parallel \vec{M}$), these spin waves are called Backward Volume Magnetostatic Spin Waves (BVMSW). When the propagation of the wave is perpendicular to the direction of the magnetization ($\vec{k} \perp \vec{M}$), these waves are called MagnetoStatic Surface Spin Waves (MSSW) or Damon-Eshbach modes and will be discussed in the next part. As $\vec{M}$ is in the plane of the layer and oriented towards the z axis, the propagation of BVMSW takes place along z with $\vec{k_z}$. The dispersion relation for BVMSW can also be approximated by [94]:

$$\omega^2 = \omega_0 \left[\omega_0 + \omega_m \left(\frac{1 - e^{-k_z t}}{k_z t} \right) \right] \tag{1.73}$$

In the graph of Figure 1.8 b) (blue dashed line), the frequency of BVMSW decreases with the wavevector. As a result, the group velocity is negative and opposite to the phase velocity which is positive. Consequently, the energy of the wave travelling with the group velocity v_g propagates in the opposite direction to the phase of the wave represented by $\vec{k}$. This original phenomenon explains the name of "backward" to qualify these spin waves. Similar to FVMSW, BVMSW waves are volume waves as their oscillation amplitude is sinusoidally distributed in the thickness of the thin film. Unlike FVMSW, BVMSW have elliptical magnetization precessions $(m_x \neq m_y)$ due to the fact that the m_x component is out of plane compared to the m_y component.

MagnetoStatic Surface Spin Waves (MSSW)

By solving the Walker equation in this case, the MSSW dispersion in the dipolar regime is written as [70]:

$$\omega^2 = \omega_0 \left(\omega_0 + \omega_m \right) + \frac{\omega_m^2}{4} \left(1 - e^{-2kt} \right) \tag{1.74}$$

The amplitude of MSSW is maximum at the surface and decreases exponentially through the thickness of the magnetic film. As a result, this type of magnetostatic waves propagates at the surface and are

therefore qualified as surface waves, contrary to FVMSW and BVMSW. As a consequence, these waves do not have thickness modes. Depending on the direction of the applied magnetic field, these surface waves propagates on the upper surface of the film when the product $\vec{k} \wedge \vec{M}$ is direct (i.e. $\vec{k} \wedge \vec{M} > 0$) and on the bottom surface of the thin film when propagating in the opposite direction (i.e. $\vec{k} \wedge \vec{M} < 0$). This can lead to frequency differences between the two directions of propagation if the two interfaces (upper and bottom surfaces) are different. It can be seen from the dispersion curve in Figure 1.8 b) that the frequency increases with the wavevector, involving a positive group velocity. In addition, analog to BVMSW, MSSW present elliptical magnetization precessions ($m_x \neq m_y$).

1.4 Spin waves in the dipole-exchange regime

So far the spin waves dispersion has been established in the dipolar regime, i.e. for small values of wavevector ($k \to 0$). With the decrease of the spin waves wavelength, the exchange interaction is no longer negligible when the wavelength approaches the exchange length Λ_{ex} (generally in the order of ~ 5 nm). The exchange interaction must be then taken into account, corresponding to the dipole-exchange regime. First, the dipole-exchange regime will be applied to the case of an infinite ferromagnetic volume and then will be applied to the case of a thin film. Finally, the influence of the cubic magnetocrystalline anisotropy will be introduced in the case of a thin film and of a magnetic waveguide.

1.4.1 Spin waves in a ferromagnetic volume

By considering the expression of the exchange field (1.10) and writing the dynamic magnetization and dynamic field on a plane wave basis such that $\vec{m} \propto e^{i\vec{k}\cdot\vec{r}}$ and $\vec{h} \propto e^{i\vec{k}\cdot\vec{r}}$, the operator $\vec{\nabla}^2$ in the expression (1.10) reduces to $-k^2$. The exchange effect can then be introduced into the magnetostatic waves dispersion (1.71) by substituting ω_0 by $\omega_0 + \omega_m \Lambda_{ex}^2 k^2$ [80]:

$$\omega = \sqrt{\left(\omega_0 + \omega_m \Lambda_{ex}^2 k^2\right)\left(\omega_0 + \omega_m\left(\Lambda_{ex}^2 k^2 + \sin^2\theta_k\right)\right)} \tag{1.75}$$

The addition of the exchange interaction gives a parabolic character to the dispersion curves for large wavevectors. Henceforth these waves are no longer stationary as in the purely dipolar regime but propagating as the group velocity is now non-zero.

1.4.2 Spin waves in a thin film

In the case of a thin film, as the exchange interaction is short-range, the magnetic moments near the surface of the film are strongly affected by this discontinuity. It is then necessary to introduce a new boundary condition in addition to the limits on $\vec{b}$ and $\vec{h}$. This condition is related to the pinning of spins at the surface of the thin film. This condition was described by Rado and Weertman [96] and is written as:

$$\frac{2A}{\mu_0 M_s^2}\vec{M} \times \frac{\partial \vec{M}}{\partial \vec{n}} + T_{surf} = 0 \tag{1.76}$$

where $\vec{n}$ is the normal to the surface of the thin film and T_{surf} represents the torques of surface interactions other than exchange. When the spin pinning is zero, $T_{surf} \to 0$, thus $\frac{\partial m}{\partial n} = 0$ involving a

maximum amplitude of the magnetization dynamic component. When the spin pinning is perfect, i.e. $T_{surf} \to \infty$, $m = 0$, leading to an immobility of the spins at the interface.

Kalinikos and Slavin [97] developed a complete theory allowing the approximate analytical calculation of the spin wave modes dispersion in the dipole-exchange regime in an isotropic thin film with an arbitrary angle between the equilibrium magnetization $\vec{M}$ and the propagation direction $\vec{k}$. One considers the coordinate system (η, ζ, ξ) such that the thickness of the thin film t is along the axis ξ and (η, ζ) constitutes the plane of the thin film, as represented in Figure 1.8 a). The ζ axis is

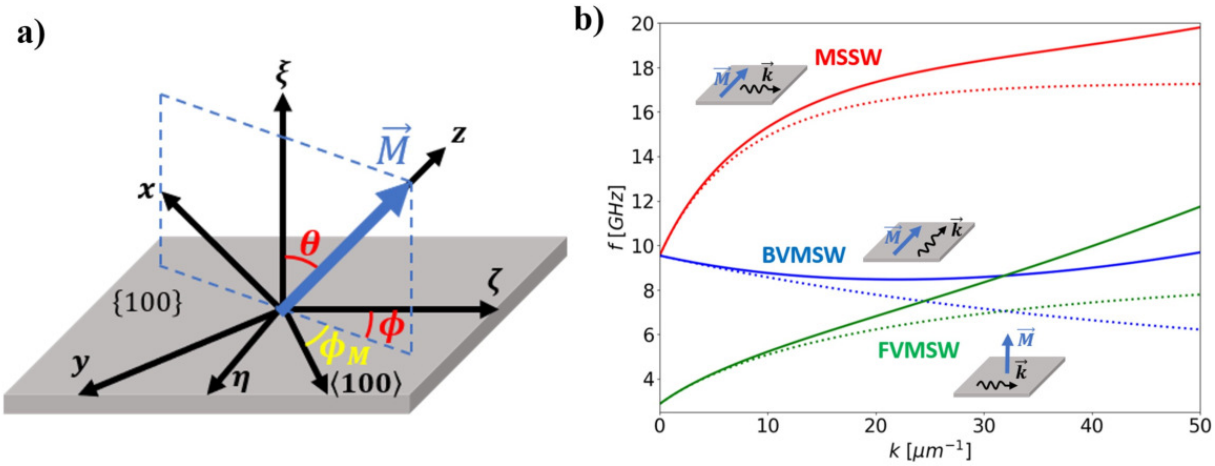

Figure 1.8: a) Schematic representation of the coordinate system for the calculation of the spin wave dispersion in the dipole-exchange regime [91]. b) Spin waves dispersion in a thin film of thickness $t = 50$ nm of type MSSW (in red), BVMSW (in blue) and FVMSW (in green) in the dipole-exchange regime (solid line) and in the purely dipolar regime (dashed line) with the Permalloy magnetic constants [7]: $M_s = 800$ kA m^{-1}, $A_{ex} = 16$ pJ m^{-1}, $H_0 = 100$ mT (for MSSW and BVMSW), 1.1 T (for FVMSW), and $\frac{\gamma}{2\pi} = 28.7$ GHz T^{-1}.

also collinear with the direction of propagation $\vec{k}$. A magnetic field is applied which is strong enough to saturate $\vec{M}$ in a direction which forms an angle θ with respect to the ξ axis and an angle ϕ in the plane of the film with respect to the ζ axis. In the case of magnetic moments uniformly pinned on both surfaces of the thin film, the spin waves dispersion relation is then [97]:

$$\omega_p = \sqrt{\left(\omega_H + \Lambda_{ex}^2 \omega_m k_p^2\right)\left(\omega_H + \Lambda_{ex}^2 \omega_m k_p^2 + \omega_m F_{pp}\right)} \tag{1.77}$$

with

$$F_{pp} = P_{pp} + \sin^2\theta \left(1 - P_{pp}\left(1 + \cos^2\phi\right) + \omega_m \frac{P_{pp}\left(1 - P_{pp}\right)\sin^2\phi}{\left(\omega_H + \Lambda_{ex}^2 \omega_m k_p^2\right)}\right) \tag{1.78}$$

where $\omega_H = \gamma \mu_0 H_i$, $H_i = H_{0z} + H_{d0z}$ (H_{0z} and H_{d0z} are the z-components of the external magnetic field and constant demagnetization field respectively), $k_p^2 = k_\zeta^2 + \kappa_p^2$ the total wavevector of the spin wave and κ_p the wavevector quantized to order p in the thickness of the thin film (Perpendicular Standing Spin Waves (PSSW)). By considering a zero pinning of the magnetic moments on the film surfaces, the matrix element allowing the dipole field to be taken into account P_{pp} is expressed:

$$P_{pp} = \frac{k_\zeta^2}{k_p^2}\left[1 - \frac{k_\zeta^2}{k_p^2}\frac{1}{(1 + \delta_{0p})}\frac{2}{k_\zeta t}\left(1 - (-1)^p e^{-k_\zeta t}\right)\right] \tag{1.79}$$

with δ_{0p} the Krönecker symbol.

In Figure 1.8 b), the dispersions of the three main spin wave configurations MSSW ($\theta = \frac{\pi}{2}$, $\phi = \frac{\pi}{2}$) (red line), BVMSW ($\theta = \frac{\pi}{2}$, $\phi = 0$) (blue line) and FVMSW ($\theta = 0$) (green line) in the dipole-exchange regime are shown assuming that the thin film is sufficiently thin so that the spin wave profile is uniform through the thickness ($p = 0$ and so $\kappa_p = 0$ and $k_p = k_\zeta = k$).

The parabolic feature resulting from the exchange interaction on the spin waves dispersion becomes non-negligible from a certain wavevector $k \approx 10\ \mu\mathrm{m}^{-1}$ in the example used in Figure 1.8 b), thus constituting the boundary between the purely dipolar regime and the dipole-exchange regime. Moreover, one can notice that the BVMSW dispersion has a minimum in frequency and thus by extension in energy when the exchange interaction starts to dominate the dipolar interaction.

1.4.3 Spin waves in a crystal anisotropic thin film

In the previous section, an approximate formula for the spin waves dispersion in the dipole-exchange regime was presented, however the magnetocrystalline anisotropy interaction had not been considered. Kalinikos and Slavin [91] also developed a comprehensive theory of spin waves dispersion in the dipole-exchange regime in a thin film with magnetocrystalline anisotropy. To include the anisotropy interaction, they used the method of effective demagnetization factors, discussed previously in section 1.2.4. Using the same representation as in Figure 1.8 a), the angle ϕ_M between $\vec{M}$ and the $\langle 100 \rangle$ axis in the plane of the thin film is introduced. The approximate analytical dispersion of spin waves in a crystal anisotropic thin film is expressed as [91]:

$$\omega_p = \sqrt{\Omega_p \left[\Omega_p + \omega_m \left(F_{pp} + F^a_{pp}\right)\right]} \tag{1.80}$$

with

$$F_{pp} = \sin^2\theta - P_{pp}\sin^2\theta\cos^2\phi + P_{pp}\left[\cos^2\theta + \frac{\omega_m\left(1 - P_{pp}\right)\sin^2\phi\sin^2\theta}{\Omega_p}\right] \tag{1.81}$$

$$\begin{aligned} F^a_{pp} =& N^a_{xx} + N^a_{yy} + \left[N^a_{xx}N^a_{yy} + N^a_{yy}\sin^2\theta - \left(N^a_{xy}\right)^2\right]\frac{\omega_m}{\Omega_p} \\ &+ \left\{N^a_{yy}\left[\cos^2\phi - \sin^2\theta\left(1 + \cos^2\phi\right)\right] + N^a_{xx}\sin^2\phi\right. \\ &\left. - N^a_{xy}\cos\theta\sin\left(2\phi\right)\right\}\frac{P_{pp}\omega_m}{\Omega_p} \end{aligned} \tag{1.82}$$

$$\Omega_p = \omega_H + \Lambda^2_{ex}\omega_m k_p^2 \tag{1.83}$$

where now $\omega_H = \gamma\mu_0\left(H_{0z} + H_{d0z} - N^a_{zz}M_s\right)$.

When one sets $F^a_{pp} = 0$ (anisotropy constants K_{u1} and K_{c1} are zero), one retrieves the expression (1.77) and thus the case without magnetocrystalline anisotropy seen previously 1.4.2. Also, in the case of a uniform precession instead of a propagating one ($k_p = 0$, by extension the exchange interaction is then neglected) in a thin film thin enough so that only the first mode in thickness ($p = 0$) remains, the parameter P_{00} is then null and one retrieves the expressions of the ferromagnetic resonances in the case of a thin film with cubic magnetocrystalline anisotropy in the plane $\{100\}$ (1.63) ($\theta = \frac{\pi}{2}$, $\phi_M = 0$), (1.64) ($\theta = \frac{\pi}{2}$, $\phi_M = \frac{\pi}{2}$), (1.65) ($\theta = 0$, $\phi_M = \frac{\pi}{2}$).

1.4.4 Spin waves in a crystal anisotropic waveguide

When spin waves propagate in a magnetic waveguide of finite width w and thickness t, their dispersion is strongly modified due to the finite width of the waveguide and this is accentuated when the width of the waveguide is of the same order of magnitude as the spin waves wavelength. In this system, the spin waves propagate along the waveguide in the y' direction, the width of the waveguide is along the x' axis and the thickness along z' as illustrated in the representation in Figure 1.9. Their

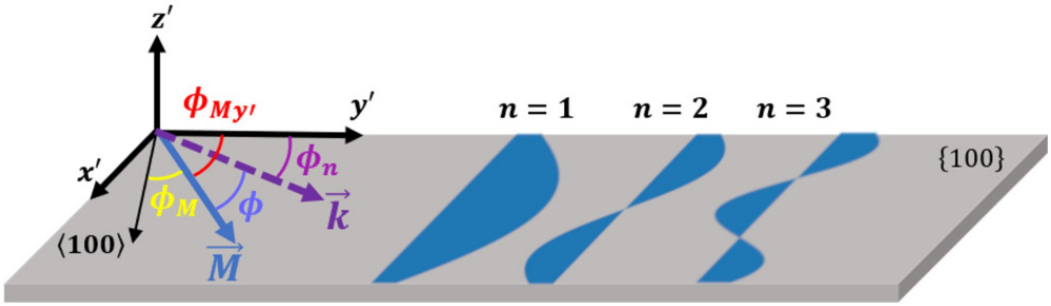

Figure 1.9: Schematic representation of the spin wave waveguide with the first three quantized modes.

propagation modes are quantized in the width w of the waveguide through the formation of standing waves and are translated via the expression of the wavevector $k_{x',n}$. The latter can only take discrete values indexed by $n = 1, 2, 3...$ corresponding to the number of antinodes of the standing wave. It then indexes the different standing spin waves modes in the x' direction. The spatial profile of the quantized spin waves in the width can be described approximately by sinusoidal functions, such as $m_{z'}(x') = A_0 \sin\left(\frac{n\pi}{w_{eff}}\left(\frac{w_{eff}-w}{2} + x'\right)\right)$, with w_{eff} the effective width of the waveguide [98–100]. As the dipolar field is not uniform in particular on the edges of the waveguide, it is necessary to introduce the notion of effective width w_{eff} [98, 100, 101] where one can consider that the effective field is constant on this width, such that:

$$w_{eff} = w\left[\frac{d}{d-2}\right] \tag{1.84}$$

with the pinning parameter d in the purely dipolar case ($w \gg t > \Lambda_{ex}$) which is written:

$$d = \frac{2\pi}{c\left(1 + 2\ln\left(\frac{1}{c}\right)\right)} \tag{1.85}$$

$c = \frac{t}{w}$ is the aspect ratio between the thickness t and the width of the waveguide w. This pinning parameter thus accounts for the decrease in mode amplitude near the edges of the waveguide.

The total wavevector is then written:

$$k_n = \sqrt{k_{y'}^2 + k_{x',n}^2} \tag{1.86}$$

with $k_{x',n} = \frac{n\pi}{w_{eff}}$. As a consequence, the angle ϕ between the magnetization $\vec{M}$ and the wavevector $\vec{k}$ now also depends on the order of quantization of the spin wave in the width. As a result, the spin wave dispersion then depends on the propagation angle ϕ_n which is calculated as:

$$\phi_n = \arctan\left(\frac{k_{x',n}}{k_{y'}}\right) \tag{1.87}$$

The dispersion relation (1.80) can be rewritten, in the case of a waveguide of small thickness ($p = 0$, $w \gg t$), by replacing k_p by k_n and ϕ by $\phi_n - \phi_{My'}$, where $\phi_{My'}$ is the angle between $\vec{M}$ and the direction along the length of the waveguide y' [99, 102, 103]:

$$\omega_n = \sqrt{\Omega_n\left[\Omega_n + \omega_m\left(F_n + F_n^a\right)\right]} \tag{1.88}$$

with

$$\begin{aligned} F_n =& \sin^2\theta - P_n \sin^2\theta \cos^2\left(\phi_n - \phi_{My'}\right) \\ &+ P_n\left[\cos^2\theta + \frac{\omega_m\left(1 - P_n\right)\sin^2\left(\phi_n - \phi_{My'}\right)\sin^2\theta}{\Omega_n}\right] \end{aligned} \tag{1.89}$$

$$\begin{aligned} F_n^a =& N_{xx}^a + N_{yy}^a + \left[N_{xx}^a N_{yy}^a + N_{yy}^a \sin^2\theta - \left(N_{xy}^a\right)^2\right] \frac{\omega_m}{\Omega_n} \\ &+ \left\{N_{yy}^a \left[\cos^2\left(\phi_n - \phi_{My'}\right) - \sin^2\theta \left(1 + \cos^2\left(\phi_n - \phi_{My'}\right)\right)\right]\right. \\ &\left. + N_{xx}^a \sin^2\left(\phi_n - \phi_{My'}\right) - N_{xy}^a \cos\theta \sin\left(2\left(\phi_n - \phi_{My'}\right)\right)\right\} \frac{P_n \omega_m}{\Omega_n} \end{aligned} \tag{1.90}$$

$$\Omega_n = \omega_H + \Lambda_{ex}^2 \omega_m k_n^2 \tag{1.91}$$

where $\omega_m = \gamma\mu_0 M_s$, $\omega_H = \gamma\mu_0 H_i$ and $P_n = 1 - \frac{1-e^{-k_n t}}{k_n t}$.

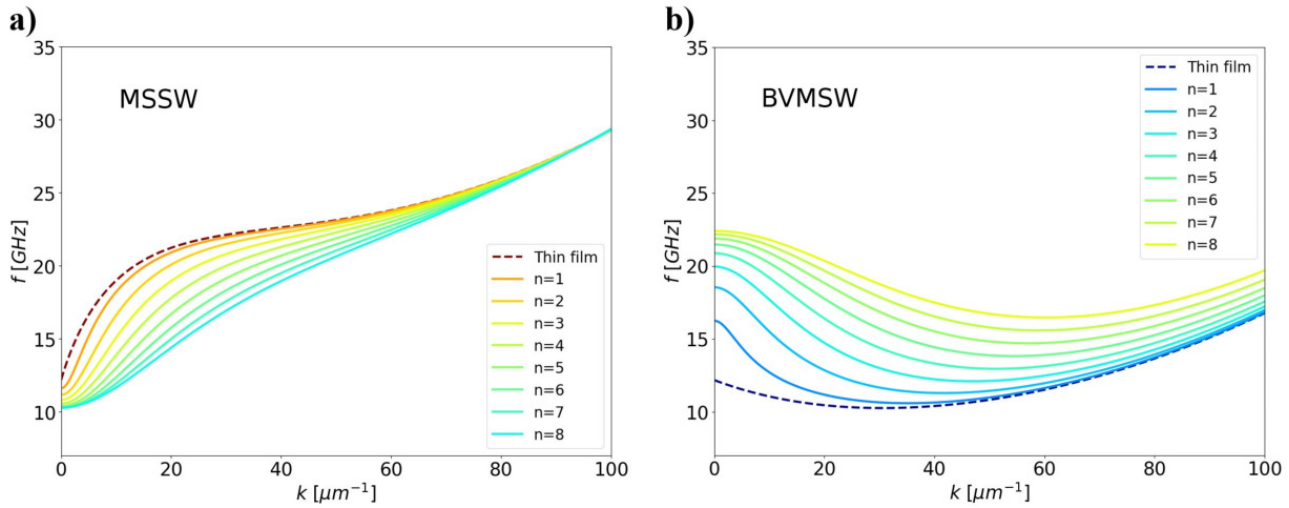

Figure 1.10: Spin waves dispersions in a CMS waveguide of width $w = 600$ nm and thickness $t = 50$ nm with a) MSSW ($\theta = \frac{\pi}{2}$, $\phi_{My'} = \frac{\pi}{2}$) and b) BVMSW ($\theta = \frac{\pi}{2}$, $\phi_{My'} = 0$). The dispersions of the quantized spin wave modes to order n are in solid lines with a color gradient and the dispersions of the thin film mode (FMR) is in dashed lines. The magnetic parameters are those of the CMS [53]: $\mu_0 M_s = 1.26$ T, $A_{ex} = 18$ pJ m^{-1}, $K_{c1} = -17$ kJ m^{-3}, $\mu_0 H_0 = 100$ mT and $\frac{\gamma}{2\pi} = 28.7$ GHz T^{-1}.

An example of calculated dispersions of quantized spin waves in a CMS waveguide of width 600 nm with the magnetic parameters of [53] in the MSSW and BVMSW configurations is shown in Figure 1.10.

It should be noted that only odd modes ($n = 1, 3, 5...$) are generally excited in the waveguide due to the symmetry of the excitation. In the case of an even-numbered mode, the quantization pattern is composed of areas with equal amplitudes but in phase opposition, as can be seen in the schematic in Figure 1.9. As a result, the torque generated by the dynamic magnetic field applied to the magnetization is cancelled out. In the same way, the more the spin wave has antinodes (large n), the weaker the torque exerted by the dynamic field will be. This is why generally only the first, third and fifth modes can be considered.

The use of this analytical formula for spin waves dispersion in a waveguide considers an effective width in the waveguide such that the effective field is constant. In the MSSW configuration, a strong demagnetizing field is at work along x' and the effective field is inhomogeneous, especially at the edges of the waveguide, where the effective field decreases drastically. Consequently the formula (1.88) is valid for spin wave modes located in the center of the waveguide (where H_{eff} can be considered as constant) but it is not valid on the edges of the waveguide and thus does not allow to predict the existence of edge modes [58, 104]. Their excitation frequencies are below the lowest excitation frequency calculating from the formula (1.88). A more complete theory considering the

inhomogeneity of the effective field in a waveguide and thus predicting the existence of edge modes has been developed by Kostylev et al. [104] and requires numerical resolution.

1.5 Magnetic relaxation processes

So far we have defined uniform precessional motions of the magnetization and spin waves without taking into account energy losses. In reality, the magnetic moments do not precess at infinity around the internal magnetic field but tend to align themselves with an equilibrium state where the magnetization is collinear with the effective field. This magnetic relaxation is achieved through a transfer of energy from the precession of spin magnetic moments to other degrees of freedom, such as phonons, electrons, impurities, defects.

1.5.1 Solving the Landau-Lifshitz-Gilbert equation

As discussed in the previous section 1.2.2, to solve the LLG equation, one linearizes the equation (1.35) such that:

$$i\omega\vec{m} = -\gamma\mu_0\left[\vec{M}_0 \times \vec{h} + \vec{m} \times \vec{H}_0\right] + i\omega\frac{\alpha}{M_S}\vec{M}_0 \times \vec{m} \tag{1.92}$$

In comparison with the equation (1.38), the determination of the Polder susceptibility tensor in the case of a dissipative regime is reduced to the following transformation:

$$\omega_0 \rightarrow \omega_0 + i\alpha\omega \tag{1.93}$$

By applying a transverse magnetic pulse excitation such that $\vec{h}_e = \delta(t)\vec{x}$, the magnetic response describes a spherical spiral which decreases exponentially towards the equilibrium state, as illustrated in Figure 1.4. This change results in a new expression of the components of the Polder tensor in a complex form: $\chi = \chi^{'} - i\chi^{''}$ and $\kappa = \kappa^{'} - i\kappa^{''}$. To find the resonance condition, one needs to calculate the $\chi_{\pm}$ eigenvalues of the Polder susceptibility tensor, which are expressed as [80]:

$$\chi_{\pm} = \chi \pm \kappa = \frac{\omega_m}{\omega_0 \mp \omega + i\alpha\omega} \tag{1.94}$$

with χ_+ the resonant circular precession eigenvalue and χ_- the non-resonant circular precession eigenvalue. χ_+ is decomposed into the complex form $\chi_+ = \chi_+^{'} - i\chi_+^{''}$:

$$\chi_+^{'} = \frac{\omega_m\left(\omega_0 - \omega\right)}{\left(\omega_0 - \omega\right)^2 + \alpha^2\omega^2} \qquad \chi_+^{''} = \frac{\omega_m\alpha\omega}{\left(\omega_0 - \omega\right)^2 + \alpha^2\omega^2} \tag{1.95}$$

The appearance of this imaginary component characterizes the damping and is reflected in the absorption of electromagnetic energy. This phenomenon allows the measurement of the ferromagnetic resonance. Considering the damping results in the appearance of an absorption peak of finite height and width as can be seen in Figure 1.11 a) and b), an example of the plotting of $\chi_+^{'}$ and $\chi_+^{''}$ as a function of the applied field and the frequency respectively. The value of $\chi_+^{''}$ is maximal when the condition $\omega = \omega_0$ is satisfied, we then have an electromagnetic energy absorption peak. Whether the imaginary part is expressed as a function of frequency or field strength, it behaves as a Lorentz function, as shown in Figure 1.11. The peak can be characterized by its Full Width at Half Maximum

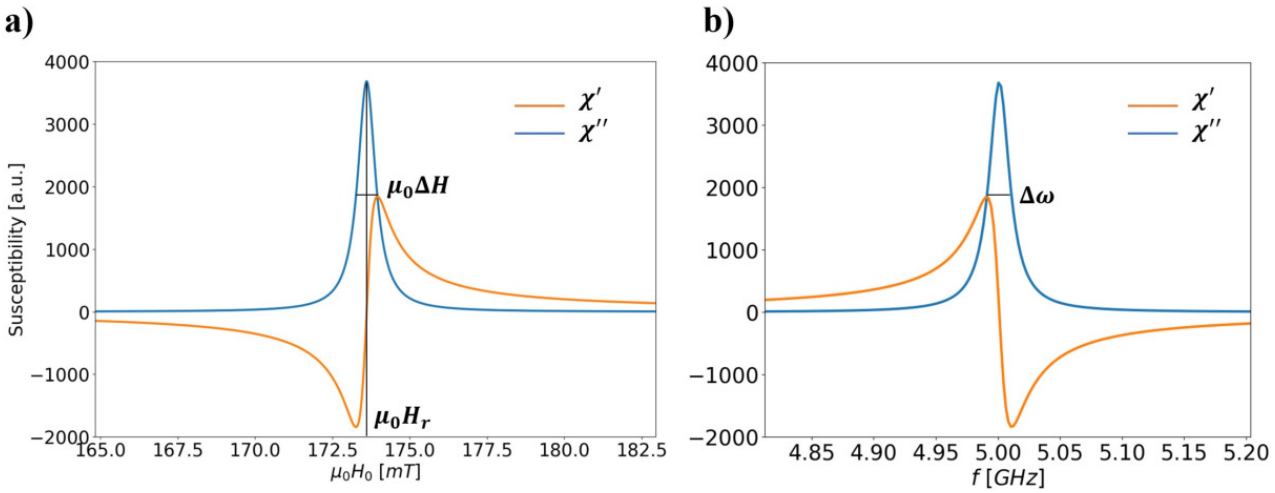

Figure 1.11: Real and imaginary parts of the resonant circular precession eigenvalue χ_+ for a) a sweep in field $\mu_0 H_0$ at $f = 5$ GHz and b) for a sweep in frequency f at $\mu_0 H_0 = 173.6$ mT. The magnetic parameters used are close to those of CMS: $\mu_0 M_s = 1.28$ T, $A_{ex} = 21.5$ pJ m^{-1}, and $\frac{\gamma}{2\pi} = 28.8$ GHz T^{-1}.

(FWHM), which is the width of the peak at half the maximum height. The FWMHs according to a magnetic field or frequency scan are respectively:

$$\Delta H = \frac{2\alpha\omega_0}{\gamma\mu_0} \qquad \Delta\omega = 2\alpha\omega_0 \tag{1.96}$$

Consequently, the Gilbert damping parameter α can be determined by measuring the width of the absorption line at the ferromagnetic resonance. Other magnetic relaxation mechanisms also contribute to the broadening of the absorption peak. Thus, experimentally, the linewidth in field is rewritten as:

$$\Delta H = \frac{2\omega\alpha}{\gamma\mu_0} + \Delta H_0 \tag{1.97}$$

with ΔH_0 the inhomogeneous broadening. The latter is the sum of the external contributions to the relaxation mechanisms. If one considers at least three extrinsic contributions, ΔH_0 can be written [105]:

$$\Delta H_0 = \Delta H_{inh} + \Delta H_{mos} + \Delta H_{2mag} \tag{1.98}$$

where ΔH_{inh} corresponds to the inhomogeous residual linewidth and results from local fluctuations due to for example crystal defects, dislocations, local variations of thickness. ΔH_{mos} is the contribution from the orientation spread of crystal phases (crystallites) and ΔH_{2mag} corresponds to the two magnon scattering contribution. When the resonance occurs along the easy or hard axis of a material with cubic crystal anistropy, ΔH_{mos} vanishes.

1.5.2 Origins of damping

Numerous mechanisms are at the origin of intrinsic and extrinsic processes of magnetization relaxation. The dissipative term in the LLG equation (1.35) is characterized by the phenomenological damping coefficient α, which is defined by both intrinsic and extrinsic relaxation processes. This parameter is measured via the linewidth of the susceptibility (1.97).

Magnetic excitations (magnons) are not isolated and thus interact with the surrounding medium such as with phonons, conduction electrons, material inhomogeneities such as crystal defects, impurities. One distinguishes "spin-spin" relaxation processes, for which a magnon diffuses on an

inhomogenity (destruction of a magnon) transforming into other magnons by energy conservation (creation of magnons), and "spin-lattice" relaxation processes which involves the transfer of energy of the magnon to the lattice (energy absorption by the lattice) [80]. The spin-lattice relaxation processes can be direct with the destruction of magnons and the creation of phonons, or can be indirect where the transfer is performed via electron scattering. In the end, the energy is generally transfered to the lattice resulting in heating.

We will discuss briefly the different relaxation processes that can occur in ferromagnetic materials.

Intrinsic relaxation processes

The instrinsic relaxation processes correspond to the natural mechanism for dissipation of energy so that the magnetization returns to its equilibrium position. The processes gather two main contributions: the relaxation of magnons via scattering with conduction electrons and the direct transfer of magnons energy to phonons.

In ferromagnetic metals, damping is majorly induced by electron-magnon interactions. This interaction with the itinerant electrons involves larger linewidth than in the case of magnetic insulators such as YIG. Depending on the conservation of spin of the conduction electrons after interaction, two different processes occur.

Spin-flip scattering, s-d interaction: In the case of scattering of a magnon and an itinerant electron of energy ϵ_k and spin σ, this process can be described by the creation and annihilation of an electron-hole pair as the itinerant electron is transfered at a higher energy ϵ_{k+q} with a flipped spin state σ'. The spin has to flip owing to the conservation of the angular momentum. If the electron-hole pair are scattered, for example with a phonon, a coherent magnon can then be emitted again. If the electron is scattered incoherently (with a phonon or a magnon), a magnon is reemitted with a phase difference. This phase difference involves a loss of coherence which will lead to damping. This mechanism is at the origin of the linear dependence of the linewidth with frequency. The latter is consistent with the Gilbert term of the linewidth.

In the case of half-metals such as $\mathrm{Co_2MnSi}$, this relaxation process is not possible in theory owing to the predicted full spin polarization. This feature is at the origin of the lower damping of half-metals compared to usual ferromagnetic metals such as Fe, NiFe.

Non spin-flip scattering, spin-orbit relaxation: The case of electron-magnon scattering without spin flip arises due to spin-orbit interaction and is detailed in [106]. A way to visualize this effect is called the "breathing Fermi surface". When the magnetization precesses, the Fermi surface is distorted periodically owing to spin-orbit coupling. The repopulation of the energy levels occurs nevertheless on a timescale of the momentum relaxation time which differs from the precession time. As a result, a phase lag arises between the magnetization precession and the pulsation of the Fermi surface leading to decoherence and thus damping. It was demonstrated by first principle calculations that the spin-orbit relaxation is the major source of damping in ferromagnetic materials [107–110].

Eddy Currents: In a metallic sample, microwave electromagnetic fields are screened by conduction electrons on a distance equal to the skin depth. This generated Eddy currents resulting from the oscillating pumping field or directly from the magnetization precession of the system can induce a major source of spin wave relaxation. It was demonstrated that this effect generates a non-zero component of the spin wave wavevector out of the plane of the thin film. The latter is written $k = \frac{1+i}{\sqrt{2}|\delta|}$ with δ the skin depth such that $\delta = \sqrt{\frac{2}{\mu\omega\sigma}}$ with σ the conductivity of the considered material and μ its permeabilitty. Due to the imaginary part of the wavevector, the spin wave is evanescent along the thickness leading to a loss of coherence. In the case of thicker samples than δ, the contribution of

Eddy currents to the damping must be considered and calculated by integrating the Maxwell's equations across the thickness. In the case of CMS thin films at room temperature, the calculated δ in the order of 200 nm is sufficiently larger than the deposited thickness ($\sim$ 45 nm) of the samples measured in this thesis to consider the effect of Eddy currents negligle [111].

Magnon-phonon scattering: Magnons can couple to the lattice leading to the formation of phonons. This can be visualized by considering a precessing spin nearby the atoms which will be periodically attracted or repelled leading to the generation of phonons. Inversely, phonons can induce spin precession that can disrupt the phase of the spin wave. This then lead to decoherence of the precession and ultimately to its damping [83].

In the end, the measured damping coefficient α is the sum of all of these contributions.

Extrinsic relaxation processes

Extrinsic relaxation processes gather energy losses mechanisms due to structural defects, inhomogeneity of the magnetic parameters, or interface effects. These contributions arise from the imperfections of the material. They can be measured via the non-zero linewidth ΔH_0 at zero frequency. The two principal sources are generally the inhomogeneity of the magnetic properties and the two-magnons scattering effect [112].

Inhomogeneity of the magnetic properties: The inhomogeneity of the magnetic parameters induces local variations of the effective field leading to the dephasing of magnetic modes and their decoherence of precession. This mechanism is the main source of damping in materials. The linewidth broadening can be expressed in this case:

$$\Delta H^A = |\frac{\partial H_{res}}{\partial A}|\Delta A \tag{1.99}$$

with ΔA coresponding to the average spread of the magnetic parameter of interest A. It can be for example the saturation magnetization or the anisotropy field. The field linewidth due to inhomogeneities is frequency and angle independent.

Two-magnons scattering (TMS): The uniform mode of magnetization precession ($k = 0$) can be scattered by defects into non-zero wavevector spin waves ($k \neq 0$) with the same energy. For this process to occur, the material needs to have defects or magnetic inhomogeneities and the FMR mode has to be degenerated with a propagating mode. This involves a non monotonous behavior of the spin waves dispersion curve. It is to be noted that in a perpendicular configuration, i.e. when the magnetization is oriented out of plane (FVMSW), there is no TMS as the dispersion relation of FVMSW does not have degenerate modes with the uniform mode.

Chapter 2

Magnonic crystals and reconfigurable applications at remanence

During this thesis, we chose to develop magnonic crystals for microwave filtering applications that can be reconfigurable at remanence. In this chapter, the concept of magnonic crystals will be introduced. First, the general case of waves propagating in periodic structures will be tackled before its use for the description of spin waves dispersion in magnetic periodic structures (magnonic crystals). Then, a non-exhaustive state of the art of magnonic crystals present in the litterature is discussed. Further details can be found in [7, 113]. Among magnonic crystals, we chose in particular two-dimensional (2D) magnetic antidot lattices for our purpose. Spin waves quantization and dispersion within these patterned structures are discussed. Several reconfigurable magnonic crystals at remanence exist and we propose the use of Co_2MnSi (CMS) Heusler alloys for the development of reconfigurable magnonic devices at remanence.

2.1 Magnonic crystals concept

2.1.1 Waves propagation in periodic structures

Waves propagation in periodic structures or crystals are studied since the end of the XIXth century [114]. In 1929, Bloch [115] has formulated the solutions as Bloch waves which since constitute the basis principles of solid state physics [10]. A major property of these structures which makes them unique and attractive is that waves propagation in such media can only be performed in particular frequency bands. A fundamental example of such phenomenon occur with electrons of a solid crystal and lead to the appearance of electronic band structures with forbidden regions called energy gaps or band gaps and allowed regions called bands.

In the case of a free electron, its energy is only kinetic. Its dispersion, which corresponds to the plot of its energy as a function of its wavevector, is then parabolic and is represented in Figure 2.1 a). Now if we take the simple case of a linear solid with a periodic arrangement of atoms, in addition to its movement the electron also weakly interacts with the periodic potential of the ions cores. As electrons can be regarded as waves, waves propagating within a crystal are partially and specularly reflected by the successive atomic planes when their wavelength is smaller or comparable to the crystal lattice constant. A constructive interference of the reflected waves can be observed for specific wavelengths

via the Bragg law [10], which is illustrated in Figure 2.1 b) and defined as:

$$2a \sin\theta = n\lambda \tag{2.1}$$

with λ the wave wavelength, a the crystal lattice constant, θ the incidence angle of the wave relatively to the atomic planes and n an integer ($n = 1, 2, 3...$). In a one-dimensional solid, the Bragg law can be reduced to the condition:

$$k = \pm n\frac{\pi}{a} \tag{2.2}$$

Electronic wavefunctions at this particular value are not exactly traveling waves as in the case of a free electron but rather an equal mix of reflected waves traveling to the right and waves traveling to the left with same group velocities but with opposite signs [114]. This leads to the formation of standing waves thus preventing its further extension within the crystal. Two standing wavefunctions can then be formed and each accumulate electrons at two different locations relatively to the atomic lattice: in between ionic potentials and in the ionic potential. This leads to two different energies for the electrons. Such difference in energy generates an energy band gap at the first Brillouin boundaries $k = \pm\frac{\pi}{a}$ as illustrated in Figure 2.1 c). Bandgaps opening due to Bragg diffraction also occur at other Brillouin boundaries indexed by the integer n.

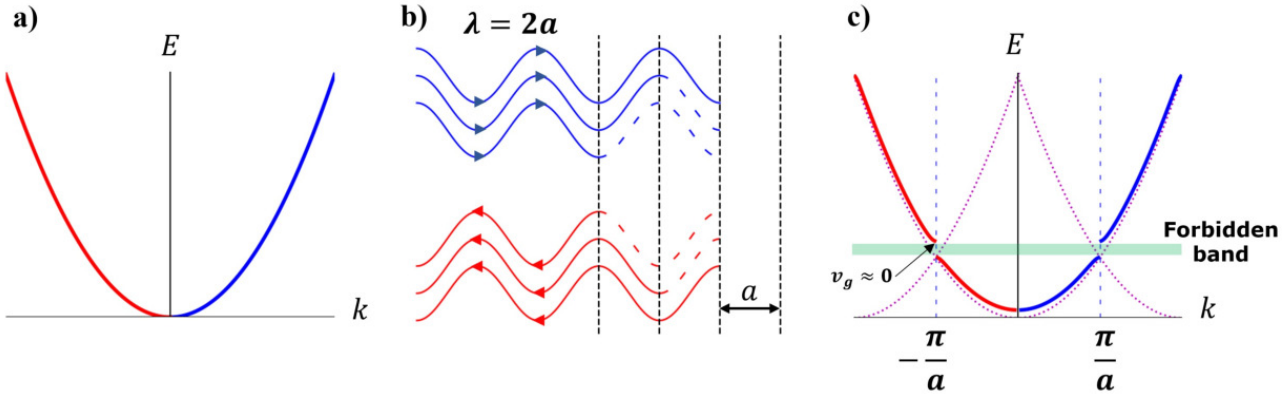

Figure 2.1: Plot of the dispersion $E(k)$ in the case of a) a free electron and c) a nearly free electron in a 1D solid crystal. b) Scheme of Bragg reflection phenomenon.

Such dispersion curve can be obtained by solving the Schrödinger equation in the case of an electron interacting with periodic atomic potentials with the help of the Bloch functions [10]. The Bloch theorem stipulates that the solutions of this problem can be expressed as a product of a plane-wave envelope function and a periodic Bloch function:

$$\psi_k(\vec{r}) = u_k(\vec{r})e^{i\vec{k}\cdot\vec{r}} \tag{2.3}$$

with $u_k(\vec{r})$ characterizing the periodicity of the crystal lattice such that $u_k(\vec{r}) = u_k(\vec{r} + \vec{T})$, and $\vec{T}$ a translation vector of the lattice periodicity.

Another way to visualize this phenomenon is with the empty lattice approximation [10]. In this approximation, an electron in a periodic potential lattice is dealt with but the potentials are sufficiently weak to consider the electron as free. Due to the periodicity of the lattice, the free electron dispersion can be repeated at each $n\frac{2\pi}{a}$ wavevectors, thus folding these parabolic dispersion branches within the first Brillouin zone, as plotted with dotted magenta lines in Figure 2.1 c). Indeed from Bragg diffraction, one can write $\vec{k'} + \vec{G} = \vec{k}$, with k' a wavevector from the first Brillouin zone. These periodic dispersion curves cross at $\pm\frac{\pi}{a}$ wavevectors. When turning on the potentials, as discussed previously, energy bandgaps open at the Brillouin zone boundaries corresponding to an anticrossing of these periodic dispersion curves. As the dispersion curves are periodic with the reciprocal lattice $\pm n\frac{2\pi}{a}$, a mirror symmetry relative to $k = 0$ exist. Consequently, band diagrams visualization can be limited to

the first Brillouin zone. In Figure 2.1 c), the dispersion plot is not restricted in the first Brillouin zone, which corresponds to the so-called extended zone scheme.

As a result, band structures of periodic media are governed by two opposing mechanism. On one hand, waves propagating through periodic scatterers first begin to be confined in-between the scatterers, which act like resonators, and then couple coherently restoring them their dispersive behavior. On the other hand, for particular wavevector values, waves propagating in such periodic media are subjected to Bragg reflection preventing their further extension throughout the periodic media. Forbidden energy or frequency bands thus arise from the periodicity of the solid crystal. The calculation of the allowed and forbidden energy bands of electrons in solid crystals are of utmost importance for determining whether the solid is an insulator or conductor. As a consequence, band engineering can be performed to obtain particular physical properties when one can artificially induce periodicities in a material.

Periodic artificial crystals can be created by the periodic introduction of defects/modifications that will act as scattering centers also called scatterers. Photonic crystals which emerged in 1987 [11, 12] constitute a well-known example of periodic artificial crystals. A photonic crystal is a material (dielectric or metallic) with a periodic refractive index whose periodicity is comparable to the wavelength of light [116]. The periodic refractive index is analog to the periodic potential in a solid crystal. Beyond the generation of photonic band gaps which allows filtering of certain light frequencies, photonic crystals can also for example guide, reflect, trap light with these band gaps [116, 117]. These effects are notably used to achieve integrated optical circuits and more efficient photovoltaic solar cells [13]. Consequently, such systems exhibit optical properties that would not exist otherwise, such as a negative refraction index [118–121]. Photonic crystals with particular dispersion features can bend light propagation in the opposite direction of the usually one described by Snell law [118, 119]. Such property could lead to the achievement of a flat 'superlens' which could result in an imaging resolution no more limited by light diffraction [119, 120].

These works suggested then many enthusiasms since 1990 to make periodical systems with other types of waves such as elastic waves [122], plasmons [123] and more particularly spin waves, thus giving rise to the concept of magnonic crystals [15, 16, 124].

2.1.2 Magnonic crystals

Magnonic crystals are magnetic materials with artificially and periodically modulated magnetic properties. Analog to electrons in a solid crystal or photons in a photonic crystal, spin waves propagating in such periodic metamaterial can be subjected to Bragg reflections leading to the appearance of frequency band gaps for specific wavevectors in the spin waves dispersion. Although periodical systems started to be studied in magnetic materials during the years of 1970 [14], surprisingly it did not gather much interest at that time compared to dielectric materials, whose works for the developement and study of photonic crystals had exploded. In fact, magnonic crystals are more suitable for nanoscale microwave devices as spin waves wavelengths in the microwave regime are several orders shorter (four to five orders) than that of electromagnetic waves in photonic crystals. In addition, magnonic crystals offer a major advantage over all of the other types of artificial crystals: its band structure is not exclusively dependent on the crystal periodicity, lattice symmetries and geometrical shape of the periodic scatterers. It can also be modified according to the spatial arrangement of the spin magnetic moments fixed by the application of an external magnetic field. Due to the anisotropic dispersion of spin waves in the particular case of in-plane magnetization (MSSW, BVMSW), the spin waves band structure generated by magnonic crystals can be modified according to the amplitude and orientation of an applied magnetic field. This additional degree of freedom gives to magnonic crystals a reconfigurable, reprogrammable property [113], standing them out from photonic crystals.

Magnonic crystals can be one-dimensional (1D), 2D or even 3D, where the periodic modulation

is along one, two or three directions in space respectively, as illustrated in Figure 2.2. They can be obtained from bulk magnetic materials or from magnetic thin films. With the aim of miniaturized magnonic devices, most of the magnonic crystals studied in the literature are made with magnetic thin films.

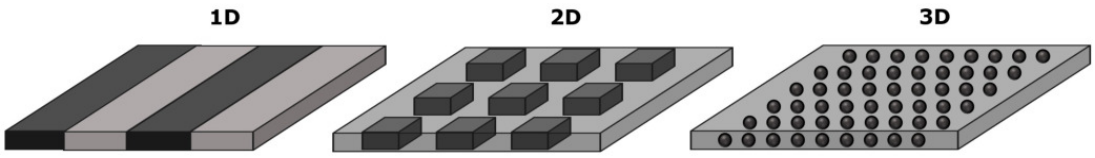

Figure 2.2: Simple schemes of 1D, 2D and 3D magnonic crystals.

Numerous periodic patterning strategies for magnonic crystals were explored in the literature and can be classified according to their dimension properties (1D, 2D or 3D) and their type of magnetic periodic modulation [113]. Several parameters can be varied in space: the geometrical shape (thickness, width, presence of holes, dots), the intrinsic magnetic parameters (saturation magnetization, exchange constant), the applied magnetic field.

1D magnonic crystals mainly gather magnetic thin films or waveguides with alternating arrays of ferromagnetic stripes and non-magnetic stripes [125] or other ferromagnetic stripes (bi-component) [126, 127] or ion-implanted stripes [26], with periodically varied width (waveguide) [18, 128, 129], with a periodic application of an external magnetic field via a shape meandered current line [130]. The latter magnonic crystal has the distinctive property of dynamic controllability with the application of current leading to the possible on-demand modification of spin waves band structure. The majority of magnonic crystals present in the literature are static as their periodic modulated magnetic properties do not change in time. 2D magnonic crystals are generally composed of periodic lattices of dipolar-coupled magnetic nanostructures/disks [19, 20], periodic lattices of antidots etched in a magnetic thin film [21, 23, 131] or ferromagnetic dots incorporated in another ferromagnetic thin film matrix (bi-component) [24, 25]. Finally, few 3D magnonic crystals exist in the literature due to their technological complexity. Still one can find magnetic thin films or waveguides with periodic etched grooves called surface-modulated magnonic crystals [17, 132], thickness-modulated single and bi-component nanowires [133] or periodic ferromagnetic spheroid embedded in another ferromagnetic matrix [61]. Consequently, the design possibilities of magnonic crystals are quasi-infinite. A rich diversity of applications thus results from magnonic crystals such as tunable filters [134] or phase shifters [135], frequency and time inverters [136], power limiters [137], sensors [138], logic circuits [139, 140] and transistors [2].

The Figure 2.3 shows two examples of 1D magnonic crystals: a periodic magnetic stripes arrays [141] and a width-modulated waveguide [18]. For the periodic stripes arrays in Figure 2.3 a), the dispersion of spin waves excited in the MSSW configuration ($\vec{H}$ applied along the length of the stripes) is measured by Brillouin Light Scattering (BLS). This technique, that will be shortly detailed in chapter 6 section 6.2.2, allows to measure the frequency bands and band gaps according to the spin waves wavevectors. In the dispersion plot in Figure 2.3 a), a large band gap occurs at the first Brillouin boundary ($k = \frac{\pi}{a}$) and another smaller band gap at a higher frequency can be seen. In the case of the width-modulated waveguide in Figure 2.3 b), the transmitted spin waves intensities were measured at a distance of $8\ \mu\mathrm{m}$ from a source antenna by space-resolved Brillouin Light Scattering microscopy for a range of frequencies. Compared to the calculated spin wave dispersion of an unpatterned waveguide, reflection bands appear for Bragg wavevectors.

When the Bragg conditions are not met, most of the propagating spin waves intensity is retrieved as few part of it is reflected. The transmission and reflection coefficients of magnonic crystals depend on the periodic structuration [17, 124, 142] and on the angle incidence of the incoming spin waves. For example, all ferromagnetic magnonic crystals such as bi-component magnonic crystals are indeed better candidates for an efficient tuning of spin waves band structure owing to their strong exchange

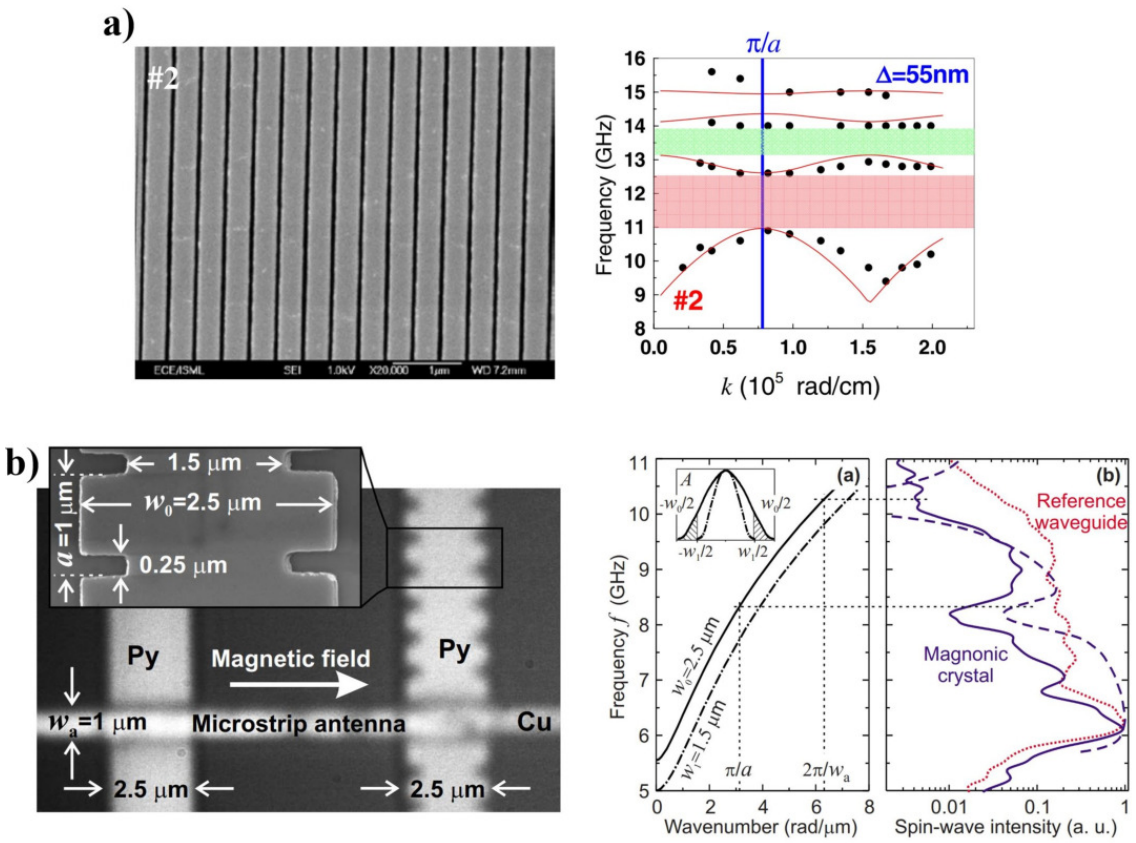

Figure 2.3: a) On the left, SEM image of permalloy (NiFe) stripes arrays, and on the right, their measured spin waves dispersion by BLS for an applied magnetic field along the length of the stripes $H = 500$ Oe [141]. b) On the left, SEM and optical images of a width-modulated magnonic crystal and a reference unpatterned waveguide. On the right, the analytical spin waves dispersion (in black), the measured transmitted spin waves intensity for the magnonic crystal (in blue) and for the reference waveguide (in red) (the blue dashed line represents calculated spin waves intensities for the magnonic crystal) [18].

coupling at the interface of the two different ferromagnetic materials and their maximized dynamic dipolar coupling [24, 143–146]. As a result, spin waves propagation is less damped and can extend more easily in the entire magnonic crystal. They can thus be subjected to more Bragg reflections leading to the opening of more bandgaps. Nevertheless, bi-component magnonic crystals are usually more difficult to make [146, 147] with the necessity of multilevel electronic beam lithography with the constraint of alignment of the two contrasting magnetic materials [148]. In our case, this would have not been possible to fabricate as we do not have a sputtering that can combine successively ion beam etching and magnetic thin film deposition neither the equipments for self-aligned shadow deposition [147].

In this thesis, we chose to study a magnonic crystal for microwave filtering applications due to the existence of the frequency band gaps. Several properties are important for the realization of a microwave filter, such as a low attenuation of the transmitted signal, a strong attenuation for the reflected signal (bandgap) and large spin waves group velocities. Numerous parameters of magnonic crystals play on the formation of band gaps, their number, position, bandwidth and on the group velocities. First, the periodicity will define the spin waves Bragg wavevectors ($\pm n\frac{\pi}{a}$) and thus will determine the frequency positions of the gaps according to the spin wave dispersion of the magnetic system with no artificial periodicity. Larger periodicities will result in a spin waves dispersion dominated by magnetostatic interactions [149], whereas smaller periodicities will imply exchange interactions majorly responsible for the generated band structure [149]. Larger bandgaps are obtained in the dipolar-exchange regime. Consequently, to obtain large bandgaps, periodic structures on the 100 nm

length scale must be targeted [131, 149]. Even larger band gaps can be obtained in the exchange regime, however this implies to produce sub-100 nm periodic features, which is for the moment technologically challenging.

The number of periodic scatterers acts on the band gaps depth. A large number of periodic scatterers will reflect spin waves more efficiently [130] and avoid the formation of pseudo-gaps, which are frequency bands with lowered intensity. Additionally, the rejection depth is also determined by the transmission and reflection coefficients of the periodic structure. The shape of the magnetic periodic structure (scattering centers) of the magnonic crystal will also play an important part on the number of frequency band gaps and their width. If the shape of the periodic structure can be approximated by a periodic rectangular function as in the Kronig-Penney model used for electrons in solids, several frequency band gaps will be generated. However, in the case of a sine profile of the periodic structure, only one frequency band gap will be opened [128, 130].

As a consequence, a wide variety of parameters gathering intrinsic magnetic properties (saturation magnetization, exchange constant, magnetocrystalline anisotropy), geometrical shape, periodicity and number of scatterers, thickness, shape of the magnetic matrix, strength and orientation of the applied magnetic field will act on the position, width and number of the allowed frequency bands and band gaps, depths of the frequency band gaps and setting of group velocities. Additionally, the spin waves band structure in magnonic crystals can not be exclusively explained by Bragg reflections [131]. Spin wave modes confinement [150] and hybridization occuring at non Bragg wavevectors [149, 151] can be responsible for the generation of additional band gaps.

To do band structure engineering, the complete calculation of the band structure from a designed magnonic crystal is required. To this end, two main numerical methods are used: the plane wave method and micromagnetic simulations. Other numerical methods exist such as the dynamical matrix method but they are less used in the literature and will thus not be detailed in this thesis.

The plane wave method is analog to the Bloch description used for the determination of electronic band structures in solid crystals [61]. The aim is to solve the linearized LLG equation (1.35) by considering a periodic modulation of the saturation magnetization M_s and of the exchange stiffness A. To solve the set of equations, the Bloch theorem [10] is used. The solutions of the equations can be written as:

$$\vec{m}(\vec{r}) = \vec{m}_{\vec{k}}(\vec{r})e^{i\vec{k}\cdot\vec{r}} = \sum_{\vec{G}} \vec{m}_{\vec{k}}(\vec{G})e^{i(\vec{k}+\vec{G})\cdot\vec{r}} \tag{2.4}$$

with $\vec{k}$ the wavevector in the first Brillouin zone and $\vec{G}$ the reciprocal lattice vector. Due to the periodic structure considered, the saturation magnetization and exchange stiffness can be expressed in the reciprocal space (Fourier transform) as:

$$M_s(\vec{r}) = \sum_{\vec{G}} M_s(\vec{G})e^{i\vec{G}\cdot\vec{r}} \; ; \; \Lambda_{ex}^2(\vec{r}) = \sum_{\vec{G}} \Lambda_{ex}^2(\vec{G})e^{i\vec{G}\cdot\vec{r}} \tag{2.5}$$

with $\Lambda_{ex} = \sqrt{\frac{2A}{\mu_0 M_s^2}}$ the exchange length. The Fourier components $M_s(\vec{G})$ and $\Lambda_{ex}^2(\vec{G})$ are then calculated by inverse Fourier transform. A finite number of reciprocal lattice vectors must then be chosen to ensure the convergence of the solutions. As a result, the problem can be reduced to a matrix form $\hat{M}\vec{m}_{\vec{k}} = i\Omega\vec{m}_k$ that can be solved by standard numerical procedures to find the eigenvalues Ω, which allow to determine the spin waves dispersion $f(\vec{k})$, and the eigenvectors $\vec{m}_{\vec{k}}$ that can be used to plot the spatial profile of the spin wave modes (amplitude in real space). The plane wave method is a powerful tool for the calculation of spin waves dispersion in periodic structures. However this numerical method has some limits as it is based on several approximations. The crystal anisotropy and damping are usually neglected [61]. This method can only be applied for fully saturated materials in the linear approximation [152]. When dealing with a planar magnonic crystals with antidots, the thickness must be sufficiently thin so that the magnetization is homogeneous in the thickness and the saturation magnetization can not be put to zero but to a small quantity.

To overcome these limitations, micromagnetic simulations constitute another candidate. It relies on solving the LLG equation with Finite Difference Method or Finite Element Method in time domain and real space. These numerical methods were used during this thesis and will be further detailed in chapter 3 section 3.1.

2.1.3 Spin waves in 2D Magnetic Antidot Lattices

During this thesis we chose to study a specific kind of magnonic crystals among those listed in section 2.1.2 for filtering applications: 2D periodic lattices of holes etched in a magnetic thin film or the so-called magnetic antidot lattices [153].

As discussed in chapter 1 section 1.3.2, three main types of spin waves (MSSW, BVMSW and FVMSW) exist in a magnetic thin film according to the relative orientations of the applied field $\vec{H}$ with respect to the spin wave wavevector $\vec{k}$. FVMSW have the advantages of a lowest propagation loss per unit time [70] and of being more isotropic (isotropic dispersion in the plane) compared to in-plane spin waves, which make them better candidates for the generation of complete band gaps in 2D magnetic antidot lattices [131]. However, a large magnetic field ($\geq$ 1 T) must be applied to saturate the magnetic antidot lattice, which will not be convenient for integrated circuits applications. Nevertheless, it is to be noted that materials with Perpendicular Magnetic Anisotropy (PMA) could be used to overcome this problem. For this reason, uniform precession and propagation of FVMSW will not be further considered in this thesis. MSSW are favored over BVMSW as they possess larger group velocities and are easier to excite. Nevertheless, BVMSW are more sensitive to Bragg reflections which can lead to the formation of larger and stronger frequency band gaps [17]. Consequently, the configurations MSSW and BVMSW seem to be suitable for the development of magnonic filters.

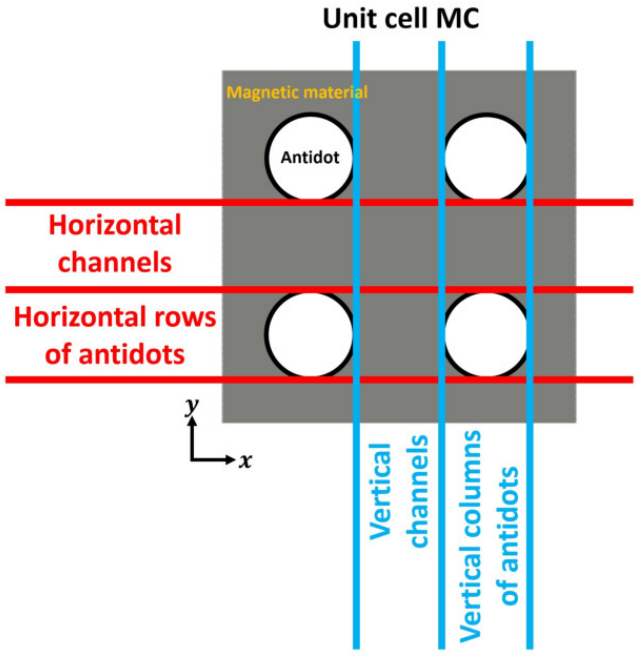

Figure 2.4: Schematic of a unit cell of a magnetic antidot lattice with circular holes showing the different terms used to identify specific regions of the structure.

In magnetic antidot lattices, the periodic antidots lead to spin wave quantization and periodic modulation of the internal magnetic field H_{int} driven by strong demagnetizing interactions. This periodic inhomogeneity of the internal field act as the periodic scatterers analog to the atomic potentials in

solid crystals or to the periodic varying refractive index in photonic crystals, and is mainly responsible for the generated allowed frequency bands and band gaps [60, 146, 154, 155]. Due to the induced spin wave quantization in magnetic antidot lattices, several spin wave modes with particular spatial profiles can be uniformly excited ($k = 0$) for specific frequencies. When these modes propagate ($k \neq 0$) through the magnetic antidot lattice, they present different dispersion features such as group velocities and sensitiveness to Bragg reflections. The spatial profiles of these modes, that can be retrieved with uniform precessions, play an important part in their dispersive behavior in such periodic structure. For the description of the different collective spin wave modes, we defined specific regions of the magnetic antidot lattice. The different terms that will be used in this manuscript are: horizontal channels, horizontal rows of antidots, vertical channels and vertical columns of antidots, and are schematized in Figure 2.4. Horizontal channels corresponds to the continuous magnetic regions in-between adjacent rows of antidots extending along the x direction in the schematic. Horizontal rows of antidots corresponds to the magnetic regions discontinued by the presence of the periodic antidots in-between adjacent horizontal channels.

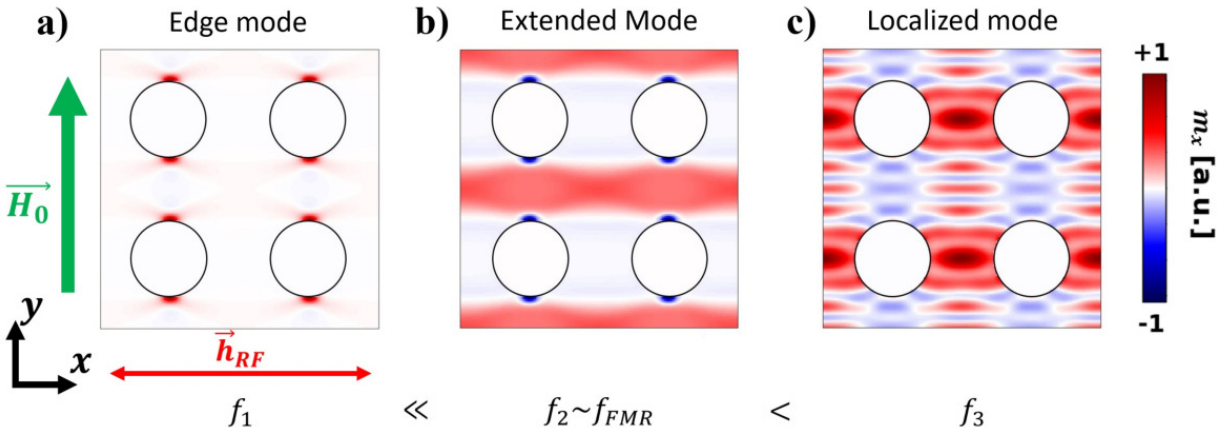

Figure 2.5: Examples of three main spatial profiles of the magnetization precession amplitudes of particular spin wave modes excited in a magnetic antidot lattice with a saturation field $\vec{H}_0$ applied along the y direction and a uniform pumping field $\vec{h}_{RF}$ applied along the x direction: a) edge mode, b) extended mode and c) localized mode. These spatial profiles were calculated via micromagnetic simulations (chapter 3 3.1.4) with the magnetic and geometric parameters of [156]. The material used is permalloy and the antidots diameter and periodicity are respectively 240 and 440 nm.

With an in-plane applied magnetic field, three main types of collective spin wave modes can be uniformly excited in magnetic antidot lattices ($k = 0$) [60, 150, 155]: edge modes, extended modes and localized modes. The edge mode [157] corresponds to the lowest frequency excited mode in the magnetic antidot lattice. Its frequency is lower than the FMR frequency of the magnetic thin film. Its high precession amplitudes are located at the vicinity of the antidots, as shown on the calculated spin wave mode profile in Figure 2.5 a). The internal field is strongly lowered close to the antidots edges in the direction of the applied field due to an increase of the demagnetizing field in these regions. Propagating spin waves are confined within these internal field deep wells. This mode resembles the edge mode arising in transversly magnetized waveguides [158, 159] mentioned in chapter 1 section 1.4.4. When increasing the frequency, different spin wave modes appear which belong to different categories. Two typical examples are shown in Figures 2.5 b) and c) obtained at a higher and even higher frequencies. In the first example, one can observe a mode whose maximum precession amplitude extends along the channels in-between rows of antidots perpendicular to the applied magnetic field. Due to its quasi-uniform spatial extension throughout the antidot lattice, this mode is qualified as an extended mode and is shown along the horizontal channels in Figure 2.5 b). In the second example, a spin wave mode arises with its precession amplitude maximized in-between adjacent antidots as shown along the horizontal rows of antidots in Figure 2.5 c) and is termed localized mode. The

strongly varying demagnetizing field in this area acts as a potential well localizing the precession of the magnetization [150]. At high frequencies, other complex spin wave modes appear. They can be described as higher-order quantized modes of mixed extended and localized modes [21, 49]. These main quantized modes propagate differently through the magnonic crystals. The propagation of the edge mode is only governed by dipolar coupling which results in lower group velocities due to strong spatial confinement. Small propagation distances can be reached with this mode even if closer antidots can facilitate its propagation. The localized modes are also less dispersive [160].

The propagation features of the extended mode can be described via the spin waves dispersion of transversely magnetized effective nanowires in-between the antidots [146, 158, 161]. However, this description can not render the frequency magnonic band gaps occuring for different Bragg wavevectors ($k = \pm n\frac{\pi}{a}$). Zivieri et al. have developped an analytical model to estimate the frequency band gaps of transversely magnetized permalloy antidot lattice of periodicity a and antidots size δ [60]. The periodicity and the antidots size is large enough (in the 100 nm range) to consider dipolar-dominated spin waves in this periodic structure. They first averaged the internal field along the direction of the applied magnetic field for the two spin wave modes extended $\langle H_{int}^{y\ extended}\rangle$ and localized $\langle H_{int}^{y\ localized}\rangle$ (here along y in Figure 2.5). Owing to the presence of antidots, these mean internal fields present periodic maxima of amplitudes along the direction of propagation (along x in Figure 2.5). By using an approach analog to the Kronig-Penney model [10] used to obtain electronic band structures in solid crystals, they demonstrated that the band gap for a particular wavevector k and particular mode i (i =extended, localized) can be approximated by:

$$\Delta\nu^{k\ i} \approx \frac{\gamma}{2\pi}(2|H_{int}^{k\ i}|M_s)^{1/2} \tag{2.6}$$

with $\Delta\nu^{k\ i} = \nu_{n+1}^{k\ i} - \nu_{n}^{k\ i}$ the frequency splitting at the Brillouin zones boundaries indexed by the integer $n = 1, 2, ...$ and $H_{int}^{k\ i}$ the k-Fourier component of the mean internal magnetic field written as:

$$H_{int}^{k\ i} = \frac{2}{k\pi}(\langle H_{int}^{y(1)\ i}\rangle - \langle H_{int}^{y(2)\ i}\rangle)\sin\frac{k\pi\delta}{a} \tag{2.7}$$

with $\langle H_{int}^{y(1)\ i}\rangle$ and $\langle H_{int}^{y(2)\ i}\rangle$ respectively the maximal and minimal mean internal field values along the direction of propagation. The Fourier coefficients $H_{int}^{k\ i}$ decrease for larger k values which is consistent with the observed trend of band gaps smaller and smaller with increasing k [60]. Besides it should be the opposite situation for BVMSW as higher-order Bragg reflections occur for lower frequencies in this case [142]. From this expression, magnetic materials with larger saturation magnetization could present larger band gaps.

As mentioned in the previous section 2.1.2, several strategies can be applied to obtain desired spin waves band structure in these magnonic crystals. The antidots shape (square, circle, triangle...), lattice symmetry (square, hexagonal, honeycomb like...) and periodicity can tune the profile of the quantized spin wave modes and the anisotropy (angle-dependence) of the spin waves band structure by the induced magnetic anisotropy [21, 162]. In specific structures, localized modes can become extended modes with the varied in-plane angle of the applied magnetic field with respect to the lattice symmetry axes [162]. For short periodicities, an overlap of the spin wave modes can occur, which may prevent them from the interaction with the periodic perturbations leading to a closing of band gaps. At the opposite, large periodicities will induce weaker Bragg reflections resulting also in band gaps closing as it tends to the case of a plain thin film [149].

Magnonic antidot lattices thus display several advantages over other types of magnonic crystals. First, they can have large frequency band gaps due to a large magnetic contrast between the magnetic thin film and the antidots scatterers (zero saturation magnetization and exchange constant) [61]. They have larger propagation velocities than lattices of interacting coupled magnetic disks/nanostructures. The band gaps generated by the latter magnonic crystals are narrow due to weak magnetic interactions (only dipolar) between the localized modes [163]. However, the presence of holes can strongly

attenuate propagating spin waves in the allowed bands compared to bi-component magnonic crystals [143], reducing their transmission efficiency in the allowed frequency bands.

Numerous applications based on magnetic antidot lattices exist: microwave filters, phase-shifters and waveguides [23, 27, 28], ultra-high density storage media for non-volatile memory [42, 43] but also sensor of magnetic nanoparticles [44, 164], and SWASER (Spin Wave Amplification by Stimulated Emission of Radiation) [165], the magnetic counterpart of LASER, where the designed magnonic crystal act as a cavity with a line defect to guide excited spin waves whose frequency lies in the band gap of the magnetic antidot lattice.

2.1.4 Reconfigurable magnonic crystals at remanence

Most of the magnonic devices and magnonic crystals from the literature and mentioned previously need to operate with a saturated magnetization state along a particular direction, in order to have a uniform magnetic state. This uniform magnetic state is essential for large FMR signal and for the straight and efficient propagation of spin waves (MSSW, BVMSW and FVMSW). To saturate the magnetization of the sample, strong magnetic fields have to be applied, which requires the use of permanent magnets in devices. Stray fields of permanent magnets may disrupt other nearby magnetic components of an integrated circuit, and this can worsen with the increase of operation frequency as it needs larger permanent magnets to provide larger magnetic fields. As a consequence, the presence of permanent magnets greatly limits the application of magnonic devices in integrated circuits. Recently, several strategies were approached to develop magnonic devices that can be reconfigurable at remanence, i.e. at zero magnetic field applied.

The reconfigurability of the device manifests through the possibility to offer different remanent magnetic states resulting in different microwave responses. Numerous works were particularly focused on the use of nanopillar lattices [29, 30], elliptical nanostructures composed of two different magnetic materials (NiFe and Co) [31], or dipolar coupled nanowires [32–34, 166]. Dipolar coupling of these structures can stabilize two remanent magnetic states, parallel (ferromagnetic) or anti-parallel (antiferromagnetic). These magnetic systems thus possess two energy minima and are qualified as bistable [113]. These two remanent magnetic states can be associated to two logic states that can be switched according to magnetization reversal processes where the direction and amplitude of one or several initialization magnetic fields relatively to the easy or hard axes of these structures are applied. These logic states are then read with the microwave response of the system. In the case of dipolar coupled nanowires [33, 167], the bistable states which exhibits ferromagnetic order (FMO) and antiferromagnetic order (AFO) allow to obtain two distinct spin waves dispersions with different frequency band gaps. In the AFO state, the periodicity is changed leading to a modification of the size of the Brillouin zone [33]. Such behavior can lead to the development of tunable spin wave filters. Concerning, the nanopillar lattices [29], spin waves propagation in these structures is predicted to be nonreciprocal [168], which can be used for microwave circulators and isolators working at remanence [113]. Nevertheless reconfigurable remanent magnetic states based on dipolar coupling presents some disadvantages. In particular, these devices are sensitive to fabrication defects, need complex and of high amplitude initialization schemes, and present low spin wave group velocities due to weak dynamic dipolar coupling.

Other works deal with the use of shape anisotropy from nanostructures to generate multiple reconfigurable remanent magnetic states [35]. A demonstration of such features was performed with the combination of nanostructures of rhomboid shape and particular dimensions as illustrated in Figure 2.6. With the application of an initialization magnetic field along the long or short axis of the rhombohedral nanostructures, two quasi-uniform remanent magnetic states can be generated, parallel or anti-parallel respectively. These two remanent magnetic configurations give two different microwave responses, which are particularly characterized by a frequency shift of the spin wave modes in the

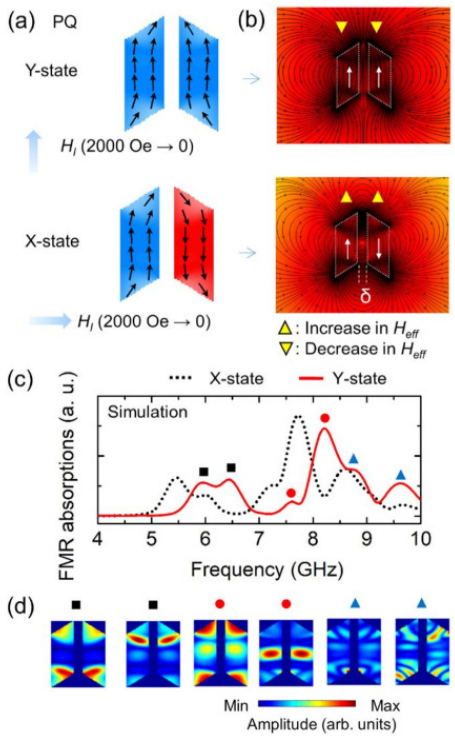

Figure 2.6: Simulated results showing the realization of reconfigurable operations with the association of two self-biased rhomboid nanostructures: a) simulated remanent states, b) simulated demagnetization field distributions c) FMR spectra of the remanent states and d) simulated spatial profiles of the different resonant modes [35]. This image is from [35].

order of 400-600 MHz according to the used configurations [36, 37].

It is important to obtain large frequency shifts in order to be able to distinguish without ambiguity the different reconfigurable operations. To achieve this, they used the same nanostructures but this time composed of several piled magnetic thin films spaced by a non magnetic material such as NiFe/Cr/NiFe. Large frequency shifts up to 5 GHz in the range 3-15 GHz were obtained according to the number of layers and their arrangement [38–40]. Beyond the scope of reconfigurable logic operations at remanence, they also demonstrated the possibility to propagate spin waves at remanence through straight and bent waveguides formed by a channel layout of these nanostructures [41]. Furthermore, a "switch" operating at remanence could have been made, letting spin waves by or not according to the direction of the initialization magnetic field [41].

Few works explored the intrinsic magnetic properties of a magnetic material to make reconfigurable microwave components at zero bias field. Thick films of magnetic ferrites such as those of hexaferrite bismuth which possess a strong magnetic anisotropy are examples [45]. Such devices are currently commercialized [46]. However due to their thickness and dimension (in the order of mm), the latter would be difficult to nanostructurate, thus preventing their application for miniaturized components. In this thesis, we propose to use the strong cubic anisotropy of Co_2MnSi (CMS) Heusler alloys to make reconfigurable microwave components at zero bias field.

2.2 Generalities on materials used in magnonics and advantages of Co_2MnSi Heusler alloy for reconfigurable magnonic crystals

2.2.1 Yttrium Iron Garnet and Permalloy

In the literature, Yttrium Iron Garnet (YIG) and permalloy (Py or NiFe) are the main magnetic materials used for the development of magnonic devices. YIG is a ferrimagnetic insulator. Its damping coefficient is the lowest measured among magnetic materials, as low as 3.10^{-5} for bulk [47] and of the order of 1.10^{-4} for thin films with thicknesses in the range of few tens of nanometers [169, 170]. Such low damping coefficient allows the propagation of spin waves over long distances up to the millimeter range in the case of samples with micrometer thicknesses [7]. Then, YIG is very well suited to adress numbers of fundamental problems and makes demonstrators such as logical operation devices based on the manipulation of spin waves [7]. However, despite its great interest for many studies, YIG thin films can show a few limitations for the development of commercial microwave devices. First, it has a relatively low saturation magnetization leading to microwave resonances in the range of a few hundreds of MHz to a few GHz at remanence or very low field values. Also, in order to be compatible with the actual CMOS technologies, the deposition of YIG must be achievable on silicon substrates with crystalline quality. Such achievements are not straightforward but huge advances have been made in this field recently and very high quality thin films have been obtained by different methods allowing to consider YIG for industrial applications [48, 171–173].

On the contrary of YIG, permalloy (Py) is a ferromagnetic polycrystalline metal. It is widely used in the literature owing to its easiness of deposition and micro/nanostructuration. Its saturation magnetization is relatively high (about 1 T), however its damping coefficient is about two orders of magnitude higher than in the case of YIG (in the order of 6.10^{-3} [7]). Consequently, the distance on which spin waves can propagate is strongly reduced to only few $\mu\mathrm{m}$, which may limit some applications such as phase shifter for example. As a consequence, strong efforts have been made for several years to develop magnetic metals with potentially a high saturation magnetization, a high spin polarization and low damping. In this context, full-Heusler alloys of general formula $\mathrm{Co_2YZ}$ appear as an interesting alternative to the magnetic materials mentioned previously.

2.2.2 Heusler-based alloys and the particular case of Co_2MnSi

In 1903, F. Heusler discovered a peculiar feature of an intermetallic compound $\mathrm{Cu_2MnAl}$: an exhibition of a spontaneous magnetization resulting from the combination of three different non ferromagnetic materials [174]. Generally, this particular property concerns some ternary intermetallic compounds of general chemical composition $\mathrm{X_2YZ}$ (full-Heusler) and XYZ (half-Heusler), with X and Y transition metal elements and Z a main group element. One major interest of Heusler alloys for spintronic applications is that many of them were theoretically predicted to be half-metals. This term was introduced by de Groot et al. in 1983 when they calculated the electronic band structure of the compound NiMnSb [175]. A half-metal is a material whose majority spin band has a metallic behavior while the minority spin band has a semiconductor or insulator behavior (for this band, the Fermi level lies in a band gap). Consequently, this means that electron transport can only be carried by majority electrons leading to a 100% spin polarization. Such materials with this feature have thus a strong potential for the development of spintronic devices, in particular magnetic tunnel junctions [176, 177]. It is also very interesting for magnonic applications since half-metals lead to low damp-

ing coefficients. Indeed, interband spin flip events that participate to the relaxation of spin waves are forbidden in half-metals [106, 109, 178].

The Heusler alloy Co_2MnSi (CMS) used in this thesis belongs to the full-Heusler class and appears to be very interesting to develop spintronic and magnonic applications. First, it is ferromagnetic with a relatively high saturation magnetization ($\mu_0 M_s \approx 1.3$ T) [52, 53], allowing microwave operations in the GHz range. A high magnetization is also interesting for magnonic crystals since frequency band gaps increase with M_s when the material is nanostructured [60, 61] as discussed in section 2.1.3. Experiments have demonstrated a spin polarization above 90% in CMS thin films [62, 63] while very low damping coefficients ranging from 2.10^{-3} [53, 64] to 4.10^{-4} [54, 65] were measured. Another interesting feature of full-Heusler compounds is their remarkably high Curie temperatures (T_c) owing to strong inter- and intra-sublattice exchange interactions. In the case of CMS, it reaches 985 K [66] ensuring a strong thermal stability for device applications. Finally, a last property that will be of particular interest in our work is the cubic anisotropy of the CMS. More particularly, values of the anisotropy constant K_c up to about 15.10^3 J m^{-3} were obtained in our group on CMS thin films [53]. We will discuss the interest of the anisotropy at the end of this chapter in the particular field of reconfigurable magnonic crystals.

Despite all these remarkable features that make CMS thin films very interesting for the development of combined magnonic and spintronic (magnon spintronic) devices [67, 68], one of their main limitation concerns their fabrication. In particular, it is of major importance to control the atomic disorder since their magnetic properties strongly depend on the crystal structure [179]. Such relationship between magnetic and structural properties in CMS have been studied previously in our group [111, 180, 181] and it is worth to mention that an impressive number of experimental and theoretical studies have been performed in the past 30 years to understand the link between structure and magnetism in Full- and Half-Heusler alloys. In this section, we remind the general properties of the different crystal orders while details about the growth process will be given in chapter 3 section 3.2.3.

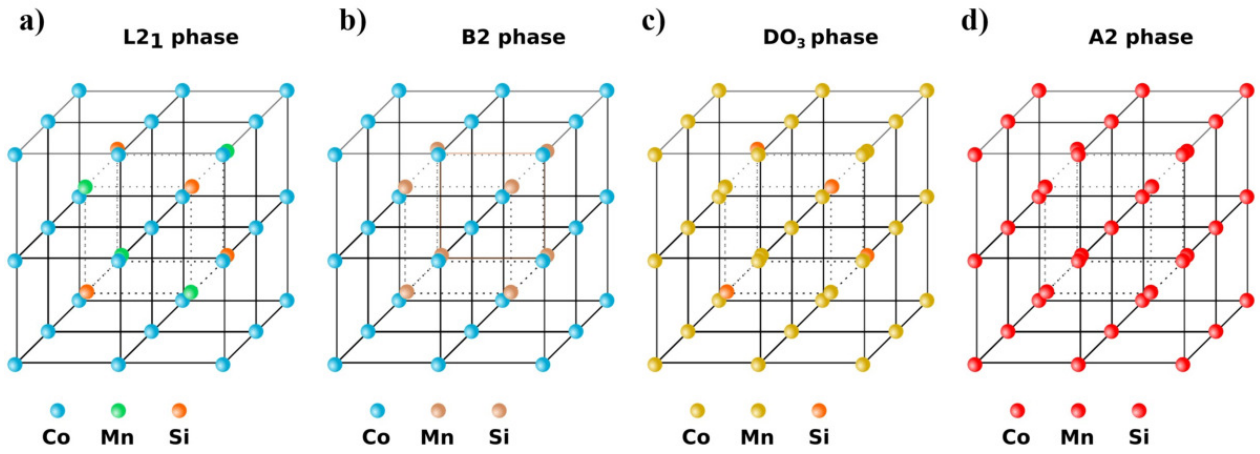

Figure 2.7: Schemes of different Co_2MnSi Heusler alloy crystal phases: a) the $L2_1$ phase, b) the B2 phase, c) the DO_3 phase and d) the A2 phase.

The most ordered crystal structure in which the CMS alloy can crystallize is the $L2_1$ order. It corresponds to four interpenetrating face-centered cubic (fcc) sublattices where two of which are composed of Co atoms, one of Mn atoms and one of Si atoms as represented in Figure 2.7 a) [182]. The two Co sublattices are positioned at $(0, 0, 0)$ and $(1/2, 1/2, 1/2)$ in the unit cell, when the ones of Mn and Si are positioned at $(1/4, 1/4, 1/4)$ and $(3/4, 3/4, 3/4)$ respectively. Other partial disordered states can also exist. The B2 order corresponds to the case where the Mn and Si atoms occupy the Mn and Si atomic sites with a 50% probability as shown in Figure 2.7 b). When Co and Mn atoms interchange their position, one obtains the DO_3 order as shown in Figure 2.7 c). Finally, a random distribution of all atoms leads to the fully disordered A2 state as shown in Figure 2.7 d).

Let's note that Figures 2.7 a), b) and c) only correspond to the three "perfect" disordered states but intermediate disorder states can appear depending on the growth conditions [179]. However, such states are metastable from a thermodynamic point of view and evolve in time.

Concerning the magnetic properties, theoretical Density Functional Theory (DFT) calculations [179, 183, 184] predict a full spin polarization, the highest magnetization value ($5\ \mu\mathrm{B/formula\ unit}$, $\mu_0 \mathrm{M_s} = 1.3\ T$), the lowest damping coefficient and a cubic crystalline anisotropy for the $\mathrm{L2_1}$ and $\mathrm{B2}$ structures. As already discussed before, experiments have confirmed these predictions for the $\mathrm{L2_1}$ phase. However, very low damping coefficients for the $\mathrm{B2}$ structure have not been reported so far, the lowest observed value being around 1.10^{-3} to our knowledge [53, 65]. In contrast, theoretical calculations have predicted a lower magnetization for the $\mathrm{DO_3}$ order [184]. In addition, our research group has studied the impact of the $\mathrm{DO_3}$ disorder on the damping coefficient by means of ab-initio calculations and has shown that it is increased by a factor of about 20 with respect to the damping coefficient in the $\mathrm{L2_1}$ phase [179]. To our knowledge, very few experimental studies deal with the magnetic properties of the $\mathrm{DO_3}$ and $\mathrm{A2}$ states, and it is not clear if the cubic anisotropy is conserved for such states. In any case, only the $\mathrm{L2_1}$ and $\mathrm{B2}$ orders show interest for magnonic and spintronic applications.

In chapter 4, we will show that we have grown CMS thin films on MgO (001) substrates which is the classical deposition process for this alloy. However, the use of such substrates limits its compatibility with existing micro-electronic devices, especially the CMOS technology. To overcome this problem, recent works have proven the possibility to grow polycrystalline CMS thin films on glass substrates without any drastic modification of neither the strong spin polarization nor its low damping coefficient (in the order of $1.5.10^{-3}$) [64]. Also, several studies focused on novel strategies to obtain high crystalline quality for CMS thin films grown on silicon substrates [185–188]. In addition to the formation of CoSi complex, one of the main problem is the annealing temperature above $500°\mathrm{C}$ to reach the $\mathrm{L2_1}$ order but the $\mathrm{B2}$ order can be reached at temperatures around $400°\mathrm{C}$. Even if many efforts have still to be done, all these works pave the way to consider CMS for industrial applications.

Interest of $\mathrm{Co_2MnSi}$ for reconfigurable magnonic crystals

In this PhD work, we focused on the possibility to make reconfigurable magnonic crystals with a simple antidot lattice geometry. As discussed in section 2.1.4, reconfigurable operations, i.e. the possibility to turn on and off some spin wave modes, require to obtain different remanent states when the system is initialized with an applied magnetic field in specific directions. Also, one expects to obtain large frequency band gaps and possibly a high number of spin wave modes showing a strong attenuation between the "ON" and "OFF" states. As it will be shown numerically in chapter 5, such conditions are met if the distance between the antidots is relatively small (not more than few times the size of the antidots) and strong spin waves attenuation is favored by uniform (or quasi-uniform) remanent states between the holes. With isotropic materials or for materials with very small crystal anisotropy (only few Oe), the local demagnetizing field related to the antidots generally induces complex non uniform magnetic configurations at remanence. Also we generally obtain the same magnetic state whatever the direction of an initializing (or saturation) field. However, materials with relatively high cubic crystal anisotropy can help to reach our goal. Indeed, a proper design of the antidots with respect to the magnetization easy axes allows to stabilize uniform alignment of the magnetization between the antidots. Indeed the crystal anisotropy thus enters in competition with the local demagnetizing field induced by the antidots. However the latter strongly depends on the saturation magnetization of the material. Therefore, reconfigurable operations with uniform remanent states can be obtained from materials showing a nice combination of cubic anisotropy and saturation magnetization. Based on the previous works performed in our group, the CMS is supposed to fill all the ticks. But for example, the same objectives could be more difficult to reach with iron as, despite its strong cubic anisotropy constant, its saturation magnetization is almost twice the one of CMS.

Then uniform remanent states could be obtained with a larger distance between the antidots, leading to a smaller number of spin wave modes.

Chapter 3

Numerical and experimental methods

In this chapter, we will detail the different techniques used during this thesis to deposit Co_2MnSi thin films and to study numerically and experimentally the fabricated Co_2MnSi magnonic crystals. The micro-nanofabrication techniques are later detailed in chapter 4. First, the micromagnetic simulations used to predict the reconfigurable properties of Co_2MnSi magnonic crystals (chapter 5) and to explain the measurements on the fabricated Co_2MnSi magnonic crystals (chapter 6) are described with the detail of the numerical procedure performed. Then the techniques of thin film deposition is approached with in particular the sputtering technique and growth conditions that allowed the deposition of Co_2MnSi thin films. Finally, the microwave measurements techniques used to characterize via FMR measurements the deposited Co_2MnSi thin films and to measure the excited spin wave modes in the fabricated magnonic crystals are detailed.

3.1 Micromagnetic simulations

Micromagnetic simulations constitute very effective computational techniques to calculate the magnetization dynamics in nano-microstructured ferromagnetic systems [152]. These techniques are based on the numerical resolution of the LLG equation (1.35) described in chapter 1 in time and spatial domains. To this end, numerical methods with time and space discretizations are used, such as Finite Difference Method (FDM) or Finite Element Method (FEM). FDM solvers use a discretization with cuboidal cells in an orthogonal grid while FEM solvers are based on tetragonal cells [189]. The latter is usually more accurate but requires more computational resources.

In this thesis, we have used two different micromagnetic solvers: OOMMF (Object Oriented MicroMagnetic Framework) [190] and MuMax3 [191] which are both based on FDM. These two simulators are open source and widely used among the magnetism community. Contrary to OOMMF, MuMax3 runs the numerical calculations on graphical processing units (GPUs) which offer optimized parallel computing. Consequently, larger numbers of discretization cells (depending on the RAM of the GPU) can be simulated in a shorter amount of time computing with MuMax3. For the simulated results presented in chapter 5 and 6, MuMax3 was majorly used.

The objective of this thesis is to propose reconfigurable magnonic crystals at remanence. Owing to their space discretization, micromagnetic simulations are particularly suited for the investigation of unsaturated magnetic configurations contrary to plane waves methods (PWM) and other analytical methods, where saturated magnetic states are required. With analytical or semi-analytical methods, it is not always possible to obtain a calculable solution. In contrast, with micromagnetic simulations, it mainly requires to choose a time step and to perform the temporal integration of the LLG equation.

As a result, in a certain manner, "anything" can be simulated. This method is mainly limited by the size of the simulated system as it depends on the number of cells that the CPU (OOMMF) or GPU (MuMax3) can support. Thus it inherently depends on the size of the cells. The implementation of periodic boundary conditions allows to overcome this issue in our case. Consequently we chose to use micromagnetic simulations for the search of reconfigurable magnonic crystals at remanence and for comparison with our measured magnonic crystals.

The numerical procedure to use and analyze micromagnetic simulations is illustrated in Figure 3.1. First the magnetic system is discretized and defined in terms of geometry and magnetic proper-

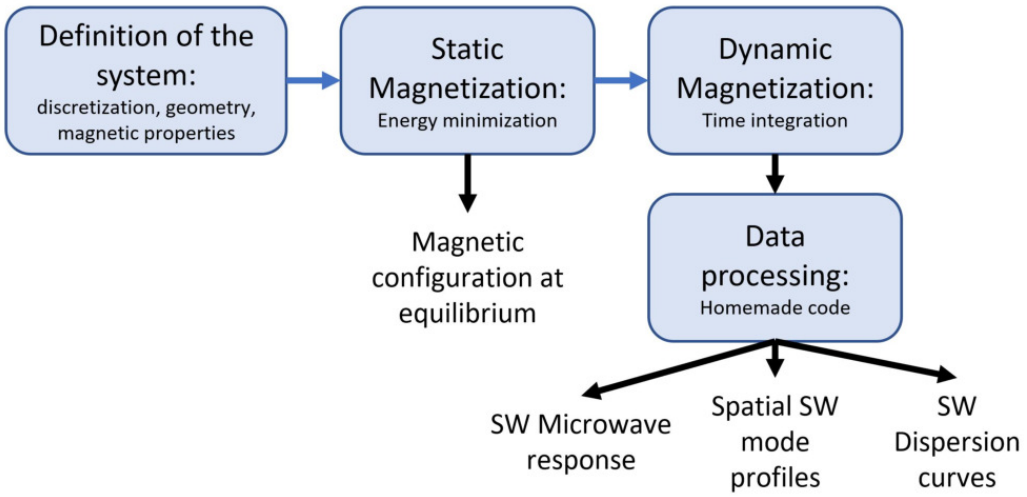

Figure 3.1: Schematic of the micromagnetic simulations procedure for the study of magnetization dynamics (SW: spin waves) in a magnetic system.

ties. Then the magnetization configuration at equilibrium is calculated by energy minimization. The latter subsequently constitutes the starting point for the dynamical simulation. Once the dynamical simulation is finished, the simulated results are retrieved and processed to calculate microwave responses, spatial profiles, dispersion curves by a homemade code in Python. Each of these steps will be detailed in the next sections.

3.1.1 Definition of the magnetic system

For a start, we define the mesh of the magnetic system to be studied by specifying its dimensions, geometry and discretization. The "universe" is a rectangular simulation box discretized with cuboidal cells. Each cell is composed of a uniform magnetic moment such as $\vec{M}(x, y, z)$ where x, y, z determines the position of the cell in the universe. In Figure 3.2, an example of a discretized portion of a magnetic antidot lattice with a square antidot (magnetic system to be simulated) is shown. The size of the cells is defined and must be below or equal to the exchange length Λ_{ex} in order to take into account the exchange interaction in the calculation of the magnetic configurations. In our case, we used cell dimensions of $5 \times 5 \times 5$ nm^3 as the exchange length of Co_2MnSi is $\Lambda_{ex} = \sqrt{2A/\mu_0 M_s^2} \approx 5.4$ nm. For MuMax3 it is generally recommended to apply a number of cells as a power-of-two value (2^n) to have the best computing performances as the calculation of the demagnetizing field is based on a Fast Fourier Transform (FFT) [191].

If the system to be simulated possesses one or two axes with a translational symmetry, such as in the case of an infinite waveguide (1D infinite) or thin film (2D infinite), 1D [192] or 2D [193] periodic boundary conditions (PBC) can be added. Nevertheless the application of these PBC is restricted to

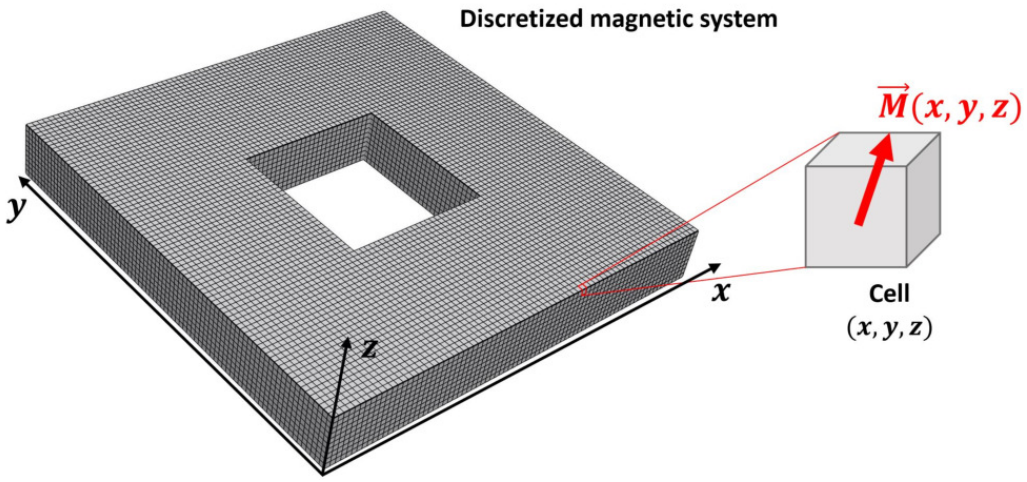

Figure 3.2: Schematic of a discretized magnetic system corresponding to a portion of a simulated magnetic antidot lattice.

the x or/and y axes of the simulation box. In MuMax3, PBC consist in virtually repeating the simulation box on each side of the magnetic system (along x or/and y) for the calculation of the dipolar and exchange interactions [194]. The use of PBC is time and computing efficient for the simulation of periodic large systems as the simulation of a unit cell of the periodic structure is only required. For the simulations presented in chapters 5 and 6, we have defined a unit cell of the magnetic antidot lattice with 2D PBC. An example of a simulated unit cell is shown in Figure 3.3. The number of repetitions was fixed at 10 on each side of the unit cell. For example, in the case of the simulations presented in section 6.2, we used 320 cells along the x and y axes with a lateral cell size of 5 nm. The lateral dimension of the unit cell size is 1.6 μm. With the application of 2D PBC, the virtual size of the simulated system becomes 32 μm. The latter is then brought closer to the real size of the sample measured.

Once the simulation box is defined, the geometry of the magnetic system and its magnetic parameters are specified. Different regions of the simulation box with different magnetic properties can be defined. One can choose the different magnetic interactions that will act in the magnetic system. Within the scope of this thesis, we used the exchange interaction, the dipolar interaction, the Zeeman interaction (in the case of an applied field) and the cubic magnetocrystalline anisotropy. Their energetic expressions are detailed in chapter 1 1.1.2. The magnetic parameters used for the simulations are mentioned in chapters 5 and 6. The sum of the energies of these interactions constitutes the Brown's Equation that will be used for the calculation of the internal field.

3.1.2 Quasi-static simulations: Energy minimization

Once the magnetic system to be simulated is defined, the first step prior to the obtain of the magnetization dynamics is to calculate the magnetic state at equilibrium. The latter constitutes the starting point for the dynamical simulations. To this end, energy minimization is performed on the magnetic system. As previously mentioned in chapter 1 section 1.1.2, the energy minimization is based on:

$$\vec{H}_{eff} = -\frac{1}{\mu_0}\vec{\nabla}_{\vec{M}}E \tag{3.1}$$

for which a minimum of energy is reached when $\vec{M}$ is collinear to $\vec{H}_{eff}$ i.e. when $\vec{H}_{eff} \times \vec{M} = 0$. Two approaches can be used in MuMax3 for energy minimization. One is based on a standard minimization scheme with the steepest conjugate gradient method [195]. This method is also the one

used by OOMMF. The second uses the LLG equation (1.35) without the precession term. The latter is more robust when relaxing magnetic states which are very different from the equilibrium state, such as for example when starting with a random distribution of the magnetization over all cells. As $\vec{H}_{eff} \times M = 0$ can not be perfectly reached in reality, a convergence criteria is used. More precisely, the stopping criteria is set by the maximum torque specified.

In all of our simulations, we started with a random distribution of the magnetization over all cells. Then, a strong magnetic field (1 T) is first applied to saturate the magnetization of the system along a particular direction, and the system is left to relax. Then the applied field is progressively decreased down to the desired applied field by field steps of 10 mT. At each step, the energy of the magnetic system is minimized. An example of an obtained magnetization configuration in a CMS antidot lattice is shown in Figure 3.3. Black arrows indicate the direction of the magnetic moments distributed over the unit cell. This magnetic state is color coded with respect to the magnitude M_x of the x-component of the magnetic moments.

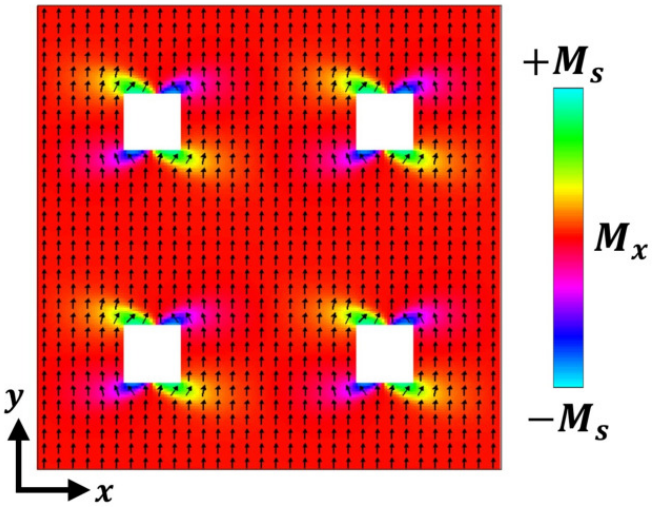

Figure 3.3: Example of a magnetic state at equilibrium of a simulated unit cell of a CMS magnetic antidot lattice at an applied field of 100 mT. Black arrows indicate the direction of the local magnetic moments. The colorbar is color coded with respect to the amplitude of the x-component of the magnetic moments M_x.

3.1.3 Dynamic simulations: Temporal integration of the LLG equation

Once the magnetic state at equilibrium is calculated, its dynamic to an applied temporal or/and spatial excitation can now be calculated. The magnetization dynamic is determined by the integration of the LLG equation (1.35) via numerical ODE (Ordinary Differential Equation) resolution methods such as Euler or Runge-Kutta methods. During the simulations, the LLG equation is solved for each cell. In our case, we chose the 4th order Runge-Kutta method in MuMax3 and OOMMF. The latter is a high-order solver which is fast and accurate for magnetization dynamics [191]. Depending on the excitation signal, the magnetic system will respond differently. It is then important to choose the appropriate excitation signal with respect to what needs to be observed.

Uniform excitation $k = 0$

To mimic a FMR experiment, we chose to apply a dynamic Zeeman field h_{RF} (pumping field) uniform over the volume of the magnetic system. Let's note that the spatial and temporal dependences of the h_{RF} field will determine the microwave response of the magnetic system. For example, a continuous wave signal (sinus-like) will only excite the magnetic system at one frequency, and its

response for this sole frequency. On the contrary a pulse signal allows to excite different frequencies at the same time. In our simulations we chose to use a cardinal sinus excitation sinc which is more convenient [189, 196]:

$$h_{RF}(t) = \frac{\mu_0 h_p \sin\left(2\pi f_c(t - t_{wait})\right)}{2\pi f_c(t - t_{wait})} \tag{3.2}$$

with t the simulation time, $\mu_0 h_p$ the amplitude of the applied dynamic field, which must be low enough to ensure a linear regime of precession for the magnetization (in the order of 1-2 mT for a damping factor of 1.10^{-3}, these amplitudes depends on the chosen damping factor, they should be set weaker (stronger) if the damping factor is lower (larger)), f_c the cutoff frequency and t_{wait} the waiting time before the triggering of the sinc pulse. An example of this sinc pulse is shown in Figure 3.4 a). The use of a sinc pulse RF excitation allows to excite all spin wave modes that can couple efficiently

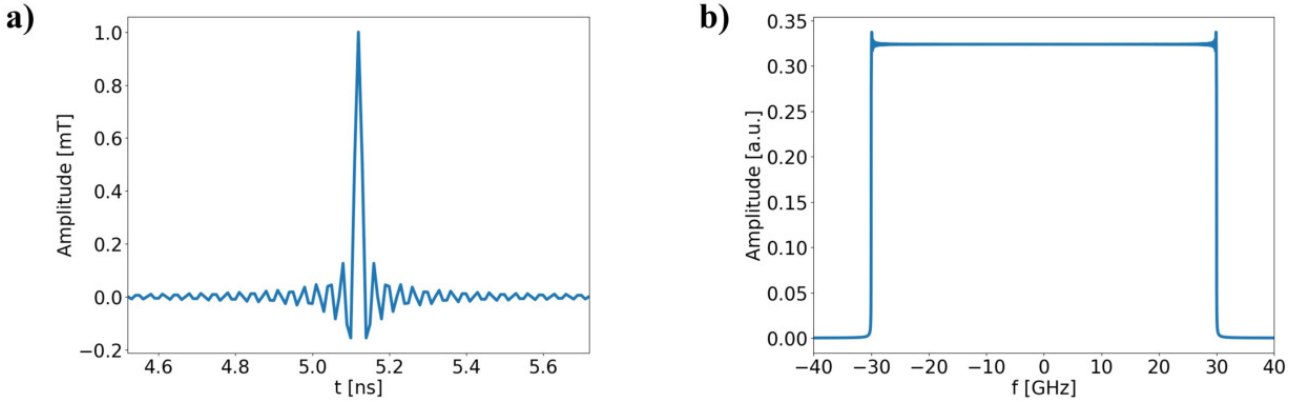

Figure 3.4: a) Sinc pulse with a cutoff frequency $f_c = 30$ GHz, an amplitude of $\mu_0 h_p = 1$ mT and waiting time $t_{wait} = 5.12$ ns. The sampling time is $\Delta t_{samp} = 10$ ps. b) FFT of the sinc pulse in a).

to the uniform RF field with the same power for all frequencies up to the cutoff frequency. This is due to the Fourier transform of the sinc pulse which is a rectangular function in the frequency domain as can be seen in Figure 3.4 b). For excited frequencies above f_c and below $-f_c$, no efficient excitation of the spin wave modes is carried. However for $-f_c < f < f_c$, the magnetic system is excited with the same amplitude in the frequency domain. This particular feature allows then to retrieve the microwave response of the magnetic system over a broad range of frequencies by performing only one simulation. This excitation must be applied continuously over the simulation time, it is then t_{wait} that will trigger the sinc pulse at the desired time. When one chooses a cutoff frequency value, the latter have to be less than the Nyquist frequency, i.e. $f_c \leq 1/(2\Delta t_{samp})$ with Δt_{samp} the sampling time.

At each time step of the simulation $n\Delta t_{samp}$ with $n = 0, 1...N$ and N the total number of time steps of the simulation, the magnetization in each cell $\vec{M}(x, y, z)$ is calculated and registered as temporal files. As it will be explained in the next section, we performed the data processings of these temporal files with Fast Fourier Transform algorithms. Therefore it is better that the number of temporal files N equals a power-of-2.

Concerning the simulations performed in this thesis, the typical simulation parameters used are: $\Delta t_{samp} = 10$ ps, $f_c = 30$ GHz, $\mu_0 h_p = 2$ mT, $t_{wait} = 5.12$ ns and $N = 4096$.

3.1.4 Data processing

When the simulation is finished and all the temporal magnetization files are generated, the temporal and spatial magnetization values $M_x(t, x, y, z)$, $M_y(t, x, y, z)$ and $M_z(t, x, y, z)$ (components

of $\vec{M}(t,x,y,z)$) are retrieved and processed with a homemade code developed in Python. The data processing is based on the works in [152, 189, 197].

Uniform excitation $k = 0$

In addition to the temporal magnetization files, the values of the averaged (over all (x,y,z) cells) magnetization components $M_x(t)$, $M_y(t)$ and $M_z(t)$ are also generated by the solver. To only focus on the dynamic part of the magnetization components $m_x(t)$, $m_y(t)$ and $m_z(t)$, we subtract $M_x(t)$, $M_y(t)$ and $M_z(t)$ to their values at equilibrium $M_x(t=0)$, $M_y(t=0)$ and $M_z(t=0)$ respectively. An example of a temporal averaged dynamic magnetization component is shown in Figure 3.5. This corresponds to the temporal response of the magnetic system to the uniform sinc excitation signal. The microwave response then corresponds to the visualization of the different excited spin wave modes in the frequency domain.

In our case, the studied magnetic systems were CMS magnetic antidot lattices with 2D PBC in the plane of the magnonic crystal (along x and y axes) and the thickness is along the z direction. To obtain the microwave response of the magnetic system, we performed a FFT on the out-of-plane averaged magnetization $m_z(t)$. The latter can also be done on the in-plane averaged magnetization which is collinear to the pumping field $\vec{h}_{rf}(t)$ ($m_x(t)$ in chapters 5 and 6). An example of the corresponding FFT is shown in Figure 3.5. The microwave response is plotted as the amplitude of the FFT: $|FFT_t(m_x(t))|$. Besides, the FFT can also be performed on the z-component of the demagnetizing field $h_{d,z}(t)$ present in an upper layer of cells out of the magnetic system (at some distance to the surface of the magnetic system). This can give an idea of the inhomogeneous z-component of the inductive field $b_{d,z}(t)$=$\mu_0 h_{d,z}(t)$, which is at the origin of the electromotive force in coplanar waveguides used as antenna (see section 3.3). Each FFT peak gives the excitation frequency of a particular spin wave mode in the magnetic system. To visualize its spatial profile, further data processing is required and, this time, we do not work on the averaged magnetization components over all cells but rather on $m_x(t,x,y,z)$ as we need the information of the magnetization temporally and spatially. We chose to show the dynamic component of the spin waves along x ($m_x(t,x,y,z_0)$) in the images presented in chapters 5 and 6 as we arbitrary applied $\vec{h}_{rf}$ in this direction. Again, as we want to only work with the dynamic component of the magnetization m_x, we subtract the value of the chosen component to its value in the initial equilibrium state for each cell of each temporal file, such as for example: $m_x(t,x,y,z_0) = M_x(t,x,y,z_0) - M_x(t=0,x,y,z_0)$. This calculation was only performed for a particular plane defined by z_0 to decrease the time calculation. As in this thesis we delt with magnetic antidot lattices made out of thin films, z_0 corresponds to the top surface of the magnonic crystal. Then, a FFT is performed on the temporal evolution of $m_x(t,x,y,z_0)$ for each individual cell: $FFT_t(m_x(t,x,y,z_0)) = \tilde{m}_x(f,x,y,z_0)$. An Inverse Fourier Transform (IFFT) is then applied on $\tilde{m}_x(f,x,y,z_0)$ at a chosen frequency f_0 (corresponding to the frequency position of a FFT peak, i.e. to a spin wave mode): $IFFT_t(\delta_{f_0}\tilde{m}_x(f,x,y,z_0)) = m_{x,f=f_0}(t,x,y,z_0)$, with δ the Kronecker symbol. The real part of the IFFT leads to a series of 4096 temporal values showing the temporal evolution of the $m_{x,f=f_0}$ component in each spatial cells at the particular excitation frequency f_0. The spatial profile can then be visualized with a temporal snapshot of $m_{x,f=f_0}$ for which the maximum of precession amplitude averaged over all spatial cells is reached. An example of a spatial profile of an excited spin wave mode is shown in Figure 3.5. The amplitude in a spatial profile is normalized according to the maximum of amplitude of this mode. The indicated normalized amplitude is specific to each spin wave mode. If we had taken as reference the maximum of amplitude of all the calculated spin wave modes profiles for a particular system, it would have been difficult to visualize clearly some spatial profiles. For example, an edge mode presents stronger precession amplitudes compared to an extended mode, however the extended mode is more spread spatially. This results in a spatially averaged precession amplitude larger than the one of the edge mode, and hence in a larger signal amplitude when measured with a micro-antenna for example (see section 3.3).

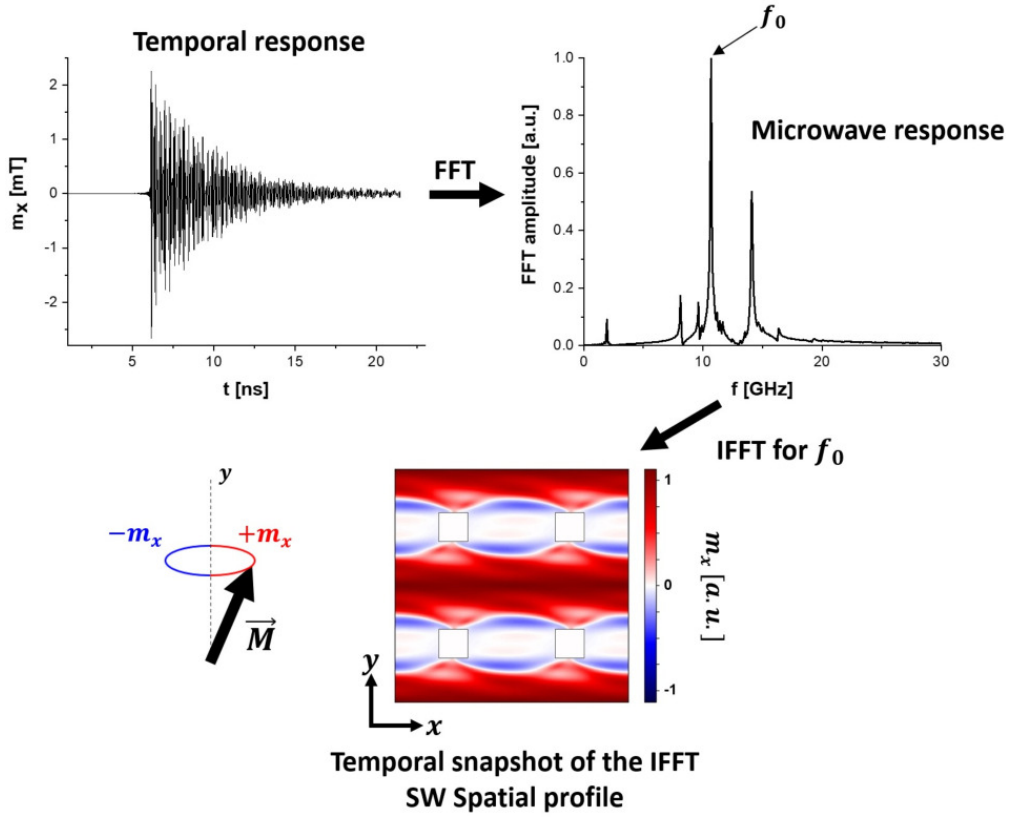

Figure 3.5: Schematic of the data processing of the temporal magnetization files to obtain the microwave response and a spatial profile of an excited spin wave (SW) mode at a particular frequency f_0 in a simulated magnetic antidot lattice with square antidots. The spatial profile corresponds to a temporal snapshot of the precession amplitude values $m_{x,f=f_0}$ in the plane (x, y) of the magnetic antidot lattice. This temporal snapshot has been taken when the maximum of precession amplitude averaged over the (x, y) space is reached. The colorbar is normalized with respect to the maximum precession amplitude of this mode.

3.2 Thin films synthesis

During this thesis, we used Physical Vapor Deposition (PVD) techniques to produce different thin films. These techniques are based on the vacuum vaporization of a material in a solid form. The transfer of the target material to a substrate takes place by condensation of the vaporized atoms on the surface of the substrate. In order to vaporize the target material, several techniques exist. During our work, we used thermal evaporation and ion bombardment (sputtering) techniques, that will be described below. In particular, we will focus on the Plassys sputtering chamber present at CEMES.

3.2.1 Thermal evaporation

In the following chapters, we will show that we have made Ti/Cu/Au micro-antennas. To this end, we used either a Joule evaporation chamber from the LPCNO (Laboratoire de Physique et Chimie des Nano-objets) laboratory of INSA Toulouse, or an electron-beam physical vapor deposition (e-beam evaporation) chamber present in our laboratory. In the case of evaporation by Joule effect, the target material is placed in a crucible, generally made of Tungsten, which will be heated by Joule effect by circulating an electric current of several tens of amperes. The target material is then heated until sublimation, and then condensation on the surface of a substrate facing it. A quartz crystal microbalance close to the substrate makes it possible to control the deposited thickness. In order to

avoid contaminations of the sample, the temperature of the crucible must be lower than its sublimation temperature. The thin films obtained via this technique are generally polycrystalline, granular, mainly because the temperature at the surface of the substrate is not high enough to favor crystallization. To have a much better quality deposit, ion bombardment techniques are necessary. Joule evaporation is therefore often used for the deposition of metals for lift-off processes: gold, aluminium, titanium, copper...

In the case of an evaporation by an electron gun (e-beam evaporation), a filament is heated in order to eject electrons. These electrons are then accelerated by a potential difference and deflected with a magnetic field towards the target material to be sublimated. The material is thus heated by this electron beam until it evaporates and condenses on the surface of the substrate. Both of these techniques involve vacuums below 10^{-7} mbar, however the working pressures (i.e. during depositions) are a few orders of magnitude higher. Nevertheless, it is important to keep vacuum pressures as low as possible to control the evaporation rates. The latter can vary from a few $\text{Å}\,\text{s}^{-1}$ to a few $\text{nm}\,\text{s}^{-1}$ for both methods.

3.2.2 Sputtering technique

In order to deposit our Co_2MnSi (CMS) thin films as well as permalloy or oxide layers, we used the ion bombardment technique, also called sputtering. This technique consists in accelerating ions resulting from the ionization of a gas towards the target material, thus ejecting the atoms on its surface by transfer of momentum. The whole gives rise to a plasma. Generally, an inert gas such as argon is used to avoid chemical reactions with the target material. Argon is ionized by applying a voltage between the target material constituting the cathode and the substrate constituting the anode. This voltage can be direct (DC configuration) or alternating (radiofrequency or RF configuration) with a frequency of 13.56 MHz. Before presenting in detail the Co_2MnSi thin film growth process, we will first briefly describe our setting.

At the CEMES laboratory, we used a Plassys-MPU-600S Sputtering chamber, schematically described in Figure 3.6 a). It consists of a cryogenic pump ensuring vacuum pressures down to 1.10^{-8} to 3.10^{-8} mbar under normal conditions. A load-lock vacuum chamber allows to transfer the substrate inside the main deposition chamber on a sample holder that can be heated up to 700°C. This deposition chamber contains three DC and two RF cathodes. In particular, each RF cathode has two face to face material targets.

The DC configuration is used for the deposition of conductive materials (metals). In this configuration, the material to be deposited constitutes the cathode and a negative potential of the order of a few tens to a few hundreds of volts is applied. The substrate on which we want to deposit the target material is placed on the anode as illustrated in Figure 3.6 b). Argon is introduced into the main chamber at a pressure of a few mbar. The free electrons accelerated by the applied DC voltage ionize the gas, and the generated Ar^+ ions are accelerated towards the cathode. This process generates more Ar^+ ions by cascading effects. The surface atoms of the target material are then ejected by energy transfer and will deposit on the substrate, while the electrons will fill the electronic vacancies of the Ar^+ ions. This energy relaxation results in the emission of photons, hence the observation of a luminous plasma.

For dielectric materials such as oxides, there would be an accumulation of charges near the target material since the electrons coming from the cathode could not neutralize the Ar^+ ions. To overcome this problem, a radiofrequency voltage (13.56 MHz) is applied between the cathode and the anode, which corresponds to the RF configuration illustrated in Figure 3.6 c). In our work, the RF power is set between 50 and 100 W. During one half part of the RF cycle, Ar^+ ions are attracted to the cathode and bombard the target. During the other part, they are repelled thus discharging the cathode.

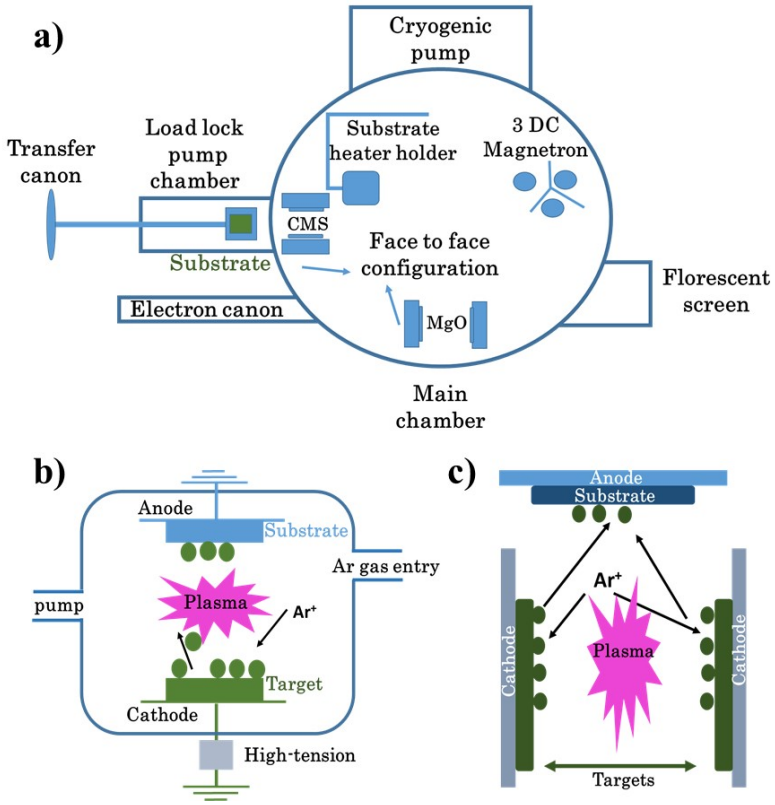

Figure 3.6: Schematics of a) the Plassys sputtering chamber, b) the deposition processes in DC or RF configurations and c) the face to face configuration used for RF sputtering in our work [111].

The deposition rate is much lower in the RF configuration (a few $\text{Å}\,\text{min}^{-1}$) than in the DC configuration (a few $\text{Å}\,\text{s}^{-1}$). Permanent magnets placed under the cathode in the RF configuration (magnetron configuration) can help to confine the plasma and increase the deposition rate. During the ion bombardment of the target material surface, secondary electrons are also ejected in addition to the atoms of the material to be deposited. The magnetic field applied in the magnetron configuration traps these electrons close to the target. By confining the electrons, the collisions allowing the generation of ions are more frequent, thus increasing the deposition rate of the material. However, preliminary studies carried out in our team a few years ago have shown that this method gives CMS deposition rates that are too high by a few $\text{nm}\,\text{min}^{-1}$, preventing the correct crystallization of the material. Consequently, we never work in the magnetron configuration. Another point of our process is that we use two targets placed face to face in the RF configuration. In such configuration, the two targets are biased with the RF potential and the substrate is placed a few centimeters above them as illustrated in Figure 3.6 c). This configuration is generally used to achieve a stoichiometric deposition of the material onto the substrate.

3.2.3 Growth of Co_2MnSi (CMS) thin films

We now present in detail the growth process to obtain CMS thin films. We followed the recipes developed during the PhD works of G. Ortiz [180] and I. Abdallah [111]. However, as mentioned at the beginning of section 4.1 of chapter 4, we emphasize that the optimal growth conditions were not met during our deposition campaign. As a result, we had to work with these deposited thin films for the rest of this thesis since the sputtering chamber is still not operational at the moment of writing this manuscript.

The CMS thin films were deposited on (001) MgO epi-polished substrates with dimensions 10×10

or 20×20 mm^2. These substrates were provided by Neyco. The choice of the substrate is important, in particular to obtain a lattice mismatch as small as possible. The lattice parameter of the CMS is $a_{cms} \approx 5.654$ Å while the one of MgO is $a_{MgO} \approx 4.211$ Å. In order to have a cube on cube growth, the CMS lattice rotates by 45° with respect to the MgO lattice as depicted in Figure 3.7. The CMS thin film then grows with the following epitaxial relation: CMS(001)[110]||MgO(001)[100]. This leads to a lattice mismatch defined as $(a_{cms} - \sqrt{2}a_{MgO})/(\sqrt{2}a_{MgO}) \approx -5.1\%$. Let's note that other substrates, such as GaAs, could achieve better lattice mismatches, however we did not have the possibility to test it during this work. In order to further reduce the lattice mismatch, a buffer thin film with an intermediate lattice parameter can be deposited onto the substrate prior to the CMS deposition. For example, the use of Cr as a buffer layer, whose crystal structure is fcc, results in lowered lattice mismatches down to -2.4% at the interface Cr/MgO and -2.6% at the interface CMS/Cr. Nevertheless, our group observed that diffusion of Cr atoms can occur at the interface CMS/Cr and this strongly affects the properties of the CMS [180].

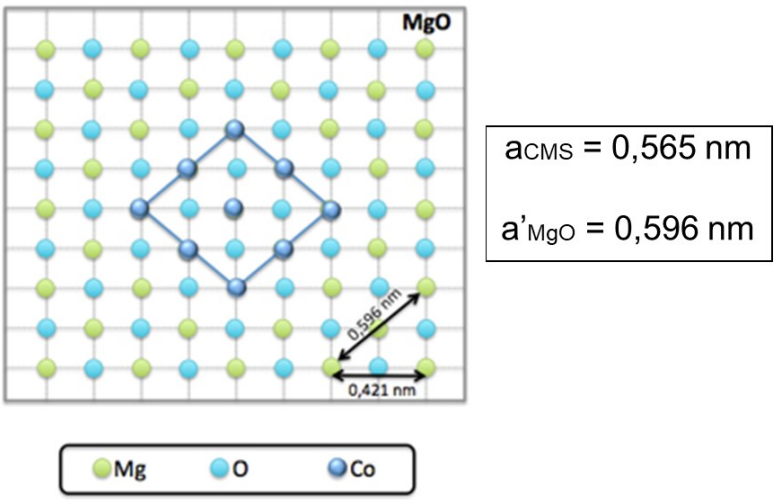

Figure 3.7: Schematic top view of the Co_2MnSi and MgO lattice orientations [180].

Prior to any deposition process, the substrate is heated up to 700°C for 1 hour to degas impurities, especially carbon and water molecules trapped at the MgO surface. Once the pressure inside the chamber is back in the range of 1.10^{-8} mbar, we realize a homoepitaxy of a MgO buffer layer to reduce the influence of terraces that can be found at the surface of the commercial MgO substrates and to avoid the diffusion of carbon atoms towards the surface during the deposition of the CMS thin film. The buffer layer is deposited at 100°C in face to face RF configuration with a RF power of 100 W, and its thickness is about 10 nm. The flow rate of the Ar gas is 50 sccm while a small amount of O_2 gas is also injected with a rate of 5.3 sccm to achieve a stoichiometric deposition of the MgO layer. The deposition rate is about 0.3 nm min^{-1}.

Following this, the substrate is heated up to 500°C for about 1 hour, and the CMS is then also deposited in face to face configuration with a power of 50 or 100 W and an Ar flow rate of 50 sccm. The two targets used as the cathodes are composed of 50% of Cobalt, 25% of Manganese and 25% of Silicon. The materials are provided by Neyco and obtained by mechanical sintering. The deposition rate is around 1 nm min^{-1}. This parameter must be kept relatively low to ensure a 2D growth. The substrate is placed 10 cm above the cathodes. During the MgO and CMS depositions, the pressure inside the chamber reaches the 1.10^{-3} mbar range. Once the CMS is deposited, the sample is annealed for 4 hours at 700°C to favor the crystallization of the $L2_1$ crystal order. The thickness of the deposited CMS thin films is between 45 and 50 nm, and was characterized by X-ray reflectometry (not shown here).

Finally, some of the CMS thin films were capped with a 100 nm thick MgO layer deposited in the

same conditions as the buffer layer ones. This capping layer allows to isolate electrically the Heusler layer for FMR characterization. However, as will be shown in chapter 4, the samples used to fabricate the CMS magnonic crystals were not capped, as we aimed at injecting electrical currents into the samples. Let's note that previous electron microscopy studies performed in our group have shown that when the CMS layer is not capped, an ultra thin amorphous oxidized layer of about 2 to 5 nm can form at the interface between the CMS and air.

3.3 Microwave device characterization techniques

In chapter 1 1.2 and 1.3, we approached the concept of ferromagnetic resonance (FMR), which corresponds to the uniform precession of the magnetization ($k = 0$), and of spin waves ($k \neq 0$) respectively. In this work, we used a microwave magnetic field, referred to as the pumping field $\vec{h}_{RF}$, to excite the FMR or the spin waves in our systems up to few GHz.

Microwave cavities with very high quality factors are often used to measure the FMR or quantized spin wave modes of a magnetic sample owing to the spatial homogeneity of the pumping field [198, 199] and their very high sensitivity. Nevertheless, the main disadvantage is that the working frequency is fixed. For broadband frequency measurements, transmission lines such as microstrips, striplines and coplanar waveguides (CPW) [199] have been shown to be quite relevant as they can offer a frequency bandwidth of several tens of GHz, despite a much lower sensitivity (due to microwave losses). These planar waveguides have dimensions that can be in the millimeter to the nanometer range making them very convenient for microwave characterization of magnetic thin films and planar nanostructures [200].

In our work, we used a micron-sized microstrip to measure the FMR mode and determine the magnetic constants of our CMS thin films. We also used micron-sized coplanar waveguides (called antenna or micro-antenna in the following) to measure the quantized spin wave modes in the CMS magnonic crystals. Even if we will not only deal with purely FMR ($k = 0$) but rather with quantized spin wave modes ($k \neq 0$), which are analog to standing waves, in the rest of this manuscript, through misuse of language we will use the expression "FMR measurements" to describe our measurements of either the FMR mode in thin films or the quantized spin wave modes in magnonic crystals. Besides, the micro-antennas used in our work have finite dimensions that can be smaller than the size of the sample, leading to a non-homogeneous microwave excitation in space. Nevertheless, we will show in chapters 5 and 6 that it can be appoximated by a spatially uniform pumping field. Finally, we used two approaches for these FMR measurements. We will refer to the first one as Field Modulation FMR (FM-FMR). In this case the frequency of $\vec{h}_{RF}$ is fixed and the external magnetic field is swept from 300 to 0 mT. The excited dynamic modes in thin films and magnonic crystals are measured with this method as it is easy to set up and offers a high signal-to-noise ratio. The second approach will be referred to as VNA-FMR. This method uses a Vector Network Analyser (VNA) to sweep the frequency of $\vec{h}_{RF}$ from 0.01 to 20 GHz while the applied field H_0 is fixed. In opposite to FM-FMR, this method requires more complex calibration procedures.

3.3.1 Transmission line model

Striplines, microstrips and coplanar waveguides correspond to miniaturized planar transmission lines which facilitates their use in integrated circuits [201]. In this thesis, we used in particular a microstrip and coplanar waveguides. These two types of transmission lines are illustrated in Figure 3.8 a) and b) respectively. A microstrip comprises a conductor in the form of a stripe deposited on a

dielectric substrate. The other side of the substrate is entirely covered with a conductor. A coplanar waveguide corresponds to one central conductor and two ground conductors separated by an air gap which are deposited on a dielectric substrate.

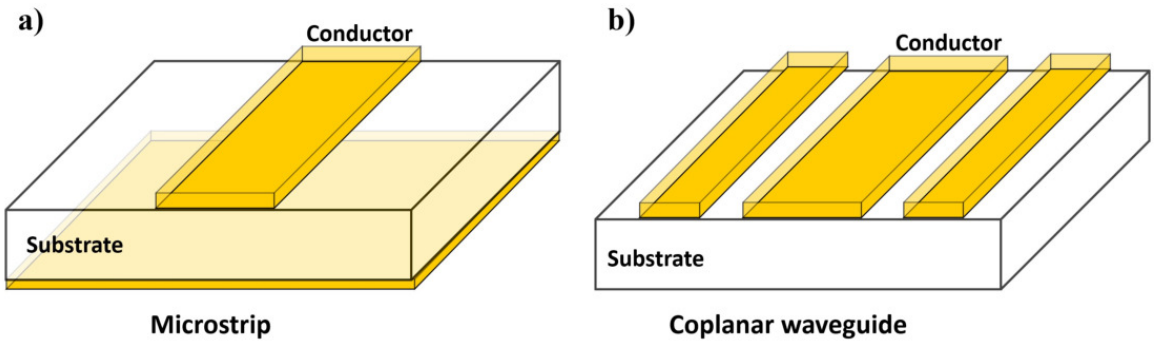

Figure 3.8: Schematics of two particular planar transmission lines, a) a microstrip and b) a coplanar waveguide.

Transmission lines or waveguides are generally represented with a dielectric medium surrounded by two (or more) conductors. A TEM (Transverse ElectroMagnetic) wave, where its electric field and magnetic field components are perpendicular to the direction of propagation, can propagate in these waveguides. To be more precise, no pure TEM mode exists in waveguides and coplanar stripes. First, the finite resistivity of the conductors induces a longitudinal component of the electric field. The second reason is the propagation at the interface between two different dielectrics, such as air and substrate in the case of coplanar waveguides. Nevertheless, it was demonstrated that for low frequencies, the propagating microwave signal can be considered as a TEM mode [202].

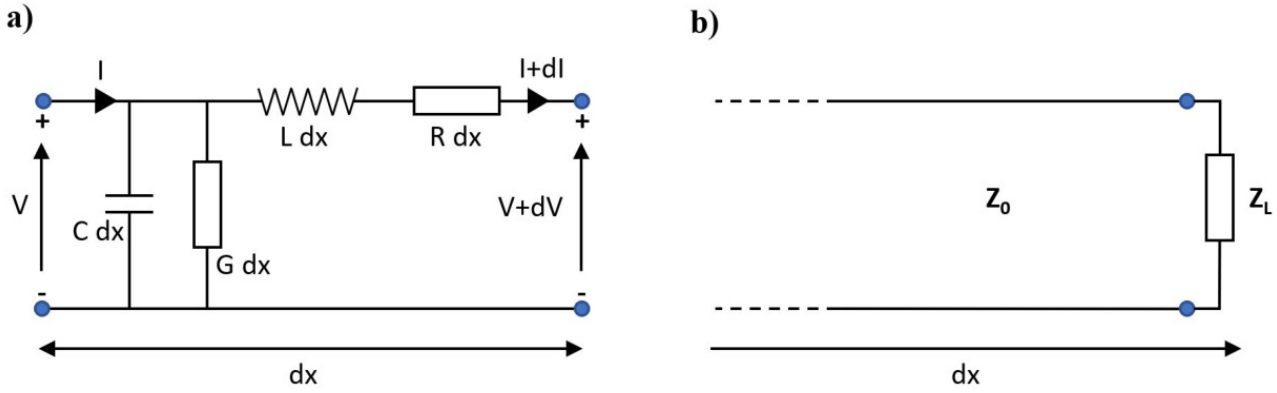

Figure 3.9: Schematics of a) a portion of an infinite transmission line modelized by a RLC circuit and b) the same transmission line terminated with an impedance load.

The propagation of a TEM wave in a waveguide can be assimilated to the notions of voltage and current [203]. The voltage between the two conductors of the waveguide generates the electric field component of the microwave and the flowing current generates the magnetic field component of the microwave. Therefore, previous works demonstrated that transmission lines can be modeled by portions of elementary RLC circuits connected in series as illustrated in Figure 3.9 a) [200, 204–206]. With this representation, classical circuit model can be applied [203]. In the RLC circuit scheme in Figure 3.9 a), the transmission line is infinite along the x direction. By considering a finite portion of the line dx, the inductance Ldx represents the magnetic response of the TEM mode and the capacitance Cdx corresponds to its electric response. To represent the losses by Joule effect in the conductors and the losses in the dielectric, the resistance Rdx and the conductance Gdx are respectively added to the circuit. By applying the Kirchoff's circuit laws and by solving the Telegrapher's

equations [200, 204–206], the characteristic impedance Z_0 of the infinite transmission line is:

$$Z_0 = \sqrt{\frac{R + i\omega L}{G + i\omega C}} \tag{3.3}$$

In the case of a terminated transmission line with a load $Z_L \neq Z_0$ as illustrated in Figure 3.9 b), the propagating microwave can be partially transmitted through and reflected by this load. The impedance discontinuity $(Z_L - Z_0)$ is at the origin of the reflections of the incident microwave [200, 204–206]. This results in losses in the transmitted microwave signal. When $Z_L = Z_0$, the microwave power is fully transmitted through the load. This property constitutes the basis of the $50\ \Omega$ impedance matching of microwave components in order to minimize losses of microwave signals.

Coplanar waveguides

For the study of our samples, short-ended coplanar waveguides (CPW) were used. They are presented in chapter 4 4.3. We will refer to them as micro-antenna in this manuscript.

Several types of coplanar waveguides can be used: source-only corresponding to one conductor stripe, Ground Source (GS) to two conductor stripes and Ground Source Ground (GSG) to three conductor stripes. We chose the GSG symmetry as it is closer to the case of a coaxial cable and may lead to a better impedance matching. A scheme of GSG CPW made and used in this thesis is shown in Figure 3.10. The microwave signal is injected in the central conductor and comes out via the two outer conductors. The width of the outer conductors was chosen half the central conductor width in order to have the same current density in all the conductors of the micro-antenna.

The central conductor width w_{in}, the spacing g between the conductors, the dielectric permittiv-

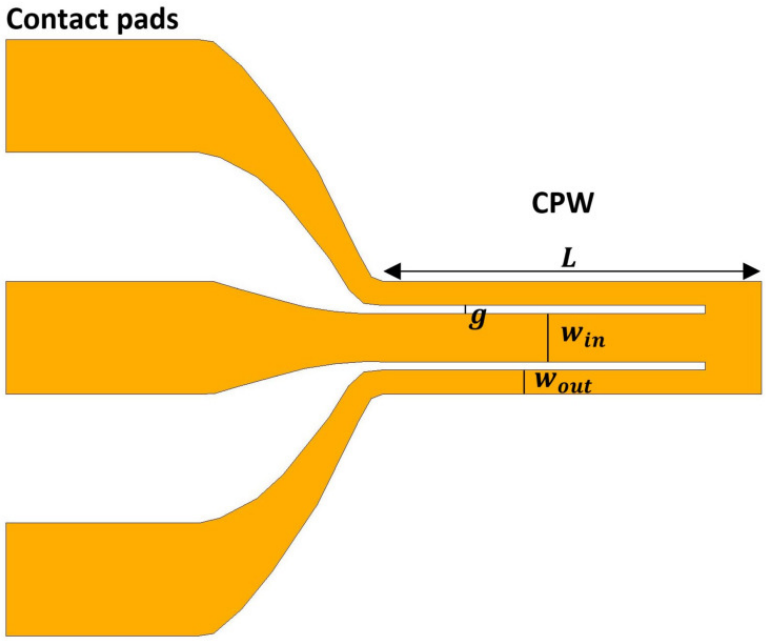

Figure 3.10: Schematic of the micro-antenna used for the sample n° 2 presented in chapter 4 4.3 and 6 6.2.

ity, and the thickness and materials of the conductors define the microwave characteristic impedance of a coplanar waveguide. Generally its design is optimized to obtain a $50\ \Omega$ impedance matching with the rest of the microwave circuitry. To calculate the characteristic impedance, one can use the TX-LINE software [207] for example. Another possibility is to use the Gupta formula in the case of a GSG coplanar waveguide with infinitely thin conductors [201]. Nevertheless, these calculations only constitute approximations of the impedance. For example the first method considers infinite ground planes (infinite widths of the outer conductors) and they do not consider the exact distribution

of current inside the conductors. To predict more precisely the impedance, Comsol Multiphysics™ simulations can be performed.

In this work, we have chosen to not take into account the impedance problem. Indeed, we chose to set the geometry of our micro-antennas with respect to the experimental constraints related to the geometry of our magnonic crystals. Such constraints are described in chapter 4. Furthermore, we did not perform propagation measurements, where in this case it would have been necessary to completely optimize the micro-antennas design. Our micro-antennas consist of a short load at the end of a small portion of GSG coplanar waveguide (the length L is $235\ \mu\mathrm{m}$). The short load allows to maximize the current flowing in the micro-antenna and consequently $\vec{h}_{RF}$. In the case of small antenna dimensions with respect to the microwave wavelength, Bailleul [200] demonstrated that the micro-antenna can be reduced to a very simple classical model with a resistance and an inductance in series (RL model). We confirmed this behavior for our micro-antennas by measuring the Z_{11} parameter (impedance calculated from one-port VNA measurements, see section 3.3.3) of one of them deposited on top of a magnonic crystal (sample #2 in chapter 4). To this end, the micro-antenna was connected to a VNA with microwave picoprobes (GGB Industries) and the calibration procedure (see section 3.3.3) was performed with the manufacturer calibration kit for picoprobes. The real and imaginary parts of the micro-antenna impedance are plotted in Figure 3.11 and are clearly resistive and inductive respectively, as expected for a RL circuit, over the frequency range (0.01-20 GHz) that will be used for the measurements. A linear fit of the imaginary part of Z_{11} was performed, leading to an inductance value

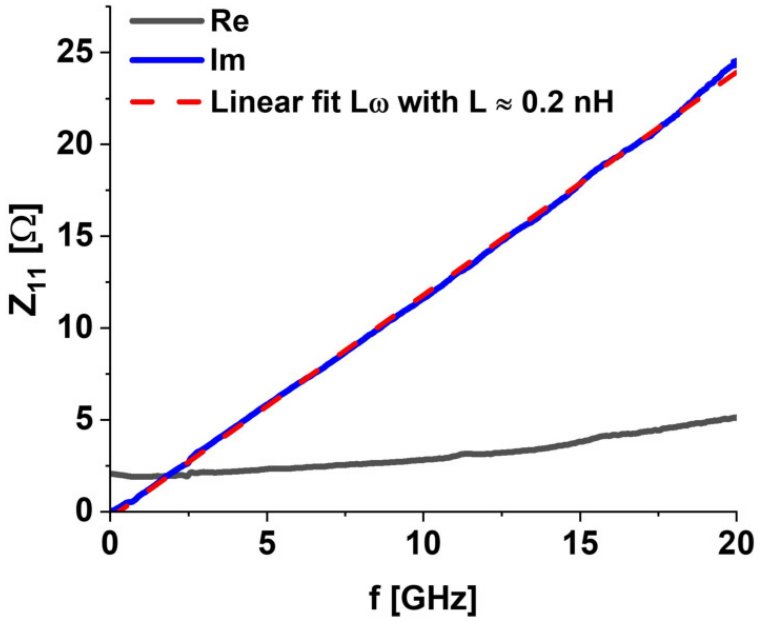

Figure 3.11: Input impedance of the micro-antenna of sample #2 measured by VNA. The blue curve corresponds to the imaginary part of the impedance while the gray curve corresponds to its real part. The red dashed line is a linear fit of the imaginary part of the impedance.

of about 0.2 nH.

The geometry/design of the micro-antenna will also define the excited wavevectors in the magnetic thin film. The maximum wavevector k_{max} can be approximately determined with the central conductor width w_{in} as $k_{max} \approx \frac{2\pi}{w_{in}}$. To be more precise, the excited wavevectors by the coplanar waveguides can be obtained by calculating the spatial Fourier transform of the density of current in the conductors [205, 208]. The density of current is approximated with rectangular functions, i.e. the current density is considered constant in the conductors widths. This calculation is in addition mainly valid for small conductors widths in the order of $2\ \mu\mathrm{m}$, but not for larger conductors in the order of $20\ \mu\mathrm{m}$ owing to skin effect [209]. The excited wavevectors are generally broadened as they present large Δk. In order to select precisely a specific wavevector, the antenna geometry must be repeated

spatially, as in the case of meander-shaped GSG coplanar waveguides in [208].

In our case, our micro-antennas were used to apply a uniform excitation over the CMS magnonic crystals (samples #1 and #2 detailed in chapter 4 and 6). To this end, large central conductors $w_{in} = 30\ \mu\mathrm{m}$ were used on slightly larger probed magnonic crystals (lateral sizes of $45\ \mu\mathrm{m}$ for sample #1 and $70\ \mu\mathrm{m}$ for sample #2). As a result the applied wavevector is close to 0 ($k \approx 0$). The discussion concerning the potential influence of the excited wavevectors with our micro-antennas on the samples can be found in section 6.2 and we demonstrate that the generated pumping field can be considered as quasi-uniform.

Inductive excitation and detection of FMR and spin waves

After having briefly described the concept of transmission lines and coplanar waveguides, we now briefly describe the physical effects at the origin of the coupling of the magnetization of a magnetic thin film to the microwave signal injected in the micro-antenna placed above.

When a microwave signal is injected into a micro-antenna, the flowing microwave current generates a microwave magnetic field, also called pumping field h_{RF}. The magnetization of the material underneath the micro-antenna can couple to this microwave magnetic field leading to its precession. In return, the precession of the magnetization generates a voltage in the micro-antenna owing to the Lenz-Faraday law. This generates a variation of the impedance of the micro-antenna leading to an increased impedance mismatch. Signal losses are then increased hence the term of power absorption to define the magnetic response to the pumping field. Such absorption modifies the amplitude of the transmitted and reflected voltages. The full description of these effects is called transduction, illus-

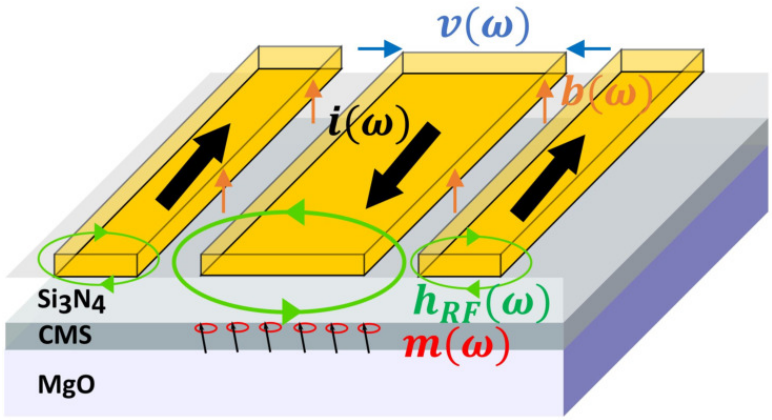

Figure 3.12: Schematic of spin waves transduction.

trated in Figure 3.12, and is beyond the scope of our work as we are not directly interested in the quantitative analysis of the amplitudes of the signals. However an important detailed description of transduction can be found in the PhD works of Bailleul [200], Vlaminck [204], Lassalle [205], Counil [210] and Bilzer [211]. This inductive coupling of the magnetization dynamics with microwave excitations is at the basis of FMR measurements [212] and spin waves transduction [208] with striplines, microstrips and coplanar waveguides .

3.3.2 Field modulation Ferromagnetic Resonance technique (FM-FMR)

Field modulation Ferromagnetic Resonance technique (FM-FMR) constitutes a powerful non destructive tool to measure the volumic magnetic properties of a material quite easily [199, 213]. Among others, one of the main interest is to obtain the intrinsic magnetic parameters without the need to know the exact thickness of the sample (except for the calculation of the exchange constant). This is, for

example, opposite to magnetometry measurements such as VSM (Vibrating sample magnetometry). This technique was used for the characterization of our deposited CMS thin films (chapter 4 4.1) and the measurements of the excited spin wave modes in the magnonic crystals (chapter 6).

Setup description for magnetic thin films characterization

The experimental setup used is illustrated in Figure 3.13. The sample is placed on a microstrip

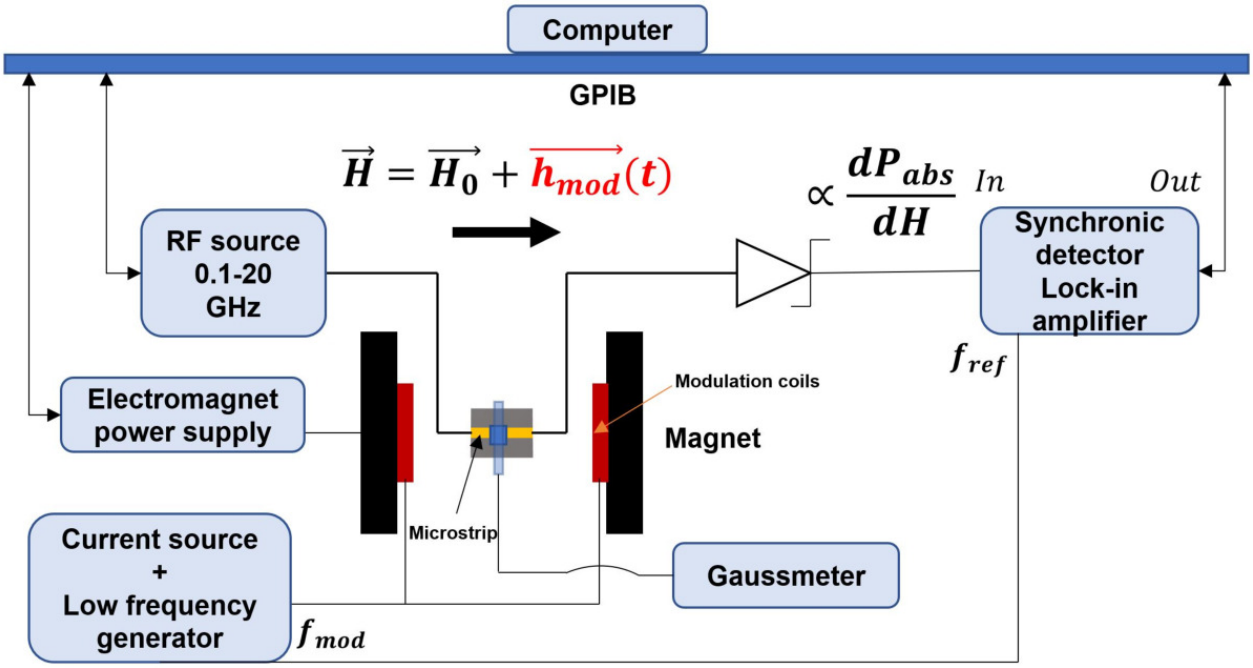

Figure 3.13: Schematic of the FM-FMR measurement setup when used with a microstrip to excite and measure FMR in magnetic thin films. The schemes are not at scale.

made of a gold line of width $600\ \mu\mathrm{m}$ deposited on an alumina substrate. This line will serve to generate the pumping field $\vec{h}_{RF}$. The other side of the substrate (down surface) is fully covered by gold to connect the ground plane of the sample holder. The magnetic surface of the sample faces the top surface of the microstrip. Prior to its placement on the microstrip, a thin passivation layer of about $10\ \mathrm{nm}$ was deposited on the magnetic thin film to prevent short circuit. The dimensions of the sample have to be quite small, in the order of millimiters so as to minimize propagation effects (not discussed in this manuscript). The sample holder is placed at the center of an electromagnet allowing to apply an in-plane static magnetic field $\mu_0 H_0$ up to about $400\ \mathrm{mT}$. Angle measurements can also be performed as the electromagnet can rotate from 0 to $180°$. In addition, Helmholtz coils are fixed to the electromagnet. These coils are supplied with a low frequency current (in the order of $110\ \mathrm{Hz}$) to modulate the static magnetic field. The amplitude of the modulation was $0.2\ \mathrm{mT}$ at maximum, which is lower than the resonance field linewidths measured.

A microwave source Agilent $(0.1 - 30\ \mathrm{GHz})$ is connected to the microstrip to provide the microwave current for the generation of the pumping field near the sample. The frequency range can be swept from $10\ \mathrm{MHz}$ to $20\ \mathrm{GHz}$ and the power injected from $-20\ \mathrm{dBm}$ to $10\ \mathrm{dBm}$. In order to remain in the case of linear precession of the magnetization (i.e. only few degrees of precession from the effective field direction), the microwave power is kept below $-16\ \mathrm{dBm}$ for our samples.

In this experiment, the static magnetic field is swept from 0 to $350\ \mathrm{mT}$ with steps of $0.3\ \mathrm{mT}$ at a fixed frequency of $\vec{h}_{RF}$. This procedure is repeated for 1 to $20\ \mathrm{GHz}$ with frequency steps of $0.5\ \mathrm{GHz}$. When the static magnetic field value for which FMR occurs (field resonance H_r) is reached, a part of the injected power in the microstrip is absorbed by the magnetic material thus triggering the uniform

precession of its magnetization. It can be shown that the microwave power absorbed by the material is proportional to $(1/2)\mu_0\omega\chi''(\omega)h_{RF}^2$ with ω the pulsation of the pumping field h_{RF} and $\chi''(\omega)$ the imaginary part of the dynamic susceptibility defined in the equation (1.95). The variation of the injected power is detected in transmission out of the microstrip via a Schottky diode. The Schottky diode allows to recover the envelop function of the microwave signal at its output. As the microwave power is modulated, the voltage produced out of the Schottky diode is then also modulated. This is schematically described in Figure 3.14 b). This voltage is then connected to the entry of the Ametek

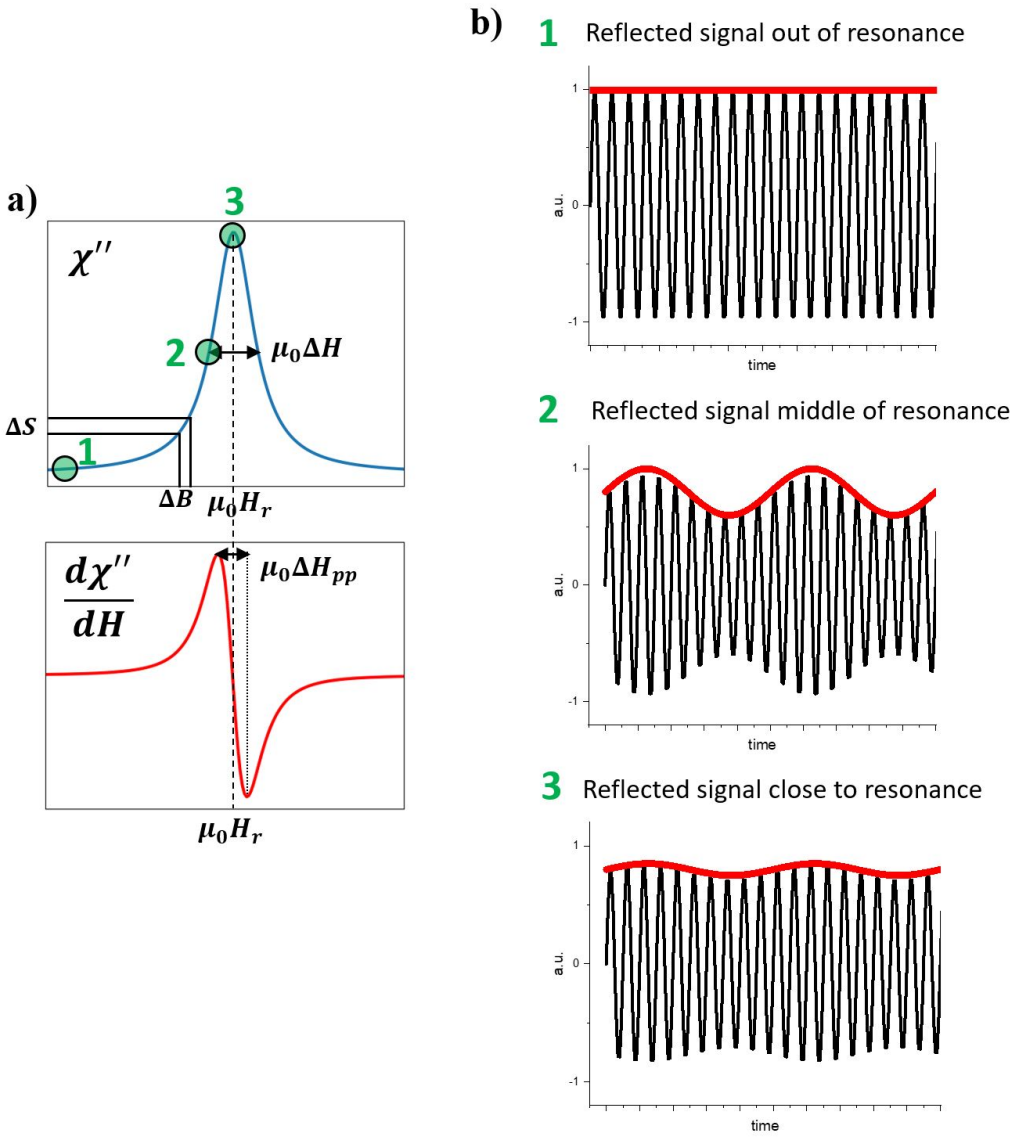

Figure 3.14: a) Scheme plots of the imaginary component of the susceptibility χ'' (blue line) and its derivative $\frac{d\chi''}{dH}$ (red line). b) Plots of the signal out of the microstrip (black curve) and after the Schottky diode (red curve) at three particular field points of χ'' curve (a)) indexed with numbers.

lock-in amplifier, whose reference signal is locked to the modulation signal of the Helmholtz coils. As a result, the combination of the Schottky diode and lock-in detection (homodyne detection) allows to detect the variation of the transmitted voltage due to the partial absorption of the microwave power.

As the absorbed power is proportional to the imaginary part of the susceptibility having a Lorentzian profile, it is thus theoretically possible to measure a signal proportional to the derivative of the imaginary part of the dynamic susceptibility $d\chi''/dh$ of the sample as illustrated in Figure 3.14 a). The measured signal have thus an anti-Lorentzian profile. The advantages of such technique is a high signal-to-noise ratio allowing the FMR measurements on ultrathin films of only few nanometers of thickness. It is also easy to set up as it does not require complex calibration procedures as in the

case of the Vector Network Analyser (VNA), that will be approached in the next section 3.3.3. It is to be noted that fine absorption peaks are more pronounced in the "derivative representation" as differentiation enhances any changes in the slope of the measurement curve [199].

Data processing

From FM-FMR measurements at each frequency, one can recover the resonance field $\mu_0 H_r$ and the field linewidth $\mu_0 \Delta H$ as illustrated in Figure 3.14 a) (blue curve). The resonance field is retrieved when the detected voltage crosses 0. The field linewidth can be measured via the peak-to-peak field linewidth ΔH_{pp} as:

$$\Delta H = \sqrt{3} \Delta H_{pp} \tag{3.4}$$

Nevertheless, this procedure works for an ideal measured imaginary susceptibility. In reality, several factors will impact the shape of the lorentzian χ'' and by extension the measured anti-lorentzian $d\chi''/dh$. For the measurements performed with the microstrip, not only this one is not perfectly adapted to 50 Ω but also the samples have dimensions of a few millimeters, which lead to small propagation effects (not discussed here, for more details the reader can refer to [200, 210]). Also, the sample is larger than the microstrip line. All of these makes the measured signal a mix of the real and imaginary part of the susceptibility. The presence of χ' and χ'' leads to the measurement of asymmetric signals.

With the expressions of χ' and χ'' in chapter 1 1.95, the measured voltage signal V is proportional to their derivative and can be fitted with the following formula to obtain $\mu_0 H_r$ and $\mu_0 \Delta H$:

$$\begin{aligned} V &= K \frac{d\chi'}{dH} sin(\phi) + K \frac{d\chi''}{dH} cos(\phi) + \text{offset} \\ &= K \left[\frac{(\frac{\Delta H}{2})^2 - (H - H_r)^2}{\left[(H - H_r)^2 + (\frac{\Delta H}{2})^2\right]^2} \right] sin(\phi) + K \left[\frac{-(H - H_r)\Delta H}{\left[(H - H_r)^2 + (\frac{\Delta H}{2})^2\right]^2} \right] cos(\phi) \\ &+ \text{offset} \end{aligned} \tag{3.5}$$

with K and offset constants, and ϕ an arbitrary dephasing angle. If the measured signal is quite symmetric, this means that $d\chi''/dH$ is dominating over $d\chi'/dH$, leading to a small ϕ value. Inversely, the more asymmetrical the measured signal is, the higher will be the ϕ value.

By fitting the measurements for all frequencies, one can retrieve the magnetic parameters of the sample. The evolution of the frequency with the resonant field $f(H_{res})$ can be fitted with the Kittel formula (1.52) or the Smit-Beljers model (chapter 1 section 1.2.4). This allows to determine the saturation magnetization M_s and the gyromagnetic factor γ. Then, the fitting of the evolution of the field linewidth with the frequency $\Delta H(f)$ via the formula (1.97) in chapter 1 allows to determine the damping coefficient α and the inhomogeneous broadening ΔH_0. For the particular case of our CMS thin films which have cubic crystal anisotropy, the determination of the magnetic parameters from FM-FMR measurements are detailed in chapter 4 4.1.

Measurement procedures for our devices with magnonic crystals

FM-FMR measurements were also performed on the samples #1 and #2 detailed in chapter 6 (Figures 6.2 and 6.10). In this case the setup is the same as in Figure 3.13 except that instead of the microstrip, picoprobes (GGB industries) are connected to the micro-antenna above the magnonic crystal. Also, we place a circulator at the output of the microwave source. The transmitted power is injected via the picoprobes to the micro-antenna. Due to the short load at the end of the micro-antenna, a large part of the incoming microwave signal is reflected towards the microwave source. As a result, we measure the variations of the microwave power absorbed by the magnetic sample as variations of the reflected voltage by the micro-antenna. Indeed, the excitation of the spin wave modes results in a variation of impedance of the micro-antenna as explained previously. The reflected power coming

back to the source is then isolated on the third port of the circulator and sent to the Schottky diode. With this configuration, measurements can only be performed from 2 to 18 GHz due to the limited frequency bands of our circulators. For these measurements, the magnetic field was first applied to saturate the magnonic crystal magnetization (300 mT) and then decreased down to 0 mT in order to favor the obtaining of reproducible measured signals when dealing with unsaturated magnetic states at low magnetic fields.

3.3.3 Vector Network Analyser Ferromagnetic Resonance (VNA-FMR)

As will be shown in chapter 6, we also measured the spin waves spectrum of magnonic crystals with a Vector Network Analyser (VNA) [213]. The main interest of a VNA is the possibility to measure the amplitude and phase of the reflected and transmitted voltages at the input and output of a device. The amplitude and phase are measured with respect to a reference signal injected by the instrument. Also, to measure the phase, one has to define a calibration plane, i.e. a position in the circuit where the analyser considers that the incoming voltage has a null phase. This involves to calibrate the VNA at a particular position in the circuit. In our case, this calibration is performed at the output of the picoprobes in order to probe only the variation of signals at the micro-antenna level.

As in the case of FM-FMR, the microwave device is placed in the center of the electromagnet as illustrated in Figure 3.15. The short-ended micro-antenna to probe the device is connected to one port of the VNA (Anritsu MS4642A) via picoprobes and a non-magnetic coaxial cable (from P2SI manufacturer). A second port can be used to connect a second antenna to measure the transmitted signal in the case of a not short-ended antenna or of detection of propagating spin waves. In VNA-FMR measurements, the applied field is fixed while the frequency is swept from 10 MHz to 20 GHz. The concept of VNA measurements is briefly described below.

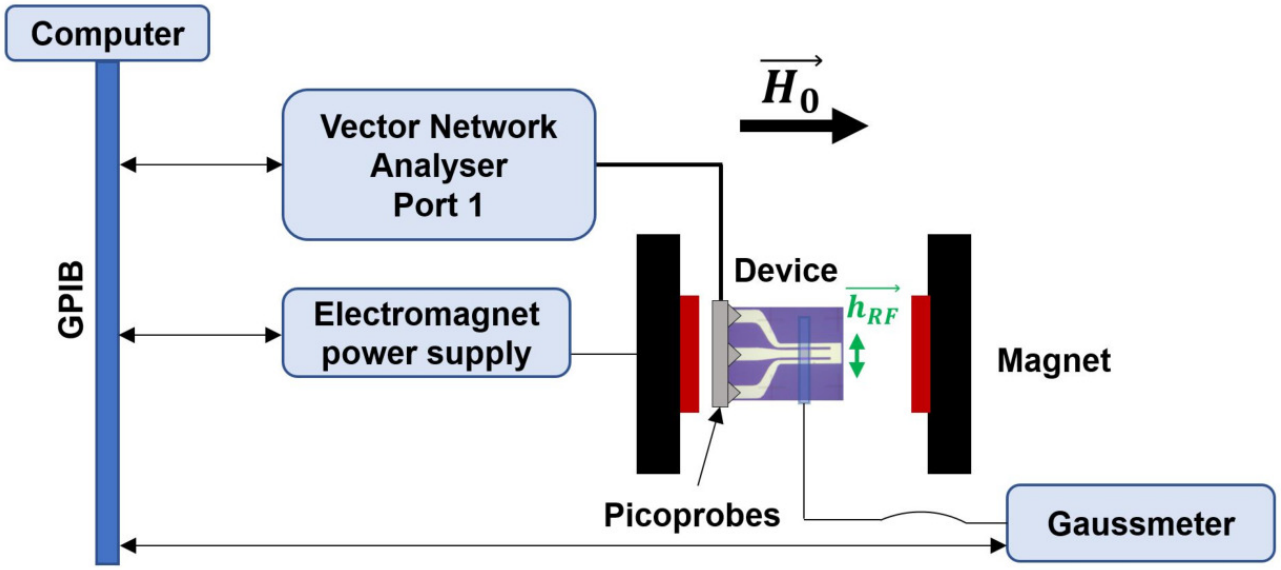

Figure 3.15: Schematic of the VNA measurement setup with a short-ended micro-antenna. The schemes are not at scale.

Scattering parameters and impedance

Every linear electrical device can be described by scattering parameters called S-parameters. If one injects a microwave signal (EM) in a port 1 with a voltage V_1^+, a part of this signal is reflected at the same port V_1^- and another part is transmitted at a second port (port 2) V_2^-. Inversely, when a

signal is injected in port 2 with a voltage V_2^+, a reflected V_2^- can be measured at port 2 and transmitted V_1^- at port 1. These S-parameters are illustrated in Figure 3.16 a). These voltages are thus linked by

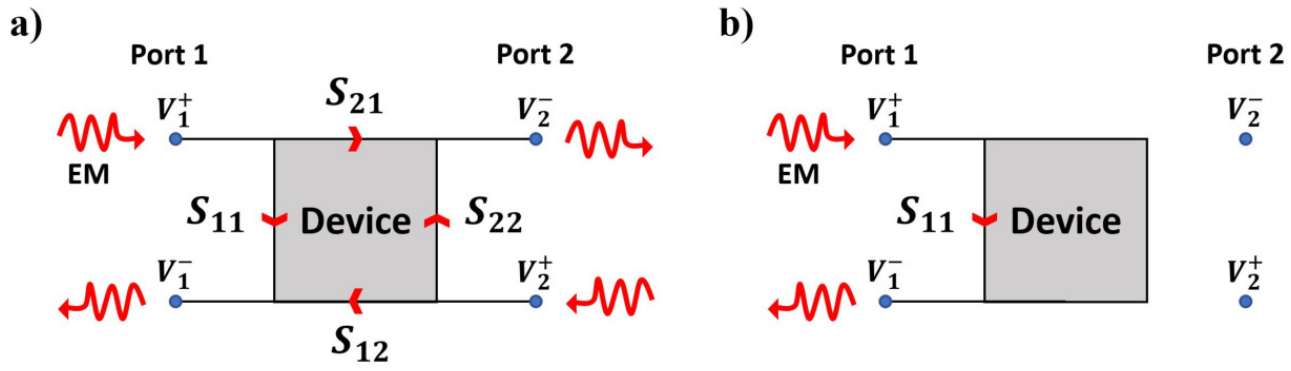

Figure 3.16: Schematic of the S-parameters for a a) two port measurement and b) one port measurement.

a matrix, called S-matrix, whose elements are the four scattering parameters:

$$\begin{bmatrix} V_1^- \\ V_2^- \end{bmatrix} = \begin{bmatrix} S_{11} & S_{12} \\ S_{21} & S_{22} \end{bmatrix} \cdot \begin{bmatrix} V_1^+ \\ V_2^+ \end{bmatrix} \tag{3.6}$$

where the parameters $S_{ii} = \frac{V_i^-}{V_i^+}$ correspond to the ratio between the amplitude of the reflected and incident voltage signal at the same port i ($i = 1, 2$) while the parameters $S_{ij} = \frac{V_i^-}{V_j^+}$ correspond to the ratio between the amplitude of the transmitted signal at port i and the incident signal at port j. These S-parameters are complex values as they are retrieved from the amplitude and phase of the microwave voltage signals.

The impedance matrix can then be built from the S-matrix:

$$\begin{bmatrix} V_1 \\ V_2 \end{bmatrix} = \begin{bmatrix} Z_{11} & Z_{12} \\ Z_{21} & Z_{22} \end{bmatrix} \cdot \begin{bmatrix} I_1 \\ I_2 \end{bmatrix} \tag{3.7}$$

where $V_i = V_i^+ + V_i^-$ and $I_i = I_i^+ + I_i^-$. The impedance parameters can be calculated with [204]:

$$Z_{ii} = Z_c \frac{(1 + S_{ii})(1 - S_{jj}) + S_{ij}S_{ji}}{(1 - S_{ii})(1 - S_{jj}) - S_{ij}S_{ji}} \tag{3.8}$$

$$Z_{ij} = Z_c \frac{2S_{ij}}{(1 - S_{ii})(1 - S_{jj}) - S_{ij}S_{ji}} \tag{3.9}$$

Operating principle

The S-parameters of the microwave device of interest can be measured by a VNA-FMR over a broad range of frequencies. These S-parameters are retrieved from the variation of amplitude and phase of the reflected and transmitted signals at the ports of the VNA. The latter thus acts as a microwave source (injects voltage signal in the micro-antenna) and detector (measures the reflected and transmitted voltage signals from the micro-antennas). Uniform or propagating spin waves induce a variation of the impedance of the micro-antennas via inductive coupling, and by extension, a variation of the S-parameters amplitude and phase with the excitation frequency and applied magnetic field. In contrast with the previous FMR experiment of section 3.3.2, the applied magnetic field is fixed while the excitation frequency (frequency of the injected RF signal in the micro-antenna) is swept from 0 to 20 GHz. Let's note that such kind of measurements are more difficult than FM-FMR measurements.

Indeed, one must avoid any part of the circuitry (such as cables) that could be sensitive to the applied field. Otherwise, changing the value of H_0 will involve parasitic signals, impedance variations... [199]. In our case, we took a particular attention to find a manufacturer able to provide completely non-magnetic cables and picoprobes.

To simply explain the functioning of the VNA [205, 214], the RF signal generated by the source of the VNA is splitted in two branches, one to serve as a reference (injected voltage) and the other to be guided from the port 1 of the VNA to the device of interest. The reflected signal is separated from the injected signal via a directional coupler. The transmitted signal is collected at the port 2 of the VNA. Each of these three voltage signals is then mixed with another signal of frequency $f + \delta f$ where δf is in the order of tens of MHz to obtain a mixed signal with in particular this δf frequency. Then this mixed signal is filtered by only selecting δf. This procedure is called heterodyning. Their detected values are then combined to calculate the S-parameters. Likewise, the same procedure is performed with the port 2 to complete the determination of the S-matrix.

Open reflection measurements

Within the scope of this thesis, only reflection measurements were performed on a single short-ended micro-antenna as illustrated in Figure 3.15. The situation is thus reduced to a one port measurement. As illustrated in Figure 3.16 b), only the reflection parameter S_{11} is extracted in this particular case. The other ports are terminated with $50\ \Omega$ matched loads. Let's note that we focused on the S_{11} parameter and not on the Z_{11} corresponding impedance because, as it will be explained later, our goal was to work on the potential microwave absorption of magnonic crystals and we assumed that the best parameter to highlight such functionality is S_{11}.

One port measurements present several advantages such as the use of a single picoprobe, simplified calibration, faster measurements as only one frequency scan on one port is needed. The latter reduces the impact of drift of the measurements as it will be later mentioned. When the magnetization precession enters in resonance (FMR), a strong absorption of the RF voltage signal injected in the micro-antenna occurs. The sole measured $S_{11}(f, H_0)$ parameter comprises mainly a field-dependant background signal that prevents the clear observation of the resonance peaks associated to spin waves excitation. Therefore, a reference measurement $S_{11}(f, H_{reff})$ taken at a reference field is subtracted to the measurement of interest to suppress the background signal:

$$\Delta S_{11}(f, H_0) = S_{11}(f, H_0) - S_{11}(f, H_{\mathrm{ref}}) \tag{3.10}$$

The reference field is generally taken the largest possible, in order to shift the resonance out of the measured frequency bandwidth.

Calibration protocol

For microwave measurements, all the elements in which the RF signal passes through (VNA components, coaxial cables, picoprobes) should have a correct impedance matching (close to $50\ \Omega$) to minimize the signal loss due to reflections at the connections between these different elements. A calibration routine have to be performed to overcome these non ideal measurement conditions by fixing these potential sources of errors.

To this end, a calibration substrate supplied by GGB Industries is used. The latter comprises several standards of coplanar waveguides commonly termed as SOLT, corresponding to Short, Open, Load and Through. The coplanar waveguides that are required for the calibration are then a short-circuit ($0\ \Omega$), an open-circuit ($\infty\ \Omega$), an impedance load ($50\ \Omega$) and a portion of perfectly $50\ \Omega$ microwave lines (through lines) if two ports are used. The calibration protocol then consists in contacted these standards and to measure them successively over the whole frequency range in the experimental conditions that will be used for the measurement of the microwave device, i.e. same power, frequency bandwidth, number of recorded frequency points. This routine is performed on both ports

of the VNA. This routine then serves for the determination of the different terms of the error model defined by the manufacturer that will shift the reference plane to the end of the picoprobes. As a result, the measured signal will then only depends on the device to be measured. It is important to perform a precise calibration in order to reach the largest signal-to-noise ratio. To this end, this calibration routine is repeated several times successively to improve the determination of the error terms. In addition, the calibration degrades with time and requires to perform the protocol routine quite often.

Chapter 4

Micro-Nanofabrication of Heusler-based Co_2MnSi magnonic crystals

In this chapter, we will first discuss the magnetic properties of the Co_2MnSi (CMS) thin films deposited at the CEMES laboratory. Then we will present in detail the micro and nanofabrication methods developed in order to obtain magnonic crystals from these films. We will emphasize the strategy followed to make antidot lattices and we will discuss the difficulties associated. This task represented one of the most critical and important points of this thesis work and required a lot of development. It was made all the more difficult as we had few CMS thin films available for testing. Then, we will show the microfabrication processes associated to the realization of the final devices. Those ones must include a magnonic crystal, but also a micro-antenna for excitation/detection of the spin wave modes and eventually electrical contacts. In particular, we will show that different kind of micro-antennas were fabricated depending on whether the final device was dedicated to FMR or Brillouin light scattering experiments.

4.1 Characterization of Co_2MnSi Heusler-based alloy thin films

Initially our goal was to obtain CMS thin films with a thickness of about 30 to 40 nm crystallized in the $L2_1$ *order. Unfortunately after the covid-related lockdown in 2020, our sputtering machine has encountered a major breakdown just few weeks after the beginning of our growth campaign. At the moment of writing this manuscript, our sputtering chamber is still broken down. As a consequence, only very few thin films could have been deposited and we were not able to optimize the growth conditions.*

FM-FMR measurements as described in section 3.3.2 were performed to characterize the magnetic constants of the CMS thin films capped with a thin layer of MgO. The results presented below suggest that our thin films were not perfectly crystallized in a single crystal order and small variations of the magnetic parameters (M_s, H_k, α) were observed from one film to another. Here we show a typical example of the CMS thin film properties observed on the set of prepared samples further used for magnonic crystals structuration.

Magnetic constants of the CMS thin films are obtained by FM-FMR measurements. The external field H_0 is applied in the plane of the sample along an easy or a hard axis, as illustrated in Figure 4.1 a). Due to the orientation of the crystalline axes of the CMS and the negative cubic anistropy constant, the magnetic easy axes are parallel to the edges of the MgO substrate while hard axes are

along the diagonal of the substrate. For the measurements, the frequency of the microwave current in the microstrip is fixed and an in-plane applied magnetic field is scanned from 0 to 300 mT.

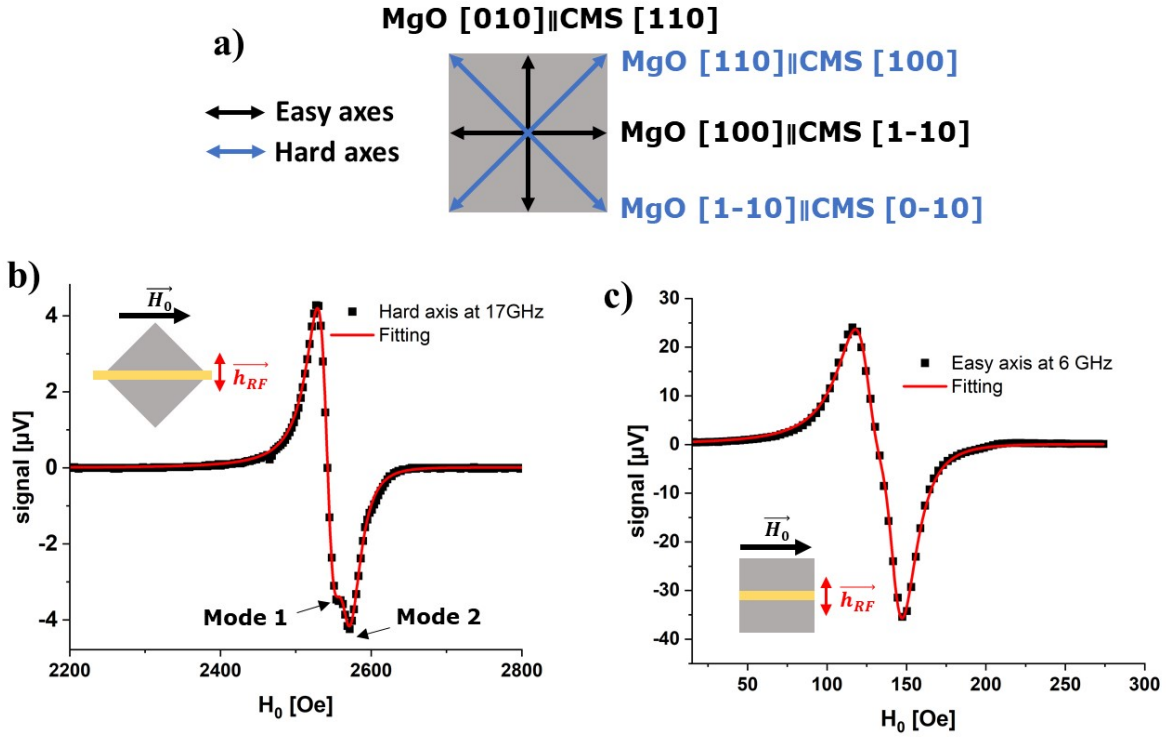

Figure 4.1: a) Schematic representation of the Co_2MnSi thin film sample, with in black arrows the directions of the magnetic easy axes, and in blue arrows the directions of the magnetic hard axes. Ferromagnetic resonance absorption spectra (black dots) and their fitting with (3.5) (red line) in the case of measurements performed in b) a hard axis at 17 GHz and c) an easy axis at 6 GHz.

As can be seen in Figures 4.1 a) and b), the anti-Lorentzian signals corresponding to the dP/dH measurements are not symmetric. We assume that this is due to the fact that our samples are not perfectly crystallized in a single crystal phase. As already mentioned at the beginning of this chapter, such films were not supposed to be used to realize the magnonic crystals during this PhD work. Besides, we did not performed a full structural analysis which would have require complex and time consuming experiments such as HRTEM-STAADF, X-ray diffraction at different wavelengths, combined with angle FMR measurements as demonstrated in [111]. Nevertheless, we relied on the experience of our research group which has studied these materials for 10 years. Based on these previous works, we assume that our samples have small grains with B2 order inside a large $L2_1$ matrix [111]. In such case, we can have very similar magnetic properties for the two phases leading to asymmetric resonance peaks. Therefore, in the following, we will consider that we have a majority (most probably $L2_1$) and a minority (most probably B2) phases in our thin films, with very similar magnetic constants.

Despite the strong peak mixing, we were able to extract the values of the resonance field H_r at each frequency for the two phases. The equation (3.5) was used to fit the measurements. More precisely, we used two anti-Lorentzian curves, one having a much higher amplitude (up to 10 times) than the other one. The $f(H_r)$ relations in the easy and hard axis directions are shown in Figure 4.2 a) as colored dots for the majority and minority phases. Let's note that the value of the cubic anisotropy field H_K can be obtained very easily as it corresponds to the inflexion point (where $f = 0$) when H_0 is applied in the hard axis direction. In this figure, the fitting lines are obtained from the Smit-Beljers equation (1.53). Using this formulation is particularly interesting when H_0 is not rigorously aligned with the easy or hard axes, and so for which the Kittel formula (1.63) and (1.64) can not be applied correctly. It also allows to fit the $f(H_r)$ points in the hard axis direction when H_0 is below H_k, i.e.

when the magnetization is not fully aligned with H_0.

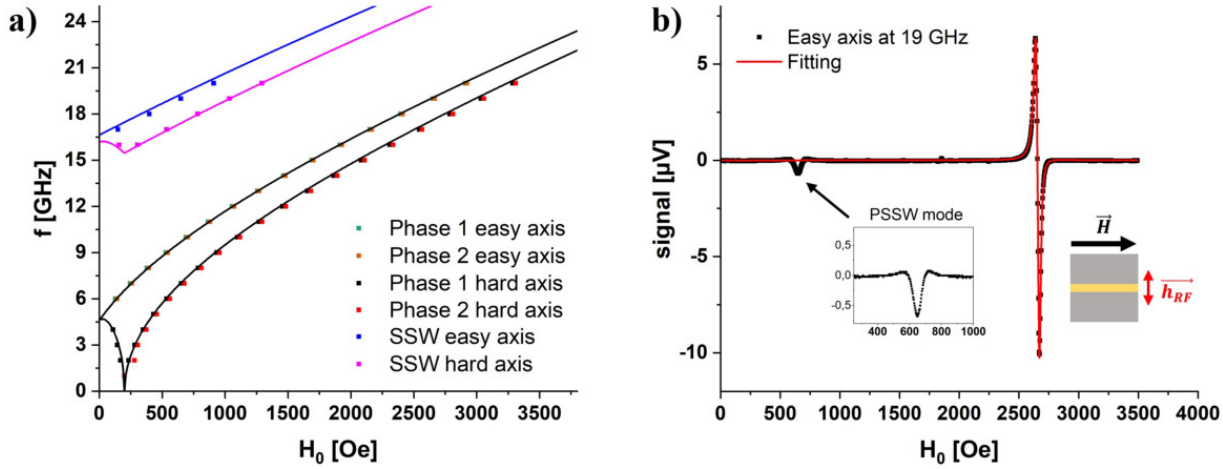

Figure 4.2: a) Evolution of the resonance frequency f as a function of the applied field H_0 when the latter is applied in the easy or hard axes (colored dots) and their fitting lines with (1.53) (black for the FMR peak resonances along the hard and easy axes, blue for the PSSW mode resonances along the easy axis, pink for the PSSW mode resonances along the hard axis). b) Example of a FM-FMR signal measured at 19 GHz. The red line is the fitting of the experimental points in black. In insert, we show the signal corresponding to the PSSW mode.

Then, the easy and hard axes $f(H_r)$ curves are fitted to extract γ and M_s. Finally, the exchange constant value A can be obtained from the first PSSW mode (Perpendicular Standing Spin Waves, which correspond to quantized standing spin waves along the thickness of the thin film) measured at a high frequency and low field as shown in the inset of Figure 4.2 b). This mode is an exchange dominated mode thus appearing at higher excitation frequencies and lower applied fields than the uniform resonance mode. It corresponds to the first quantized (i.e. stationnary) mode along the thickness of the film. As this signal is very weak, we assume that it is associated to the majority phase only. The value of A obtained from this peak relies on the assumption that the frequency separation between the PSSW and the FMR modes equals to $(2A/\mu_0 M_s)k_z^2$. In theory, the expression of k_z depends on the pinning conditions of the spins at the two surfaces of the film. Full and free pinning conditions correspond to spins at the interfaces that can or can not precess respectively. In our case, this pinning parameter could not be determined as the measurement of at least two PSSW modes are required, which involves to perform measurements at frequencies above the limit of our microwave source. We made the assumption of full pinning conditions with $k_z = \pi/t$, with $t = 45$ nm (the thickness t was measured via x-ray reflectometry). Possible discrepancies between the calculated and the real value of A might exist. However, we mention here that the micromagnetic simulations of the spin wave modes in the CMS magnonic crystals presented in chapter 6 section 6.2, which were performed with the calculated value of A are in very good agreement with the experimental results. Consequently, this suggests that our assumption is relevant.

The magnetic constants values for the majority phase obtained from the FMR measurements are summarized in table 4.1. These results are close to the one obtained in the previous works of I. Abdallah [53, 111], except that the cubic crystal anisotropy field is lower than expected (in the order of 30 mT). From one film to another, we obtained H_K values from 200 to 250 Oe ($\mu_0 H_k = 20$ to 25 mT). The saturation magnetization M_s value is close to the theoretical one of the $L2_1$ or B2 crystal order. This value varies from 1.28 to 1.29 T from one film to another. The exchange constant A value is in very good agreement with the reported values in the literature [215–218].

With the dP/dH measurements (FM-FMR), it is possible with the equation (1.97) to obtain the value of the Gilbert damping coefficient α from the evolution in frequency of the linewidth ΔH of the FMR peaks. However, due to the proximity of the peaks associated to the majority and minority

Saturation magnetization $\mu_0 M_s$ [T]	**Cubic crystal anisotropy field** $\mu_0 H_k$ [mT]	**Cubic crystal anisotropy constant** K_{c1} [J m^{-3}]	**Gyromagnetic ratio** $\frac{\gamma}{2\pi}$ [GHz T^{-1}]	**Exchange constant** A [pJ m^{-1}]
1.28	20	-10186	28.8	21.5

Table 4.1: Magnetic parameters obtained from the fitting of the measured $f(H_r)$ curves by FM-FMR.

phases, such treatment was quite difficult to achieve. Nevertheless, as the majority peak has a higher amplitude than the minority one, it was easier to obtain reasonable values of ΔH for this phase. Consequently, we have chosen to show in Figure 4.3 a) only the $\Delta H(f_r)$ plots for the majority phase when H_0 is applied in the direction parallel to the easy (black dots) and hard (red dots) axes. As can be seen, the calculated error bars are relatively important. The value of α is roughly similar for both directions of the applied field and is around 2.10^{-3}, which is quite reasonable as we did not remove the contribution from two-magnon scattering [105]. Indeed, two-magnon scattering leads to a linear increase of the field linewidth with the frequency, but it vanishes when H_0 is applied perpendicularly to the surface of the film. Unfortunately, our electromagnet does not allow us to apply a field sufficiently strong to saturate the sample magnetization out of plane.

The extrinsic contribution ΔH_0 is quite important (about 20 Oe) which reflects the "poor" crystallinity of our samples. It results from local fluctuations owing to the microstructure such as local defects, roughness, local variations of thickness [105]. Two-magnon scattering also contributes to ΔH_0 [105]. As a consequence, the effective damping at a particular frequency, which can be given by the equation (1.96), is much higher than the intrinsic damping at low frequencies as shown in Figure 4.3 b). It is only for frequencies above 15 GHz that the influence of extrinsic contributions becomes less dominant.

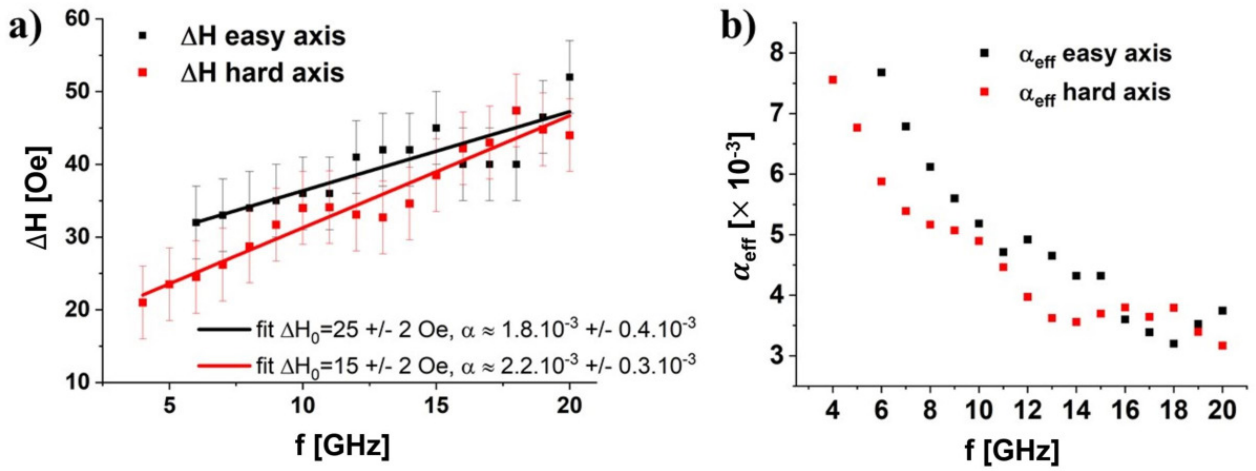

Figure 4.3: a) Evolution of the field linewidth ΔH with the frequency f for H_0 applied along the easy axis (black dots) and along the hard one (red dots). The solid lines are linear fittings with 1.97. The calculated error bars are represented. b) Evolution of the calculated effective damping α values from the equation 1.96 with the frequency f, along the easy (black dots) and hard (red dots) axes.

To conclude on this section, we have shown that our CMS thin films are not perfectly crystallized. Nevertheless their magnetic parameters are close to what could be expected for the $L2_1$ order. For the experimental study of the magnonic crystals presented in chapter 6 section 6.2, we have considered that we have mainly measured the majority phase as the measured signals are rather weak. Also, we used the magnetic parameters presented in table 4.1 when performing the micromagnetic simulations to describe the experimental measurements on the magnonic crystals. Only the damping coefficient

was set to 1.10^{-3} in the simulations, in order to have well resolved peaks in the FFT spectra.

4.2 Micro/Nanostructuration of magnonic crystals from Co_2MnSi thin films

In this thesis, we chose to study a particular type of magnonic crystals: squared magnetic antidot lattices. The latter correspond to a periodic lattice of etched squared holes in magnetic thin films. Different nanostructuration techniques for the fabrication of antidot lattices have been reported in the literature. The main ones are Focused Ion Beam (FIB) [219–222], combination of deep ultraviolet lithography and lift-off processes [22, 223, 224], combination of Electron Beam Lithography (EBL) and ion milling [49, 225], combination of EBL and lift-off processes [226], or template synthesis in porous membranes [227].

This section is dedicated to the presentation of the micro and nanofabrication steps that have been developed at the CEMES to produce our magnonic crystals from CMS thin films. These tasks represented the major part of the experimental developments that I carried out during this thesis. In order to fully understand these different stages, it is important to present the constraints that we have set ourselves for the fabrication of the samples:

- Firstly, we chose to make antidot lattices with squared patterns having "realistic" dimensions, i.e. which are large enough to be achieved routinely with the nanostructuration techniques that we will detail below, while being small enough to have significant effects for spin waves (generation of forbidden bands, reconfigurable effects). Many numerical studies on magnonic crystals have been carried out on systems having dimensions of the order of a few nanometers, which makes it possible to have band gaps of several GHz, however without experimental studies associated with them [149]. This can probably be explained by the great technological challenge represented by the manufacture of systems in the range of a few tens of nanometers. Consequently, we aimed for dimensions of the squares s ranging from 100 to $300\ \mathrm{nm}$ with spacings d between them such that $s \leq d \leq 3s$.

- The lateral dimensions of the entire magnonic crystal had to be large enough so that we could consider our system as almost infinite. This depends in particular on the size of the patterns and the distance separating them, but we considered that we needed at least 50 periods ($= s + d$). In addition, we wanted to study the spin wave modes in these crystals with micro-antennas several microns wide in order to achieve conditions close to a uniform excitation (FMR). Ideally, antidot lattices of a few hundred microns wide would have fulfilled all the conditions and would have made it possible to place several micro-antennas above the crystal for spin waves propagation studies for example. However, since such a field of view was not accessible either in e-beam lithography or in FIB at CEMES, we have sought to produce antidot lattices of sizes of the order of a few tens of microns.

To make the patterns from a CMS thin film, we used dry etching techniques. When I arrived at the laboratory, the e-beam lithography was not yet in operation. Therefore, we first tried to make the patterns by FIB etching with Ga^+ ions. This technique has the advantage of a direct writing of the patterns in the material, however it also presents certain limitations to achieve our objectives, in particular those associated with the implantation of Ga^+ ions. The latter will be discussed in chapter 6 section 6.1. This is why I have worked in parallel in the development of e-beam lithography and lift-off equipments at CEMES in order to produce antidot lattices by etching CMS thin films with Ar^+ ions through a resist mask. In this case, one of the major difficulties we encountered comes from the slow etch rate of the CMS thin films. As a result, we had to test different electron-sensitive resists (e-

beam resists) in order to find the one that could bear the necessary time for the etching of 45 to 50 nm thick CMS thin films. In addition, the Ion Beam Etching (IBE) chamber that we use in the laboratory is not a commercial equipment but a prototype, which also required significant development works.

We will start by presenting the techniques used, the strategy implemented and the associated limitations to achieve square antidots in a thin film of CMS. Then in the next section 4.3, we will present all the necessary steps in addition to the realization of the antidot lattices to obtain a measurable sample either by FMR or by Brillouin Light Scattering (BLS).

4.2.1 Ion milling principle

The concept of ion milling has already been approached when we detailed the Plassys sputtering chamber in chapter 3. Sputtering relies on the ejection of atoms by incoming ions (Ar^+ in the case of the thin film deposition). In the case of FIB milling, we used Ga^+ ions from an ion source that will be described below. The different physical mechanisms at the origin of ion milling (or sputtering) are quite complex and many books treat these phenomena [228, 229]. Our goal here is to give general information about them. Basically, it relies on the interaction between an incoming ion that has been accelerated and the atoms of the material to be milled. The ions will interact through elastic and inelastic collisions with the atoms of the target. The former is predominantly related to the electronic shells of the species while the second is more related to nucleus interactions even if both effects are always present. However, nuclear interactions always lead to inelastic scattering.

The milling process is schematically depicted in Figure 4.4 b). Incoming ions travelling inside the material lose their kinetic energy to the surrounding targeted atoms through the elastic and inelastic interactions that can be modelled with a collision cascades mechanism [230, 231]. As an example, in the case of a crystalline material, the targeted atom receiving the ions energy can move from its initial place to insert itself in-between placed atoms (interstitial atom) and thus creating a vacancy. This phenomenon can occur if the ions energy exceeds the displacement energy of the targeted atom. This primary collision can then lead to subsequent collisions if each time the energy transfered remains sufficiently high to displace atoms. For surface atoms, if the transmitted kinetic energy of ions is large enough to overcome the binding energy of the material [232], the targeted atoms are sputtered away from the surface leading to an effective milling of the material surface.

4.2.2 Focused Ion Beam etching of Co_2MnSi antidot lattices

4.2.2.1 The dual FIB-SEM equipment

The Focused Ion Beam (FIB) technique is widely used in semiconductor industries and academic research facilities, especially for the preparation of samples which are then studied by Transmission Electron Microscopy (TEM), in particular in the fields of microelectronic devices and integrated circuits. It is also used for the prototyping of devices as it is a direct micro/nanostructuration mask-free process [230], with a versatile fine focusing provided by a wide variety of ion species. For some applications it shows some advantages over conventional nanostructuring techniques as UV or e-beam lithography and deposition/etching processes.

In this thesis we used a FEI Helios Nanolab 600i dual beam FIB-SEM [233, 234]. It is equipped with both a SEM (Scanning Electron Microscope) and a FIB columns, as illustrated in Figure 4.4 a). The main advantage of this instrument is that live observation of the milling process can be performed with the SEM column. Let's note that imaging can be performed with the ion column but it leads to the damage of the observed area. The FIB column is basically composed of an ion source, ion optics

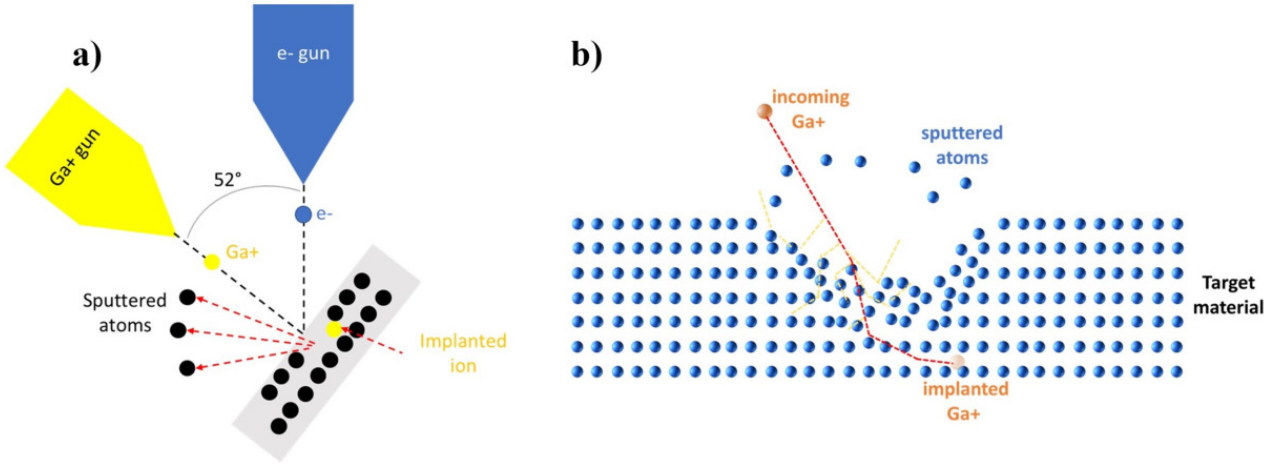

Figure 4.4: Schematics of a) a dual FIB-SEM instrument, and b) the effects of ion milling. The red and yellow dotted lines represent the trajectories of the incoming ion and atoms of the target respectively.

with electrostatic lenses and apertures to focus and deflect the ion beam onto the sample surface, a motorized stage with the sample attached to it and a vacuum chamber. It is possible to use different ion species but Ga^+ Liquid Metal Ion Source (LMIS) is the most used in the literature due to its liquid state at room temperature and low steam pressure facilitating its use in high vacuum. It is the ion species used in our equipment. A sharp tungsten needle (W) is in contact with the Ga^+ LMIS and is wet by the latter. A high extraction field ($> 10^8$ V/cm) is applied to pull the gallium liquid at the tungsten tip into a sharp cone of radius up to $5 - 10$ nm. An applied high electric field will then generate the emission of positive Ga^+ ions from the gallium cone.

When the Ga^+ beam impacts the sample surface, several physical phenomena occur in addition to ion milling such as the generation of secondary electrons, the implantation of Ga^+ ions, and amorphisation/recrystallisation of the material [235]. Depending on the energy of the Ga^+ ions defined by the high voltage applied, the damaged layer will be more or less deep. Efficient sputtering of material is reached with highly energetic ions. In our case the Ga^+ ions are accelerated at 30 keV. The etching efficiency can be characterized by the sputter yield which is the ratio of atoms sputtered per one incident ion for specific ion beam settings (high voltage, current) and is specific to the material being milled. To this end, working at 30 keV offers a high sputter yield. It also allows to obtain a very small spot size of the ion beam [231]. At 30 keV, the penetration depth of incident Ga^+ ions depends on the material but it typically ranges from 5 to 40 nm.

FIB etching quality and resolution are limited by two main effects. The first one is redeposition of sputtered atoms. While most of the ejected atoms of the target are pumped by the vacuum system, those ejected at low angles are not energitically stable and tend to accumulate and condense in a solid phase nearby etched areas. Also, the smaller is the pattern to be etched, the more will be the redeposition as sputtered atoms have less possibilities to "go out". The second limitation concerns implantation of Ga^+ into the material. These ions can chemically interact with the atoms of the target and potentially modify the physical (mechanical, electrical, magnetic optic) properties of the material. Implantation appears mainly on a small volume surrounding the hole. It comes from the trajectory of the ions, as depicted in Figure 4.4 b).

Scan methods or beam and processing parameters can help to reduce the impact of these issues. The scan method concerns the way of moving the ion beam on the surface of the sample. Different strategies can be set to etch the holes called serial or parallel modes. In the serial mode, one hole is fully etched before moving to another one. This involves to stay a sufficient time on each hole, increasing potentially the redeposition. In the parallel mode, the ion beam is moved successively on each hole of the lattice and each hole is only milled for a small amount of time. Multiple scans over the entire lattice are performed until all the holes are completely etched. These modes are depicted in

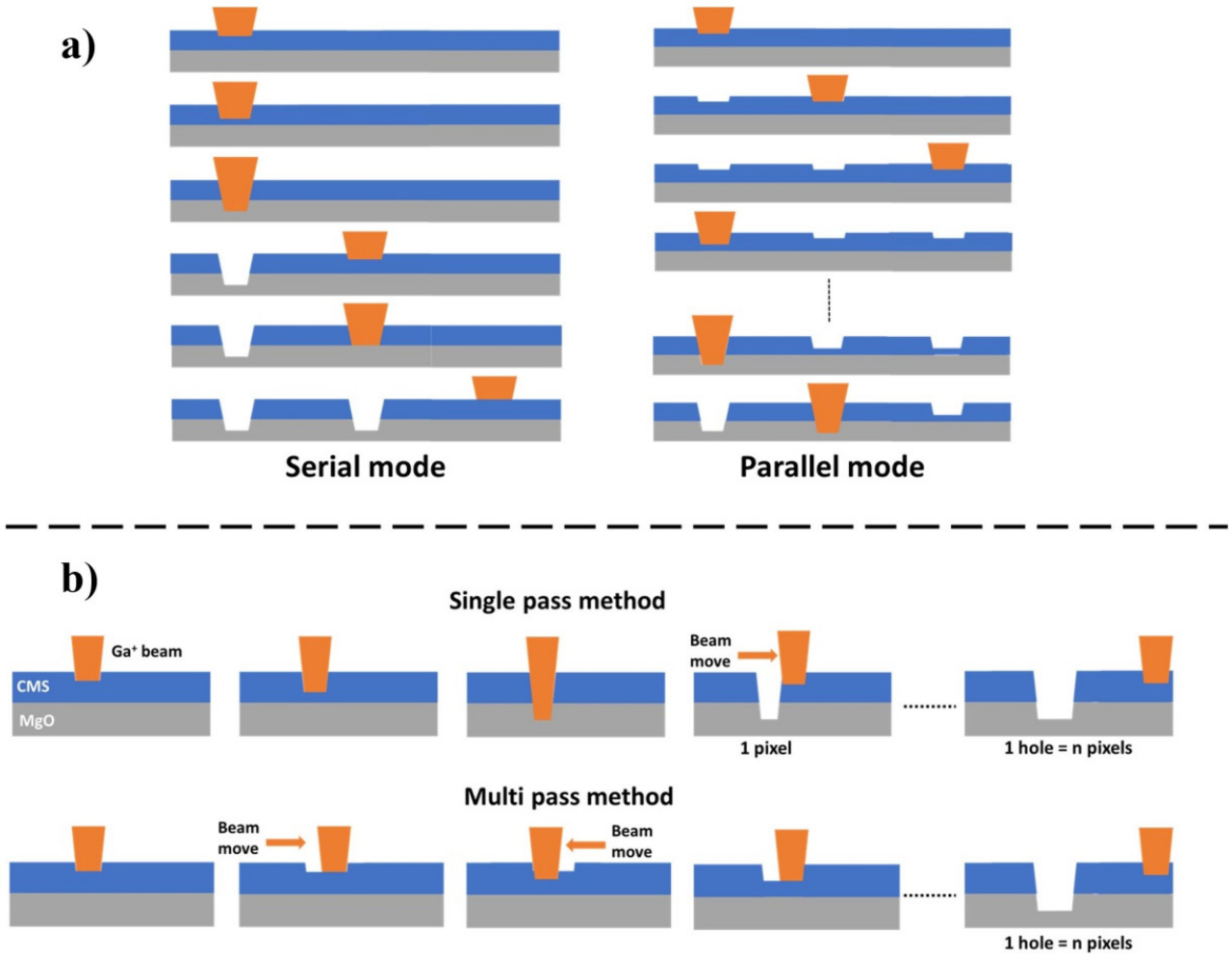

Figure 4.5: Schematics of a) the serial and parallel scan modes, and b) the single and multi-pass etching strategies.

Figure 4.5 a). The parallel mode is normally used to reduce the redeposition around one hole induced by the ejected atoms coming from the surrounding holes [236]. Now for both the serial and parallel modes, one can choose to work either in the single pass method or in the multi-pass method as depicted in Figure 4.5 b). These two methods are similar to the serial and parallel modes but for a single hole. In fact, a hole pattern is composed of multiple pixels which are roughly corresponding to the size of the ion beam spot. The number of pixels to form a hole pattern depends on the size of the hole and the size of the ion beam spot. In the single pass method, a pixel is fully etched before moving to the adjacent one while in the multi-pass method all pixels are etched in parallel. In the latter case, the beam stays a very short time on each pixel. It is much faster than the single pass method but it is potentially less precise.

In order to have the best spatial resolution, and thus the best pattern as possible, one might be tempted to work with a very small spot size. However, this is not always relevant for large lattices, such as ours, as the total milling time will increase and defects such as misalignment of the holes will appear due to mechanical and electronic drifts. Other parameters also play a major role in the good resolution of the pattern and the total milling time. For example, the latter increases when increasing the dwell time (duration over which the focused ion beam stays at the pixel position) or when increasing the overlap (the pitch between two pixels). But it can be reduced by increasing the ion current density that depends on the ion species, their energy and the diaphragm aperture. Therefore a compromise between all the experimental parameters and the total milling time has to be found. To help the user to tune all these parameters, the FIB is equipped with the Thermo Scientific Nanobuilder

Software that controls the milling process [237].

4.2.2.2 Antidot lattices processed by FIB

Many tests were performed to optimize the milling conditions to obtain squared antidot lattices. In this section we will show a few examples which are significant of the difficulty to fulfill our experimental constraints described at the beginning of this section. Before that, let's mention that a high number of people work with the FIB at CEMES. Therefore, each person has access to the equipment only once or twice a week. One session lasts 4 hours but it is possible to have sessions at night for 8 hours. The limited time and small number of working sessions forced us to compromise on the quality of the pattern.

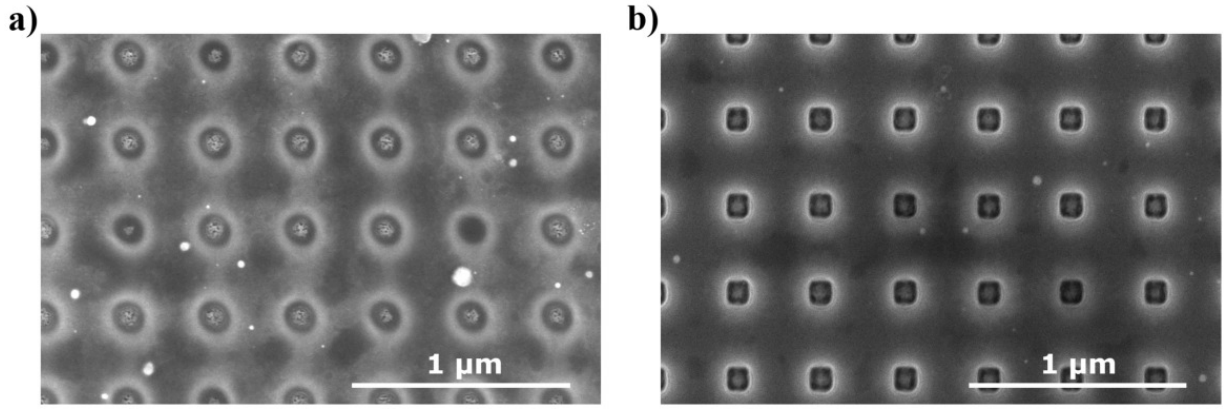

Figure 4.6: SEM images of the FIB etched Co_2MnSi squared antidot lattice ($40\ \mu m \times 40\ \mu m$) of antidots size 100 nm and spacing 300 nm with a) a parallel multi-scan strategy and b) a serial multi-scan strategy.

As a first example, Figure 4.6 shows the difference we observed between the parallel and serial milling modes. These images were done with the SEM column. We always worked with the multi-scan method for both modes as it reduces redeposition. For this test, we aimed to etch a $40\ \mu m \times 40\ \mu m$ lattice of squared antidots with expected lateral dimensions of 100 nm and edge-to-edge separation of 300 nm. The experimental conditions are summarized in Table 4.2. From Figure 4.6 a), it is

High voltage [kV]	**Writefield** [μm^2]	**Current** [pA]	**Theoretical beam spot size** [nm]
30	100×100	70	21

Table 4.2: FIB experimental conditions

obvious that we were not able to find the correct experimental parameters to obtain squared patterns in the parallel mode. Indeed, the shape and size of the antidots are not respected and the entire CMS thickness was not milled. The reason for such a failure is not clear at all for us. It could be related to a deflection of the beam not precise enough to mill the exact same area at each scans, resulting in a larger area exposed to Ga^+ ions and a lower milling depth. In contrast, the SEM image in Figure 4.6 b) shows that the serial multi-scan strategy leads to quite well-defined squared antidots. However, the vertices of the squares are rounded and their lateral dimensions are about 140 nm instead of 100 nm. Nevertheless the center-to-center distance is 400 nm as expected. Also, we can observe some kind of white halo around the hole that we will discuss below. Therefore, we chose to work in the serial mode to make our final device presented in section 4.3.1. Let's note that the time needed to produce this antidot lattice was 8 hours in the case of the serial milling strategy while it was about 1 hour for the

parallel mode. With the constraint of access to our FIB, it means that the maximum lateral dimensions of the antidot lattice are about 40 to 50 μm for 100 nm squared antidots with 300 nm spacing.

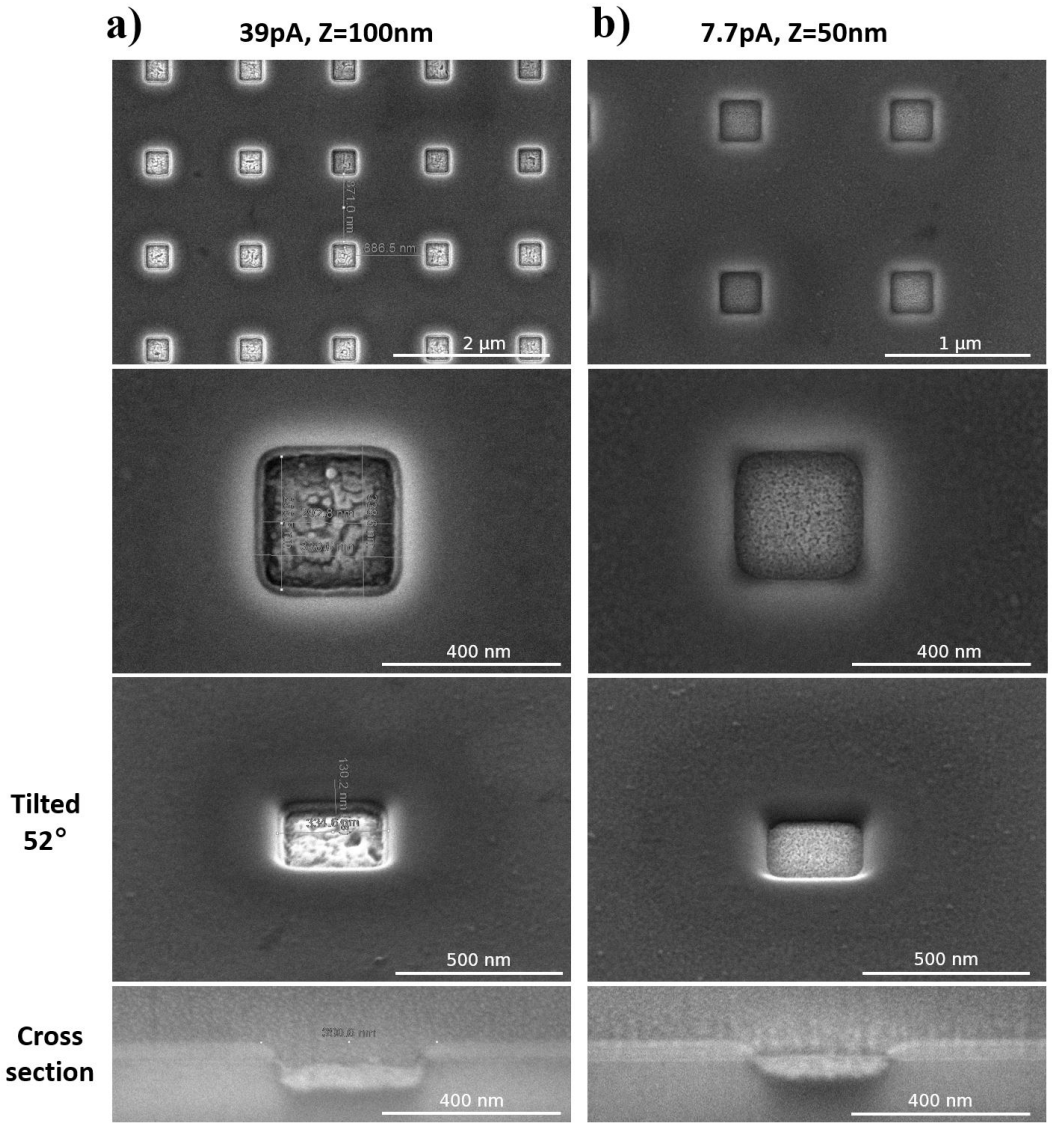

Figure 4.7: SEM images of FIB etched CMS antidots with an ion beam current and etching depth Z of a) 39 pA, $Z = 100$ nm, and of b) 7.7 pA, $Z = 50$ nm respectively. For both a) and b), the second row corresponds to zoomed SEM images on a single antidot of the first row SEM images, the third row corresponds to 52° tilted SEM images of the antidots and the fourth row to their cross-sections.

The white halo around the holes and the rounded shape of the vertices of the squares have been observed for every antidot lattice we realized by FIB milling, whatever the size of the antidots or the spacing in-between them. The amplitude of the ion beam current turned out to have no effect either, nor the depth at which we want to etch the holes. Examples are shown for CMS squared antidots with a nominal size and spacing of 300 and 900 nm respectively. In Figure 4.7 a), the ion beam current was decreased compared to the conditions used to obtain the structures shown in Figure 4.6 b). In Figure 4.7 b), the ion beam current was further decreased while we also reduced the etching depth Z. In both cases, the halo corresponds to a variation of contrast induced by the fact that the sidewalls of the holes are not vertical. In particular, the holes present a bowl shape that can be observed in the SEM images obtained at a 52° tilted angle (third row of Figure 4.7 a) and b)) or when looking at the profile of a cross section in the middle of the holes (fourth row of Figure 4.7 a) and b)). The bowl shape is a little less pronounced for the lowest ion beam current and decreased milling passes as could be expected. Indeed, the current is decreased by selecting a smaller diaphragm in the column, leading

to a smaller spot size. A possible explanation of the bowl shape relies on both the conical shape of the beam and the fact that we always focused the beam onto the surface of the sample. As can be seen in Figure 4.8 a) representing the trajectories of Ga^+ ions calculated with the SIMION software [238], when the beam is focused onto the surface (red dotted lines in Figures 4.8 a), b), c)), the density of ions is maximum at the center of the beam and weaker on the sides. The corresponding FIB and SEM observations show the bowl shape as observed in our experiments. Now when underfocusing the beam, we can see an optimum (Figure 4.8 b)) for which the sidewalls are straight. Therefore, additional studies performed with different focusing conditions would be necessary to test the shape of the antidots under different focusing conditions. Finally, it also appears that reducing the current seems to improve slightly but not drastically the right angles of the squares vertices. In any case, even if working at low currents can improve the quality of the etching, the fabrication of a large antidot lattice will take too many hours, the pattern would then be sensitive to mechanical and electronic drifts.

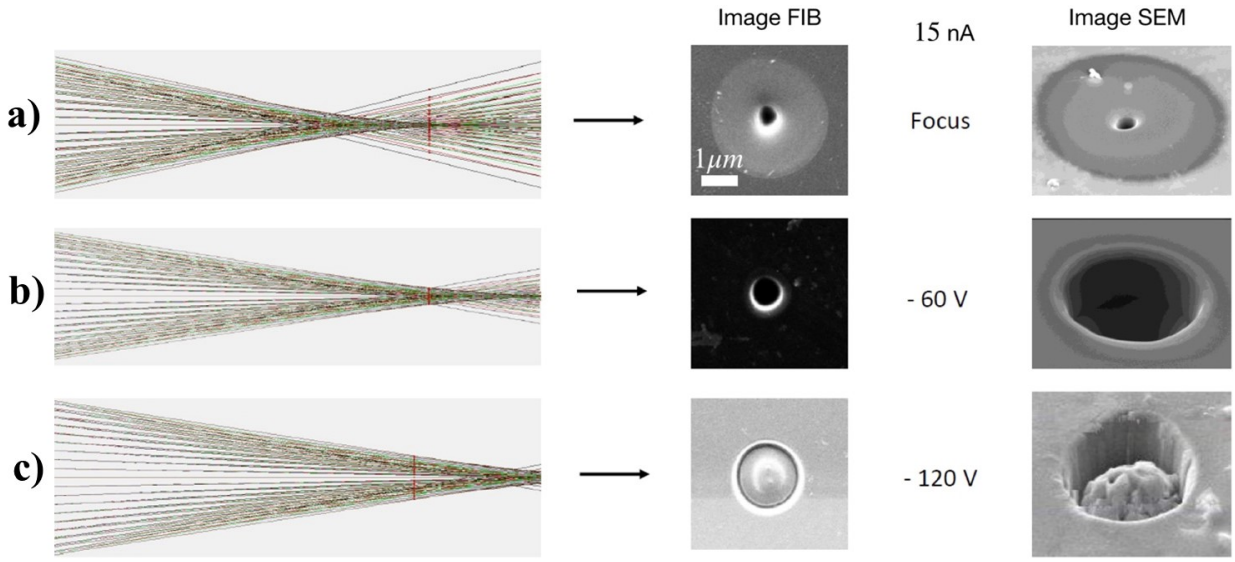

Figure 4.8: (Left) Simulation performed with the SIMION® software [239] of the Ga^+ ions trajectories in a FIB experiment with corresponding FIB (middle) or SEM (right) images of the holes. From a) to c) the beam goes from focus to increasing underfocus. Reproduced with permission from [238].

To conclude here, we have realized a sample for FMR measurements with the experimental conditions described in table 4.2. This sample is presented in section 4.3.1. In addition to the geometrical discrepancies with respect to the expected ideal geometry, FMR experiments demonstrated that Ga^+ implantation around the sidewalls induces a strong modification of the CMS magnetic parameters, to the detriment of the possibility to achieve reconfigurable magnonic crystals. These effects are presented in chapter 6 section 6.1. As a consequence we did not pushed further our studies to obtain better geometries with the FIB technique. Instead, we developed another approach presented in section 4.2.3.

Nonetheless, other avenues can be explored to overcome the bowl profile and Ga^+ implantation. A first possibility consists in depositing a protective thin film such as Si_3N_4 onto the CMS thin film prior to the FIB etching [240]. In this case, the bowl shape due to the broader ion beam spot will be printed onto the protective thin film. Ga^+ implantation might be reduced also. Annealing at a high temperature can also be tested to re-crystallize the CMS after the FIB milling but it can also lead to Ga^+ ion migration towards both the surface and between the holes where the CMS is intact [241]. Finally, we think that the main parameter concerns the shape of the ion beam. This involves a fine adjustment of the focus and astigmatism [230]. When adjusting the focus and astigmatism for a sharp ion beam, the operator will logically tend to optimize the resolution of the image for the largest

magnification (as we did). This consists in placing the target surface in the so-called Gauss optimum geometrical plane as illustrated in Figure 4.8 a), where the ion beam presents a narrow and intense central part and non-negligeable tails. To reduce the lateral tails of the focused ion beam, one should place the target surface in a different plane, called the plane of the "circle of less confusion" [230], where this time the focused ion beam profile resembles a bell-type whose tails are much weaker. As a consequence, the latter fine focus strategy is to be favored to reach the maximum resolution in FIB milling.

4.2.3 Combination of electron beam lithography and ion beam etching for the fabrication of antidot lattices

In the litterature, several magnetic antidot lattices were fabricated by a combination of e-beam lithography and ion beam etching [49, 225]. Contrary to the FIB technique presented above, it is no longer a direct milling approach. Indeed, in a first step we must transfer the desired pattern into a mask. In a second step, the pattern is transferred into a target material by ion etching through the mask. For this step, the sample is generally placed in an IBE (Ion Beam Etching) chamber allowing milling with inert ions such as Ar^+, contrary to FIB milling. Another main interest is that anisotropic milling is relatively easily achieved, favoring vertical sidewalls of the holes.

Several strategies have been developed to realize the mask. In this work, we used an electron sensitive resist which is one of the most common method. The different steps are schematically illustrated in Figure 4.9. The resist is first spin-coated and baked on the sample to etch ("target material"). Then, e-beam lithography is performed to define the pattern into the resist. After development, ion beam etching is carried out through the holes opened in the resist, while the rest of the sample is protected. Finally, the sample is placed in a solvant to remove the resist. Let's note that photo-sensitive resist and UV lithography can also be used but for patterns with dimensions above the micron.

It is worth to mention that it is also very common to use metallic or dielectric materials as a "mechanical" mask instead of a resist. In this case, these layers must have lower etching rates than the target layer of interest (high selectivity) or to be thick enough so that it can prevent the underlying thin film from etching. The main interest of such approach is to greatly improve the verticality of the holes sidewalls owing to the hardness of the metallic mask as compared to polymer resists [242]. Such process is often used to make pillars and in semiconductors technology. The major difficulty is to add additional stages to the fabrication process. Indeed, the mechanical mask must be deposited on the target sample by lift-off process, which first involves a UV or e-beam lithography step to define the mask as the inverse of the final expected pattern transferred to the target material. Another issue is related to the removal of the mechanical mask. For example, it can require an extremely precise thickness and etching rate calibrations so that the mask and the target material below are completely milled at the very same time. Other processes use particular metals such as Al, Cr or Au that can be removed chemically. In this case, the thin film below the mask must not be sensitive/reactive to the chemical compound.

In this section, e-beam lithography and the Ion Beam Etching (IBE) machine used in this thesis will be described. Then, the different tests to find processing conditions for the correct etching of antidots lattices in a CMS thin film will be approached.

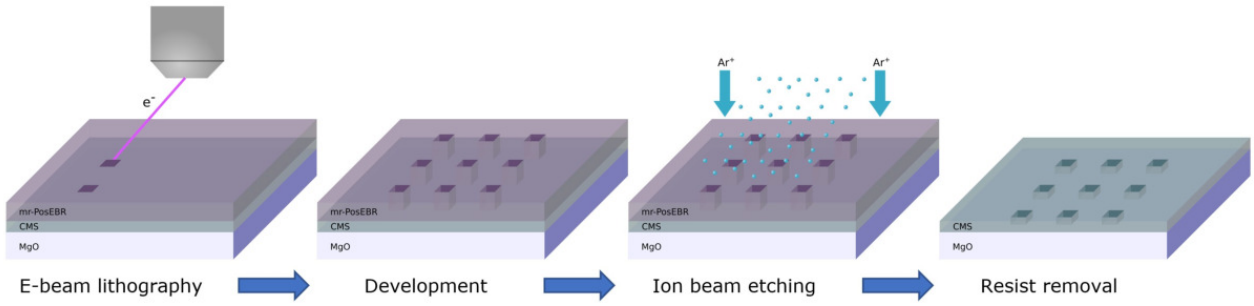

Figure 4.9: Scheme of the combined e-beam lithography and ion beam etching process for the fabrication of antidot lattices in the CMS thin film.

4.2.3.1 Electron beam lithography (EBL)

Electron Beam Lithography (EBL) or e-beam lithography is a lithography technique which uses a focused electron beam to write a predefined pattern onto an electronic sensitive resist. The e-beam exposition changes the solubility of the resist in an appropriate developer. The EBL patterning is illustrated in Figure 4.10. This technique is widely used in numerous research fields for the realization

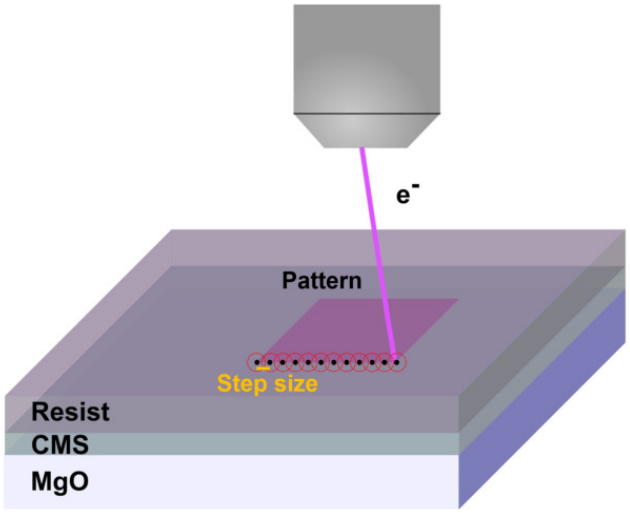

Figure 4.10: Schematic of the EBL patterning on a resist.

of nanostructures [243]. EBL indeed provides high resolution owing to the small wavelength of electrons (in the order of picometers or less) and its small spot size. Such features allowed the realization of sub-10 nm line patterns [244].

EBL has the same functioning as a SEM except that the focused electron beam is managed with a deflection control, pattern generator and beam blanker to scan a certain area with patterns [245, 246]. The beam deflectors serve to direct the e-beam onto the resist for the exposition with respect to the specified pattern location. The beam blanking deflects the e-beam away from the sample to not irradiate the resist that should not be exposed. EBL can be performed on a SEM equipped with an EBL module or with dedicated EBL machines. In the case of a SEM equipped with an EBL module, generally the maximum high voltage can be up to 30 kV while it can reach 50 to 100 kV in the case of dedicated EBL equipments. In this thesis, we worked on the ZEISS SEM equipped with an ELPHY Multibeam Raith module of the CEMES clean room facility. Some tests were also performed on the JEOL SEM equipped with an ELPHY Quantum Raith module at the AIME (LPCNO, INSA Toulouse).

Prior to the patterning with EBL, an e-beam resist is deposited on the substrate. When the fo-

cused e-beam irradiates the resist, the latter undergoes chemical reactions. Resists can be classified in two main types depending on their reaction under electron irradiation: positive or negative. Under irradiation, positive resists are degraded, and in an appropriate developer, the irradiated portion is eliminated. In contrast, negative resists are strengthened by the e-beam irradiation and persist after development while the rest of the resist is removed.

The major objective of EBL is the achievement of patterns with the highest resolution, density and reliability [246]. The achievement of this objective relies on the manipulation of many parameters, such as the quality of the electron optics, the resist properties, the substrate, the process conditions and the developer.

Procedure

Prior to the writing of the patterns, the operation of the EBL is mainly decomposed in three steps. First, with the choice of the high voltage and beam current, one performs the SEM adjustments (focus, astigmatism, wobble) to obtain the smallest beam spot as possible. The high voltage corresponds to the energy given to the electrons and impacts the reaction within the resist. For example, high energy electrons will go deeper and straighter into the resists leading to less interactions on the sides, reducing the proximity effect. The latter is later discussed in the subsection dealing with proximity effects. As a result, the application of a high voltage is to be favored for the realization of fine structures. The choice of the high voltage also depends on the resist properties. The beam current is determined by the choice of the diaphragm. The smaller the diaphragm is the smaller will be the e-beam spot size. Nevertheless, in the case of low beam currents, the adjustment of the SEM to perform EBL becomes difficult, which can affect the correct realization of the spot size [245]. Generally a compromise is made between smallest spot size and beam current. The beam current generally used for fine features is below 50 pA [245]. The quality of the beam spot can be checked by letting the beam focused in a spot on the resist during a certain time ($10 - 30$ s). A spot "imprinted" onto the resist can then be seen. A correct spot must be circular and well-defined, otherwise further adjustments on the focus and astigmatism are required.

In a second step, the writefield calibration is performed. This consists in calibrating the beam deflection with respect to a chosen square scanning area called writefield. Generally in EBL, the stage is moved to a particular position and then remain fixed while the e-beam scans the patterns enclosed in the writefield. To a writefield corresponds a magnification. The higher the magnification, the smaller the writefield is. A writefield is defined with a grid of pixels. For the writing of the pattern, the e-beam will scan pixel-by-pixel the pattern which is part of the writefield (Figure 4.10). The center-to-center distance of consecutive pixels is the step size. The minimum achievable step size is defined by the writefield size. The writefield calibration consists in determining the appropriate zoom, shift and rotation values of the SEM image seen by the deflection control. This procedure allows the correct patterning (size, shape) of the predefined patterns. This procedure should always be performed each time prior to the lithography of the patterns as the SEM settings drifts in time and other users of the SEM can also involve changes in the SEM settings.

Finally, the last step before launching the lithography is the setting of the exposure parameters. As mentioned previously, the electron beam scans an area of the resist pixel by pixel in a single pass. The dose corresponds to the number of electrons per unit area to achieve changes in the resist [247]. Its value depends on other exposition parameters such as the step size, the dwell time, which corresponds to the duration for which the beam stays on a pixel before moving to the other one, and the beam current. As the beam current is fixed at the beginning by the user and the step size choosen with respect to the writefield size, increasing or decreasing the dose corresponds mainly to an increase or decrease of the dwell time. The correct determination of the dose requires to perform beforehand several EBL writing tests, called dose tests. Besides, for the patterning of fine structures, smaller writefields 200×200 μm^2 down to 50×50 μm^2 are favored [245]. It is indeed better to be as close as

possible to the minimum step size possible to achieve the best resolution. Dose tests will then allow to find the corresponding dwell time. Finally, the beam speed is also an important parameter. The latter must not be too fast (it is recommended below $5\ \mathrm{mm/s}$ for fine structures) otherwise distorted patterns can occur.

Applications

Subsequently to EBL, another process step is achieved to finalize the "imprint" of the pattern onto the substrate. EBL is indeed an intermediate process which provides a definition of the pattern. Generally, this definition of the pattern is then used either for the deposition of a material on the substrate by lift-off or for the etching of the substrate. In the first case, an undercut profile of the resist after EBL and development is favored to facilitate the lift-off, as illustrated in Figure 4.11. To

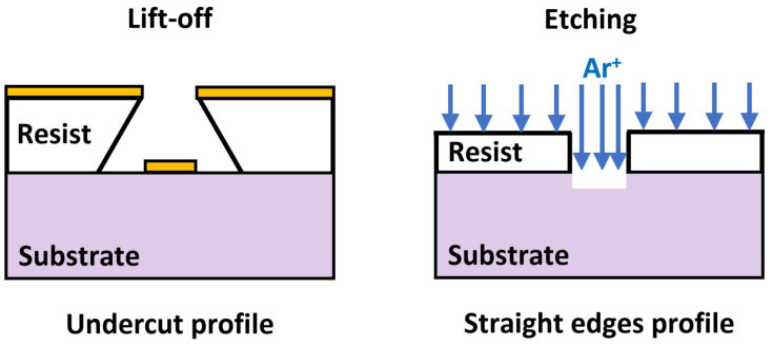

Figure 4.11: Schematics of possible resist profiles. The undercut profile (on the left) with thick resists is adapted for lift-off processes while the straight edges profile (on the right) with thinner resists is more suitable for etching processes.

this end, several resist layers which have different abilities to react to the e-beam exposure, such as PMMA 450 and 950, are added to obtain this profile. The thickness of the resist should be at least 2-3 times the thickness of the deposited material to ensure a correct lift-off. For etching applications, it is better to obtain a resist profile with straight sidewalls as shown in Figure 4.11 to ensure straight etched edges in the substrate. Besides, a smaller thickness of resist is preferred to offer the best resolution for fine features. The difficult task lies in finding a resist that will stand the etching while offering the best resolution.

The choice of the resist is important for the correct realization of targeted patterns during EBL and after EBL with the subsequent process [247]. E-beam resists are characterized by different features: sensitivity, contrast and selectivity to etching. The sensitivity corresponds to the extent of alteration in the resist under e-beam exposure. The contrast corresponds to the property of a resist to differentiate between exposed and unexposed areas and is closely related to the resolution. Selectivity to etching process defines the resistance of the resist when used as an etch mask. The ideal resist for the best resolution in etching processes has a low sensitivity, a high contrast and a high selectivity to etching. The main limitations of EBL resolution come then from the e-beam resists (chemical structure) and subsequent processes, such as etching and lift-off [243].

Proximity effects

Electron scattering in the resists constitutes an important limiting factor for the realization of sub-$100\ \mathrm{nm}$ patterns [248]. When energetic electrons enter the resist, some are scattered in the resist layer. These scattered primary electrons are called forward electrons and irradiate unintentionally adjacent sides of the resist. Back scattered electrons from the substrate can also further irradiate the resist. These scattering effects can generate secondary electrons on their way through the resist layer by inelastic collisions of the forward and back-scattered electrons. These phenomena lead to the

undesired exposition of wide adjacent resist regions inducing a distortion of the patterns as illustrated in Figure 4.12. This effect is called proximity effect [249, 250] and constitutes the main limitation

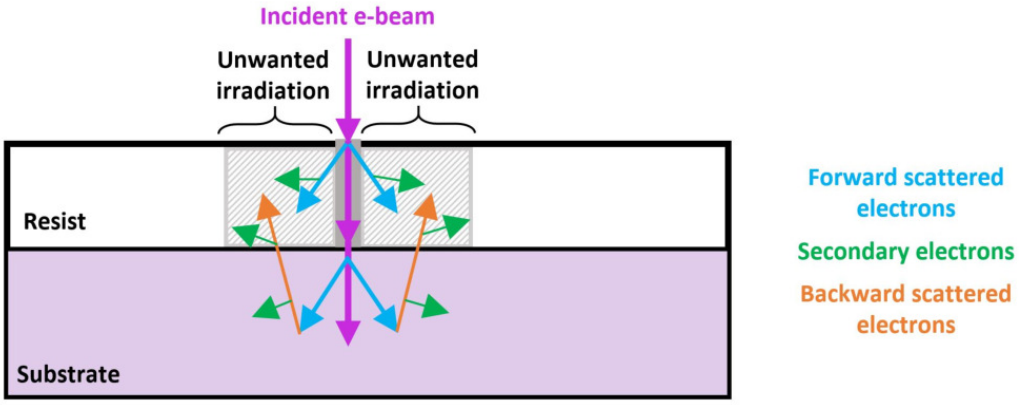

Figure 4.12: Schematic of proximity effects.

to resolution in EBL. Proximity effects can be reduced by the increase of the high voltage. At low voltages (10 kV or less), high proximity effects can occur as slower electrons may interact more with the resist, making them more subjected to scattering.

4.2.3.2 The Ion Beam Etching (IBE) chamber

An IBE chamber allows a relatively smooth etching of theoretically every materials. However, it is especially fitted for thin metallic or dielectric films with thicknesses up to a few tens of nanometers. Those chambers are quite similar to the sputtering chamber discussed in section 3.2.3, at the difference that this time the etched material is the sample itself. Ions are extracted from a plasma formed from an inert gaz, such as generally argon, but other species can be used such as oxygen to speed up the milling via chemical reactions with the target sample. In nanotechnology platforms and clean room facilities, IBE chambers are not as common as RIE (Reactive-Ion Etching) chambers that are devoted to deep etching (depths in the micron range) and especially for insulating materials. Let's note that the CEMES acquired in 2017-2018 the only IBE chamber available among all physics laboratories in Toulouse. However, this machine is a prototype developped by the Polygon Physics and Axesstech companies.

Our system is schematically described in Figure 4.13. It is composed of a vacuum chamber (vacuum down to the 10^{-7} mbar range obtained with a turbo pump), a resonant plasma cavity and a rotating substrate holder. The resonant plasma cavity uses the ECR (Electron Cyclotron Resonance) technology to generate and maintain a Ar^+ plasma. The gas is injected into the cavity where a RF discharge initiates the plasma at a pressure of around 5.10^{-3} mbar. Then, a small static magnetic field B_0 induces the circular precession motion (cyclotron motion) of the free electrons around the field lines. B_0 is generated by permanent magnets placed around the plasma cavity. The precession frequency of the electrons equals the Larmor frequency defined as $f = eB_0/2\pi m_e$, where e and m_e are the electronic charge and mass, and $B_0 = 87.5$ mT. The frequency is then 2.45 GHz. By superimposing a magnetic field B_{rf} oscillating at this exact frequency and oriented perpendicularly to B_0, the free electrons enter into resonance, i.e. they will be continuously accelerated at each half cycle of the RF field (we then speak of "hot" electrons). B_{rf} is generated by RF sources and microwave waveguides placed at the top of the plasma cavity. Hot electrons then collide with the atoms of the gas which lose electrons by transfer of kinetic energy. A cascade phenomenon takes place and stabilizes the plasma as an equilibrium is reached between the Ar^+ ions which recombine with the free electrons

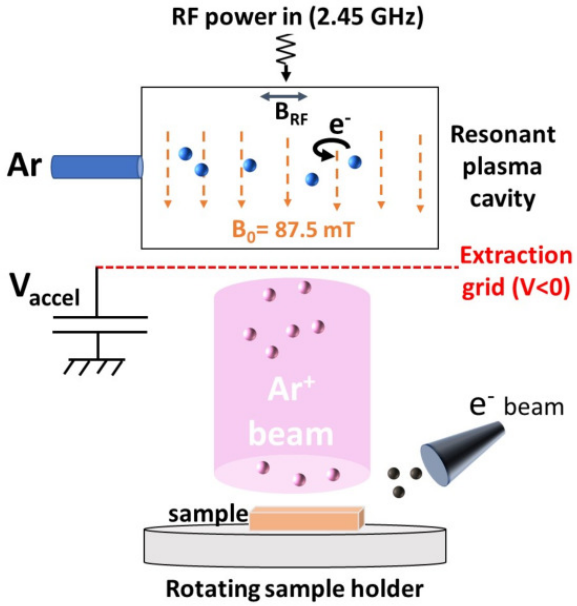

Figure 4.13: Schematic principle of an IBE chamber with ECR based Ar plasma.

and those which are extracted from the cavity and accelerated by a grid placed at a negative potential (cathode). The acceleration voltage is 1 keV in our case. The Ar^+ ions thus arrive in the form of an anisotropic beam on the sample to be etched.

The particularity of the technology developed by the Polygon Physics company is the miniaturized ECR cavity system allowing high ion beam current for very low microwave input power. Details can be found at [251]. 7 RF sources at 2.45 GHz are placed at the top of the cavity chamber. Each RF source can generate an ion beam with a diameter of approximately 3 cm. When all the sources are switched on, the beam covers an area of about 81 cm^2 (about 10 cm in diameter). The optimization of the RF waveguides makes possible to generate a plasma for powers as low as 1 or 2 W (the maximum power delivered by each source is 10 W). For example the ion beam current reaches about 14 mA for 2 W on all RF sources, leading to an etching rate of the CMS of about 7 ± 2 nm min^{-1}. Therefore it takes about 7 to 8 minutes to etch entirely our thin films in such conditions.

As our system is a prototype, it presents a few disadvantages that we had to consider in our experimental developments. For example, in commercial IBE systems, incoming ions are neutralized by electrons before reaching the sample to be etched in order to avoid charge accumulation and eventually chemical reactions. In our system, the electron beam has been added by Axesstech after the installation of the ion source. The electron beam is undersized and is focused directly onto the sample as schematized in Figure 4.13. It crosslinks electron sensitive resists, making them extremely difficult to remove afterwards. Therefore, after many tests, we decided to work without the electron beam at the risk of positive charge accumulation in our resist etch mask and thin film. To reduce this risk, the etching was performed over several intervals and the sample was connected to the metallic sample holder with conductive copper tapes. Another disadvantage of our machine relies on the orientation of the sample holder. In commercial systems, an option allows to have the sample holder tilted up with respect to the ion beam direction. This is known to reduce a lot the redeposition of etched materials when the sample rotates on itself. In our system the sample holder can rotate on itself but it is perpendicular to the ion beam.

4.2.3.3 Antidot lattices processed by e-beam lithography and IBE

The main difficulties of this approach lie in finding operating conditions allowing to match the desired pattern resolution. In particular we must find a resist sufficiently resistant to stand the ion milling while being quite easily removable after harsh etching conditions. Usually, negative resists such as HSQ [248] or ma-N2400 [252] are used to realize nanodots because they are quite resistant to ion etching. However they are not relevant for making antidot lattices since during e-beam lithography, the beam have to scan the areas in-between the antidots. For large lattices as expected in our case, this approach would lead to very long processing times and potential beam drifts. Furthermore these negative resists are generally difficult to remove and need harsh chemical removers that may damage the Co_2MnSi thin film. Therefore, we chose to use positive resists to make our magnetic antidot lattices.

Contrary to lift-off patterning which requires an undercut profile as mentioned in section 4.2.3.1, it is better to have straight vertical edges in the resist when it is used as a mask for dry etching. It ensures vertical sidewalls in the underlying thin film. We have tested two different resists: PMMA and mr-PosEBR by Micro Resist Technology GmbH [253, 254]. The first one is very widely used in micro and nano electronics in particular for lift-off processes where several layers of PMMA with different molecular weights (450 and 950) are used to obtain the undercut profile. Here we used only 950-PMMA due to its extreme resolution that can reach sub-10 nm and easiness of removal (aceton). However it is known for having a low resistance to ion milling [255–257]. Thus, if the edges of the resit patterns show a sloping profile, it is very likely that the transferred patterns will show a bowl profile after IBE. This is typically what we obtained in our antidots and despite a very high number of tests on the conditions for spin coating (thickness), baking, IBE process (base pressure, accelerating voltage, electron neutralization) and lithography (dose, energy), we were not able to find conditions leading to satisfactory antidot lattices. Therefore we will not give too much details on this part of our work but only some general comments. Basically, we observed that antidots had rough edges and inhomogeneous shapes probably due to the formation of bubbles and holes by degassing of the resist during ion etching. This has been shown to lead to inhomogeneous and distorted flanks of the mask [255–258]. Also, the PMMA layers appeared to be very difficult to remove after ion beam etching. We assume that the incident ions induce a strong crosslink of the resist resulting in harder dissolution in solvants [252, 259]. We tested different removing processes such as long time ultrasonic baths in $40°C$ aceton. Even specially dedicated removers for highly crosslinked resists such as PG remover [260] and SVC-14 [261], its non-toxic alternative, combined with ultrasonic baths were not efficient to fully remove the PMMA. Only mechanical friction (with Q tips cleanroom swabs) allowed to remove most of the resist but it damages the surface of the Co_2MnSi thin film.

As a consequence, we had to find another resist to make our antidot lattices. We chose the mr-PosEBR resist during the second year of my PhD. It is an acrylate-based resist highly sensitive to electrons and suitable for etching applications due to its high resistance to dry etching. This resist was never used in our laboratory and we had to develop all the recipes including optimal thickness, baking temperature and time, dose factors, electron current and energy for e-beam lithography, development time, ion milling parameters... Even if it is time-consuming, all these steps were mandatory to achieve our goal. The main parameters are presented in Table 4.3. Due to the limited number of Co_2MnSi thin films at our disposal, many tests were performed on permalloy layers that we had or on Ti/Au layers deposited on Si/SiO_2 substrates with an e-beam evaporator at the CEMES.

The main problem we encountered was related to proximity effects, which induce a volume around the resist pattern where the resistance to ion etching is lowered with respect to the "bulk" parts of the resist. Preliminary tests performed with a 150 nm thick layer (mr-PosEBR 0.1, process conditions of first column of Table 4.3) showed that after development in mr-Dev800 and prior to etching, the sidewalls of the resist seemed vertical. But after etching, a very marked bowl shape appeared. A

	Process conditions 1	**Process conditions 2**	**Process conditions 3**
Resists	mr-PosEBR 0.1	mr-PosEBR 0.3	mr-PosEBR 0.3
Spin coater speed [rpm]	1500	4000	4000
Resist thickness [nm]	≈ 150	≈ 330	≈ 330
Prebake temperature [°C]	150	150	150
Prebake time [min]	2	1	1
EHT [kV]	20	20	30
Current [pA]	40	40	40
Focus on close marks	No	Yes	Yes
Area Dose [$\mu C.\mathrm{cm}^{-2}$]	75	224	224
Developer	mr-Dev800 (amyl acetate)	mr-Dev800 (amyl acetate)	mr-Dev800 (amyl acetate)
Development time [s]	60	60	60
IBE high voltage [V]	1000	1000	1000
IBE pressure [mbar]	$\approx 3.3.10^{-3}$	$\approx 3.3.10^{-3}$	$\approx 3.3.10^{-3}$
IBE current [mA]	14	14	14
Etching time [min]	7	8	8
Remover	ultrasonic bath SVC-14 45°	ultrasonic bath SVC-14 45°	ultrasonic bath SVC-14 45°

Table 4.3: Table of the main parameters of three processing recipes used to fabricate magnetic antidot lattices in a 45 to 50 nm thick CMS thin films.

typical example is shown in Figure 4.14 a). These SEM images have been obtained for a NiFe thin film, however similar shapes were obtained in CMS thin films.

To compensate the fast erosion of the resist, we chose to work with the mr-PosEBR 0.3 which gives a 330 nm thickness when spin coated at (4000 rpm). The thicker the resist, the longer it will stand until the thin film underneath is completely etched. However working with thicker resists is at the expense of resolution, and small patterns (typically around 100 nm) may be more difficult to achieve. Figures 4.14 b) and c) show typical results obtained with this resist and with the process conditions 2 and 3 detailed in the second and third column of Table 4.3 respectively. The difference between the two is the energy of the electron beam during lithography. 20 kV is the "classical" acceleration voltage used by others in our laboratory for processing PMMA. 30 kV is the maximum voltage that can be reached in our equipment.

General considerations can be given from these SEM images recorded on antidot squares with nominal dimensions 300 nm and edge-to-edge spacing 900 nm. Let's note that before the lithography, the focus and astigmatism were fine-tuned close to the antidot lattice zone on metallic marks. SEM images recorded after development in mr-Dev800 and before ion etching show that the squares opened in the resist have dimensions closer to the expected ones when increasing the high voltage. Also, we clearly observe for both voltages a bright halo around the holes that we attribute to the extent of the main proximity effects. Even if these bright parts have not been developed, the change of contrast compared to the furthest resist parts indicate a modification of the resist properties. After etching, this halo is imprinted in the underneath CMS for a voltage of 20 kV. This can be seen as a clear bowl shape either in the SEM tilted image (third line of Figure 4.14 b)) or in the cross-section image obtained by FIB etching across the hole (fourth line of Figure 4.14 c)). However the situation is different when the voltage is 30 kV. Indeed it can be seen in the SEM and FIB cross-section images that the bowl shape is much less pronounced and almost vertical sidewalls were obtained in the CMS. We can also notice that the corners of the squares are less rounded for 30 kV. Nonetheless, we observed some

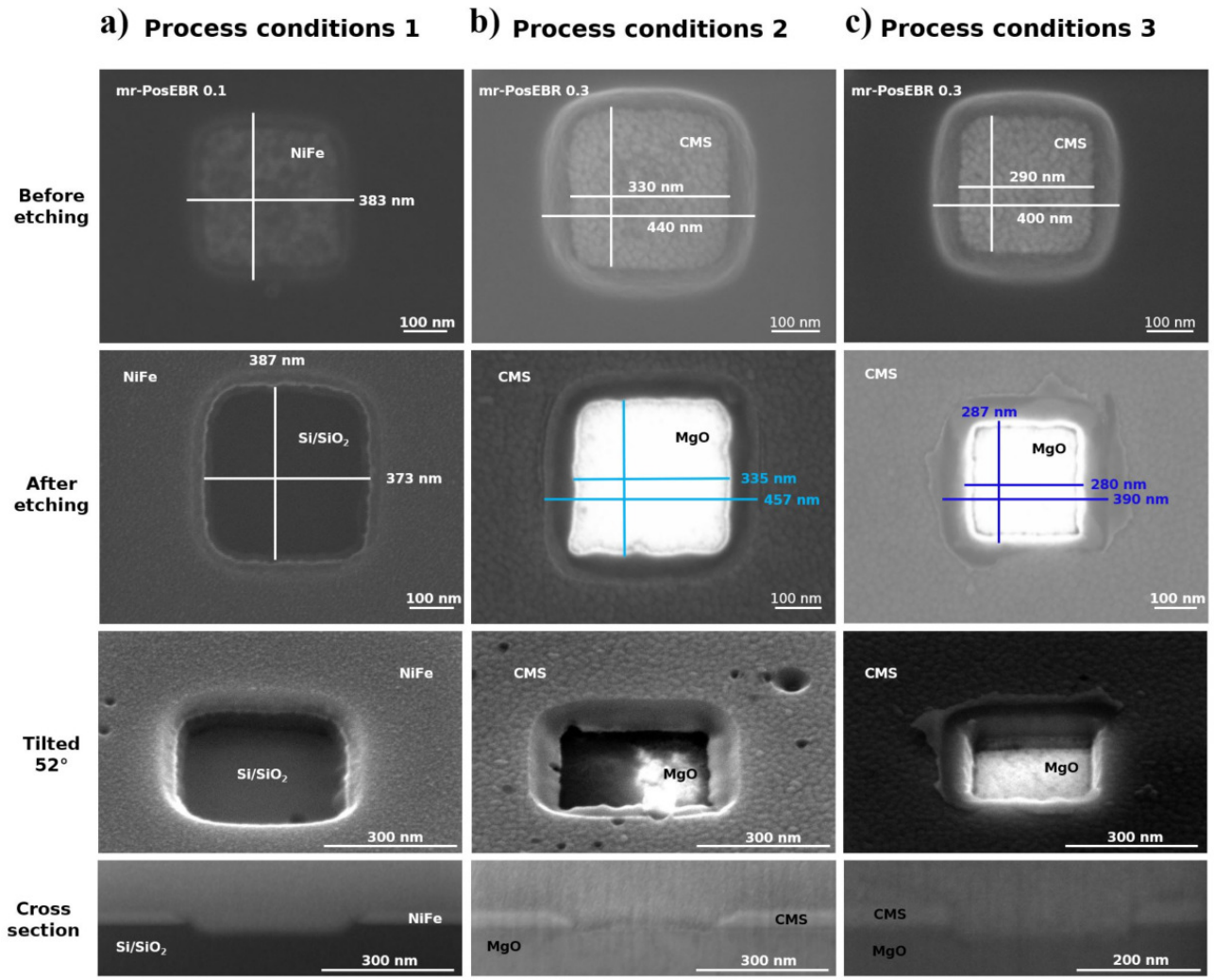

Figure 4.14: SEM images made before the etching (first row), after the etching and removal of the resist mask (second row), tilted 52° (third row) and cross-section (fourth row) of a) a NiFe-based square antidot made with the process conditions 1, b) a CMS-based square antidot made with the process conditions 2 and c) with the process conditions 3. The targeted antidot size was 300 nm. The process conditions are detailed in Table 4.3.

irregular forms at the surface of the CMS that were not seen at 20 kV. These forms/residues are also inhomogeneous across the entire lattice as shown in Figure 4.15 a). Figures 4.15 b), c) and d) show a few examples of these surface residues which can be partially or totally removed after the cleaning procedure. It is not clear what is their origin. It can be redeposited CMS material or resist residues. Our assumption is that it is most probably resist residues, however we do not have a clear evidence for it. In any case it is important to observe that the squared antidots are well resolved over the entire lattice.

It is worth to mention for the reader that we have tested many parameters in order to reduce the presence of these residues at the surface of the CMS. We will not discuss them here as they did not bring noticeable improvements. Among the parameters, we tested the influence of the resist baking conditions, reducing the size of the e-beam spot to reduce proximity effects, working at different electron dose at the expense of decreasing the current intensity down to the minimum value of the equipment (20 pA). In the end, the best conditions we found to obtain squared antidots with the desired dimensions and almost vertical sidewalls are the one corresponding to the process conditions 3 in Table 4.3.

The last test presented in this section is the influence of the antidot sizes. In Figure 4.16, we show

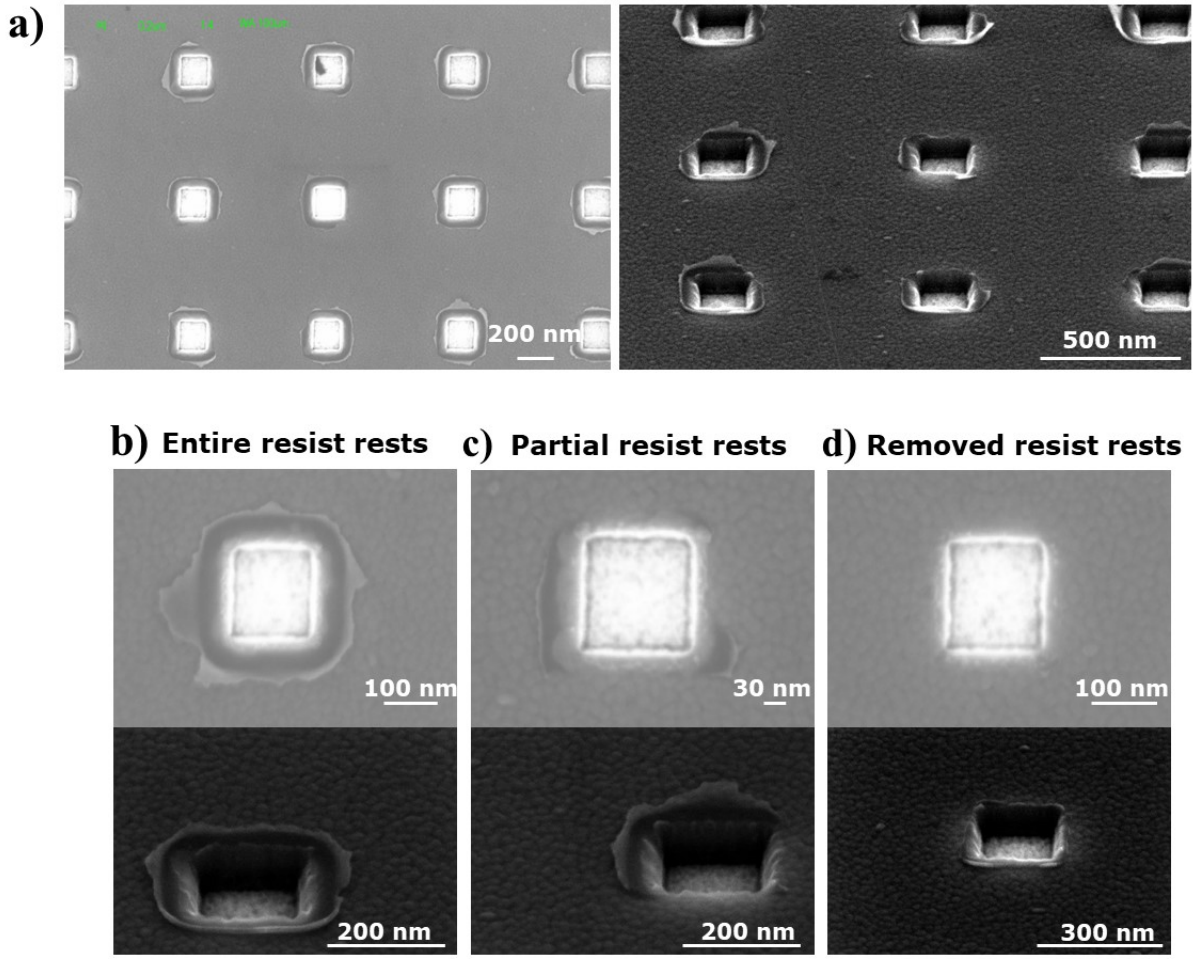

Figure 4.15: SEM images of non-tilted and tilted (52°) sample of a) several CMS-based antidots (lateral size 200 nm), of a particular antidot with b) complete resist/material residues attached to it, c) with partial resist/material residues removed and d) free from resist/material residues.

SEM images of 40 μm × 40 μm squared antidot lattices with varying nominal dimensions of the antidots from 300 to 100 nm while keeping the ratio between the size and the edge-to-edge distance constant. The only difference here with the process conditions 3 discussed above is that the etching time is 7 minutes instead of 8 minutes and "harder" cleaning conditions (about 8 hours in SVC-14 heated at 70°C). In such conditions, the antidot sizes are a little smaller with respect to the expected ones and residues at the vicinity of the antidot edges seem more important when the dimensions are reduced. In the case of 100 nm squared antidots, these resist residues or redeposited materials can be clearly observed. In addition, at 100 nm, it is not clear if the entire CMS thickness has been etched properly.

To conclude, we succeeded in obtaining correct squared antidot lattices with dimensions down to 200 nm from 45 to 50 nm thick CMS thin films with the last process conditions presented above (third column of Table 4.3). The samples prepared for measurements described in chapter 6 sections 6.2 and 6.3 were made with these conditions. However there is still some room to improve the quality of the antidots without having to apply harsh cleaning conditions (ultrasonic baths). For example, correction softwares such as NanoPECS [250] could be tested to reduce proximity effects. In particular, such correction will be important in the case of close packed patterns as for example antidots with shorter spacings. This type of software calculates the energy distribution simulated by primary and scattered electrons on listed resists for a specified pattern to adapt the e-beam dose (dwelltime) distribution relatively to the position of each surrounding patterns constituting the total structure. Hence lower

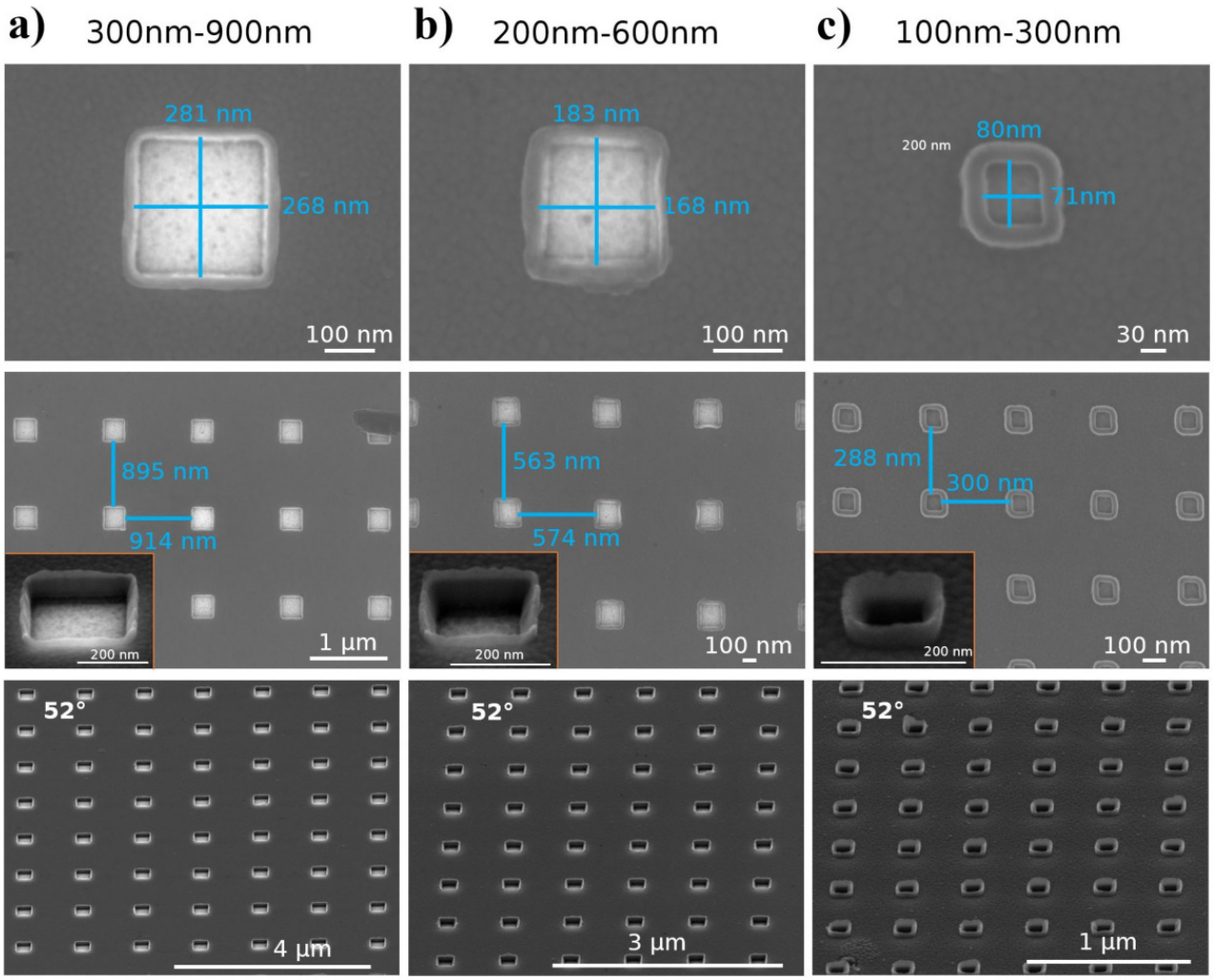

Figure 4.16: SEM images for different magnifications (first and second row) and a $52°$ tilted view (third row) of CMS-based antidot lattices of sets of square size and spacing a) 300 and 900 nm, b) 200 and 600 nm and c) 100 and 300 nm respectively. In insets are shown tilted SEM images of an antidot with corresponding size.

dose will be applied to close patterns and larger dose for isolated patterns. Also, it can adjust the dose between the center and the edge of one hole.

The lattices for FMR measurements could be extended to 80 $\mu\mathrm{m} \times 80$ $\mu\mathrm{m}$ at maximum with a 100 $\mu\mathrm{m}$ writefield used. Larger 200 $\mu\mathrm{m}$ and 400 $\mu\mathrm{m}$ writefields were tested, however the squares presented irregularities and were less well-defined. Larger writefields entail a larger minimum pixel step size and consequently a loss in resolution leading to inhomogeneous patterns [243]. The best solution for making large lattices would be using a field stitching strategy. Field stitching consists in using multiple small writefields displaced by stage movement to expose the patterns over large areas. Such procedure needs an extremely accurate displacement control of the stage, which can only be performed with a SEM equipped with laser-interferometer stage control.

Finally, we wanted to mention to the reader that at the end of the thesis, the production of the mr-PosEBR resist series was stopped by the manufacturer. To replace this resist, our procedure could be performed in principle with the AR-P 6200 (CSAR 62) e-beam resists [262] whose properties (sensitivity, etching resistance, resist preparation and developer) seem quite similar to the mr-PosEBR resist.

4.3 Complete magnonic crystal devices

In this part we present all the micro and nanofabrication steps allowing to obtain the samples measured during this thesis. We studied a magnonic crystal prepared by FIB (sample #1) and another prepared by e-beam lithography and IBE (sample #2). Our objective for these two samples was first to characterize their spin wave modes. For this, we placed above the crystals a micro-antenna whose width is several microns in order to be in conditions close to uniform excitation. Also for the sample prepared by e-beam lithography and IBE (sample #2), we deposited electrical contacts by lift-off since we wanted to be able to inject a DC current into the magnonic crystal and observe its effect on the spin waves spectrum. Finally, we prepared several magnonic crystals on a CMS thin film of $10 \times 10\ \mathrm{mm}^2$ in order to perform measurements of the spin waves spectrum and wave propagation by Brillouin Light Scattering (sample #3). Let's note that the CMS thin films used for the samples #2 and #3 are two individual parts of dimensions $10 \times 10\ \mathrm{mm}^2$ originating from a larger CMS thin film sample of $20 \times 20\ \mathrm{mm}^2$.

Each sample required different micro and nanofabrication steps which will be presented individually for each of them. However, the methods and equipments employed are similar and briefly described below:

1) Laser Lithography: we used a Dilase 650 from Kloe. Laser lithography is equivalent to e-beam lithography except that this time we use an optical microscope equipped with a laser. This one scans the surface of the sample and draws a pattern by exposing a UV photosensitive resist AZ-5214 (positive resist) about $1\ \mu\mathrm{m}$ thick. The pattern is then revealed by developing the resist in the MF-319 developer from Microposit. The parameters of spin coating and prebake used were 4000 rpm and $105°\mathrm{C}$ respectively.

2) Ti/Au or Ti/Cu/Au metallic deposits by lift-off: these deposits are made in a dedicated Joule heating chamber equipped with an electron gun in the CEMES clean room facility. The chamber is equipped with 4 crucibles which allow the deposition of multilayers. The deposits are made at room temperature and the sample is placed about $15\ \mathrm{cm}$ from the crucibles on a rotating sample holder cooled with water. The speeds and thicknesses of deposits are controlled by a quartz crystal microbalance near the sample holder. Deposition rates are of the order of a few $\mathrm{Å\,s}^{-1}$ for each material.

3) Deposits of dielectric layers: they are made in a dedicated sputtering chamber in the CEMES clean room facility. A Si_3N_4 target is placed at the cathode and the material is deposited in RF mode. The sample is placed about $15\ \mathrm{cm}$ above. The deposition rate is of the order of 1 to $2\ \mathrm{nm\,min}^{-1}$.

4.3.1 FIB etched Co_2MnSi magnonic crystal device

For the sample #1, a $47\ \mu\mathrm{m} \times 47\ \mu\mathrm{m}$ squared antidot lattice was made by FIB in a $50\ \mathrm{nm}$ thick CMS thin film with the method presented in section 4.2.2.2 and parameters given in Table 4.2. The sides of the squared lattice were aligned with the two magnetic easy axes of the CMS thin film. The nominal dimension of the squares is $100\ \mathrm{nm}$ and the edge-to-edge distance $300\ \mathrm{nm}$. SEM images are shown in Figure 4.17 a), b) and c). As shown in section 4.2.2.2, we recover the brighter ring around the antidots according to the bowl shape. This one is indeed clearly observed either in the tilted SEM image (Figure 4.17 c)) or in the cross-section shown in Figure 4.17 d) of a similar antidot lattice performed in the exact same conditions on another piece of CMS thin film.

From the Figures 4.17 a), b) and c), we can observe the complex geometry of the holes. While

the geometry seems to be quite well squared at the bottom of the antidots (Figure 4.17 a)), it appears rather circular at the top surface (Figure 4.17 b)). In addition the diameter of the etched area is clearly larger at the top surface than at the bottom of the antidots, as confirmed with the cross-section showing also the bowl profile of the sidewalls. The antidots size at the bottom is approximately 140 ± 10 nm while it is 200 ± 20 nm at the top. These values are similar for both the measured sample and the one for the cross-section prepared in the exact same conditions (Figure 4.17 d)). The center-to-center distance between two antidots corresponds to the targeted periodicity (400 nm).

The antidot lattice was then completed by additional microstructuration processes to make a

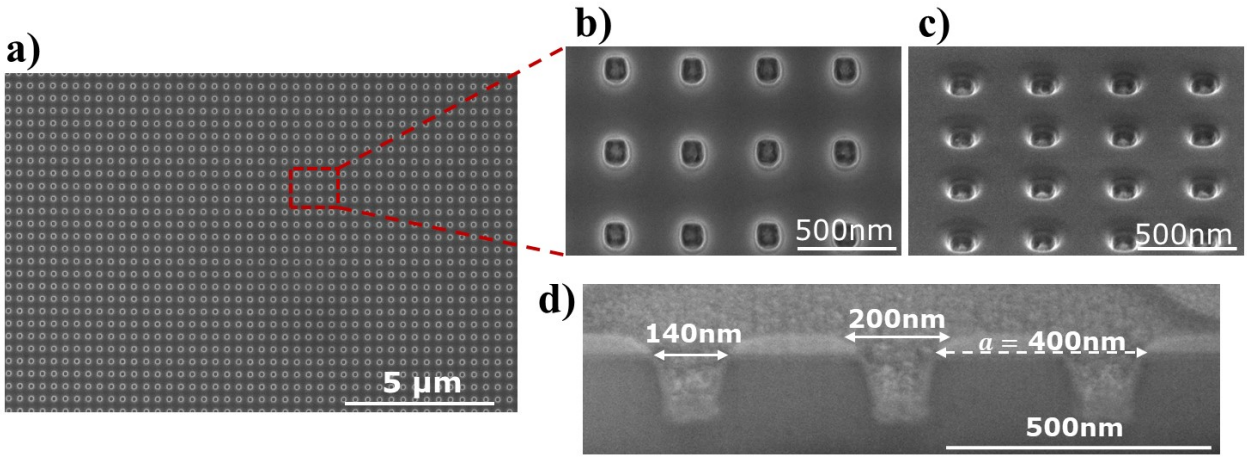

Figure 4.17: SEM images of the FIB etched CMS squared antidot lattice (sample #1) (47 μm $\times$ 47 μm) of size 140 nm and spacing 260 nm: a) top view at a large magnification, b) zoomed top view, c) zoomed tilted view at 52° and d) cross-section view.

measurable device with a micro-antenna. The measurements and analysis are tackled in chapter 6 section 6.1. First, the antidot lattice had to be isolated from the rest of the CMS film. For this, we performed an excavation all around the antidot lattice by laser lithography and IBE. The antidot lattice was protected by a layer of AZ-5214 resist. After removal of the resist, a 200 nm thick Si_3N_4 passivation layer was deposited by laser lithography and lift-off on the excavation and magnonic crystal areas. Finally, a large micro-antenna is patterned onto the Si_3N_4 to measure the microwave response of the crystal. The antenna is made by laser lithography and lift-off of Ti_{10nm} (stitching layer) and Au_{150nm}. It is placed in the middle of the crystal and its long axis is parallel with the edge of the crystal. The passivation layer allows to isolate electrically the magnonic crystal from the antenna. As shown in Figure 4.18 the antenna consists of a portion of coplanar waveguide in Ground-Signal-Ground configuration. The waveguide is ended with a short load in order to maximize the amplitude of the microwave current in the central conductor, and thus the microwave pumping field. The widths of the central and outer conductors are respectively $w_{in} = 30$ μm and $w_{out} = 15$ μm. The gap between the conductors is $g = 10$ μm. The central conductor does not cover the entire surface of the magnonic crystal as we wanted to avoid probing the dynamic magnetic states on the lateral edges of the magnonic crystal. Indeed, we will show in chapter 5 section 5.2.2 that the finite size of the sample leads to magnetic inhomogeneities at low magnetic fields on the very first antidots columns with frequencies slightly different from the central part of the magnonic crystal.

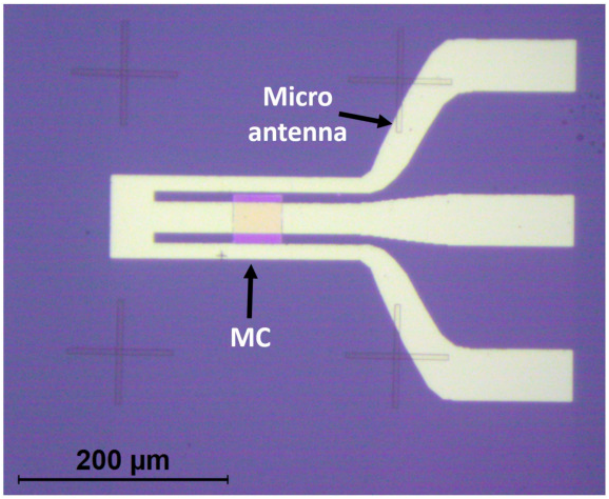

Figure 4.18: Optical image of the micro-antenna on top of the FIB etched CMS-based antidot lattice (sample #1).

4.3.2 Combined e-beam lithography and ion beam etching Co_2MnSi magnonic crystal devices

Two kinds of samples were processed by e-beam lithography and IBE etching. The first one (sample #2) was dedicated to FMR measurements at the CEMES with the objective to observe reconfigurable spin wave modes at remanence. The second sample (sample #3) is made of several magnonic crystals with different dimensions. The micro-antennas were designed for Brillouin Light Scattering experiments performed at the University of Perugia in the group of Professor S. Tacchi.

4.3.2.1 Device for FMR measurements

The sample #2 consists in a $70\ \mu\mathrm{m} \times 70\ \mu\mathrm{m}$ squared CMS antidot lattice with nominal antidot lateral dimensions of $200\ \mathrm{nm}$ and edge-to-edge distance of $600\ \mathrm{nm}$. The sample was realized with the process conditions 3 detailed in Table 4.3. Before patterning the magnonic crystal, large ($40\ \mu\mathrm{m}$) and small $5\ \mu\mathrm{m}$ L-shape marks were realized by UV laser lithography and lift-off of $\mathrm{Ti}_{5\mathrm{nm}}$ and $\mathrm{Au}_{20\mathrm{nm}}$ layers. These marks allows to precisely align the edges of the magnonic crystal with those of the substrate so that they correspond to the magnetic easy axes of the CMS. The smaller marks also allow to precisely tune the focus and astigmatism of the electron beam in the area where the crystal is made.

In the SEM images of Figures 4.19 a) and b), the measured squared antidots size is $200 \pm 10\ \mathrm{nm}$ and their spacing is $600 \pm 10\ \mathrm{nm}$ on average. Unfortunately, at the end of the process, we realized that the vertical axis of the antidot lattice was not exactly perpendicular to the horizontal axis, but tilted with an angle of $1.2°$ as can be seen on the SEM image in Figure 4.19 b). Such problem had not been observed on the other antidot lattices made during the previous tests. This issue actually results from the electronic alignment on the four small marks surrounding the antidot lattice, which themselves appeared to be slightly shifted between them. This is probably due to stage drift during the UV lithography of the L marks or unprecise calibration of the writefield. By chance, we will show in chapter 6 section 6.2 that this seemed to have almost negligible effect on the measured spin waves spectrum.

To isolate the magnetic antidot lattice from the rest of the CMS thin film, e-beam lithography with the mr-PosEBR 0.3 resist and ion beam etching have been used to create a large excavation area

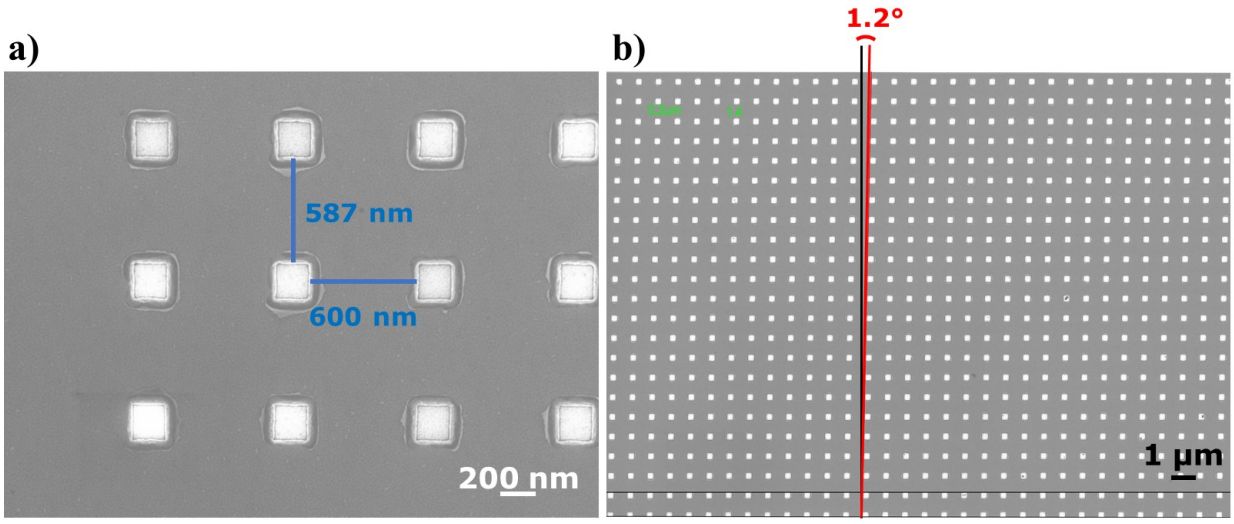

Figure 4.19: SEM images of a) the CMS antidot lattice made by e-beam lithography and Ar^+ ion beam etching (sample #2), b) the same structure at a larger magnification where the non orthogonality of the antidot lattice axes can be seen.

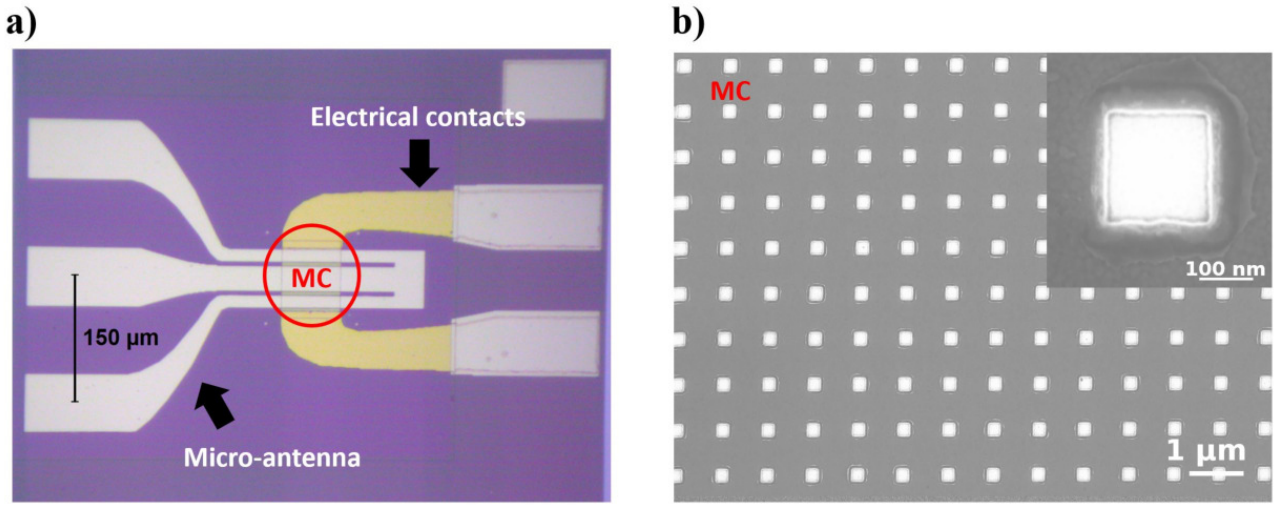

Figure 4.20: a) Optical image of the CMS-based magnonic crystal device made by e-beam lithography and Ar^+ ion beam etching (sample #2). b) SEM image of a part of the CMS antidot lattice with square antidots size 200 nm and spacing 600 nm. In the inset, a SEM image of an antidot at a large magnification.

extended over 300 μm from the borders of the crystal. E-beam lithography with an electronic alignment according to the small L-marks was used instead of UV lithography in order to have a precise placement of the excavation area around the antidot lattice (minimum 500 nm of precision required). Then, a Si_3N_4 passivation layer with a thickness of about 50 nm was deposited to compensate the milling of the excavation. Electrical contacts were then deposited by UV lithography and lift-off of $Ti_{10nm}\backslash Cu_{200nm} \backslash Au_{30nm}$. These contacts were made to study the possible variations of the FMR response of the magnonic crystal with an injected electrical current. Let's note that these contacts cover a 12 μm length of unpatterned CMS film on each connected side.

Finally, UV lithography and lift-off were performed to cover the electrical contacts (except the pads) and the crystal with an insulating Si_3N_4 layer and a micro-antenna made of $Ti_{10nm}\backslash Cu_{200nm} \backslash Au_{30nm}$. The use of Cu instead of Au as the main conductor layer allows a smaller impedance of the micro-antenna. Indeed, the resistivity of copper is lower than the one of gold for polycrystalline layers deposited by Joule heating at the CEMES. The final device is shown in Figure 4.20 a). Similarly to the sample #1, it is a shorted portion of coplanar waveguide. The widths of the inner and

outer conductors are 30 μm and 15 μm respectively and the gap is 5 μm. Contrary to the sample #1, here the entire antenna (with the ground conductors included) covers the magnonic crystal but stays in-between the electrical contacts. We chose such geometry in order to reduce as much as possible a direct inductive and capacitive coupling of the antenna with the electrical contacts and to avoid probing the FMR response of the unpatterned CMS parts on both sides of the crystal. In the end, this device required 7 micro and nanopatterning steps.

4.3.2.2 Devices for Brillouin Light Scattering measurements

At the end of the thesis, a device (sample #3) with 6 magnonic crystals and micro-antennas were made for Brillouin Light Scattering (BLS) measurements as part of a collaboration with Dr. Silvia Tacchi, researcher of the Perugia Institute Officina dei Materiali (IOM) of the National Research Counsil (CNR). Dr. Silvia Tacchi and her colleagues are currently conducting the BLS experiments on this sample. All crystals correspond to 80 μm $\times$ 80 μm squared antidot lattices with nominal antidots size 200 nm and varied edge-to-edge spacings 400 nm, 600 nm and 800 nm. Each crystal has been doubled. In addition, we added an area with an unpatterned CMS thin film with a micro-antenna covering it. A last magnonic crystal of antidots size 200 nm and spacing 800 nm having a micro-antenna rotated by 90° was also added. Optical images of one of the different zones are shown in Figure 4.21.

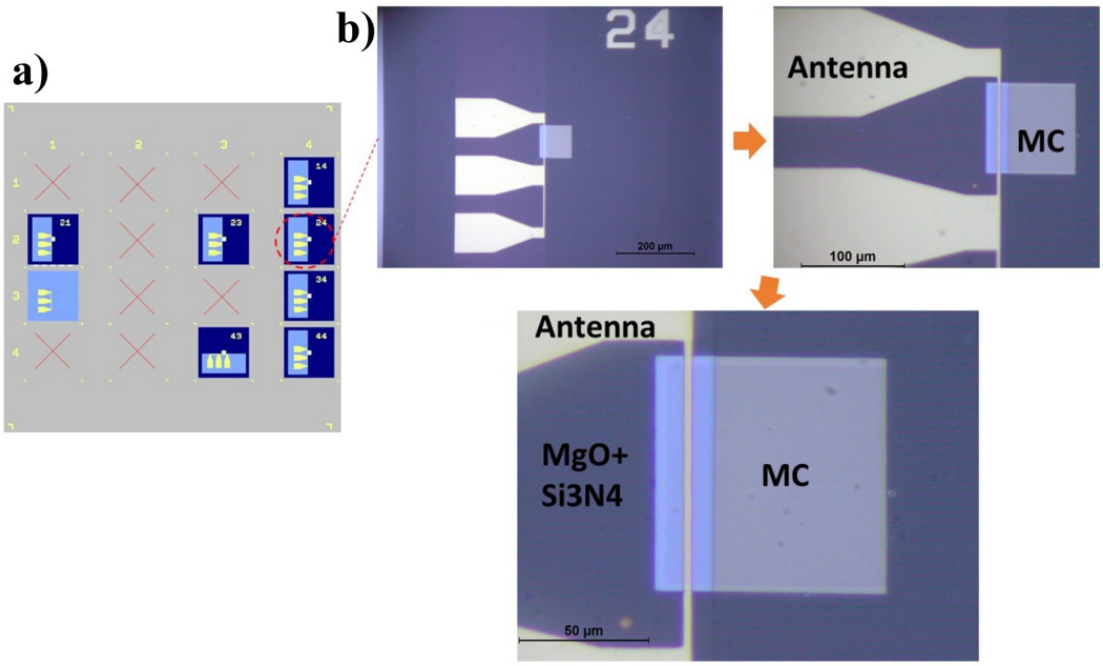

Figure 4.21: a) Schematic of the sample containing the different CMS-based antidot lattices (magnonic crystals (MC)) devices for BLS measurements (sample #3). b) Different zoomed optical microscope images of one of the devices.

Even if the micro and nanostructuration processes are identical to those used for the sample #2, there are several differences. First, the shape and resolution of the antidots were not as good as the other samples. As already mentioned, we realized this sample at the end of the PhD work, when our mr-PosEBR resist and remover were expired. Consequently, we had to adjust and optimize our experimental parameters in order to obtain antidots with correct dimensions. SEM images of the patterns are shown in Figure 4.22 a), b) and c). The averaged dimensions and spacings of the antidots are respectively 205 $\pm$ 10 nm and 780 $\pm$ 10 nm (Figure 4.22 a)), 215 $\pm$ 10 nm and 575 $\pm$ 10 nm

(Figure 4.22 b)), and 220 ± 10 nm and 380 ± 10 nm (Figure 4.22 c)). It also seems that the closer the antidots are brought, the larger they become. This may be due to close proximity effects arising during the e-beam exposure of the resist. In addition, the non orthogonality of the antidot lattice axes was corrected for these devices.

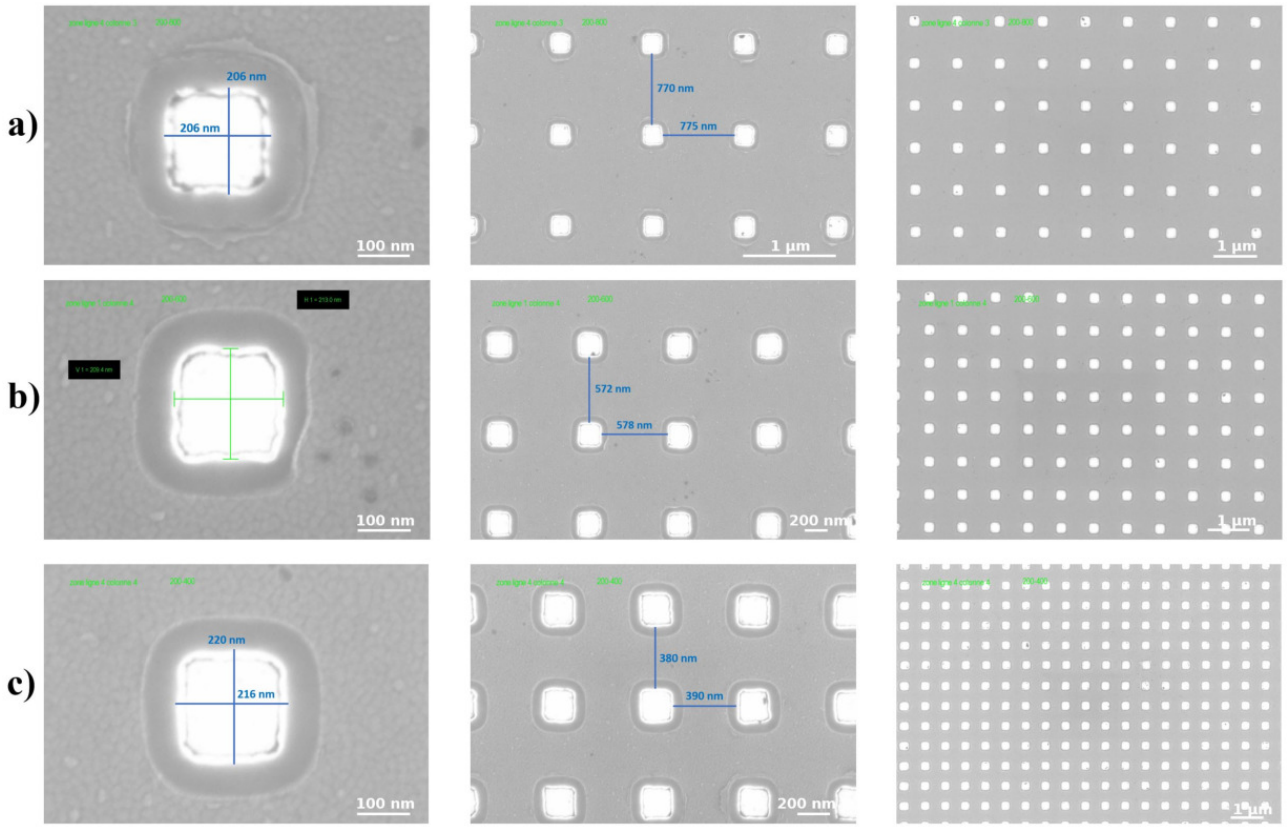

Figure 4.22: SEM images at different magnifications of CMS antidot lattices of sample #3 with square sizes and spacings of respectively a) 200 nm-800 nm, b) 200 nm-600 nm and c) 200 nm-400 nm.

Another difference with the sample #2 is that the excavation area around the lattice have been done by UV lithography at the expense of alignment precision. This is because making e-beam lithography of such areas for the 7 crystals was too long to be achieved in one day. Each etched area extends over 400 μm from the borders of the antidot lattice. Then, the Si_3N_4 insulating layer is deposited in two steps. In a first step, we deposit a 50 nm thick layer on each crystal in order to cover the MgO substrate. This one is known to trap impurities (carbon, H_2O...) present in the air, which could disrupt the BLS measurements. At the same time, this layer had to be thin enough to limit losses in the BLS measurements. In a second step, an additional Si_3N_4 layer was lifted-off only over a small area of the crystal, where a $Ti_{10nm}\backslash Cu_{200nm}\backslash Au_{30nm}$ micro-antenna was then made. This additional insulating layer ensures to avoid electrical discharges between the antenna and the crystal. A schematic cross-section of the final device is shown in Figure 4.23 a). For the BLS experiments, the shape of the antenna is different from the one of the samples for FMR measurements. Here, the spin waves are excited by one part of the short load at the end of the coplanar waveguide as shown in Figure 4.21 d). This line exciting the spin waves is 2.5 μm wide.

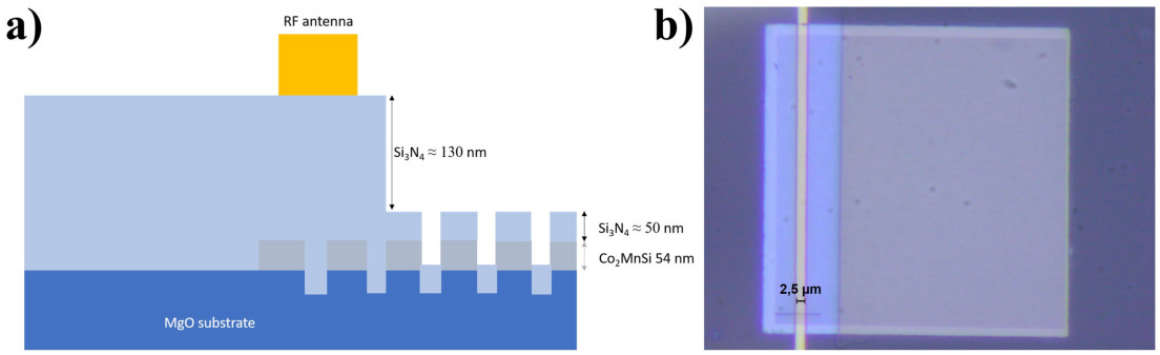

Figure 4.23: a) Schematic cross-section of a device of sample #3. b) Corresponding top view optical image showing the part of the micro-antenna on top of the magnonic crystal allowing to excite spin waves.

Chapter 5

Reconfigurable dynamic states in Co_2MnSi Heusler magnonic crystals at remanence

As approached in chapter 2, we propose to use CMS Heusler-based magnonic crystals for the development of reconfigurable microwave operations at remanence. Magnetic antidot lattices were chosen for this task and in this chapter we prove numerically the possibility to achieve an ON/OFF switching of several spin wave modes in a device operating with zero bias field. The results presented in this chapter were published in Ref. [263].

5.1 Numerical study of Co_2MnSi magnetic antidot lattices

5.1.1 Numerical procedure

Micromagnetic simulations were performed with MuMax3 [191] for the calculation of the remanent states of CMS magnetic antidot lattices and their microwave responses. We used 2D periodic boundary conditions (PBC) in order to simulate an infinite magnonic crystal while reducing the size of the simulated system. Indeed we simulated the magnetic states of only one unit cell of the magnonic crystal composed of four squared antidots arranged in a square lattice as shown in Figure 5.1. The size of the antidots and their spacing from one edge to the other are respectively s and d. The finite lateral sizes of the unit cell are thus $2s + 2d$. The square lattice symmetry axes are oriented along the x and y axes.

The CMS magnetic parameters used for the simulations are the saturation magnetization $M_s = 1003.10^3\ \mathrm{A\,m^{-1}}$, the exchange constant $A = 18.10^{-12}\ \mathrm{J\,m^{-1}}$, the cubic magnetocrystalline anisotropy constant $K_{c1} = -17.10^3\ \mathrm{Jm^{-3}}$ which corresponds to a cubic anisotropy field $\mu_0 H_k \approx 35\ \mathrm{mT}$, and the gyromagnetic ratio $\gamma = 29\ \mathrm{GHz\,T^{-1}}$. Those values are similar to the ones obtained experimentally in previous experiments performed by our research group [53]. The direction of the crystalline anisotropy axes are along the diagonals of the unit cell. As K_{c1} is negative, the magnetic easy axes are along the x and y directions. The unit cell is discretized with cubic cells of dimension $5 \times 5 \times 5\ \mathrm{nm^3}$, which is below the calculated exchange length $\Lambda_{ex} = \sqrt{2A/\mu_0 M_s^2} \approx 5.4\ \mathrm{nm}$. The damping coefficient was set to 1.10^{-3}, which is in accordance with our previous findings [53] and recent reported values in the literature [64, 65, 264]. The film thickness is $20\ \mathrm{nm}$, which is thin enough to consider a uniform magnetization along the thickness.

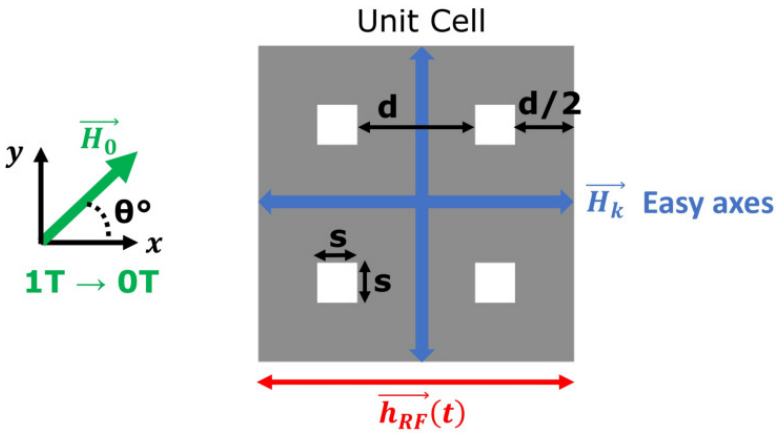

Figure 5.1: Schematic representation of the simulated unit cell of the Co_2MnSi magnetic antidot lattice. s and d are respectively the antidots size and spacing, $\vec{H}_k$ is the cubic crystal anisotropy field, $\vec{H}_0$ the applied initialization magnetic field and $\vec{h}_{RF}$ the microwave pumping field.

Simulations of the static remanent states

In order to obtain the dynamic spin wave modes, the first step consists in calculating the equilibrium remanent states (i.e. when no magnetic field is applied, $\mu_0 H_0 = 0$ mT). We applied the method described in section 3.1.2. For the simulation, we begin with a random orientation of the magnetization, then an initialization magnetic field $\mu_0 H_0$ of 1 T is applied to saturate the magnetization $\vec{M}$. $\vec{H}_0$ forms an angle θ with respect to the x axis, as shown in Figure 5.1. To avoid the calculation of metastable remanent states arising from the cubic symmetry of the discretization cells, the magnetic field is deliberately misaligned with an angle of 1° with respect to the x or y directions. Once the system has been relaxed at 1 T, the amplitude of $\vec{H}_0$ is progressively decreased down to zero with field steps of 0.01 T. At each step, the energy of the magnetic system is minimized. The calculated remanent states constitute the starting point for the calculation of the dynamic modes.

Dynamic simulations

To determine the different spin wave modes that can be excited with a uniform microwave excitation in the CMS magnetic antidot lattice, we applied the method described in section 3.1.3. A uniform magnetic field pulse along the x axis of the magnetic system is applied, which is analog to FMR experiments. The pulse has a sinc form with $\mu_0 h_p = 1$ mT the amplitude of the pumping field, which is low enough to ensure a linear regime of precession for the magnetization, $f_c = 30$ GHz the cutoff frequency and $t_{wait} = 20.48$ ns the waiting time before the triggering of the sinc pulse. The calculated magnetization values at each cell $\vec{M}(t, x, y, z)$ are recorded with a sampling period of 10 ps, which corresponds to a a Nyquist frequency of 50 GHz (half of the sampling frequency), above the cutoff excitation frequency. 4096 temporal magnetization files are recorded in addition to the values of the dynamic $m_x(t)$, $m_y(t)$ and $m_z(t)$ components averaged over all (x, y) cells in the $z = 20$ nm top plane. The spin wave modes frequencies are then obtained from a Fast Fourier Transform (FFT) of the averaged $m_z(t)$ component.

The spatial profile of each spin wave mode is obtained by applying first a FFT on the temporal $m_x(x, y, t)$ component of each individual cell followed by an inverse FFT (IFFT) at the frequency of interest. Let's note that the remanent magnetic state is subtracted first to each temporal file in order to only have the dynamic evolution of the magnetization in each cell $m_x(x, y, t)$. The IFFT leads to a series of 4096 temporal files showing the temporal evolution of the m_x component in each cells at the spin wave mode frequency. The spatial profiles shown in Figures 5.3 to 5.6 correspond to temporal snapshots at the time for which the maximum of precession amplitude in the central cell is reached.

Search for reconfigurable remanent states

In order to have a device for which one can select different microwave absorption spectra at zero field, we first performed numerous micromagnetic simulations by varying the size of the antidots and their spacing. As stated in chapter 2, we were looking for clearly distinct remanent equilibrium states when applying a magnetic field either in the x or y direction. This is required to obtain very different microwave responses of the device to a uniform microwave field (applied along x for example), which is the basics of reconfigurable operations. Also, we were looking for remanent states with the most uniform magnetic configuration as possible around the antidots as will be discussed below. We wanted to keep the distance between the holes as small as possible in order to keep frequency band gaps as large as possible. Finally, we also tend to focus our attention on antidot size reasonably achievable by standard nanostructuration techniques as discussed in chapter 4. For the microwave response, we focused on spatially uniform stimulus because we aim at realizing a device whose dimensions are much smaller than the wavelength of microwave in vacuum. For example, the wavelength at 10 GHz in vacuum is 3 cm. Then a device with dimensions of about 100 μm will sense roughly a uniform microwave field.

To achieve these goals, we applied the following method. We started with a specific antidots size s and antidots spacing d. We calculated the remanent states after the initialization field is applied in the x and y directions, and the corresponding spin waves spectra. As long as the difference between the two FFT spectra was not clear (at least -10 dB attenuation for at least two spin wave modes from one configuration to the other), the antidots spacing d was varied and the procedure was executed again until our criteria were met. In a second step, the antidots size was varied while keeping the ratio s/d constant. Following this procedure, we considered that optimized reconfigurable remanent states were obtained for an aspect ratio $s/d \leq 1/3$, and it will be demonstrated later in section 5.1.3.

5.1.2 Microwave responses of different remanent states

Stabilization of different remanent states

We first present the results obtained for a magnonic crystal with antidots size $s = 300$ nm and spacing $d = 900$ nm. In figure 5.2 a), four simulated remanent states were obtained according to the direction of the initialization field $\vec{H}_0$ with respect to the one of the x axis, with θ the corresponding angle between these two directions. The antidot lattice symmetry axes are here aligned with the cubic magnetic easy axes, indicated by $\vec{H}_k$. Among these four remanent states, the configurations A1 ($\theta = 0°$) and A4 ($\theta = 90°$) present a quasi-uniform magnetization aligned along the direction of the initialization field $\vec{H}_0$, i.e. along x or y respectively. These remanent states mostly resemble to saturated states, except that very small magnetic domains appear close to the antidots edges, that we refer as edge domains. The configurations A1 and A4 are stabilized for $0° \leq \theta \leq 40°$ and $50° \leq \theta \leq 90°$ respectively.

In the range $40° \leq \theta \leq 50°$, magnetic domains form in the diagonal joining two antidots. In these domains, referred below to as $45°$ domains, the magnetization is mainly oriented along the diagonal of the unit cell, i.e. along the magnetic hard axis. By applying $\vec{H}_0$ below or above $45°$, the remanent A2 or A3 configurations can be obtained respectively as they differ only by the orientation of the magnetic moments between the $45°$ domains either along x or y.

The A1 to A4 configurations result from the competition between the demagnetizing field induced by the presence of the antidots (shape anisotropy), the intrinsic cubic crystalline anisotropy of the CMS, the exchange interaction and the applied initialization field $\vec{H}_0$. The symmetry of the square antidot lattice induces an in-plane four-fold shape anisotropy. The latter favours an alignment of the magnetization along the diagonal directions of the lattice (crystal hard axes) while the alignment along

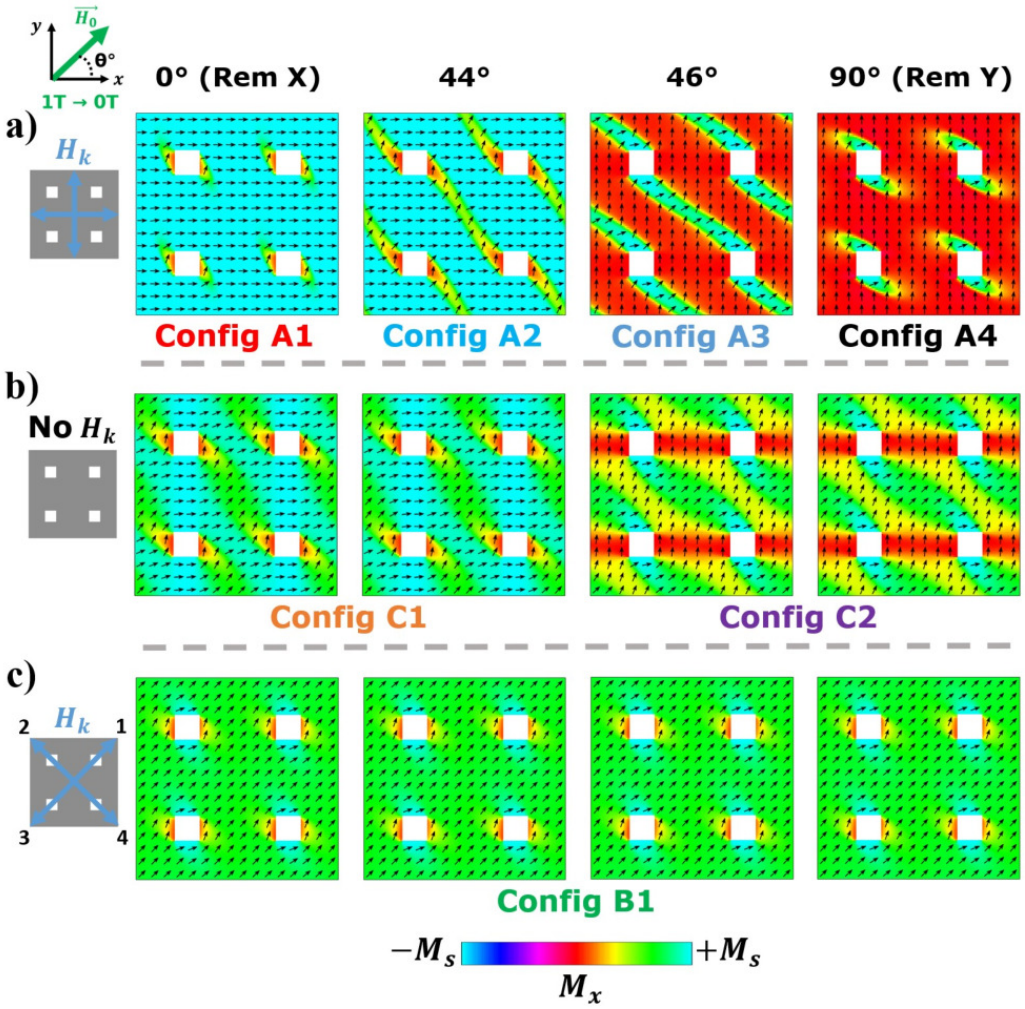

Figure 5.2: Simulated remanent states in Co_2MnSi magnetic antidot lattices with $s = 300$ nm and $d = 900$ nm as a function of the angle θ between the applied initialization field $\vec{H}_0$ and the x axis in the case of a) the cubic anisotropy axes aligned along the antidot lattice symmetry axes, b) with no cubic anisotropy ($H_k = 0$), and c) the cubic anisotropy axes rotated by $45°$ with respect to the antidot lattice symmetry axes. The remanent states are color coded with respect to the value of the x-component of the magnetization M_x, ranging from $-M_s$ when M_x is oriented along the $-x$ direction to M_s when M_x is oriented along the x direction.

the next nearest antidots (x or y, crystal easy axes) is less favorable, in particular very close to the antidot edges where the demagnetizing field is very strong [162, 265, 266]. In the case of the A1 and A4 configurations, the amplitude of the intrinsic cubic anisotropy of the CMS and the direction of $\vec{H}_0$ allow to overcome the four-fold anisotropy induced by the artificial lattice. This leads to a quasi-uniform magnetization along the axes x (A1 configuration) or y (A4 configuration). In the case of the A2 and A3 configurations, the direction of the initialization field stabilizes the magnetization along a direction close to the magnetic hard axis. When $\mu_0 H_0$ is decreased down to about 8 mT, the $45°$ domains start to appear while the rest of the magnetization between the antidots rotates either in the x (A2 configuration) or y (A3 configuration) directions owing to the strong intrinsic cubic anisotropy. However, the $45°$ domains remain down to $\mu_0 H_0 = 0$ mT as they are stabilized by the four-fold shape anisotropy induced by the antidot lattice. The A2 and A3 states are metastable due to the presence of the $45°$ domains. Indeed, some part of the magnetization is aligned along the hard axis and we have domain walls increasing the exchange energy. Thus the lowest energy remanent states are the A1 and A4 configurations. One should note that the A1 and A4 states are not sensitive to small variations of $\theta = 0°$ and $\theta = 90°$ respectively. This is also true for the A2 and A3 states but with a more restricted range. This stability of the different remanent states is of crucial importance for the design of robust

and reliable devices. They should not however be stabilized close to $40°$ and $50°$ as it is at the junction between two possible remanent states.

In order to demonstrate the interest of using a magnetic material with strong cubic anisotropy, we compared these results with the one obtained in the school case of the same CMS magnetic antidot lattice (same saturation magnetization, exchange constant, damping coefficient, gyromagnetic factor) but with no cubic crystal anisotropy ($K_{c1} = 0$ J m^{-3}). The simulated remanent states are shown in Figure 5.2 b). Two remanent states named C1 and C2 can be observed for $0° \leq \theta \leq 45°$ and $45° \leq \theta \leq 90°$ respectively. These two remanent configurations are strongly non uniform regardless of the direction of the initialization field $\vec{H}_0$. In this case, the four-fold shape anisotropy plays a major role and induces multiple domains directed in a zigzag fashion, with the antidots acting as pinning centers [49, 265].

Finally another type of configuration was studied with this time the antidot lattice rotated by $45°$ with respect to the cubic anisotropy easy axes of the CMS thin film. As can be shown in Figure 5.2 c), only one remanent state, termed as B1 is obtained. This is because the intrinsic cubic crystalline anisotropy and the four-fold anisotropy from the antidot lattice are both aligned along the diagonal directions of the antidot lattice. The major consequence is a quasi-uniform state with the magnetization aligned at about $45°$ from the x or y axis. It is to be noted that the magnetization can be aligned either along the directions 1, 2, 3 or 4 as shown in the illustration of Figure 5.2 c), depending on the direction of $\vec{H}_0$. Here we have restricted our analysis only to the quadrant $0° \leq \theta \leq 90°$.

Tunable microwave responses at remanence

When excited uniformly by a microwave excitation pulse $\vec{h}_{RF}$ along the x axis as illustrated in Figure 5.1, these different remanent magnetic states offer different microwave responses. The microwave spectra of the A1 (red curve) and A4 (black curve) configurations are shown in Figure 5.3 a). Several frequency modes can be observed up to 10 GHz and the main ones with relevant amplitude in the A4 state are indexed with numbers on the graph. The amplitude of the spin wave modes calculated from the FFT was normalized with respect to the amplitude of the mode with the highest amplitude of the A4 configuration (mode 2 here). We recall here that the amplitude of the modes in the FFT spectra corresponds to the precession amplitude of the magnetic moments averaged over all cells. Then, two parameters defined the averaged amplitude of a particular mode. First it will depend on the total magnetic volume that enters in precession at this particular frequency. Second, it will depend on the local phase of the magnetic precession. For example, a strong peak in the FFT spectra can correspond to a large magnetic volume precessing in phase with a moderate amplitude while a minor peak can correspond to areas precessing in phase opposition but with a large amplitude. The spatial profiles of the spin wave modes excited in the CMS antidot lattice in the A4 configuration are shown below the graph with snapshots of the dynamic m_x component at the indexed frequencies. As the precession amplitude of the different modes is not the same, we choose to normalize the m_x component of each mode by its own maximum amplitude for an easier visualization.

The lowest frequency spin wave mode (mode 1) corresponds to a large precession amplitude within the edge domains. Its frequency is lower than the FMR frequency of the plain CMS thin film ($f_{FMR} = 6.07$ GHz calculated with the Kittel formula (1.63)) due to the lowered local effective field arising from the local demagnetizing field nearby the antidots. This spin wave mode is reminiscent of the edge modes that can be observed in saturated magnetic antidot lattices [156] as discussed in chapter 2 section 2.1.3. Nevertheless, as compared to these, its spatial profile is asymmetric and can extend further between the antidots owing to a larger edge domain in the remanent state.

The second mode, which is the largest in amplitude in the A4 configuration, presents a large precession amplitude extending along the horizontal channels. This mode resembles to the extended mode that can be observed in saturated magnetic antidot lattices as also discussed in chapter 2 2.1.3 and to the uniform precession mode appearing in uniformly magnetized stripes [267]. We thus refer

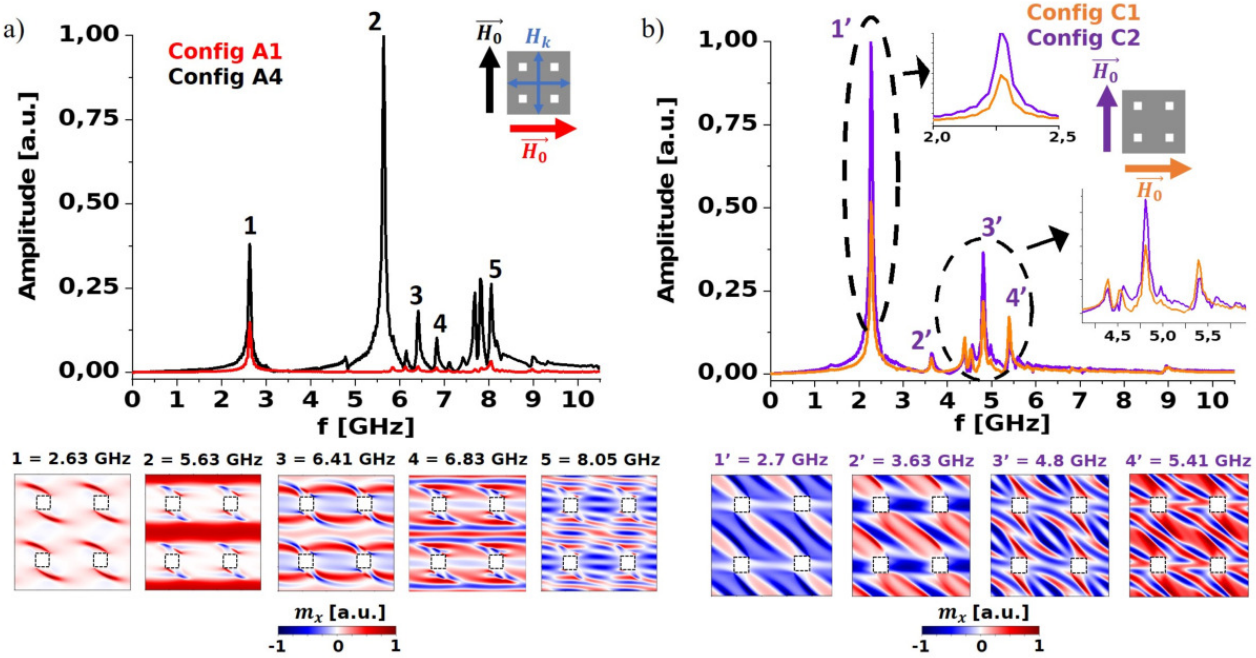

Figure 5.3: FFT amplitude spectra for the different remanent magnetic states presented in Fig. 5.2: a) in the case of a CMS magnonic crystal with cubic anisotropy axes aligned along the antidot lattice symmetry axes with the A4 (black curve) and A1 (red curve) remanent states, and b) in the case of the same magnonic crystal but with no cubic anisotropy with the C2 (orange curve) and C1 (purple curve) remanent states. Each mode with relevant amplitude are indexed with numbers. The amplitude of the spin wave modes was normalized with respect to the highest amplitude mode (mode 2 of configuration A4 in a), mode 1' of configuration C2 in b)). Below each FFT spectrum, temporal snapshots of the dynamic m_x component for specific frequency modes (of the A4 configuration in a), of the C2 configuration in b)) indexed in the FFT spectra are shown. The m_x component of each mode is normalized with respect to its own maximum amplitude for an easier visualization.

to this mode as a quasi-uniform stripe mode. However, this mode is not completely equivalent to the extended modes in saturated states as in our case a strong magnetization precession can be also observed inside the edge domains with a node in the center of the domains. Consequently, the magnetization precession extends over an effective width of about $450\ \mathrm{nm}$ which is approximately half of the antidots spacing.

The third excited spin wave mode is mainly related to the magnetic precession in the horizontal rows of antidots. Finally, the fourth and fifth modes correspond to complex quantized spin wave modes in the horizontal channels with a quantization number of 5 (5 antinodes) and of 7 (7 antinodes) along the y axis respectively. The fifth mode seems to be also quantized along the x direction.

Switching from the A4 configuration to the A1 configuration, one can observe that most of the spin wave modes are strongly attenuated. In particular the second mode is almost extinct. Such differences result from the quasi-uniform magnetization of the remanent states. In the A1 configuration, most of the magnetization is aligned along the direction of the microwave pumping field thus preventing an efficient and direct coupling to the magnetization. The latter is valid as long as the power of the microwave excitation remains low enough to not generate nonlinear processes such as Suhl instabilities [82, 83].

In FMR experiments, the microwave response of the magnetic system under test is often measured in terms of the absorbed microwave power. Thus, we chose to quantify the attenuation of the different modes as the variation of the power of the m_z dynamic component that can be calculated in dB with $20\log_{10}(m_z^{A1}/m_z^{A4})$ with m_z^{A1} (m_z^{A4}) the z-dynamic magnetization component of the A1 (A4) remanent state. A strong attenuation of $-40\ \mathrm{dB}$ is reached for the second mode. The modes 3, 4 and 5 are attenuated by $-16\ \mathrm{dB}$ up to $-20\ \mathrm{dB}$. Finally, concerning the first mode, its attenuation is

only of -8 dB. Contrary to the other excited modes, this mode only precesses in the edge domains. As these domains are not fully magnetized along the direction of the microwave pumping field even in the A1 configuration, they can always present a non-zero value of the averaged m_y component that can still couple to $\vec{h}_{RF}$.

To quickly conclude, by applying an initialization field along two different directions, it is possible to obtain two different microwave responses at remanence in a same CMS antidot lattice. This difference is translated in the extinction of the spin wave modes, thus having the same functionality as a switch, allowing reconfigurable operations at remanence.

To further demonstrate that the reconfigurable property at zero bias field is made possible thanks to the strong magneto-crystalline cubic anisotropy of the CMS, the dynamic states were calculated for the C1 and C2 configurations presented previously (Fig. 5.2 b)). Their microwave spectra are shown in Figure 5.3 b). The spatial profiles of the indexed spin wave modes are shown below the graph. All the indexed spin wave modes present a strong precession in the $45°$ domains. The zigzag configuration appearing both for the C1 and C2 states induces that there is always some part of the magnetic volume that can couple to $\vec{h}_{RF}$. Again, we calculated the attenuations of the FFT peaks in the C1 configuration in dB as $20\log_{10}(m_z^{C1}/m_z^{C2})$ with m_z^{C1} (m_z^{C2}) the z-dynamic magnetization component of the C1 (C2) remanent state. The maximum attenuation achieved in such system is only of -6 dB with the first mode $1'$. This value is far shorter that the one that could be obtained in the case of a material with sufficiently strong cubic anisotropy (-40 dB).

In the CMS magnetic antidot lattice with cubic anisotropy, in addition to the A4 and A1 configurations, the A2 and A3 remanent states can be obtained (Fig. 5.2 a)). Therefore we also compared the microwave spectra of the A2 and A3 remanent states with respect to the microwave spectrum of the A4 remanent state in Figure 5.4 a). Owing to the presence of the $45°$ domains, one can observe that the extended mode no longer exists in the A2 and A3 configurations compared to the A4 configuration. When looking at the different spatial profiles, strong precessions occur in these domains with an increasing number of nodes and antinodes as the frequency increases. In particular, the first mode $1''$ of the A3 configuration is shifted towards a lower frequency compared to the first mode 1 of the A4 configuration. This frequency shift is of 1.3 GHz. Consequently, this results in an attenuation of -34 dB of the first mode 1 of the A4 remanent state when switching from A4 to A2 or A3 states. As a consequence, the possibility to induce the formation of a $45°$ domain by switching from the A4 to the A2 or A3 configurations offer extra reconfigurable functionalities by shifting spin wave modes in frequency in addition to the "simple extinction" process.

Finally, the microwave response of the B1 configuration (Fig. 5.2 c)) was also studied and is shown in Figure 5.4 b) with the spatial profiles of the modes below. In such device, the microwave response will always be the same regardless of the direction of $\vec{H}_0$ as the averaged M_x and M_y components have always the same amplitude. Such feature could be useful for microwave applications which require a robust response against external magnetic perturbations. In this configuration, the edge-domain mode is absent. The first dynamic mode appears around 5 GHz, which is closer but still lower than the FMR frequency of the CMS thin film, and tends to resemble to a quasi-uniform stripe mode with this time the stripe oriented along the diagonals of the antidot lattice. As the magnetization of the remanent state is majorly aligned along the diagonals, all the spin wave modes are spreading along the diagonals of the sample. When the frequency of the observed modes increases, the number of nodes and antinodes increases as well.

To conclude, a magnetic device based on a magnetic antidot lattice with strong cubic crystal anisotropy (configurations A1 to A4) can offer many reconfigurable possibilities at remanence depending on the direction of an initialization field. In particular, it can perform an on and off switching of several spin wave modes at specific frequency positions through strong attenuations in the range

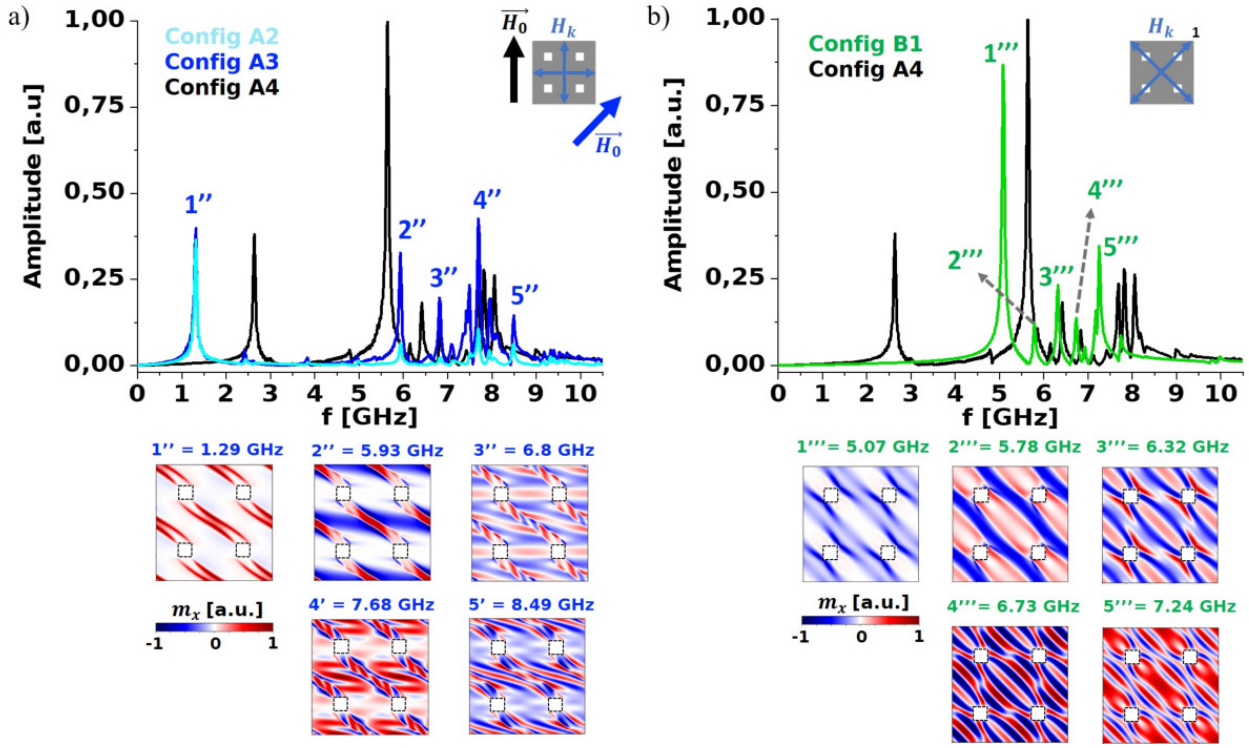

Figure 5.4: FFT amplitude spectra for the different remanent magnetic states presented in Fig. 5.2: a) in the case of a CMS magnonic crystal with cubic anisotropy axes aligned along the antidot lattice symmetry axes with the A4 (black curve), A3 (dark blue curve) and A2 (light blue curve) remanent states, and b) in the case of the same magnonic crystal but with the cubic anisotropy axes rotated by $45°$ with respect to the antidot lattice symmetry axes with the B1 remanent state (green curve) in comparison with the A4 configuration (black curve). Each mode with relevant amplitude are indexed with numbers. The amplitude of the spin wave modes was normalized with respect to the highest amplitude mode (mode 2 of configuration A4 in a) and b)). Below each FFT spectrum, temporal snapshots of the dynamic m_x component for specific frequency modes (of the A3 configuration in a), of the B1 configuration in b)) indexed in the FFT spectra are shown. The m_x component of each mode is normalized with respect to its own maximum amplitude for an easier visualization.

$1 - 10$ GHz. These results were obtained for a particular antidots size and spacing. Variations of both of these parameters could destroy or enhance the reconfigurable properties.

5.1.3 Influence of the aspect ratio

To optimize the design of the CMS magnonic crystal device for targeted reconfigurable properties in desired frequency ranges, a study of the influence of the antidots size s and spacing d have to be achieved. Here the antidot lattice symmetry is collinear to the cubic crystal anistropy axes and the initialization field $\vec{H}_0$ is applied either along the y or x axis thus giving rise to a remanent state called Rem Y or Rem X respectively. This situation is analog to the previous studied cases with the A4 and A1 remanent states. Each FFT spectrum is normalized according to the most intense mode.

Variation of the antidots spacing d with a fixed antidots size s

Figure 5.5 shows the remanent states, microwave spectra and spatial profiles of the different spin wave modes in the Rem Y and Rem X configurations for two different values of spacing d (600 nm and 300 nm) while the size s is kept constant ($s = 300$ nm). The case of an aspect ratio $s/d = 1/2$ is

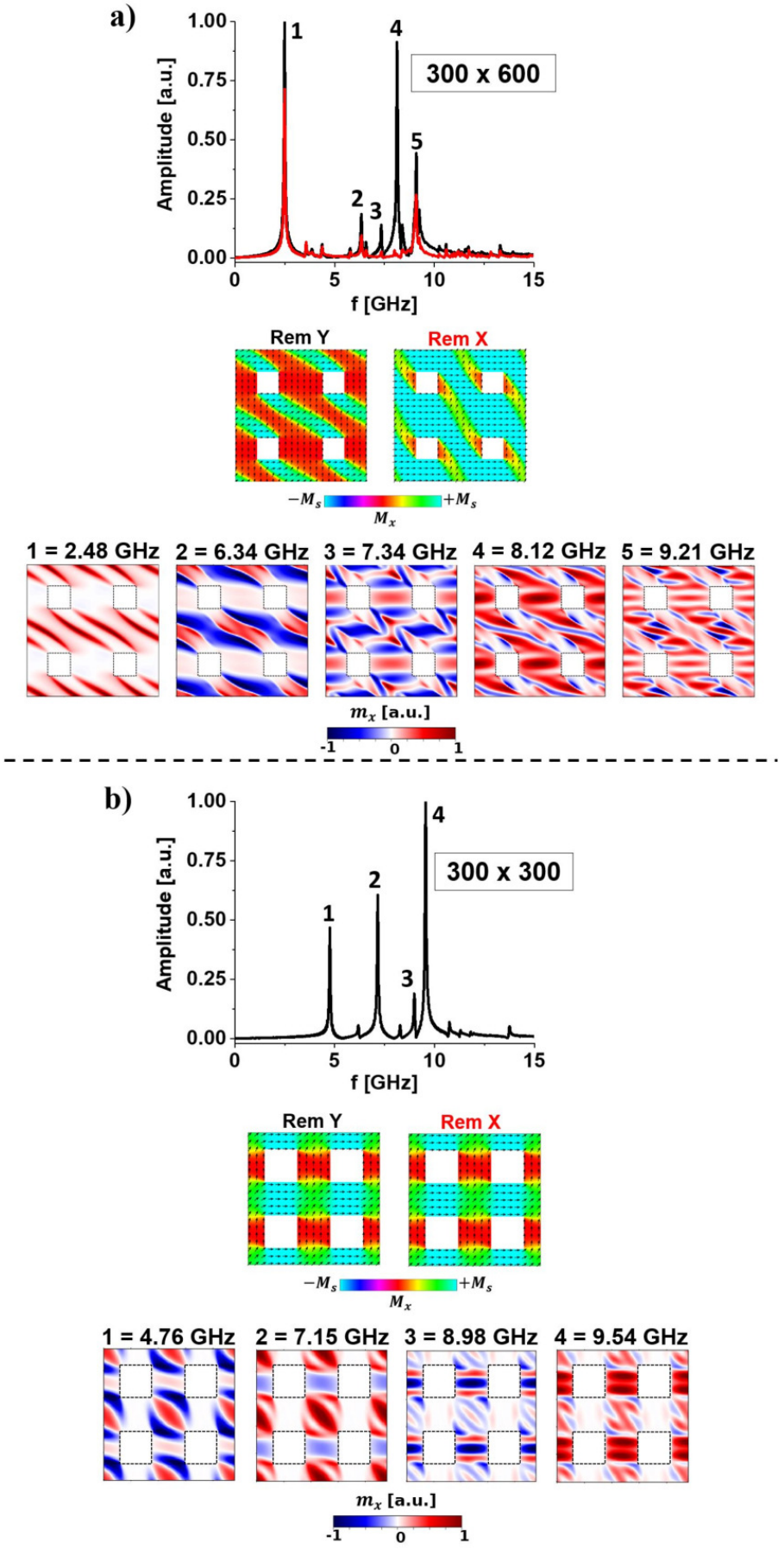

Figure 5.5: (Top) FFT spectra of the Rem Y (black curve) and Rem X (red curve), (Middle) the remanent magnetic states Rem Y and Rem X, and (Bottom) the m_x temporal snapshots for the indexed modes, in the case of a CMS magnetic antidot lattice (cubic crystal easy axes aligned along x and y) with a fixed value of $s = 300$ nm and a) $d = 600$ nm and b) $d = 300$ nm. The amplitude of the spin wave modes was normalized with respect to the highest amplitude mode. The remanent states are color coded according to M_x.

shown in Figure 5.5 a). Contrary to the A4 and A1 configurations (aspect ratio $s/d = 1/3$) approached in the previous section 5.1.2, $45°$ domains appear for both the Rem X and Rem Y states. The rest of the magnetization is again either aligned along the x or y axis depending on whether $\vec{H}_0$ is applied with an angle below or above $45°$. The spatial profiles of the first five modes are composed of complex spatial precessions, mainly related to the $45°$ domains. The different modes are very similar to the ones observed in the A2 or A3 configuration described in the previous section. Here, the first and fourth modes are the most intense. The first mode presents large magnetization oscillations at the boundaries between the $45°$ domain and the rest of the magnetization aligned along x or y. This can be assimilated to a domain-wall resonance. The attenuation is only of -3 dB when switching from the Rem Y to the Rem X states since the domains are always present. Such attenuation value is not very attractive for reconfigurable functionalities. On the contary, a -30 dB attenuation is reached with the mode 4. This mode resembles a localized mode as described in chapter 2 section 2.1.3 as it presents strong magnetization precession in the horizontal rows of antidots. Contrary to the first mode, this strong attenuation is obtained as the magnetization in the horizontal rows of antidots weakly couples to the RF field in the Rem X state. Finally, the other spin wave modes present low attenuations that can not reach -20 dB. Consequently, reconfigurable configurations can be performed with an aspect ratio of $s/d = 1/2$, however with less performance than in the case of an aspect ratio of $s/d = 1/3$ as approached in the previous section 5.1.2.

The case of an aspect ratio of $s/d = 1$ is shown in Figure 5.5 b). One can observe that the Rem X and Rem Y configurations are exactly the same thus leading to no difference in their microwave response. As the spacing d is decreased, the local shape anisotropy due to the antidots becomes dominant over other contributions. This leads to the rotation of the magnetization towards the x (y) axis between two vertical (horizontal) antidots. The areas between vertical antidots are strongly magnetized along x thus it can not couple to the pumping field. The magnetization precession is mainly localized in the central part of the unit cell for modes 1 and 2 and in-between horizontal antidots for modes 3 and 4.

As a result, we conclude from this study that having quasi-uniform states at remanence is the best way to ensure a high number of modes showing important attenuation values. With the magnetic parameters of the CMS Heusler alloy used in this numerical study, such quasi-uniform states are observed for an aspect ratio of $s/d = 1/3$. Lower aspect ratios can also be convenient, however the more the antidots are separated, the more we will bring closer the magnetic system to the case of a plain thin film. Less quantized spin wave modes will be thus excited to converge towards the FMR mode of a plain thin film. Of course, these results are material dependent meaning that different values of cubic crystal anisotropy constant, saturation magnetization and exchange constant may require other aspect ratios s/d to optimize reconfigurable states.

Variation of the antidots size s with a fixed aspect ratio $s/d = 1/3$

We now study how the value s tune the microwave spectrum of the magnonic crystal while keeping $s/d = 1/3$. In Figure 5.6, the remanent states, their microwave spectra and spatial profiles of the main spin wave modes are shown for antidot sizes ranging from 200 nm to 50 nm. We observed in particular, that for antidot sizes $s \leq 200$ nm, only two remanent states (Rem X and Rem Y) could be stabilized. Remanent states analog to the A2 or A3 configurations approached in section 5.1.2 with $45°$ domains could not have been generated when $\vec{H}_0$ was applied towards the $45°$ direction. As a result, the remanent states Rem X and Rem Y appear for an applied initialization field below or above the $45°$ direction respectively.

In Figure 5.6 a), the case of a CMS magnetic antidot lattice with antidot size $s = 200$ nm and spacing $d = 600$ nm is shown. To some extent, the remanent states Rem Y and Rem X are similar to the A4 and A1 configurations in section 5.1.2. However, the lowest frequency mode is the most intense in this case and its attenuation is only of -10 dB when switching from Rem Y to Rem X state.

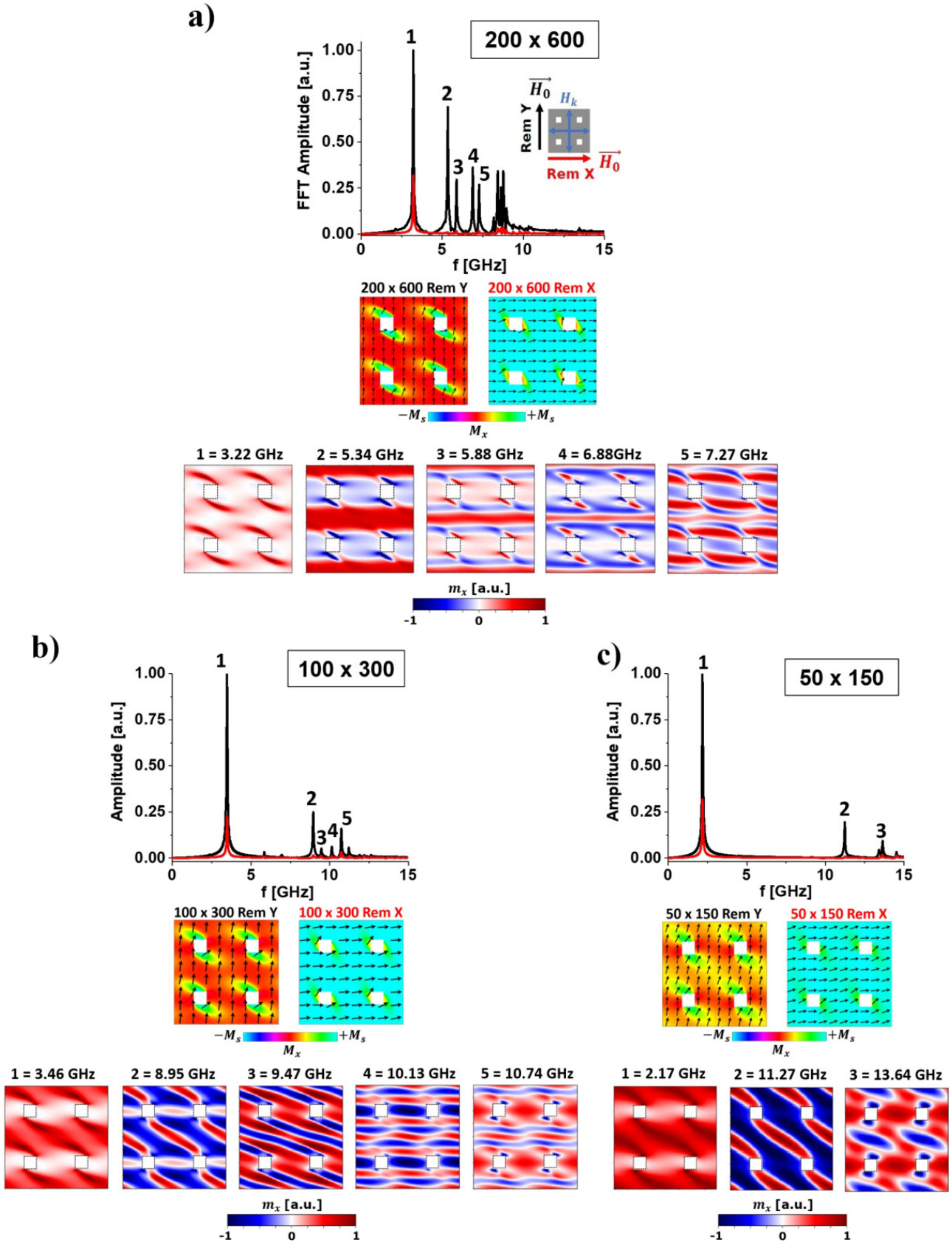

Figure 5.6: (Top) FFT spectra of Rem Y (black curve) and Rem X (red curve), (Middle) Remanent magnetic states Rem Y and Rem X, and (Bottom) m_x temporal snapshots of the indexed modes in the case of a CMS antidot lattice aligned with the cubic crystal anisotropy axes with varied values of s and fixed aspect ratio $s/d = 1/3$: a) $s = 200$ nm, $d = 600$ nm, b) $s = 100$ nm, $d = 300$ nm and c) $s = 50$ nm, $d = 150$ nm. Each FFT spectrum is normalized according to the most intense mode. The remanent states are color coded according to M_x.

On the other hand, the second mode is attenuated by -42 dB. Concerning higher frequency modes, attenuations better than -20 dB can be reached. This configuration present more spin wave modes with relatively high intensities (Rem Y) and attenuations (Rem X) compared to the case $s = 300$ nm (section 5.1.2) making it even more suitable for reconfigurable operations at remanence due to its increased flexibility.

When further decreasing the antidot size towards 100 nm and 50 nm, one can observe that the central part of the unit cell is no longer completely aligned along the x or y axis in the Rem X or Rem Y state respectively. The misalignement of the magnetization increases when decreasing s as shown in the case of $s = 50$ nm. This is because when the antidot size is reduced, the edge domains start to spread in the central part of the unit cell. The spin wave modes in a smooth non uniform magnetic state was adressed in Ref. [268]. The authors studied the modes in a permalloy based antidot lattice with circular antidot size and spacing 450 nm showing a small tilt of the magnetization with respect to the lattice symmetry axes. In their study the small tilt of the magnetization was induced by a relatively weak (20 mT) magnetic field applied at a few degrees from the lattice symmetry axes. In particular, they demonstrated that the lowest frequency modes, usually assimilated to edge modes in the saturated case, are in their case a combination of an edge mode with an asymmetric channel mode. They call such modes "dragonfly modes" (see Figures 4 d) and 5 in Ref. [268]). They also reported that the maximum precession amplitude was located in the channels linking opposite antidots in the diagonal. Our results are similar even though we deal with remanent states and a different system. Indeed, the spatial profiles of our first mode in Figure 5.6 b) and c), are similar to their "dragonfly modes" as the magnetization precession is not only confined in the edge domains but also extends between antidots diagonally aligned. The frequency of such mode is still very low (under the FMR frequency of the thin film) and within the same range as observed for $s = 200 - 300$ nm. This is due to the fact that the magnetization precession occur mainly in the "extended" edge domains where the effective field is lowered.

Similar to Ref. [268], we also observe that the higher frequency modes (2, 3...) are shifted towards higher frequencies when the tilt of the magnetization in the central part of the unit cell is increased. This occurs in our case when the antidot size s is decreased. Indeed the frequencies of the modes 2 and 3 for $s = 100$ nm (around 9 and 9.5 GHz respectively) are shifted to higher frequencies for $s = 50$ nm (around 11.2 and 13.6 GHz). One possible explanation of this shift relies on the non uniform state which is the source of an increased contribution of the exchange energy to the effective field. This phenomenon can be considered as analog to steeper slopes in the dispersion curves $f(k)$ induced by the contribution of exchange energy for the different quantized spin wave modes in a magnetic stripe [159].

Finally, there is another difference between the configurations with $s = 300$ nm or 200 nm and the configurations with $s = 100$ nm or 50 nm. Indeed, the relative amplitude of the higher frequency modes with respect to the main mode are reduced in the Rem Y state. Nevertheless, reconfigurable operations at remanence can still be performed in the cases of $s = 100$ nm or 50 nm. When switching from the Rem Y state to the Rem X state, an attenuation of the second mode of about -30 dB and of higher-order modes around -20 dB can be achieved.

These results were obtained in the particular case of square antidots with specific antidot sizes. As a consequence, one can tune the antidot sizes and eventually shape to fix the desired frequency range for particular microwave reconfigurable operations.

5.2 Applicability of reconfigurable Co_2MnSi magnetic antidot lattices

5.2.1 Switching performances

To further demonstrate the interest of such device for microwave reconfigurable operations, two crucial parameters have to be studied to take into account the easiness of use for potential applications: the minimum amplitude of the initialization field $\vec{H}_0$ and the minimum required time to switch from one remanent state to another. In particular, in the actual context of reducing the energy consumption of futur devices, these two parameters are of particular importance.

We have tested the switching performances of our artificial device for an aspect ratio of $s/d = 1/3$ and different antidot sizes $s = 300, 200, 100, 50$ nm. In order to compare with published studies (but obtained with permalloy-based nanostructures[269–271]), we followed the same methodology as described in the pioneering works of Ref. [270] tackling the problem of switching easiness. We have tested the transition from the remanent state Rem Y to Rem X with a field pulse of amplitude P and duration 1 ns applied along the x direction. The transition from the A4 state (Rem Y) to the A3 remanent state is also considered and the applied field pulse is in this particular case directed along the 45° direction. The results are shown in Figure 5.7. Regardless of the antidot size s, the switching

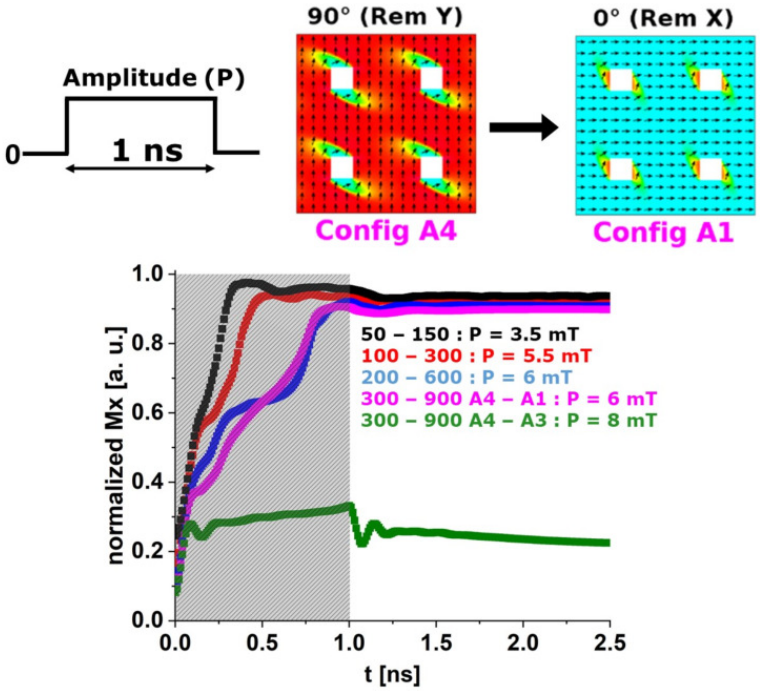

Figure 5.7: Simulations of the switching (Rem Y to Rem X) times for different antidot sizes s and fixed aspect ratio $s/d = 1/3$. The minimum magnetic pulse of amplitude P and duration 1 ns was applied along the x axis except in the case of the transition from the A4 state to the A3 state (green curve) where it was applied towards the 45° direction. The black, red, blue and pink curves correspond to the cases of $s = 50, 100, 200, 300$ nm respectively.

times reach approximately 1 ns. The transition from the A4 to the A3 (green curve) state however needs a larger time around 1.2 ns to effectively switch. The minimum field amplitude required for the switching is of a few mT, up to 6 mT in the case of an antidot size $s = 300$ nm and down to 3.5 mT concerning an antidot size $s = 50$ nm. As a result, decreasing the size of the antidots leads to smaller amplitudes of the field pulse to initiate the transition. A larger amplitude of the field pulse (8 mT)

was required in the transition A4 to A3 state.

Compared to the results obtained with permalloy-based nanostructures [269–271], our pulse amplitudes are one order of magnitude lower. However they designed magnetic systems that can be used for nanoscale on-chip integration, while ours will be on a larger scale as we consider the case of 2D infinite structures. As will be approached in the next section 5.2.2, the 2D infinite case can be reduced to micrometer-scale devices, where the reconfigurable properties are still observed. To easily switch the magnetization and allow on-chip integration, one can use a simple scheme as proposed in Ref. [270] with two perpendicular current lines placed above the magnetic antidot lattice. Nevertheless, the application of such magnetic fields to switch the remanent states still requires high currents. To reduce the energy consumption, additional studies on the device design, notably concerning the antidot shape or the antidot lattice symmetry (hexagonal symmetry for example), should be tested.

5.2.2 Influence of finite dimensions on the device

In the previous sections, we demonstrated that reconfigurable operations at remanence can be obtained in the case of a 2D pseudo-infinite magnetic antidot lattices based on the CMS magnetic properties. In reality, the device will have finite dimensions and thus the validity of our approach for finite size devices must be put to the test. Its finite size will inevitably induces flux closure domains at the edges of the device. To adress this question, we performed micromagnetic simulations with OOMMF on two large samples with different dimensions $14400 \times 14400 \times 20$ nm^3 and $13500 \times 13500 \times 20$ nm^3. Compared to the previous simulations, we used OOMMF instead of MuMax3 since we observed that OOMMF was faster than MuMax3 in the convergence of the energy minimization calculation of the remanent states. The simulations of such large systems required the use of the High-Performance Computing (HPC) resources of the CALMIP supercomputing center. To determine the initial remanent states, we used the evolver "Oxs_CGEvolve" and for the microwave response, we used the driver "Oxs_mindriver". The convergence criteria was set to $\vec{m} \times \vec{H} \times \vec{m} = 10$ A m^{-1} ($\vec{m} \times \vec{H} \times \vec{m}$ damping torque) and we verified that the results were the same down to 1. The simulated device is constituted of a square antidot lattice with square antidots of size $s = 300$ nm and aspect ratio $s/d = 1/3$.

We have tested two geometries. For the first one, the sample has dimensions of $14400 \times 14400 \times 20$ nm^3 and the spacing between the edge of the last antidots of the last row (or column) and the edge of the sample is equal to half of the spacing between the antidots d, i.e. 450 nm. This can be seen with the remanent states in Figure 5.8 a) and b). For the dimensions $13500 \times 13500 \times 20$ nm^3, there is no spacing between the last antidots of the last row (or column) and the edge of the device, as shown in Figure 5.9 a) and b). Other dimensions were simulated from $9900 \times 9900 \times 20$ nm^3 up to $29400 \times 29400 \times 20$ nm^3 and in all of these cases, equivalent remanent states as in the one presented in Figures 5.8 and 5.9 were obtained.

Finite device $s = 300$ nm and $s/d = 1/3$ with dimensions $14400 \times 14400 \times 20$ nm^3

The Rem Y configuration is presented Figure 5.8 a). One can observe that the magnetization on the right and left edges of the device is uniform and aligned along the y direction in the areas between the last antidots column and the edges of the device. At the top and bottom of the sample, the magnetization is this time uniformly aligned along the x direction in-between the last antidots rows and edges of the sample. These uniform magnetic areas close to the borders of the sample, which we will refer as uniform domains, extend on a width of 450 nm. The same result is observed in the Rem X configuration with a rotation of $90°$ of the system, as can be seen in Figure 5.8 b). These uniform domains can couple to the microwave pumping field $\vec{h}_{RF}$, in particular in the Rem X configuration, and therefore could disrupt the reconfigurable properties. In this case, these uniform

domains cover a small portion of the total sample, which we estimate around 6% of the total magnetic volume.

We simulated the microwave response of this sample to study the influence of these uniform

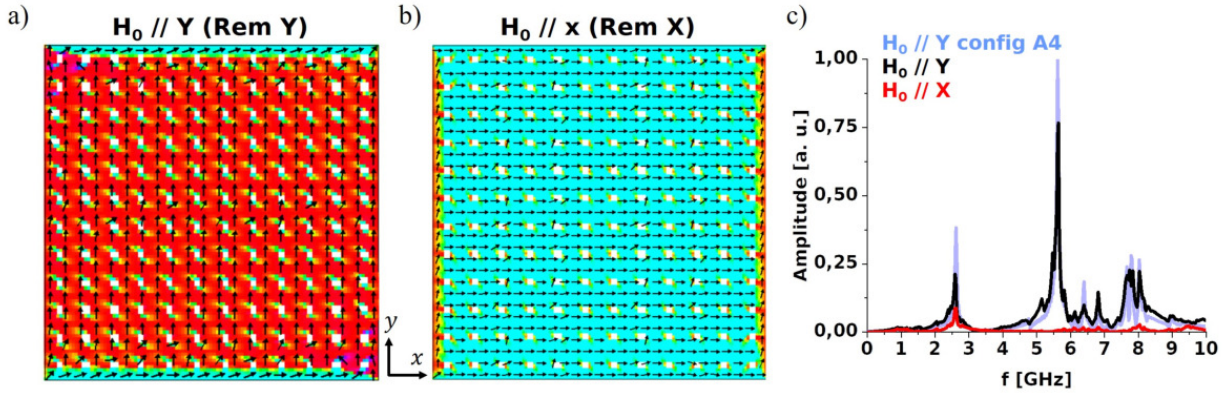

Figure 5.8: Remanent magnetic states of a finite-size device with lateral dimensions 14.4×14.4 μm^2 in a) with $\vec{H}_0$ along y (Rem Y) and b) with $\vec{H}_0$ along x (Rem X). The remanent states are color coded as the ones in Figure 5.2. c) The FFT amplitude spectra of Rem Y (black curve), Rem X (red curve) and A4 state (infinite case) (light blue curve). The amplitude of the FFT spectra are normalized according to the maximum amplitude reached in the A4 state.

domains. The microwave spectra of the Rem Y (black curve) and Rem X (red curve) states are shown in Figure 5.8 c). For comparison, the microwave response of the A4 remanent state (2D infinite case) of section 5.1.2 is plotted in light blue on the graph. The amplitude of the microwave responses were normalized with respect to the maximum value obtained in the A4 remanent state. The microwave spectra of Rem Y and Rem X states are very similar to those obtained in the 2D infinite approximation (A4 and A1 states respectively) in Figure 5.3. Also, the resonance peaks for all modes are widened and a small satellite mode appear at 5.15 GHz with respect to the infinite case. The amplitude of the excited modes is also slightly lowered compared to the infinite case, except for the fourth mode (6.81 GHz) where it is barely increased. The attenuation values obtained when switching from Rem Y to Rem X state are also equivalent to those reached with the A4 and A1 states. These small differences should be rectified when the size of the sample is increased thus further reducing the effects of these uniform domains.

These results were also verified in the case of a sample with the same dimensions and aspect ratio but with antidot size $s = 100$ nm. The microwave spectra of the Rem Y and Rem X states were also similar to those obtained in the infinite case shown in Figure 5.6. Consequently, the pseudo-infinite approximation is valid for this geometry with finite dimensions to study reconfigurable operations.

Finite device $s = 300$ nm **and** $s/d = 1/3$ **with dimensions** $13500 \times 13500 \times 20$ nm^3

For this geometry, the previously considered uniform domains are here non-uniform and spread on a larger extent within the magnonic crystal, as shown with the remanent states Rem Y and Rem X in Figures 5.9 a) and b) respectively. This results in a larger fraction of about 17% of non-uniform magnetized domains with respect to the total magnetic volume. When looking at the microwave responses of the Rem Y (black curve) and Rem X (red curve) states of this finite sample compared to the A4 state (light blue curve) in Figure 5.9 c), the spectra are also quite similar except that a small low-frequency mode appears at 1.71 GHz, the satellite peak at 5.15 GHz previously observed in the first dimension is further increased and the relative amplitudes of higher frequency modes after the main mode are even more decreased. As a consequence, the attenuation values for these modes is decreased by 10 to 40%. This corresponds to limited attenuations of -10 to -20 dB with this finite size geometry.

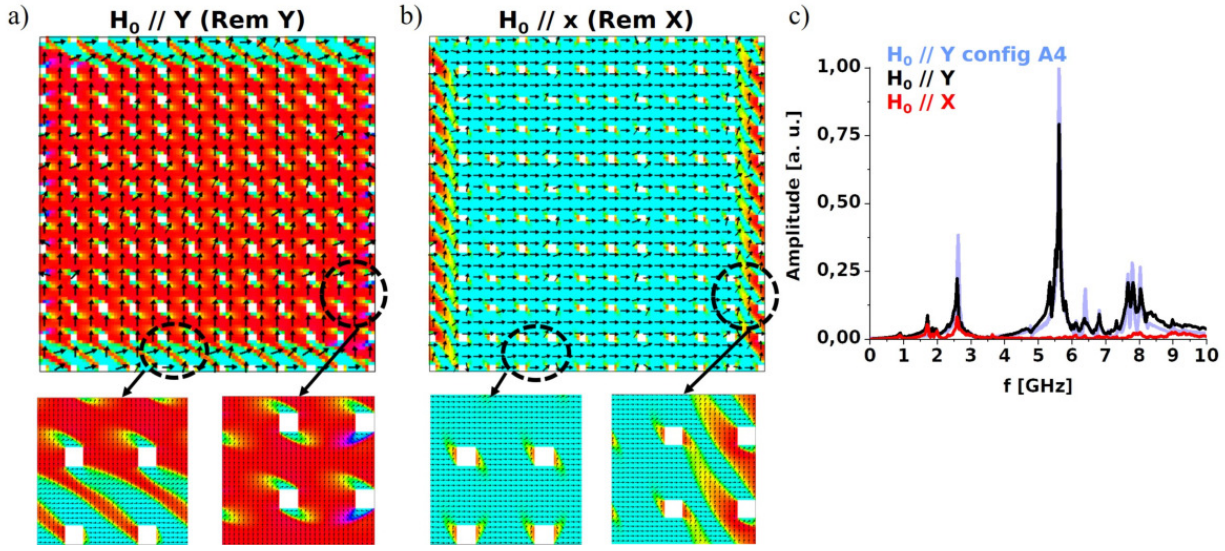

Figure 5.9: Remanent magnetic states of a finite-size device with lateral dimensions $13.5 \times 13.5\ \mu\mathrm{m}^2$ in a) with $\vec{H}_0$ along y (Rem Y) and b) with $\vec{H}_0$ along x (Rem X). The remanent states are color coded as the ones in Figure 5.2. c) The FFT amplitude spectra of Rem Y (black curve), Rem X (red curve) and A4 state (infinte case) (light blue curve). The amplitude of the FFT spectra are normalized according to the maximum amplitude reached in the A4 state.

To conclude, the effects of flux closure magnetic domains arising from finite size devices on the reconfigurable properties of the magnonic crystal can be lowered with a proper design of the latter. The finite dimensions must be taken into account to evaluate the performances of small devices, i.e. typically for dimensions especially below 10 μm. This means that our system is worth for micrometers microwave patches for example but probably not as it is for nanoscale integration.

Chapter 6

Impact of the nanostructuration techniques on Co_2MnSi Heusler magnonic crystals properties

In this chapter, we discuss how the choice of the nanofabrication techniques impacts the excited spin wave modes in a CMS magnonic crystal. To this end, we present the FMR spectra measured on the samples #1 and #2 presented in chapter 4 section 4.3.1 and 4.3.2. For the sample prepared by FIB (#1), we demonstrate that it is not sufficient to take into account only the exact geometry of the holes to obtain a qualitative agreement between the simulated and measured FMR spectra. One also has to consider the local variations of the magnetic parameters induced by Ga^+ milling. In contrast, concerning the sample prepared by e-beam lithography and Ar^+ milling (#2), simulations and experiments agree very well for an ideal geometry. Such studies will serve as a basis to conclude about the relevance of using Ga^+ FIB milling to achieve a "real device" based on CMS thin films.

6.1 Influence of Ga^+ FIB milling on the spin wave modes in a Co_2MnSi magnonic crystal

The results presented in this section were published in Ref. [272]. For this article, we used magnetic parameters based on previous reports obtained in our group. Indeed, the batch of samples that we used for FIB patterning were not capped during the sputtering deposition. Recently, we found a possibility to measure by FMR the magnetic properties of a thin film grown in the same conditions of the one used to make the sample #1. The measured magnetic parameters are very close to those given in [272] except for the value of the cubic crystal anisotropy constant K_{c1} ($-12\ \mathrm{kJ/m^3}$ instead of $-17\ \mathrm{kJ/m^3}$ in the article). In this manuscript we present simulations performed with the last measured parameters but we highlight here that the difference of anisotropy constant induces only small variations of frequencies and it does not change the physical phenomenon discussed below.

The geometrical features of the sample #1 have already been described in section 4.3.1. Here we remind the main points for the sake of clarity. The antidot lattice covers an area of $47 \times 47\ \mu\mathrm{m}^2$. The antidots have a bowl shape with a relatively squared geometry at the bottom surface while it is almost circular at the top surface. The center-to-center distance is $400\ \mathrm{nm}$. The different dimensions are recalled in Figures 6.1 a), b) and c). In particular, a cross section performed on another sample

prepared in the exact same FIB conditons allows to evaluate the antidots dimensions at the bottom and top surfaces of the antidots. The antidot lattice symmetry axes are aligned along the cubic crystal anisotropy easy axes of the CMS thin film.

A micro-antenna was deposited on top of the magnonic crystal with its long axis parallel to

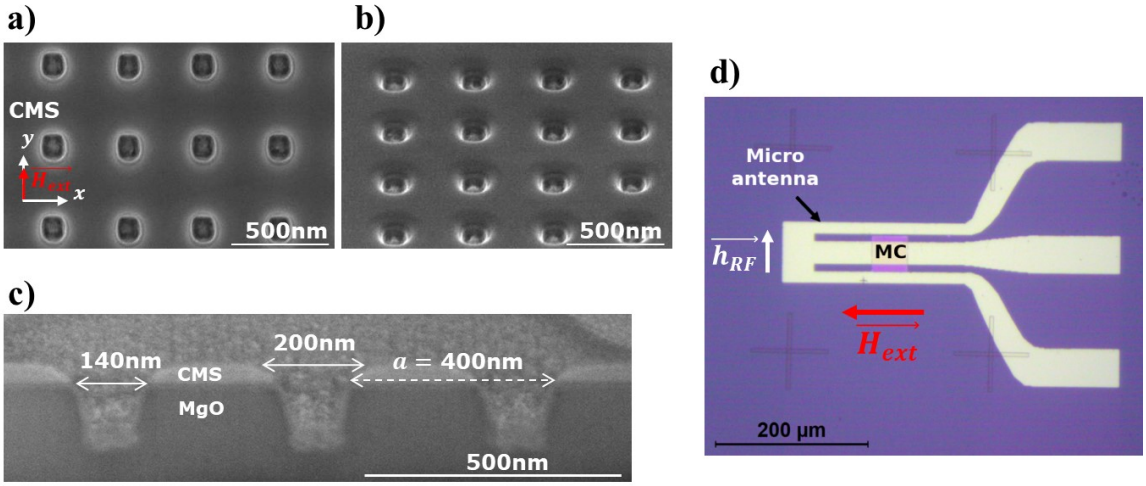

Figure 6.1: SEM images of a) the top view, b) the tilted view at $52°$ and c) the cross section view of the CMS magnetic antidot lattice (MC) patterned by FIB milling (sample $\#1$). d) Optical image of the micro-antenna on top of the CMS magnetic antidot lattice. The magnetic field is applied along the length of the micro-antenna.

the edges of the lattice. As shown in Figure 6.1 d), the magnetic field is applied along the length of the antenna to ensure a MSSW configuration ($\vec{k} \perp \vec{M}$, at least in the magnetically saturated regime). The width of the central conductor is sufficiently large to consider a quasi-uniform pumping field over the magnonic crystal. The central conductor indeed covers about 65 $\%$ of the magnonic crystal. As the maximum wavevector that can be excited is very weak (approximately $k_{max} \approx \frac{2\pi}{w_{in}} = 0.209\, rad\mu\mathrm{m}^{-1}$), it should have a negligible influence on the position and linewidth of the FMR peaks. A discussion on the estimation of the induced frequency shifts is later approached in the case of the sample $\#2$ in section 6.2. The FMR measurements were performed with the FM-FMR measurement technique detailed in chapter 3 section 3.3.2. The frequency of the microwave excitation is fixed while the applied magnetic field is swept from 350 mT to 0 mT with field steps of 0.3 mT. This process is repeated for each frequency from 1 GHz to 18 GHz with frequency steps of 0.5 GHz.

6.1.1 FM-FMR measurements and numerical study of variable antidot geometries

FM-FMR measurements

The evolution of the microwave absorption spectrum with respect to the frequency f and applied field H_0 is shown in Figure 6.2. The amplitude of the voltage measured by lock-in detection (proportional to the derivative of the absorbed power) is color coded with respect to the colorbar on the right of the graph. One can first observe a large absorption band in which few distinctive peaks can be resolved. In particular one mode is clearly distinct at high frequencies. An example of the measurement at 9 GHz can be seen in the inset of Figure 6.2 where the presence of several resonance peaks are pointed out with black arrows. As discussed in chapter 2 section 2.1.3, these resonances correspond to the excitation of quantized and confined spin wave modes in the antidot lattice contrary to the case of a plain magnetic thin film where only the uniform (i.e. $k = 0$, FMR) mode can be excited

(and eventually also perpendicular standing spin waves (PSSW)). We can observe that the different resonant peaks can not be well distinguished individually as they are broad and overlap. The most intense mode which appears for the lower field (i.e. higher frequency) has the smallest peak-to-peak field linewidth (≈ 2 mT) while it reaches up to 13 mT for other modes. Such large broadening of the resonance peaks results in their very low amplitudes.

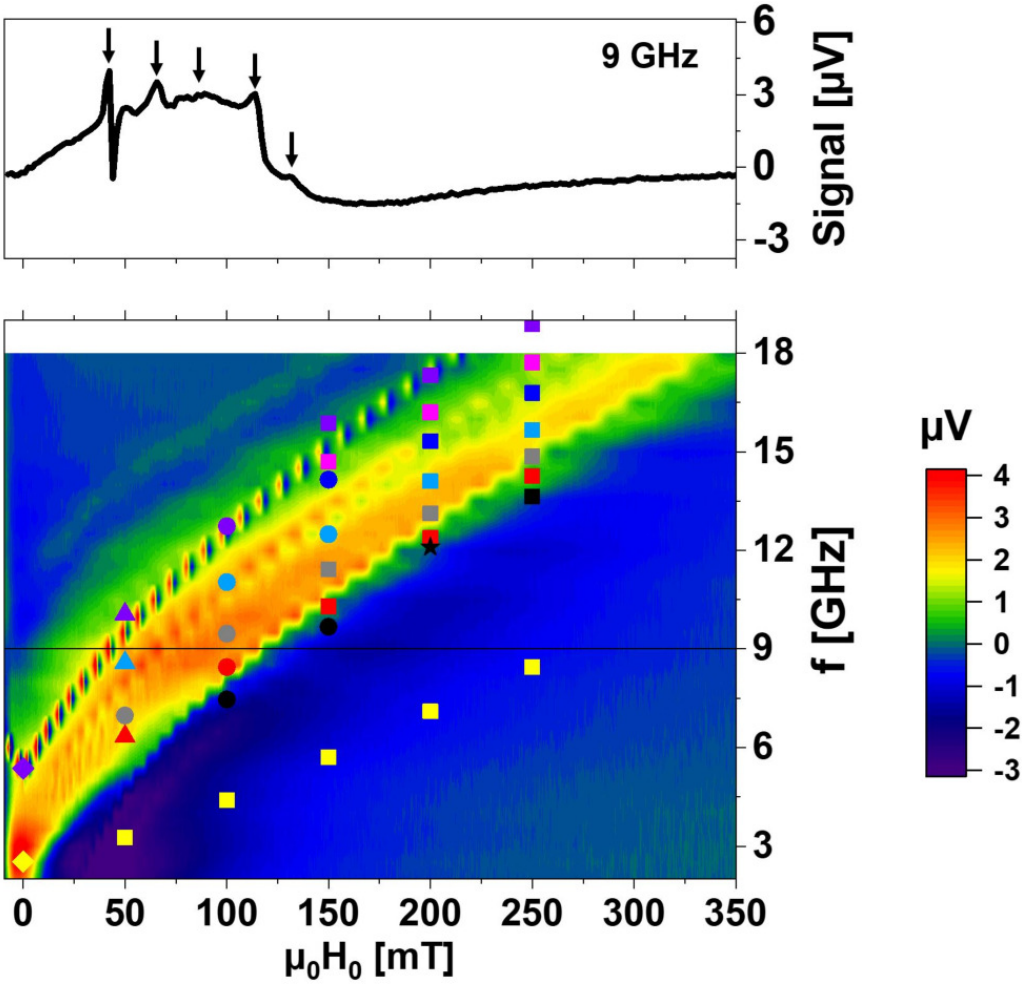

Figure 6.2: Evolution of the microwave power absorbed by the CMS magnetic antidot lattice nanostructured by FIB (sample #1) according to the applied magnetic field $\mu_0 H_0$ and frequency f. The amplitudes of the FMR signals are color coded with respect to the colorbar on the right. An example of the FMR spectrum measured at 9 GHz is shown at the top of the main figure (black line). The different resonance peaks correspond to different spin wave modes excited in the magnonic crystal and are indexed with black arrows. The colored symbols on the main graph correspond to the frequency positions of the simulated spin wave modes for different field values. These symbols are the same as those in Figure 6.6.

Numerical modeling of the FIB etched antidots

To explain these measurements, micromagnetic simulations were performed with MuMax3 to understand not only the kind of spin wave modes excited in our structure but also the variation of the resonance frequencies as a function of H_0 and the large broadening of the peaks. Owing to the complex shape of the antidots observed in Figure 6.1, we started by testing several simple geometries such as square, circular, rounded square and bowl shapes. These geometries are illustrated in Figures 6.3 a) and b). The bowl shape is the closest geometry to the one deduced from the SEM images (Fig. 6.1 a), b), c)). Simulations were performed on a unit cell of the antidot lattice by using 2D periodic boundary conditions (2D PBC) to mimic an infinite lattice. For all geometries, the center-to-center

distance (periodicity) of the antidots is always equal to 400 nm. For the square and circular antidots, the lateral dimensions or diameters are 140 nm. The rounded square geometry was obtained as the intersection between a square with lateral size 140 nm with a circle of diameter 160 nm. Concerning the bowl shape illustrated in Figure 6.3 b), we defined the bottom of the antidots as rounded squares such as described previously, then the geometry becomes circular with increasing diameters up to 200 nm when going up to the top layer of the sample. For all the geometries, the unit cell has dimensions of $800 \times 800 \times 50$ nm^3. The simulations were performed with a discrete mesh of $5 \times 5 \times 5$ nm^3 cubic cells.

The cubic crystal anisotropy easy axes are along the antidot lattice symmetry axes (x and y).

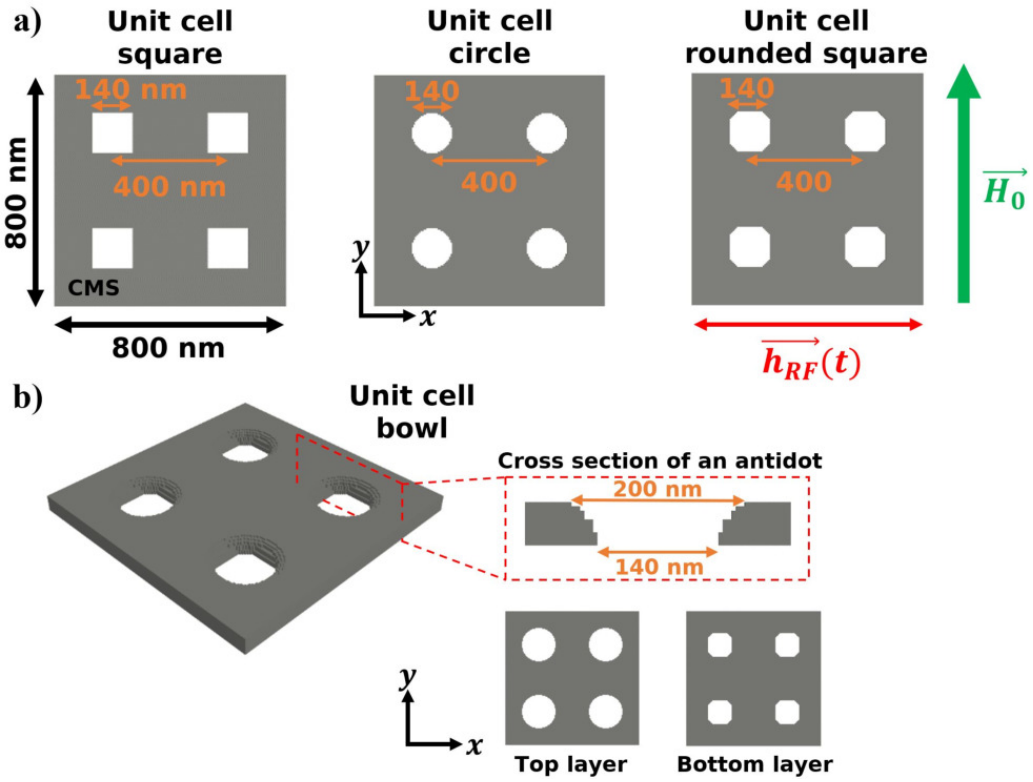

Figure 6.3: a) Schematics of the unit cells used for the micromagnetic simulations with the antidot geometries (in white) in the CMS thin film (in grey): square, circle and rounded square. b) Schematics of the bowl geometry with its cross section, top and bottom layers surface.

Saturation magnetization M_s [T]	Cubic crystal anisotropy field H_k [mT]	Cubic crystal anisotropy constant K_{c1} [J m^{-3}]	Gyromagnetic ratio $\frac{\gamma}{2\pi}$ [GHz T^{-1}]	Exchange constant A [pJ m^{-1}]	Damping factor α
1.28	24	-12223	28.8	20	0.001

Table 6.1: CMS magnetic parameters used for the micromagnetic simulations.

The static and dynamic magnetic states are calculated with the method described in chapter 3 section 3.1 in the case of a uniform field pulse excitation. The magnetic parameters used for the simulations are indicated in Table 6.1. For these simulations, the external magnetic field was applied with a slight deviation of 5° with respect to the y axis. This angle was estimated experimentally and results from a misalignement of the applied field H_0 with respect to the edges of the magnonic crystal when we put our sample into the electromagnet setup.

For the calculation of the spin wave mode spectra, the FFT was here performed on the z-component

of the dynamic stray field $h_{d,z}(t)$ in a plane located at 5 nm from the top surface of the magnonic crystal. We used this approach to obtain a qualitative description of the amplitude of the expected FMR signals for each excited spin wave modes. Indeed, while it is very convenient to consider that the variations of reflected microwave power from the antenna comes from the power absorbed by the magnetic sample, it is also possible to consider the effect of the stray field at resonance. Via the Lenz-Faraday law, the z-component of the dynamic stray field induces a microwave voltage in the antenna that can be modeled as a change of the antenna impedance (theory of spin waves transduction) as described in chapter 3 section 3.3. It is to be noted that we obtained the same results for the FFT performed on $h_{d,z}(t)$ and for $M_z(t)$. As a result, the total volume of the simulated magnetic system was $800 \times 800 \times 60$ nm^3. The spatial profiles of the excited spin wave modes were obtained following the procedure described in chapter 3 section 3.1.4.

It is worth to mention that we also tested a few simulations on a finite size CMS antidot lattice, which covers an area of 40×40 μm^2, to be as close as possible to the experiment. The microwave excitation was applied on a finite width of 30 μm (which extends on + and - 15 μm from the center of the magnonic crystal). These large simulations were run with OOMMF and required the use of the HPC (High Performance Computing) resources provided by the Calmip supercomputing center in Toulouse. As such simulations are extremely time consuming (several days for each field) it is not relevant for testing many geometries and many field values. However, we emphasize that during these tests no particular differences were observed for the frequency positions of the spin wave modes with respect to the results presented in this section.

Microwave responses of different antidot geometries

In the literature, discrepancies between measured spin wave frequencies and simulations are often reported. Such variations are generally attributed to geometrical variations of the antidots, notably to edge roughness [21, 220, 273]. To our knowledge, few studies are however performed to demonstrate and quantify the impact of geometrical variations [22, 156]. Figure 6.4 a) shows the FFT spectra corresponding to the microwave responses of the CMS antidot lattices for the different geometries presented in Figure 6.3. The spectra have been calculated for $\mu_0 H_0 = 200$ mT. The spatial profiles of each dynamic mode for each geometry are shown in Figure 6.4 b) for the top surface of the antidots. The relaxed magnetic states are also shown next to the spatial profiles.

One can observe that each geometry leads to several main spin wave modes whose frequencies lie relatively well with our experimental measurements (Fig. 6.2). In order to compare the different geometries, we chose to index the different modes with a number (mode 1,2,3...) according to quite similar spatial profiles. The mode 2 for all geometries resembles to an extended mode as its maximum precession amplitude extends along the horizontal channels (i.e. along x) between the rows of antidots. The terms defining the different regions of the magnetic antidot lattice used in this text (horizontal channels for example) are detailed in chapter 2 section 2.1.3. The mode 1 is an extended mode along the horizontal channels (like mode 2) but it is quantized along the width (i.e. along y) of the channels, with a quantization number of $n = 3$ (3 antinodes). Mode 5 can be assimilated to a mix of a localized mode and extended mode quantized with $n = 7$. The other modes present complex spatial profiles that can not be easily described.

An important result of these FFT spectra concerns the dependence of the frequency of the different modes with the shape of the antidots. For example, a 1 GHz shift is observed for the mode 1 between the square and circular shapes. The frequencies of the mode 2 for the square, rounded square and bowl geometries are relatively close from each other (150-250 MHz gaps) while a discrepancy up to 800 MHz can be found for the circular shape. In contrast, other modes like 3 and 4 are relatively constant. These two modes seem to be less sensitive to the antidot shape but more to the size of the antidots as the third mode of the bowl shape is slightly shifted at lower frequencies compared to the third mode of the other geometries which superposes on the same resonance frequency. As a result,

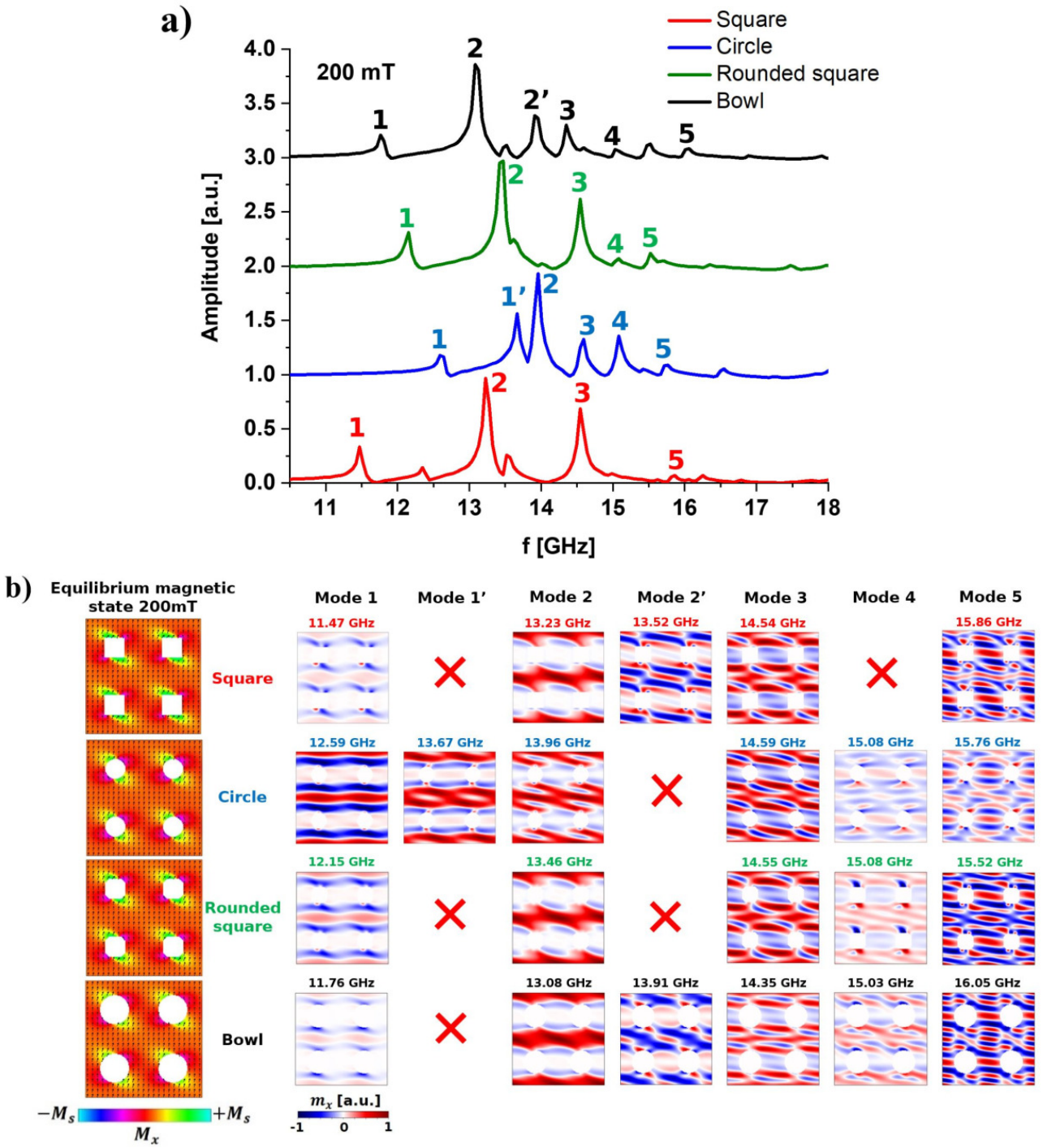

Figure 6.4: a) FFT spectra obtained from different antidot shapes shown in Figure 6.3 at $\mu_0 H_0 = 200$ mT (square in red curve, circle in blue curve, rounded square in green curve and bowl in black curve). The FFT spectra of each of these geometries were artificially shifted in amplitude for better visualization. The excited spin wave modes with quasi similar spatial profiles are indexed with numbers. b) The corresponding equilibrium magnetic states and spatial profiles of the excited spin wave modes of the different antidot geometries at $\mu_0 H_0 = 200$ mT. The color code used for the relaxed magnetic states is applied according to the amplitude of the x-component of the magnetization M_x. The calculation and color code for the spatial profiles of the excited spin wave modes are explained in section 3.1.4. A red cross indicates that the spin wave mode was not observed or too weak in amplitude.

local variations of shape and dimension of the antidots relative to each others (as can be seen in Figure 6.1 a)) occurring over the entire antidot lattice may be at the origin of the observed broadening and overlapping of the experimental resonance peaks. As in our experiment the applied field is swept at a fixed frequency, these local variations in the antidot shape and dimension result in small variations of the resonance field $\mu_0 H_r$ over the antidot lattice. This phenomenon thus induces a smearing out of the field resonance linewidths.

Additionally, the presence of satellite peaks close to the main modes, as can be observed in Figure 6.4 a) around the modes 2 and 3, can enhance the broadening of the resonance peaks. In contrast, as the modes 3 and 4 seem to be less sensitive to local geometrical variations, they should appear more discernible in the FMR spectra as can be seen in Figure 6.2. Another source of broadening of the lower frequency modes can come from modified magnetic parameters. For example, an increase of the damping coefficient up to 5.10^{-3} makes the satellite modes collapses on the closer main modes in the FFT spectra resulting in larger frequency linewidths.

Despite the fact that the frequencies of the dynamic modes for the geometries tested agree reasonably well with our experimental observations, we were not able to reproduce the most intense mode experimentally observed around $17.2\ \mathrm{GHz}$ at $200\ \mathrm{mT}$, neither in frequency nor in amplitude even when varying the antidot shape. The bowl shape, which is the closest geometry of the FIB-etched antidots observed on the SEM images, is not sufficient to explain this issue. To go further, we then needed to consider local modifications of the CMS magnetic properties arising from the Ga^+ FIB milling.

Consideration of local modified magnetic properties by Ga^+ FIB milling

As approached in chapter 4 section 4.2.2.1, high-energy incident Ga^+ ions can induce multiple collision cascades in the CMS crystal. This can result in the generation of Frenkel pairs, corresponding to the displacement of an atom leaving its initial place (vacancy) to lodge in-between other atoms (interstitial), or swaps between atoms due to the created vacancies. These phenomena have been observed for example in the case of irradiated CMS thin films with high-energy He^+ ions at $30\ \mathrm{keV}$ [274] or $150\ \mathrm{keV}$ [52, 53]. In particular, they both demonstrated that for low fluences (the number of incoming ions/cm²) of the order of 10^{14} to 10^{15}, the $\mathrm{B2}$ order is favored at the expense of the $\mathrm{L2_1}$ order due to induced $\mathrm{Mn/Si}$ swapping. For higher fluences, it was observed a degradation of the $\mathrm{L2_1}$ order with a decreased saturation magnetization M_s and an increase of the Gilbert damping factor α. Additionally to atomic disorder, implantation of Ga^+ ions can also occur during FIB milling. In particular, this could lead to the modification of the local CMS electronic structure in the regions nearby the etched antidots. These two effects, structural damages (atomic disorder) and Ga^+ implantation, which are illustrated in Figure 6.5 a), are material dependent and increase with the ions fluence. In the literature, it has been shown that Ga^+ irradiation may affect the magnetic properties of ferromagnetic thin films through reduced saturation magnetization, exchange constant and magneto-crystalline anisotropy [275–279]. The origin of these variations has been attributed to amorphization, Ga^+ implantation, chemical mixing or vacancy generation [280–282]. In Ref. [276], unexpected localized spin wave modes at low frequencies were measured in magnetic antidot lattices of CoPd/multilayers nanostructured by FIB etching with Ga^+ ions. The authors stated that they correspond to spin wave modes localized in a shell with modified magnetic properties around the antidots due to FIB milling. More precisely, they attribute the appearance of these modes to a local decrease of the perpendicular magneto-crystalline anisotropy in the shell region around the antidots which favors the magnetization to lie in the plane of the magnetic antidot lattice.

To determine the extent of the damaged CMS volume nearby the antidots, simulations of damage were performed with IPROS, a homemade Monte-Carlo software for ion implantation, by Dr. Alain Claverie of our research team. This simulation software considers stoichiometric amorphous materials and the crystal structure and binding energies are not taken into account. However, it gives a good

order of magnitude of the ion stopping range. The density of the CMS thin film is 8.85×10^{22} at/cm^3 (7.396 g/cm^3). We have found that the stopping range of incident 30 keV Ga^+ ions reaches a depth of 30 nm into the CMS alloy and lateral damages extend over 20 nm all around the trajectory of the incident ions. This damage volume around the antidots corresponds approximately to the difference of the antidot radius at the bottom of the antidots (140 nm) and at the top (200 nm). The lateral damage and ion implantation are most likely to vary gradually from the inner edge of the antidots to the bulk CMS and also from the top surface of the antidots through the CMS thickness [283]. Nevertheless, due to the complexity of a system with mixed disordered CMS atoms and implanted Ga^+ atoms, we tried to describe our system with a very simple model for the micromagnetic simulations. We have made the assumption that the impacted volume around the antidots is uniformly modified. For the micromagnetic simulations, the bowl shape was used with the addition of a volume of 200 nm diameter with degraded magnetic properties encircling the antidots. This unit cell model is shown in Figure 6.5 b), where the impacted volume is represented in light-grey color.

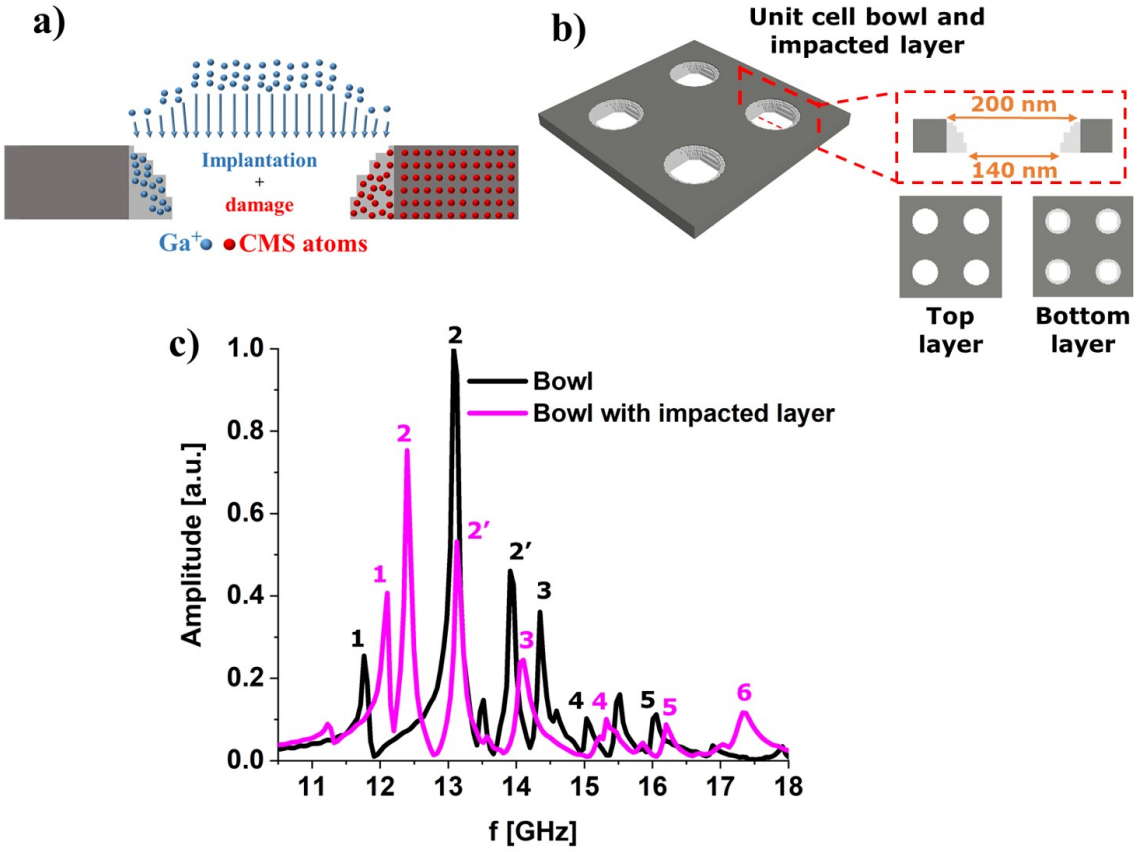

Figure 6.5: a) Schematic cross section of the lateral structural damage and Ga^+ implantation induced by the FIB milling around the antidots. b) Schematics of the unit cell comprising antidots with a bowl shape and a magnetic volume encircling the antidots impacted by FIB milling highlighted in lighter gray. c) FFT spectra of the bowl shape with no impacted volume (in black) and with an impacted volume around the antidots (in pink) at $\mu_0 H_0 = 200$ mT and with $\beta = 0.18$. The excited spin wave modes with relevant amplitudes are indexed with numbers. The amplitude of the FFT peaks was normalized according to the one of the most intense mode.

To perform the micromagnetic simulations, we needed to assess the damage factor of the magnetic properties in the impacted layer. To our knowledge, few studies on the interaction of Ga^+ ions with Heusler alloys exist. Among them, Hamrle et al. tackle this problem for ultra-thin Co_2FeSi film (11 nm) [275]. This Heusler alloy presents similar magnetic properties with the CMS Heusler alloy. In particular, the authors demonstrated that when increasing ion fluences, the material was progressively

modified from a ferromagnetic to a fully paramagnetic state when reaching an ion fluence threshold of 9.10^{16} ions/cm^2. They observed that even for moderate ion fluences of 6.10^{15} and 3.10^{14} ions/cm^2 the exchange constant and second order contributions to the spin-orbit coupling (which may affect the cubic crystal anisotropy) were respectively reduced. From the experimental conditions presented in chapter 4 section 4.2.2.2, we estimated the fluence of Ga^+ ions in the tail of our beam spot between 1.10^{18} and 1.10^{19} ions/cm^2 by considering 10% of ions in the tail. This fluence value is one order larger than the paramagnetic transition threshold fluence found in the works of Hamrle et al. [275]. Consequently, we expect a strong reduction of the CMS magnetic properties in the impacted volume around the antidots in our sample. As we have made the simple assumption of a uniform damaged volume, the values of the saturation magnetization M_s, the exchange constant A and the cubic crystal anisotropy constant K_{c1} were multiplied by a damage factor β while the damping factor α was divided by the same damage factor. To determine β, its value was varied until a qualitative and quantitative agreement between the calculated spin wave frequencies and the FM-FMR measurements was found. Values of β in the range 0.1 to 0.3 qualitatively fits the FM-FMR spectra, and the best agreement was found for $\beta = 0.18$.

An example of the microwave response at 200 mT of this unit cell comprising the bowl geometry with the impacted volume and a damage factor of $\beta = 0.18$ is shown in Figure 6.5 c) (pink curve). For this value of β, the impacted layer around the antidots is not fully paramagnetic but the magnetic properties are stongly reduced compared to their nominal values. In comparison, the microwave response of the magnonic crystal with the sole bowl geometry of the antidots (black curve) is also plotted. The spatial profiles of the spin wave modes of the damaged geometry at 200 mT can be found in Figure 6.6 b). First, one can observe that the frequencies of most of the spin wave modes in the case of an impacted volume are shifted towards lower frequencies compared to the spin wave modes in the case of the bowl shape alone, at the exception of the first mode. Due to the presence of the almost paramagnetic volume around the antidots, the situation is as if the antidots size was unintentionally increased. As a result, the spacing between the antidots is reduced resulting in an increase of the demagnetizing field along the y direction and by extension in a decrease of the effective field [284]. Concerning the first mode, its spatial profile (black star in Figure 6.6 b)) strongly resembles to the spatial profile of the mode 1' in the case of the circular antidot shape in Figure 6.4 b). Likewise, its frequency position is closer to the one of the mode 2. As the impacted layer around the antidots is defined circularly and uniformly, the damaged bowl geometry is brought closer to the case of a circular shape.

Finally, a sixth mode appears at 17.32 GHz with a relative intense amplitude. This mode matches the frequency position of the measured high frequency FMR signal that could not be retrieved previously without the consideration of the damaged layer around the antidots. To explain why it appears as an "intense" mode in the experiment we remind that the frequency positions of the modes 1 and 2 are strongly sensitive to local variations of the shape of the antidots, leading to low amplitudes and broad FMR signals. Contrary to the modes 1 and 2, the mode 6 is less sensitive to these variations as it results from the "virtual" increase of the antidots size related to damage. This may explain why this high frequency mode is less broadened and thus more intense in the FMR measurements. In other words it is not this mode which is intense, it is the others which are weak.

6.1.2 Evolution of the spin wave spatial profiles with the magnetic field

To go further in the analysis of our measurements, we now describe the evolution of the spin wave frequencies and profiles with the applied field $\mu_0 H_0$. For this, we calculated the equilibrium magnetic states and the spatial profiles of the main spin wave modes for the impacted bowl geometry with $\beta = 0.18$ and for $\mu_0 H_0 = 250, 200, 150, 100, 50, 0$ mT. The results are shown in Figures 6.6 a) and b) and examples of FFT spectrum are shown in Figure 6.7. The magnetic states in Figure 6.6 a) have

been plotted for the top plane of the antidot lattice. The main spin wave modes have been indexed with colored symbols which have been reproduced also in Figure 6.2. We applied the following strategy to attribute a symbol and a color to each mode. A same color is used to identify the modes with roughly similar spatial profiles and following a same $f(H_0)$ tendency that can be observed in Figure 6.2. In addition, the change of symbol indicates a drastic change in the spin wave mode profile. It is to be noted that red crosses are put in Figure 6.6 b) when a mode "disappears" (non observed or too weak amplitude) while a blank space means that the mode profile is quite equivalent to the one shown at a higher field. From Figure 6.2, the calculated dynamic modes appear to be in very good agreement with the microwave spectrum.

We first discuss the evolution of the relaxed (i.e. equilibrium) magnetic states with respect to the amplitude of the applied field. It is clear that the equilibrium magnetic configuration strongly varies with the amplitude of H_0 as can be seen in Figure 6.6 a). At 250 mT, the magnetization is quasi-uniformly oriented along the direction of H_0 (y direction) except on the edges of the antidots where the demagnetizing field is strong, leading to a local rotation of the magnetization roughly along x. Since these edge domains involve that the magnetization is not fully aligned with H_0 everywhere, this equilibrium state is referred to as quasi-saturated. It is to be noted that edge domains are still present for applied fields as high as 300 mT. The spatial profiles of the spin wave modes excited in this quasi-saturated configuration are taken as the reference to describe the modes at lower H_0 values. They are all indexed with a square symbol colored differently according to the $f(H_0)$ tendency.

While the applied magnetic field is decreased down to 150 mT, the equilibrium magnetic states do not change drastically and can still be classified as quasi-saturated states. Therefore, there are almost no changes in the spatial profiles of the calculated spin wave modes except for the modes 1 and 4. However, at 100 mT, one can observe in Figure 6.6 a) that edge domains start to extend in the diagonal of the antidot lattice but a horizontal channel with some part of the magnetization aligned in the direction of H_0 is still "opened". The spatial profiles of the spin wave modes are either only slightly changed (mode 1, 2, 2', 3, 6) or not present (modes 4 and 5). Lowering further the H_0 values, the equilibrium states become strongly non-uniform with the generation of magnetic domains between diagonally opposite antidots. At 50 mT, the magnetization in these domains is aligned roughly along the diagonal of the unit cell, i.e. approximately at $45°$ from the x axis. These domains are quite similar to the $45°$ domains discussed in chapter 5. As the equilibrium magnetic state is non-uniform, the spatial profiles of the excited spin wave modes differ significantly from those in the quasi-saturated states. Only the mode 2' is not significantly different as its spatial profile already connects two diagonally opposite antidots even in the quasi-saturated state. Finally, when reaching 0 mT, the remanent magnetic state is organized in a zig-zag configuration [49, 265] of large magnetic domains where the magnetization lies along the x or y directions in-between vertical columns or horizontal rows of antidots respectively. A large magnetic domain with the magnetization oriented along the $45°$ direction can also be observed in the central part of the unit cell. This mode is reminiscent of the remanent states obtained with a magnetic antidot lattice with the CMS magnetic properties but without cubic crystal anisotropy as seen in chapter 5 section 5.1.2. In fact, the artificial increase of diameters of the antidots due to the damaged layer induces a strong local demagnetizing field prevailing over the cubic crystal anisotropy field. Then the magnetization is oriented in such a way to decrease the local demagnetizing energy. Such strong non-uniform magnetic states induce complex spin wave mode profiles. For the main mode (mode 6), the precession is mainly localized in the $45°$ domains with a quantization of the wavevector along the diagonal of the unit cell. Finally, we mention that the edge mode (yellow square) found in the micromagnetic simulations were not observed experimentally, except at very low field. It is usually difficult to observe the collective response of this mode [220]. This difficulty is generally attributed to their sensitivity to edge roughness and shape of the antidots as they are strongly confined at the vicinity of the antidots. Our guess is that once again it is related to the geometrical and magnetic variations across the sample. This mode indeed becomes more and more

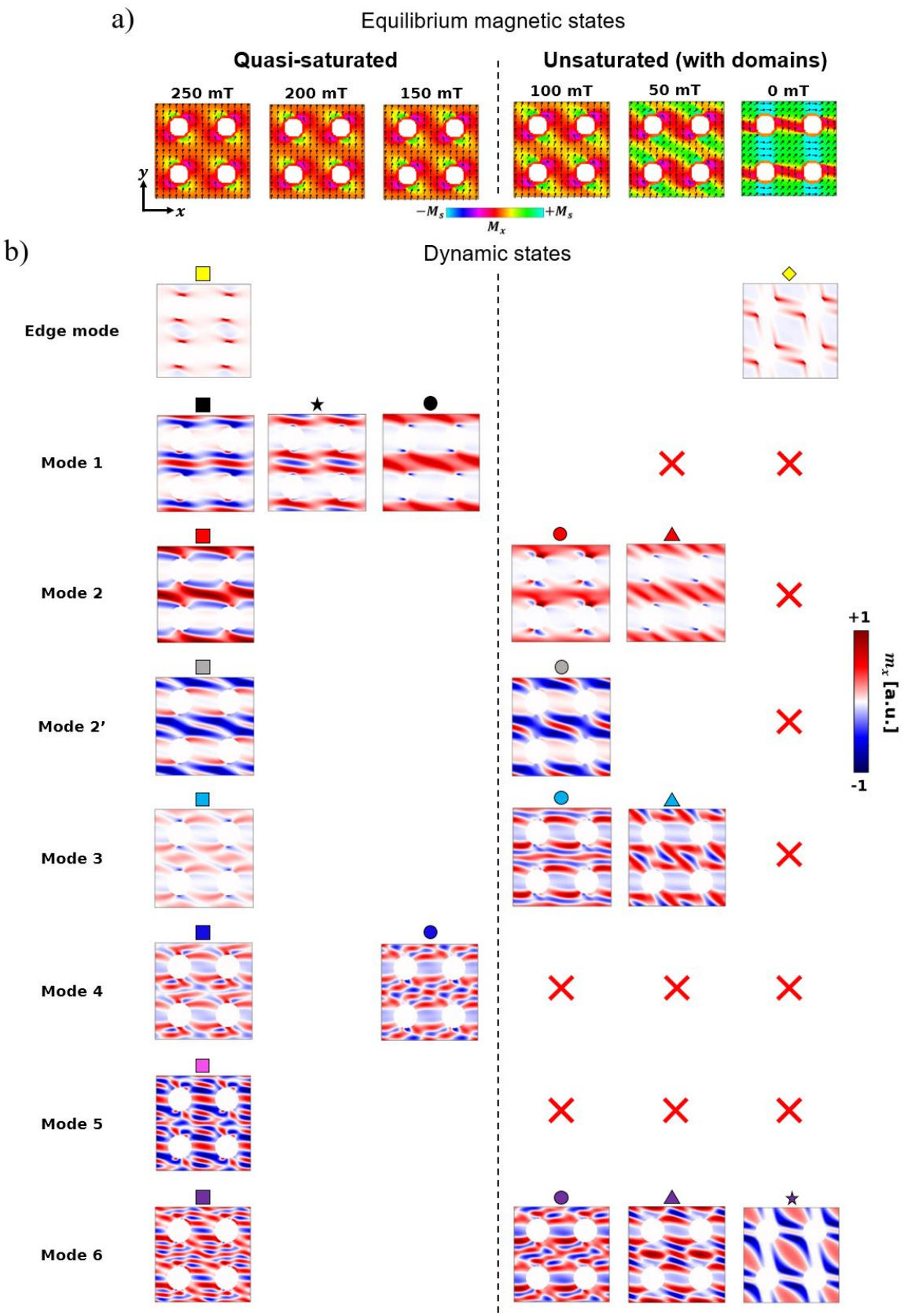

Figure 6.6: a) Equilibrium magnetic states for different values of $\mu_0 H_0$. The colorbar is color coded according to the x-component value of the magnetization M_x. b) Spatial profiles of the main excited spin wave modes (indexed with numbers and colored symbols) for different values of $\mu_0 H_0$. These spatial profiles correspond to temporal snapshots of the calculated dynamic x-component of the magnetization m_x as detailed in chapter 3 3.1.4. The m_x component of each mode is normalized according to its own maximum amplitude. A same symbol color is used to identify modes with roughly similar spatial profiles and following a same $f(H_0)$ tendency in Figure 6.2. A change of symbol indicates a drastic change in the mode spatial profile, a red cross, that the mode was not observed and a blank space, that the mode profile is quite equivalent to the one at a higher field.

localized within the edge domains as the field is increased (see yellow square and diamond in 6.6 b)). Thus it is one of the most sensitive mode to local magnetic and geometrical imperfections leading to a rapid and large broadening of the signal.

In the simulations, the transition field from the unsaturated (where large magnetic domains appear) to quasi-saturated states (where most of the magnetization is aligned along H_0) is between 100 and 150 mT. From the microwave measurements, it is relatively difficult to determine this transition region. To explain this, we recall that it is obvious that the transition field depends not only on the geometrical variations of the antidots but also on the local variations of magnetic properties induced by Ga^+ etching. For example if β is close to 1, then the transition field will be lowered as the antidots look artificially further from each other. In opposite if β tends to 0, antidots look artificially nearer leading to an increase of the transition field due to an increase of the demagnetizing field betweeen the antidots. Therefore, the local variations of antidot shapes and damage in our sample are most probably at the origin of the large variations of the transition field across the sample. This could explain the strong red contrast observed from $150\ \mathrm{mT}$ to $50\ \mathrm{mT}$ in Figure 6.2 as one can expect to encounter multiple spin wave modes in this transition "zone".

Finally, we discuss the evolution of the spin wave mode spatial profiles and amplitudes with the external field. It is obvious that most of the modes can not present the same spatial profiles when the equilibrium state goes from the quasi-saturated to the unsaturated one, mainly due to the domain formation and domain walls acting as boundaries for spin wave modes. For example, the extended modes (mode 1 and 2) in the quasi-saturated states can no more spread over the x direction below $50\ \mathrm{mT}$. Also, one may think that a strong modification of the spatial profile could lead to an abrupt variation of the frequency of the mode. This can be the case for the mode 3 (blue square), in particular if one looks at its frequency position at 50 and $200\ \mathrm{mT}$ in Figure 6.2. However our simulations show that it is not the case for all the other modes. The example of mode 6 particularly highlights this point. As an example, the FFT spectra at $200\mathrm{mT}$ and $100\mathrm{mT}$ are shown in Figure 6.7. The purple

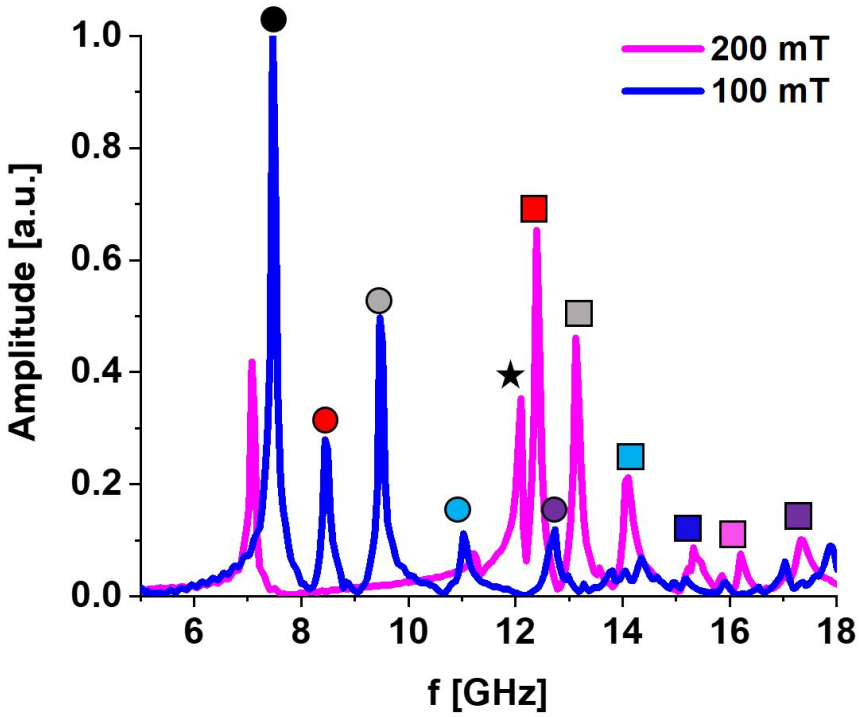

Figure 6.7: FFT spectra in the case of the bowl shape with the impacted volume around the antidots with $\beta = 0.18$ at $200\ \mathrm{mT}$ (pink curve) and $100\ \mathrm{mT}$ (blue curve). The amplitude is normalized according to the maximum of amplitude of the FFT curve at $100\ \mathrm{mT}$. The main spin wave modes are indexed with colored symbols that can also be found in Figure 6.2 and their spatial profiles in Figure 6.6.

mode is always the most intense at the highest frequency but it can be seen in Figure 6.6 b) that the spatial profile is not the same for the two different field values. The FFT spectrum at 100 mT also shows a series of very small and broad peaks at frequencies above 14 GHz which might correspond to the green contrast in Figure 6.2. The FFT spectra describe also the appearance of modes 4 (dark blue square) and 5 (pink square) at $200\ \mathrm{mT}$ which present weak amplitudes such as observed in the experimental measurements, while they collapse and disappear at the transition field.

Conclusion

To conclude, we performed FMR measurements on a CMS magnonic crystal patterned by FIB with a periodic lattice of antidots. We demonstrated the importance of considering both the geometrical and magnetic variations arising from FIB milling in order to explain qualitatively and quantitatively the microwave response of this magnonic crystal in the entire field range (from quasi-saturated to unsaturated states). A simple model was used in the numerical simulations to assess the local variations of the CMS magnetic properties. The good agreement of this simplified model with the experimental results suggests that the magnetic properties of the Ga^+ irradiated volume of CMS nearby the antidots are strongly reduced but without reaching a full paramagnetic state. However, a full modeling would imply further studies on the variation of the CMS magnetic properties with respect to applied Ga^+ fluences. With this model, we stated that the variations of magnetic parameters result in the excitation of a high-frequency spin wave mode which probably would not exist in perfect structures. While other simulated spin wave modes are well consistent with the experimental measurements, we assume that small variations of geometry and magnetic properties over the whole sample is at the origin of the large measured absorption band. While strategies can be set to reduce geometrical imperfections during FIB milling as discussed in chapter 4 section 4.2.2.2, it is clear that implantation will remain a major limitation to achieve CMS magnonic crystal with this approach.

6.2 Study of a Co_2MnSi magnetic antidot lattice made by e-beam lithography and ion beam etching

This section is devoted to the microwave study of the magnonic crystal nanostructured by e-beam lithography and ion beam etching (sample #2) detailed in chapter 4 sections 4.2.3.3 and 4.3. As for the sample #1, we recall first the characteristics of this crystal for the sake of clarity. The fabricated CMS magnetic antidot lattice is composed of a periodic square lattice of square antidots of lateral dimensions $200 \pm 10\ \mathrm{nm}$ and spacing $600 \pm 10\ \mathrm{nm}$ (periodicity $800 \pm 10\ \mathrm{nm}$) as can be seen on the SEM images in Figures 6.8 a) and b). The antidot lattice covers an area of $70 \times 70\ \mu\mathrm{m}^2$. The thickness of the CMS thin film is of $45\ \mathrm{nm}$. On the SEM images in Figures 6.8 a) and b), one can observe that the square shape and size of the holes are well respected and that the edges of the antidots are rather straight as wanted. Some resist residues are still around some antidots as explained in chapter 4 section 4.2.3.3. Such achieved antidots contrast with those obtained by FIB patterning, and this will significantly improve the measurements, as discussed below.

For this sample, two areas of the CMS thin film on both sides of the magnonic crystal were not nanostructured to deposit electrical contacts. We initially planned to study the evolution of the magnonic crystal microwave response with respect to an applied DC or RF electrical current. These measurements will not be presented in this manuscript as the data treatment and interpretation could not have been yet performed by the end of the manuscript. The microwave response of the crystal is measured via a micro-antenna placed above the magnonic crystal. The magnetic field $\mu_0 H_0$ is applied perpendicularly to the generated dynamic pumping field h_{RF} (MSSW configuration) to maximize the amplitude of the measured signals as illustrated in Figures 6.8 c) and d).

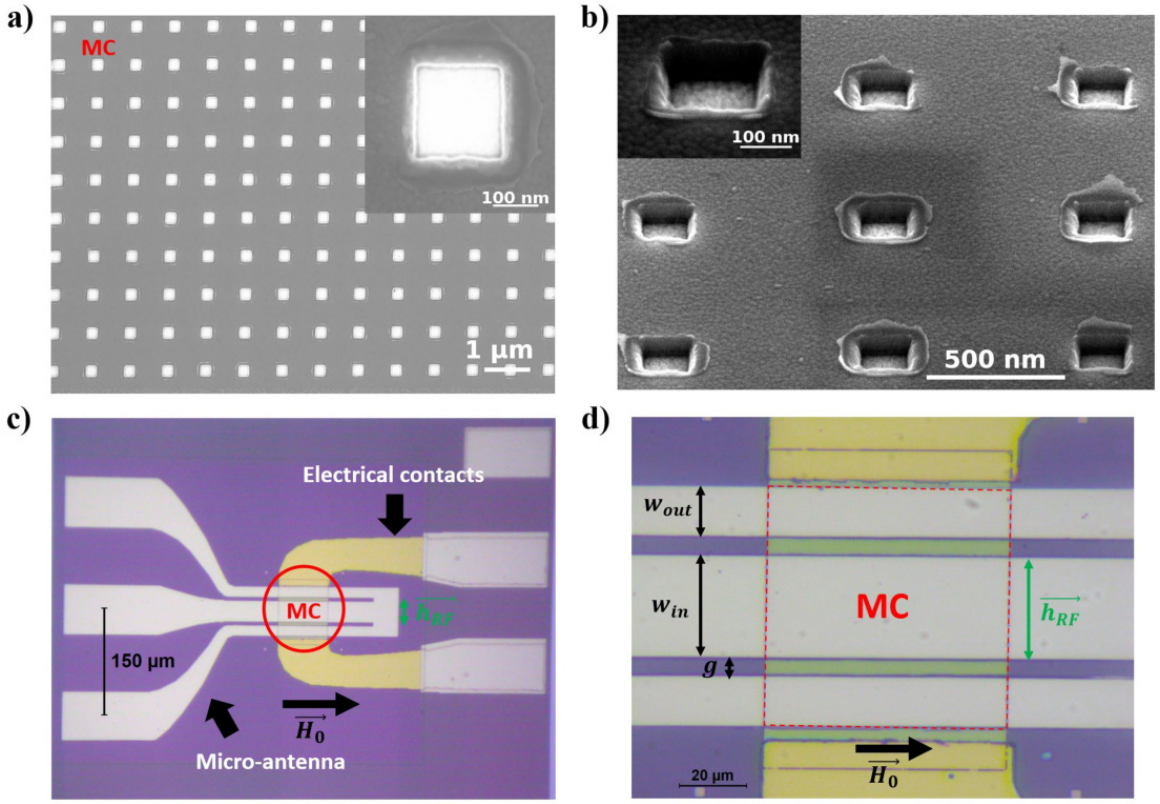

Figure 6.8: SEM images of the CMS magnetic antidot lattice made by EBL and IBE (sample # 2) at a) a top view and b) a tilted angle of 52°. Optical images of a) the overall device (sample # 2) comprising the CMS magnonic crystal (MC) with electrical contacts and a micro-antenna placed above, and c) the zoomed in on the micro-antenna showing its entire position (outer conductors included) on the magnonic crystal. w_{in} and w_{out} are respectively the inner and outer conductor widths, and g the spacing between the inner and outer conductors. The magnetic field $\vec{H}_0$ is applied parallel to the length of the micro-antenna (MSSW configuration).

As explained in chapter 4 section 4.3.2.1, the entire CPW (with the ground conductors included) covers the magnonic crystal leading to a non uniform pumping field over the entire magnonic crystal. Spin waves with a finite wavevector can then be excited. Due to the large widths of the conductors (in the order of tens of μm) compared to the CMS exchange length ($\approx$ 5 nm), only magnetostatic spin waves (long wavelength) can be excited. The maximum wavevector that can be excited depends approximately on the width of the conductor, which is here $k_{max} \approx \frac{2\pi}{w_{in}} = 0.209\ rad\mu\mathrm{m}^{-1}$. We tried to evaluate the influence of this inhomogeneous pumping RF field. For this we calculated the difference between the $k = 0$ FMR frequency as a function of the applied field H_0, $f_{k=0}(H_0)$, and the one for $k = k_{max}$, $f_{k=k_{max}}(H_0)$. As our thin film is patterned it is not relevant to use the analytical formula for thin films (1.74) (MSSW configuration) [200]. As discussed in chapter 2, the horizontal channels of a magnetic antidot lattice transversely magnetized can be assimilated to effective stripes [158] in which spin waves can propagate. Thus to determine approximately the frequency shift induced by the micro-antenna, we calculated the difference between $f_{k=k_{max}}(H_0)$ and $f_{k=0}(H_0)$ with the analytical formula (1.88) presented in chapter 1 1.4.4 for the quantized spin wave modes with $n = 1, 3$ and 5 in a transversely magnetized waveguide of width 600 nm corresponding to the spacing between the antidots. These results are plotted in Figure 6.9. The frequency shift depends on the applied magnetic field value $\mu_0 H_0$ and on the quantization number n. At maximum the frequency shift is of around 30 MHz. These results only constitute approximations as the FMR of a magnetic antidot lattice is more complex than this simple case and we can not predict the frequency shift of the localized modes with this method. However, the frequency shift is very weak and then we consider relevant to simulate a uniform RF pumping field in the micromagnetic simulations. We will see below that this approach

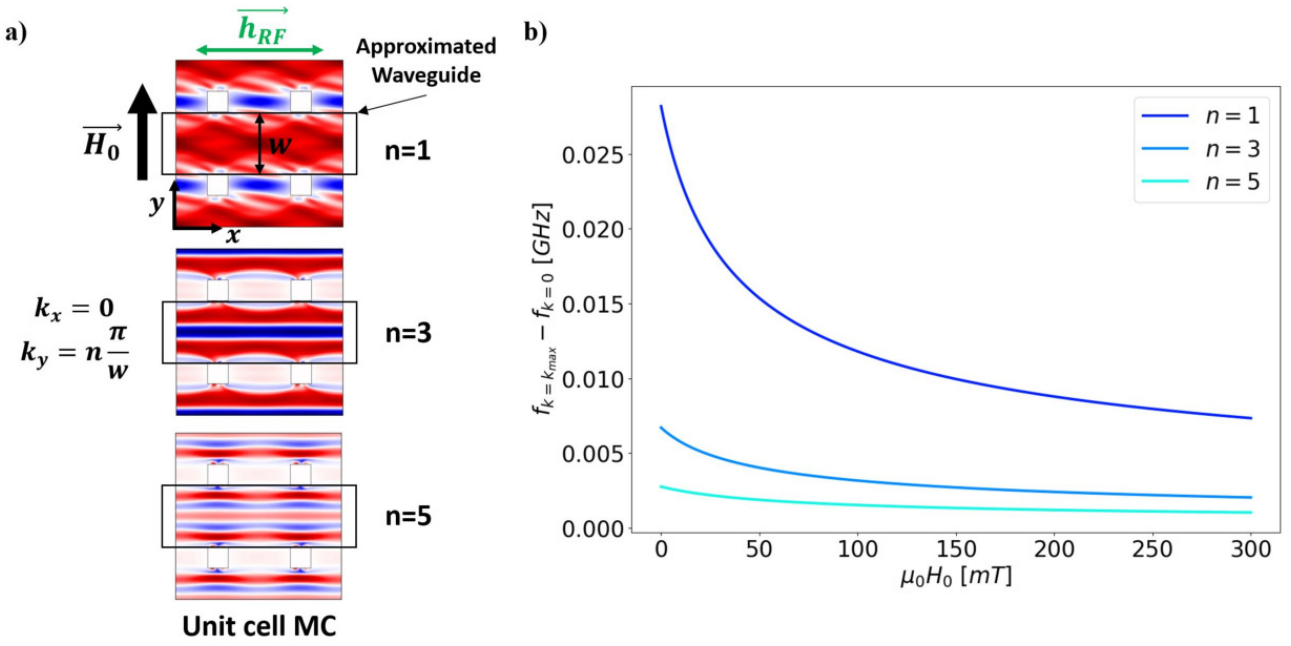

Figure 6.9: a) Schematic of quantized ($n = 1, 3, 5$) extended modes spatial profiles in a magnetic antidot lattice (MC) whose horizontal channels are transversely magnetized along $\vec{H}_0$. These quantized modes can be approximated with quantized modes in a transversely magnetized waveguide of the same width as the horizontal channels of the MC. b) Frequency difference between $f_{k=k_{max}}(H_0)$ and $f_{k=0}(H_0)$ for quantized spin wave modes $n = 1, 3, 5$ in a transversely magnetized waveguide of width 600 nm.

is validated by the good agreement between the experimental and simulated results.

6.2.1 Ferromagnetic Resonance measurements

FM-FMR measurements were performed on this sample #2 as detailed in chapter 3 section 3.3.2. The microwave absorption spectra $f(H_0)$ are shown in Figure 6.10. Micromagnetic simulations were performed on a unit cell with 2D PBC of a square antidot lattice with squared antidots of size $s = 200$ nm and spacing $d = 600$ nm. The magnetic parameters used in the simulations are summarized in Table 6.2 and were measured on another piece of unpatterned CMS thin film from the same deposition batch. The numerical procedure is the same as detailed in chapter 3 section 3.1. The calculated

Saturation magnetization M_s [T]	**Cubic crystal anisotropy field** H_k [mT]	**Cubic crystal anisotropy constant** K_{c1} [J m^{-3}]	**Gyromagnetic ratio** $\frac{\gamma}{2\pi}$ [GHz T^{-1}]	**Exchange constant** A [pJ m^{-1}]
1.28	20	-10186	28.8	21.5

Table 6.2: CMS magnetic properties used for the micromagnetic simulations for the device #2.

equilibrium magnetic configurations and spin wave mode spatial profiles for different values of H_0 are presented in Figures 6.12 and 6.11 respectively. The plotted spatial profiles were obtained for the top plane of the magnonic crystal. In the simulations, colored symbols were used to index the individual spin wave modes with similar spatial profile as can be seen in Figure 6.15 later discussed. Contrary to the sample #1, the spatial profiles of the main modes do not vary much with H_0. The frequency positions of these different spin wave modes are superposed in Figure 6.10 with indexed

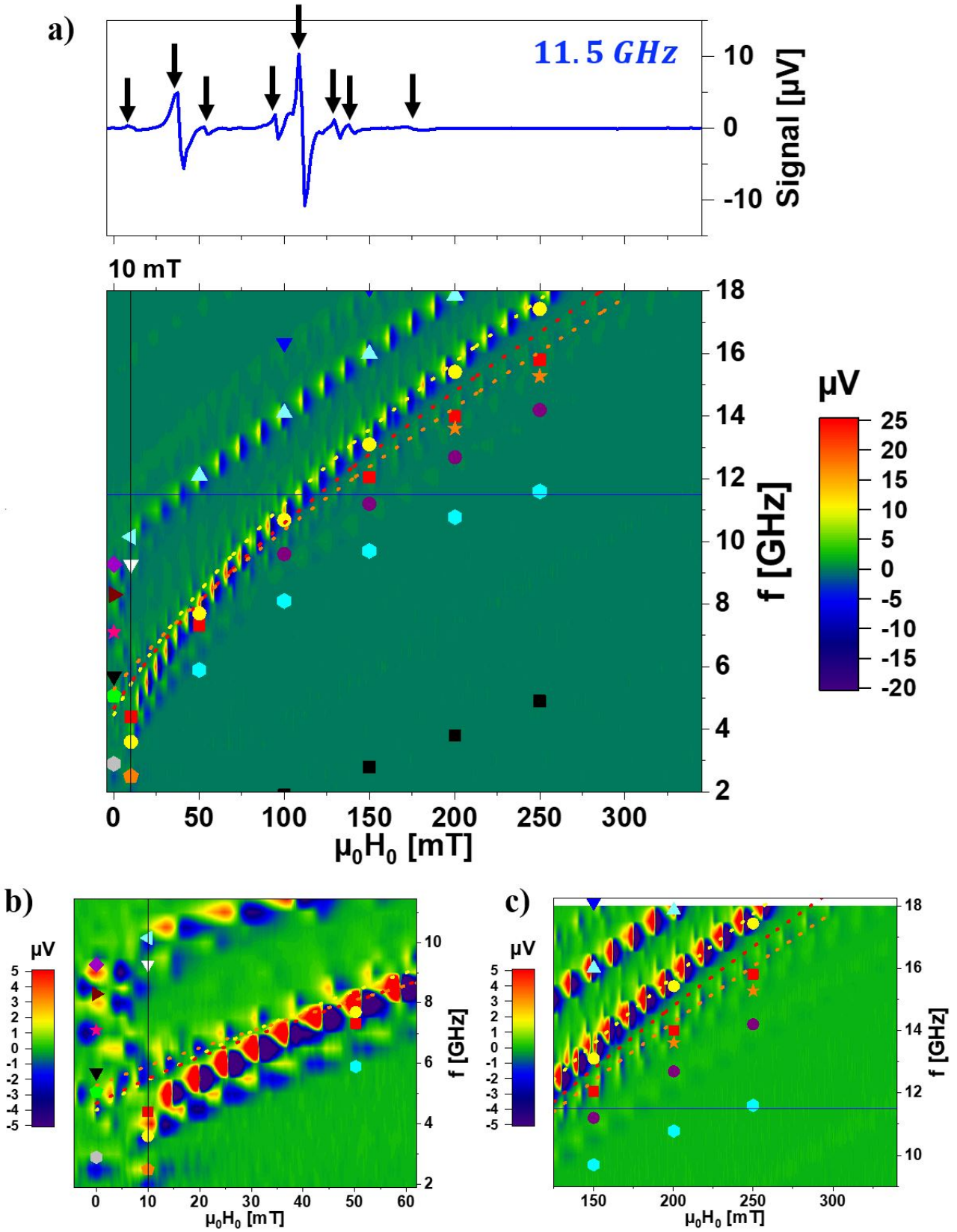

Figure 6.10: a) Evolution of the microwave power absorbed by the CMS magnetic antidot lattice nanostructured by EBL and IBE (sample #2) according to the applied magnetic field $\mu_0 H_0$ and frequency f. The amplitude of the FMR signal is color coded with the colorbar on the left. An example of the FMR spectrum measured at 11.5 GHz is shown at the top of the main figure (blue line). The black arrows indicate the excited spin wave modes. The colored symbols correspond to the frequency positions of the simulated spin wave modes for different field values. These symbols are the same as those in Figure 6.11. The dotted lines correspond to $f_n(H_0)$ analytical curves ($n = 1$ (yellow), 3 (red), 5 (orange)) calculated in the case of modes in a 600 nm wide CMS waveguide with (1.88). b) Zoomed plot of a) for $\mu_0 H_0 \leq 60\text{mT}$, c) for $\mu_0 H_0 \geq 125\text{mT}$.

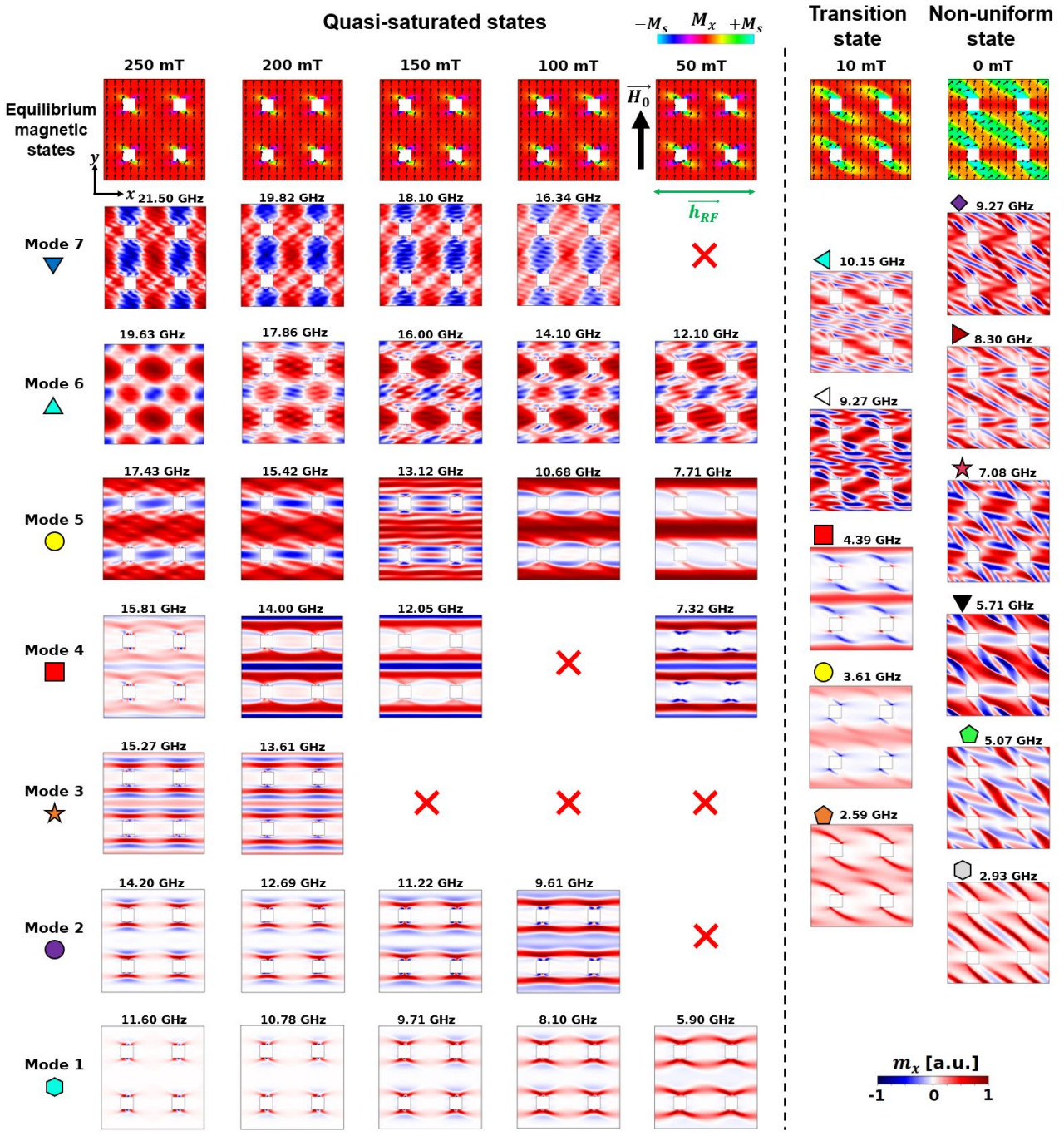

Figure 6.11: (Top) Equilibrium magnetic states for different values of $\mu_0 H_0$ of the simulated CMS magnetic antidot lattice of sample #2. The latter can also be better visualized in Figure 6.12. The colorbar is color coded according to the x-component value of the magnetization M_x. (Bottom) Simulated spatial profiles of the main excited spin wave modes (indexed with numbers and colored symbols) for different values of $\mu_0 H_0$. These spatial profiles correspond to temporal snapshots of the dynamic m_x calculated as detailed in chapter 3 3.1.4. The m_x component of each mode is normalized according to its own maximum amplitude. Each color and symbol corresponds to excited spin wave modes with a similar spatial profile. A red cross corresponds to the non-observation of a spin wave mode in the simulations due to a too weak amplitude. The black square symbol and number 0 in Figures 6.10 and 6.15 correspond to an edge mode with a spatial profile at $\mu_0 H_0 = 250$ mT shown in Figure 6.13 (left). As this spatial profile is rather similar for the other field values and as this mode was not observed experimentally, the evolution of its spatial profile with the applied field is not shown here for better visualization of the other modes.

colored symbols. We recall that the terms indicating specific regions of the magnetic antidot lattice (horizontal channels, horizontal rows of antidots...) that will be used in the text are defined in Figure 2.4 of chapter 2.

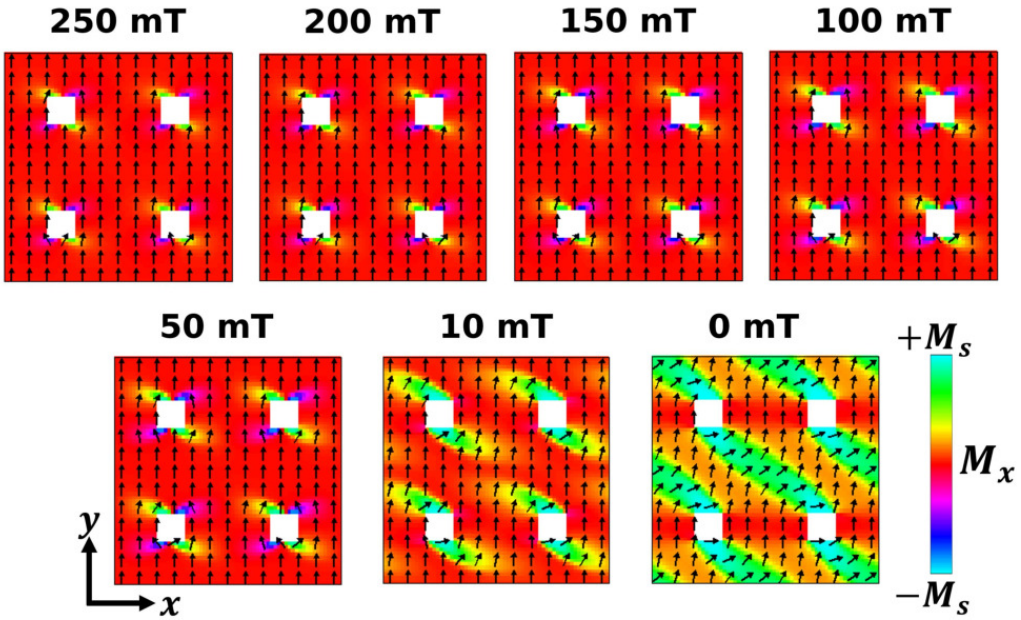

Figure 6.12: Equilibrium magnetic states of the simulated unit cells of sample #2 for different values of $\mu_0 H_0$. The colorbar is color coded according to the x-component value of the magnetization M_x.

Even though the targeted antidot size and spacing are larger in this sample compared to the one etched by FIB (sample #1) , it is possible to make general comments on the aspect of both microwave spectra. The most striking difference is that the microwave signal of the different spin wave modes are much well resolved for this sample. As a consequence we do not have a large absorption band as for the sample #1 but well resolved peaks. This can be observed for example in the inset of Figure 6.10 a), showing the measured signal at $f = 11.5$ GHz. Eight absorption peaks (pointed by black arrows) with different field linewidths are clearly and individually distinguished over a wide field range from 345 to 10 mT.

Over the whole FMR spectra, high amplitudes reaching up to 25 μV could be measured owing to the low field linewidths of the signals. The field linewidths of the different modes range between around 2 mT for the most intense mode (yellow mode, at 58 mT and 8.5 GHz) to around 6 mT for the weakest signals that can be found at high magnetic field and frequency values. Contrary to the sample #1, sample #2 presents small geometrical variations of the holes shape and size over the entire lattice. Such feature prevents from the broadening of the field linewidths. In addition, the high amplitudes and good field resolution of the different peaks in the microwave spectrum allow to clearly observe the splitting of the different excited spin wave modes with the increase of H_0. A part of these splittings may result from the quantization of the spin wave modes in the channels of the antidot lattice [225, 285]. In transversely magnetized waveguide structures, it has been shown that the boundary conditions (finite width of the waveguide) cause spin wave mode splitting due to the formation of standing spin waves along the width of the waveguide [286]. Other splittings could come from the non-uniform demagnetizing field owing to the periodic presence of antidots which also leads to the excitation of non-uniform spin wave modes [287]. Below 10 mT, one enters in the unsaturated regime as can be seen on the magnetic configurations at equilibrium in Figure 6.12 leading to less pronounced signals as will be discussed later in this section.

From Figure 6.10 a), one can observe that the frequencies of the simulated spin wave modes (shown with colored symbols) in perfectly squared antidots with nominal size and spacing are already

in excellent qualitative and quantitative agreement with the experimental measurements. As a result, contrary to the sample #1, it was not required to model a complex geometry of the antidots nor to introduce chemical or magnetic variations around the antidots to recover the measured absorption signals. Then, concerning IBE with accelerated Ar^+ ions, the use of a relatively thick resist mask (around 300 nm) prevents the CMS sample from surface and in-depth Ar^+ irradiation of the CMS volumes nearby the antidots. In the case of lateral Ar^+ irradiation that can occur during the etching of the antidots, these inert-gas ions with low energy 1 keV may less damage the surrounding CMS volumes.

Description of the excited spin wave mode profiles in quasi-saturated magnetic configurations

The evolution of the equilibrium magnetic states as a function of the applied field value is shown in Figure 6.12, while Figure 6.11 summarizes the different spin wave modes obtained from the FFT spectra (examples of FFT spectra are presented later in Figure 6.15 and 6.18). The equilibrium states are quasi-uniform between 250 and 50 mT. However, even at very low field values such as 10 mT, the central portion of the horizontal channels with a magnetization aligned along H_0 are still observed and it is only at remanence that a full 45° domain appears in the middle of the unit cell, with the magnetization along its diagonal. The very good agreement between our simulations and the FMR spectra allows to state that the different $f(H_0)$ trends in Figure 6.10 a) and c) correspond to specific spin wave modes whose spatial profile does not change significantly with the decreasing of $\mu_0 H_0$ down to 50 mT.

The black squares correspond to the edge modes as defined in chapter 2 section 2.1.3 and an example is shown in Figure 6.13 (left) for $\mu_0 H_0 = 250$ mT. As for the sample #1 these particular modes were not measured in the quasi-saturated states. They strongly depend on the shape and edge roughness of the antidots making it difficult to observe them from a collective response [220]. The mode 1 (cyan hexagon) is the first mode in frequency that can be observed in the FFT spectra right after the edge mode. While we detect it in the FMR spectra for 50 mT $\leq \mu_0 H_0 <$ 100 mT, we were not able to measure it clearly for higher fields. Looking at its spatial profile can help to understand such observation. As the amplitude of $\mu_0 H_0$ increases, this mode resembles more and more a localized edge mode but as if it was quantized with 3 antinodes ($n = 3$) in the edge domains as can be seen in Figure 6.13 (right). Its resemblance with an edge mode involves that this mode is sensitive

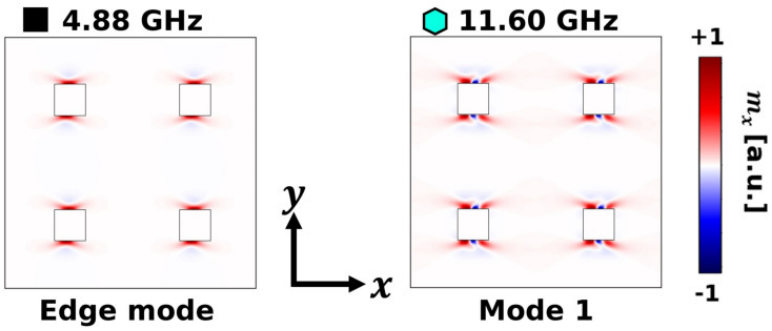

Figure 6.13: Temporal snapshot of the spatial profiles of the dynamic m_x in the plane of the unit cell for the edge mode (left) and for the mode 1 (right) at $\mu_0 H_0 = 250$ mT. The m_x component of each mode is normalized according to its own maximum amplitude.

to the antidot shape, size and roughness, the variations of which may explain why we do not detect it at high fiels. However when $\mu_0 H_0 \leq$ 100 mT, the magnetization precession of this mode further extends along the x axis, linking horizontally neighbouring antidots and giving rise to the precession of a larger magnetic volume. As a result, the precession of the magnetization may become less sensitive to edge roughness of the antidots leading to the better detection of the collective response

of this mode. This mode is reminiscent of the edge mode that can form and extend in transversely magnetized waveguides [104]. In the FM-FMR measurements at $50\ \mathrm{mT}$, this mode is shifted of about $+600\ \mathrm{MHz}$ compared to its frequency position found numerically.

Higher frequency modes (mode 2 to mode 7 in Figure 6.11) are well retrieved in the experimental measurements. The evolution of the spatial profile of the mode 2 (purple circle) is quite similar to the one of the mode 1 as the dynamic precession is focused more and more within the edge domains when $\mu_0 H_0 \geq 200\ \mathrm{mT}$. This may explain why it seems to disappear when increasing further the field. In addition, for $100\ \mathrm{mT} \leq \mu_0 H_0 \leq 150\ \mathrm{mT}$, the maximum precession amplitude of the mode 2 extends in small horizontal channels connecting the antidots along the x direction. At $50\ \mathrm{mT}$, the spatial profile of the mode 2 tends to resemble the spatial profile of mode 4 (red square). Further reducing $\mu_0 H_0$ down to $50\ \mathrm{mT}$ results in the "collapse" of the mode 2 on the mode 4 whose spatial profiles become similar.

The modes 3 (orange star), 4 (red square) and 5 (yellow circle) correspond to well-known spin wave modes excited in magnetic antidot lattices that can be found in the litterature [288] as approached in chapter 2 section 2.1.3 concerning the mode 4. These spin wave modes are analog to extended modes in the horizontal channels (along x, $k_x = 0$), with a quantization of their wavevector $k_{n,y} = n\pi/w_{eff}$ (w_{eff} effective width of the quantized modes) between vertical antidots along y with 5, 3 and 1 antinodes (quantization number $n = 5, 3, 1$) for the modes 3,4 and 5 respectively. As mentioned previously, these modes can usually be approximated by quantized spin wave modes that can form in magnetic waveguides with an effective width close to the spacing of the antidots [158]. For comparison, we calculated the analytical $f_n(H_0)$ curves for these effective stripes spin wave modes with the CMS magnetic parameters from Table 6.2 via the formula (1.88) approached in chapter 1 section 1.4.4. These curves are shown in yellow, red and orange dotted lines in Figure 6.10 for the respective quantization numbers $n = 1, 3, 5$. One can observe that the analytical $f_{n=1}(H_0)$ curve (calculated with (1.88)) in Figures 6.10 a) and c) quantitatively fits the experimental signal showing the highest absorption amplitude and corresponding to the simulated mode indexed with a yellow circle. Concerning the two other analytical $f_n(H_0)$ curves for $n = 3$ and $n = 5$, they only qualitatively match the experimental signals and the frequencies deduced from the micromagnetic simulations. This larger discrepancy may be explained by the fact that the spatial profiles of these two modes present non ideal antinodes profiles compared to those that can form in a stripe. In addition, the effective width of the area where the magnetization precesses depends on the size of the edge domains which vary with field. This variation of effective width is not taken into account in the theoretical model. This is particularly true for the mode 4. Even though these analytical $f_n(H_0)$ curves only constitute approximations of the quantized extended spin wave modes appearing in the horizontal channels of the magnonic crystal, they are consistent with the FMR signals found experimentally and thus further confirm the associated spin wave mode profiles found numerically. These curves are however only relevant for quasi-saturated magnetic states (in Figure 6.12) from 250 to $50\ \mathrm{mT}$ as the analytical formula do not take into accound unsaturated configurations of the magnetization.

The mode 6 (cyan triangle) corresponds to a localized mode as the maximum of the magnetization precession is confined in the horizontal rows of antidots. This mode also seems to present a quantized precession with a non null wavevector along the x direction $k_x \neq 0$ in the horizontal channels. One can notice that when the amplitude of the applied field increases, the amplitude of the FM-FMR signals corresponding to the localized mode 6 (cyan triangle) or the extended modes (5,3,1) respectively increases and decreases. This amplitude evolution with field in the case of the extended modes is consistent with FM-FMR measurements on plain magnetic thin films as owing to the Gilbert damping, the field linewidth of the FMR signal increases with the frequency. This thus leads to the decrease of the amplitude of the FM-FMR signal as the total area under the peak is mostly conserved. Finally, the mode 7 (blue triangle) possess weak amplitudes in the simulations and in the FM-FMR measurements, and seems to resemble a MSSW spin wave mode with a quantized wavevector along x linked to the periodicity a of the antidot lattice: $k_x \approx 2\pi/a$.

Influence of the demagnetizing field on the evolution of the extended spin wave mode profiles with the applied field

In Figure 6.11, one can notice that the spatial profile of the most intense spin wave mode, the mode 5, is not exactly the same for field values between 250 to 150 mT on one hand and for 100 to 50 mT on the other hand while being in quasi-saturated magnetic states (Fig. 6.12). For example, we observe that for high applied fields, the magnetization precesses in phase opposition between the horizontal channels and the horizontal rows of antidots, while in a simplified way, it precesses only in the horizontal channels for 100 to 50 mT. Moreover, in Figure 6.11, we can observe some small oscillations of the dynamic m_x amplitude along the x direction in the horizontal channels for 250 to 150 mT while the precession amplitude seems to be more uniform along x for 100 to 50 mT.

These complex spatial profiles may result from changes in the distribution of the dipolar field between the antidots [289]. Indeed, for large values of H_0 applied along y, the magnetization tends to align with the applied field. This effect is reinforced by the cubic crystal anisotropy with easy magnetic axes along x and y. When the magnetization rotates in the y direction, the demagnetizing field increases at the edges of the antidots. When reducing the field value, the magnetization on the edges of the antidots rotates towards x in order to minimize the local demagnetizing energy.

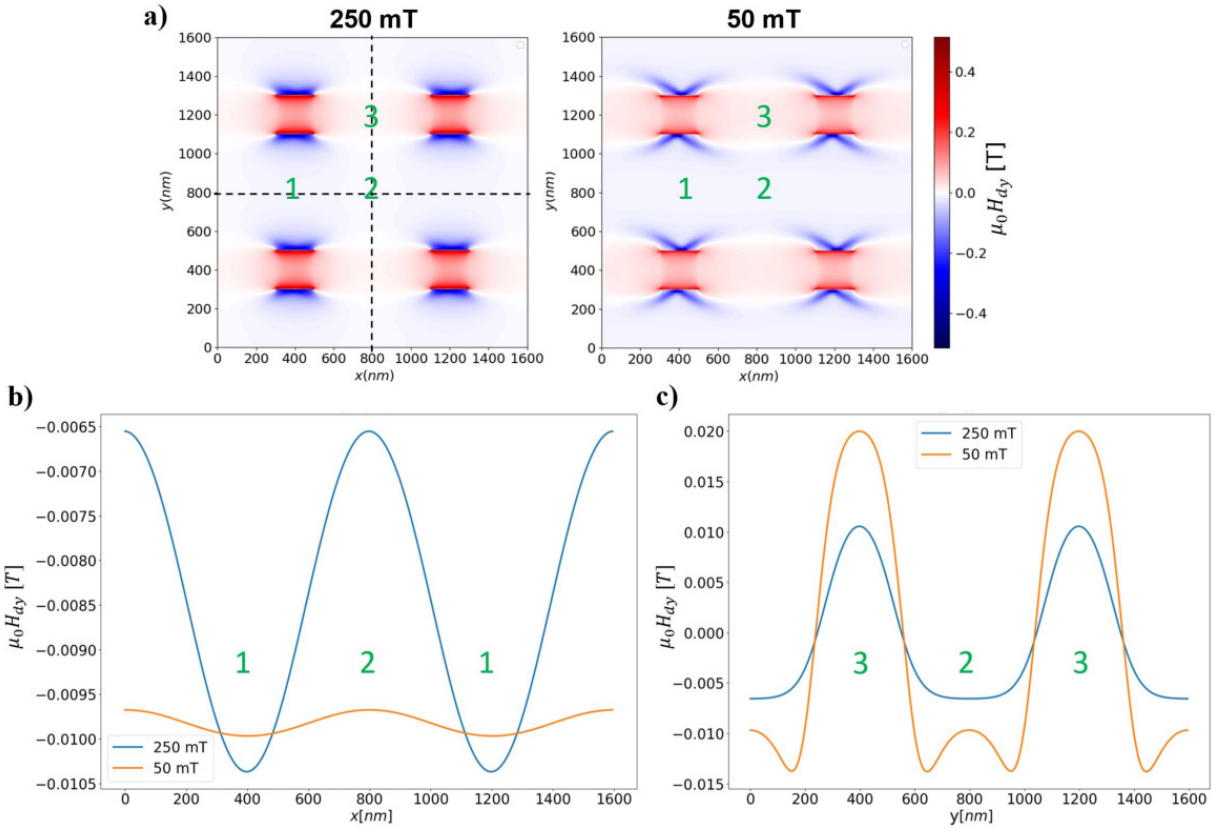

Figure 6.14: a) 2D colormaps of the simulated y-component of the dipolar field $\mu_0 H_{dy}$ in the unit cell of the CMS magnetic antidot lattice at $\mu_0 H_0 = 250$ mT (left) and $\mu_0 H_0 = 50$ mT (right). b) Evolution of $\mu_0 H_{dy}$ as a function of the position x in the unit cell at $y = 800$ nm (along the horizontal dotted line in the center of the horizontal channel in a)) for the applied fields 250 (blue line) and 50 mT (orange line). c) Evolution of $\mu_0 H_{dy}$ as a function of the position y in the unit cell at $x = 800$ nm (along the vertical dotted line in the center of the vertical channel in a)) for the applied fields 250 (blue line) and 50 mT (orange line).

To illustrate this point, the 2D mappings of the y-component of the dipolar field $\mu_0 H_{dy}$ simulated at $\mu_0 H_0 = 250$ mT and $\mu_0 H_0 = 50$ mT are shown in Figure 6.14 a). Extended modes (such as typically the mode 5) which are spreading in the horizontal channels are subjected to local variations of the dipolar field along the x direction. This can be seen in Figure 6.14 b) showing the variations

of $\mu_0 H_{dy}$ along the horizontal dotted line in Figure 6.14 a). As expected, the amplitude of $\mu_0 H_{dy}$ at position 1 is always higher than at position 2. However the difference is much more pronounced for $\mu_0 H_0 = 250$ mT than for $\mu_0 H_0 = 50$ mT. We assume that this strong local variation of $\mu_0 H_{dy}$ at higher fields is at the origin of the variation of the precession amplitude of extended modes along x (such as observed for mode 5). Indeed, for $\mu_0 H_0 = 50$ mT the variation of $\mu_0 H_{dy}$ is very weak and the spatial profile of the mode is homogeneous along x. But for $\mu_0 H_0 = 250$ mT, the variation of $\mu_0 H_{dy}$ is stronger and the spatial profile becomes slightly less homogeneous along x.

Now a similar effect arises in the y direction. However this time $\mu_0 H_{dy}$ is maximum for $\mu_0 H_0 = 50$ mT. This can be seen in Figure 6.14 c) showing $\mu_0 H_{dy}$ along the vertical line in Figure 6.14 a). At low field values, $\mu_0 H_{dy}$ increases at the position 3 because of flux closure of the edge domains. Then, we assume that this strong local variation of $\mu_0 H_{dy}$ along the vertical channel is at the origin of the extinction of the precession of the magnetization in the horizontal rows of antidots.

Transition to non-uniform magnetic states

At 10 mT, the magnetic edge domains extend more towards the center of the unit cell (Figure 6.12). However the majority of the magnetization is still aligned along the y direction. This magnetic state resembles those observed at remanence in chapter 5 (Figure 5.2 a)). Due to its quasi-uniform magnetization, two extended modes (yellow circle and red square) are still observed for this low field value. Below 10 mT, the edge domains further spread towards the center of the unit cell and at remanence (0 mT) a domain with its magnetization oriented along the 45° direction is stabilized as can be seen in Figure 6.12. Owing to these non-uniform magnetic states, the simulated spin wave mode spatial profiles are different from the one observed in the quasi-saturated regime (Mode 1 to 7). As a result, these modes are indexed with other colored and shaped symbols on the FM-FMR measurements (Figures 6.10 a) and b)).

For $\mu_0 H_0 \leq 10$ mT, as can be seen in Figures 6.10 a) and b), the FMR signals start to be weak and broadened in the frequency range 2 to 10 GHz. Nevertheless, one can observe that below 10 mT, the FMR signal which corresponded to an extended mode (yellow circles), seems to appear again with increasing frequencies while the applied field is lowered. This inflexion point may indicate the transition field, here at 10 mT, corresponding to a change of the magnetic configuration [224, 290]. The magnetization is no more uniformly collinear to the applied field. This transition field may be assimilated to the anisotropy field generated by the presence of the antidot lattice [291]. At this particular field value, the latter may cancel with the anistropy field of the lattice, leading to the possibility of reorientation of the magnetization (hard axis behavior). This results in a drop of the resonance frequency to a minimum value owing to the vanishing torque exerted by the applied field [291]. Above this transition field, the Zeeman field strengthened by the cubic crystal anisotropy field (easy axes along x and y) are stronger than the anisotropy field of the lattice whose hard axes are along x and y directions and easy axes along the 45° directions [266]. This results in quasi-uniform states magnetized along the direction of the applied field $\vec{H}_0$. Below this transition field, the Zeeman field and cubic crystal anisotropy field are no longer dominant over the anisotropy field. Consequently, 45° domains are favored below 10 mT.

Despite the obtained non-uniform remanent states in contrast to what was aimed in the simulations in chapter 5, it is to be noted that the cubic crystal anisotropy nevertheless contributes to stabilize quasi-uniform states down to lower magnetic fields compared to the case of a same material with no cubic anisotropy. Indeed, the change of magnetic configuration occurs for a higher magnetic field of about 20 mT without cubic crystal anisotropy. As a result, classical modes that can be observed in saturated magnetic antidot lattices could be retrieved down to lower applied field values owing to a relatively strong cubic crystal anisotropy of the CMS thin film.

VNA measurements

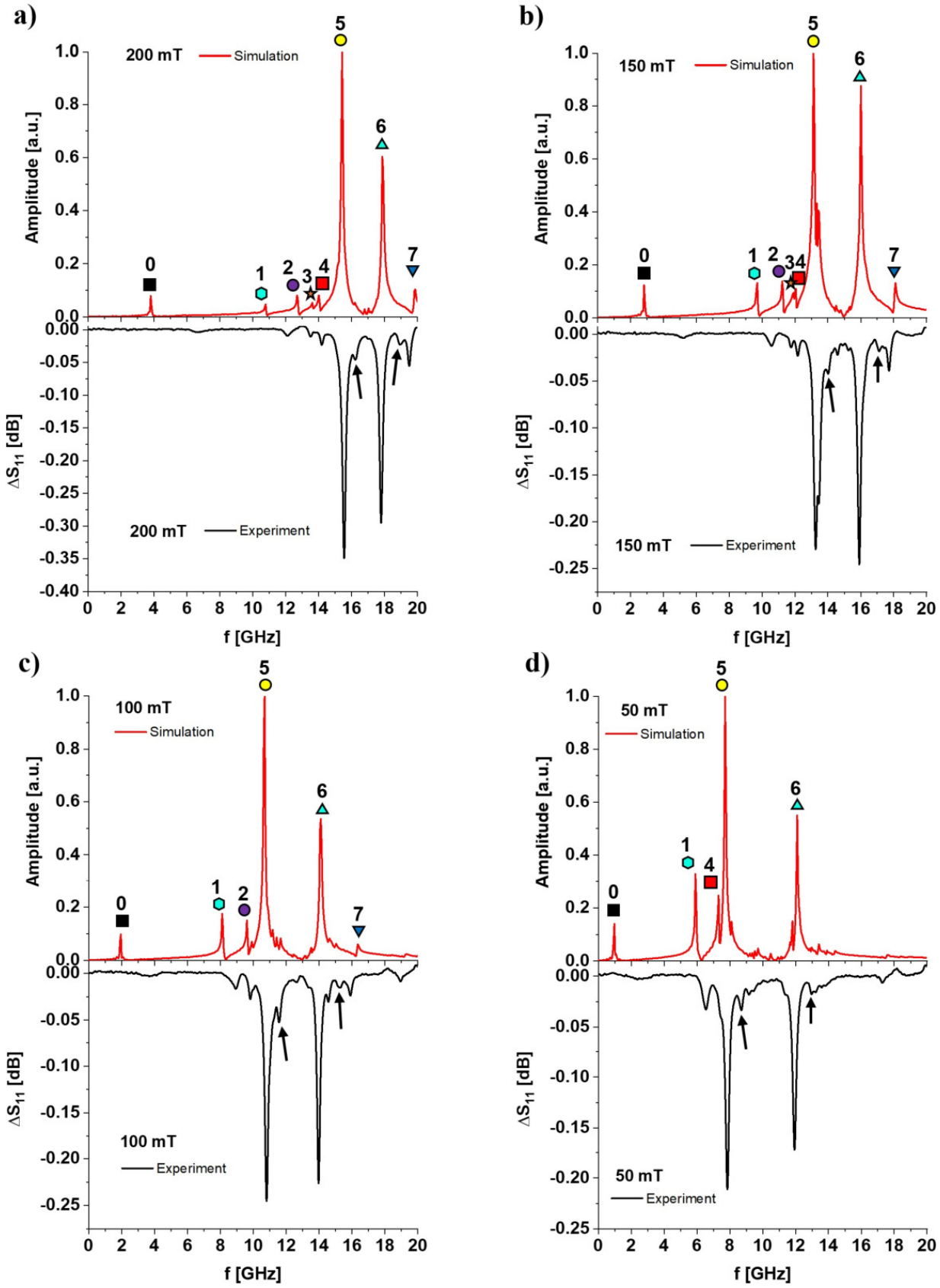

Figure 6.15: Plots of the numerical FFT spectra (upper graph, red line) and the measured ΔS_{11} parameter by VNA-FMR (lower graph, black line) at the applied magnetic fields $\mu_0 H_0$ a) 200 mT, b) 150 mT, c) 100 mT and d) 50 mT. The excited spin wave modes are indexed with numbers and colored symbols corresponding to those in Figure 6.11. The black arrows indicate measured spin wave modes that could not have been explained by the micromagnetic simulations.

Most of the measured FM-FMR signals in Figure 6.10 were retrieved and explained via micromagnetic simulations. To go further in the analysis of this sample, VNA-FMR measurements as described in chapter 3 3.3.3 were performed. The measured ΔS_{11} parameters for different applied field values ($\mu_0 H_0 = 200, 150, 100, 50$ mT) are shown in Figure 6.15. The simulated FFT spectra for the different $\mu_0 H_0$ are also plotted in comparison with the ΔS_{11} graphs. These FFT spectra previously served for the indexation of the excited spin wave modes in Figures 6.10 and 6.11.

Obviously, the simulated results quantitatively fit the experimental VNA-FMR results as for the FM-FMR experiments. However, VNA-FMR measurements allow to observe details in the spin wave spectrum in frequency and to obtain a direct comparison with micromagnetic simulations. We retrieve the two high intense modes, extended (yellow circle, mode 5) and localized (cyan triangle, mode 6) and low amplitude signals corresponding to the rest of the modes. All the measured modes present a slight frequency shift, whose value differs from one mode to another, with respect to the frequency obtained in the simulated FFT. In particular, the modes 2, 3, 6 and 7 are shifted downwards in frequency of about -600, -150, -100 and -400 MHz respectively while the mode 5 is shifted upwards of about $+130$ MHz over the field range $250 - 150$ mT.

In addition, two absorption peaks with moderate amplitudes are present close to the two main intense spin wave modes (extended and localized modes). These resonances are indexed with black arrows in the ΔS_{11} graphs of Figure 6.15. Such peaks are also observed in Figure 6.10 but VNA-FMR measurements allow to obtain a better resolution of these two modes. Surprisingly, they are not described in the micromagnetic simulations. In chapter 4, we mentioned that similar unpatterned CMS thin films show two FMR peaks associated to a majority and minority crystal order. In the easy axis direction, the minority peak appears at a higher field value compared to the majority one for field sweep measurements at a fixed frequency. As a result, it should appear at a lower frequency in the frequency sweep measurements at fixed applied field (VNA-FMR), which is in opposition to our observation. Therefore, we do not believe that this two additional peaks can be associated to the minority phase of the CMS thin film even if it is not easy to transpose the reasoning on thin films to patterned magnonic crystals. Another potential source may be the pumping field generated by the micro-antenna. However, we show in the next section that these additional modes are also observed in propagating Brillouin Light Scattering experiments employing a micro-antenna with a different geometry. Then, we think that these satellite peaks are intrinsic to the material but we have no explanation for their origins at the moment.

6.2.2 Micro-Brillouin Light Scattering measurements

To go further in the analysis of this CMS magnonic crystal, we compared our results to micro-Brillouin Light Scattering (BLS) experiments performed on the sample #3 as described in chapter 4 4.3.2.2. For the sake of clarity we remind that this sample #3 was made with the same method as the sample #2 (EBL and IBE for the patterning of the antidots). On one substrate we succeeded in making 6 magnonic crystals, three of them having a squared antidot lattice with nominal squared antidot size and spacing of 200 nm and 600 nm respectively. Only micro-BLS measurements were performed on these magnonic crystals. The experiments were performed in the team of Dr. S. Tacchi from the university of Perugia.

The aim of micro-BLS measurements is to provide an investigation of propagating spin wave modes between 5 and 500 GHz with a spatial resolution of about 300 nm when conventional BLS spectroscopy offers a spatial resolution around 30 μm [292, 293]. This technique thus allows the imaging of propagating spin waves in micro-nano magnetic structures. BLS and micro-BLS techniques rely on the inelastic scattering of photons by thermal or inductively excited spin waves. For the micro-BLS measurements, a laser spot of spatial resolution 300 nm was focused on the magnonic

crystal and the spin waves were excited by a microwave waveguide of width $w = 2.6\ \mu\mathrm{m}$ as detailed in section 4.3.2.2. The spin wave wavevectors that can be excited are up to $k_{max} \approx \frac{2\pi}{w} \approx 2.42\ rad/\mu\mathrm{m}$. A small area of $5 \times 5\ \mu\mathrm{m}^2$ close to the micro-antenna was scanned by the laser spot as can be seen in Figure 6.16.

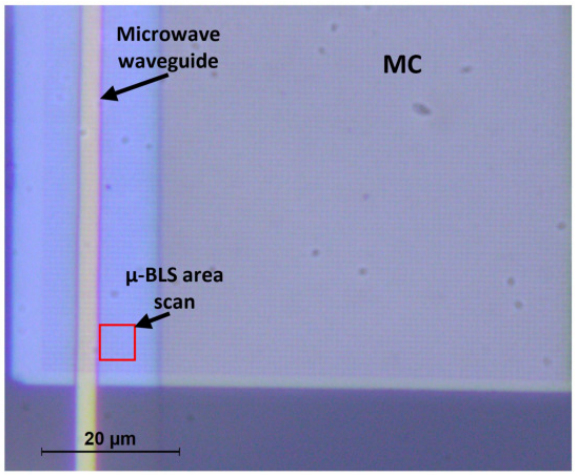

Figure 6.16: Optical image of one of the devices of sample #3 (CMS magnonic crystal (MC) with $s = 200\ \mathrm{nm}, d = 600\ \mathrm{nm}$) with the indicated area scanned by micro-BLS.

The intensity of the frequency scans measured by micro-BLS for $\mu_0 H_0 = 100\ \mathrm{mT}$ and $\mu_0 H_0 = 50\ \mathrm{mT}$ are shown in Figure 6.17 a) and b) respectively. For comparison, the calculated FFT spectra of the magnonic crystal at the same field values are recalled in Figure 6.17. One can observe that the experimental and numerical results are also in good agreement. The frequencies of the two main spin wave modes in the magnonic crystal, mode 6 (localized) and 5 (extended), are retrieved in the micro-BLS spectra. The mode 1 is also measured around $8.5\ \mathrm{GHz}$ for $\mu_0 H_0 = 100\ \mathrm{mT}$ and at around $5.8\ \mathrm{GHz}$ for $\mu_0 H_0 = 50\ \mathrm{mT}$. As with the VNA-FMR measurements on the sample #2, the modes 1 and 6 are slightly shifted towards higher and lower frequencies respectively compared to the simulated values. The mode 1 is shifted in frequency of about $+400\ \mathrm{MHz}$. The mode 6 at $13.40\ \mathrm{GHz}$ is slightly shifted of $-400\ \mathrm{MHz}$ compared to the simulated mode. Finally, it is important to mention that for $100\ \mathrm{mT}$, the satellite peaks that were reported in FM-FMR and VNA-FMR experiments on the sample #2 seem to be also observed at $11.51\ \mathrm{GHz}$ and at $14.51\ \mathrm{GHz}$. This means that our nano/micro-fabrication processes were rather reproducible for the samples #2 and #3.

Micro-BLS spatial mappings of our sample allow to validate even more our micromagnetic simulations by mapping the spin wave spatial profiles corresponding to the detected resonance peaks. More precisely, micro-BLS is not phase resolved here, only the amplitude of precession is recovered. The major information for us with micro-BLS is then to observe the spatial localization of the modes (even if the spatial resolution is weak with respect to the distance between two antidots in our magnonic crystal). Our colleagues performed the mappings at 10.4 and $13.7\ \mathrm{GHz}$ for $\mu_0 H_0 = 100\ \mathrm{mT}$ and 7.7 and $11.8\ \mathrm{GHz}$ for $\mu_0 H_0 = 50\ \mathrm{mT}$. The spatial mappings are shown as insets in Figures 6.17 a) and b).

For $\mu_0 H_0 = 100\ \mathrm{mT}$ and excitation frequency $10.4\ \mathrm{GHz}$, the maximum amplitude of precession is continuous and quasi-uniform along the horizontal channels, as expected for an extended mode such as the mode 5. In contrast, at $13.70\ \mathrm{GHz}$ corresponding to the predicted localized mode, the maximum of precession amplitude occurs non-continuously along the x axis, in the horizontal rows of antidots. These measurements thus confirm the numerically predicted extended and localized modes. It is to be noted that the spin waves propagation at $13.70\ \mathrm{GHz}$ is attenuated on a shorter distance than the spin waves at $10.40\ \mathrm{GHz}$. This is consistent with the fact that the localized modes, which are spatially confined by nature, are weakly dispersive (lower propagation velocities) thus preventing their further propagation throughout magnonic crystals [60]. The same spatial mappings were also

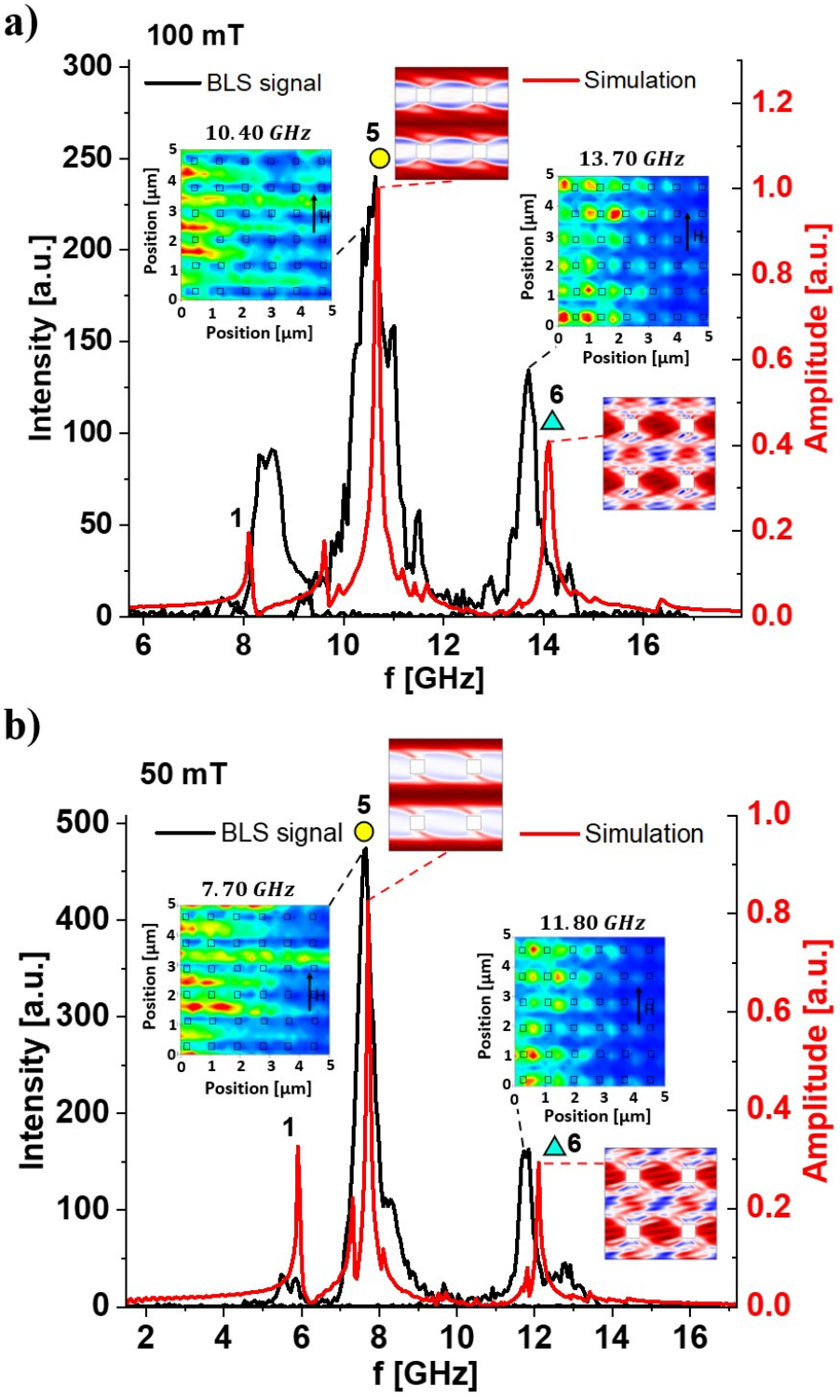

Figure 6.17: Micro-BLS intensity (black curve) and FFT (red curve) spectra at the applied magnetic fields a) 100 mT and b) 50 mT of one of the devices of sample #3 (CMS magnonic crystal with antidot size $s = 200$ nm and spacing $d = 600$ nm). Insets of the 2D spatial colormaps of the amplitude of the two main propagating spin wave modes (extended indexed with yellow circle and localized indexed with cyan triangle) are shown in a) and b). For comparison, the numerical spatial profiles of the two main spin wave modes that can be found in Figure 6.11 are also shown.

acquired at $\mu_0 H_0 = 50$ mT for 7.70 GHz and 11.80 GHz and are shown in Figure 6.17 b). Similar results were also obtained in this case. These micro-BLS measurements tend to validate our simulations and nanostructuration techniques.

Even if it is not the main point of our work, it is interesting to highlight that the propagation distances of spin waves in the extended mode are relatively short as compared to what is expected for low damping coefficient materials. In addition, the BLS mappings are not very uniform across the full scanned area. Then other data analysis such as the group velocity and the attenuation length measurements could not have been performed. Some explanations can be given concerning these facts. First, the passivation layer may be too thick, thus decreasing the detected micro-BLS signal. Then, the weak propagation distances can be related to the large effective damping presented in section 4.1 Figure 4.3. The quite non-uniform propagation of spin waves could also come from the crystal phase mixing of the $L2_1$ and B2 phases in our thin films. Finally, the BLS measurements were performed close from the border of the antidot lattice as can be seen in Figure 6.16, where we numerically demonstrated in chapter 5 5.2.2 that the magnetic states can be non inhomogeneous. Further measurements are required, notably on an area more located near the center of the magnonic crystal and on the unpatterned CMS thin film area of sample #3, to know which cause is the most probable.

6.3 Experimental demonstration of a reconfigurable property at remanence with a Co_2MnSi magnonic crystal

In chapter 5, we numerically demonstrated the possibility to stabilize quasi-uniform magnetic configurations at remanence in a CMS magnetic antidot lattice with specific antidot sizes, spacings and magnetic properties. The key parameter to obtain quasi-uniform remanent states is a strong cubic crystal anisotropy whose easy axes are along the square antidot lattice symmetry axes (x and y axes). By applying an initialization magnetic field $\vec{H}_0$ along the x or y axis, one can either uniformly stabilize most of the magnetization of the antidot lattice along the x (the magnetization state is referred to as Rem X) or y (the magnetization state is referred to as Rem Y) axis respectively. As a result, when a uniform microwave pumping field $\vec{h}_{RF}$ is applied along the x axis for example, two different microwave responses can be obtained at remanence corresponding to a reconfigurable operation. In this particular case, some spin wave modes that are well excited with high amplitudes in the Rem Y state due to an efficient coupling with the pumping field, are strongly attenuated when switching to the Rem X state. In this numerical study, an optimal antidot aspect ratio s/d of $1/3$ was found for the magnetic parameters of the CMS thin films based on the previous works of our research team [51–53, 111, 180].

In the previous sections, we have presented the evolution of the microwave response of the sample #2. The antidot size ($s = 200$ nm) and spacing ($d = 600$ nm) for this sample were chosen according to the numerical results obtained in chapter 5 as we wanted to demonstrate experimentally the reconfigurable property. However at the time of fabricating the sample, we did not know that the crystal anisotropy constant was lower than expected.

For the sample #2, the cubic crystal anisotropy is still sufficiently important to have quasi-uniform magnetic configurations down to a low field value of about 10 mT but not sufficient to maintain it at remanence. Even though the remanent state of this sample is clearly not ideal as micromagnetic simulations predict a 45° domain at the center of the unit cell, this remanent state seems to be less "non-uniform" that the one obtained in chapter 5 in the case of a CMS thin film with no cubic crystal anisotropy ($K_{c1} = 0$). Then, we attempted to measure if reconfigurable operations of particular spin wave modes could be achieved in our sample.

We first applied a saturation field of $\mu_0 H_0 = 300$ mT along y (i.e. along the length of the antenna).

After recording the ΔS_{11} signal with VNA-FMR (as the reference signal), we decreased the applied field down to 0 mT where ΔS_{11} is recorded again. The simulated remanent magnetic configuration is referred to as Rem Y and is shown in Figure 6.18 b) (on the left). This remanent configuration is the same as the one in Figure 6.12. Secondly, the same procedure was carried out with $\vec{H}_0$ applied parallel to the x axis (i.e. perpendicular to the long axis of the antenna). The remanent state is referred to as Rem X and is also shown in Figure 6.18 b) (on the right).

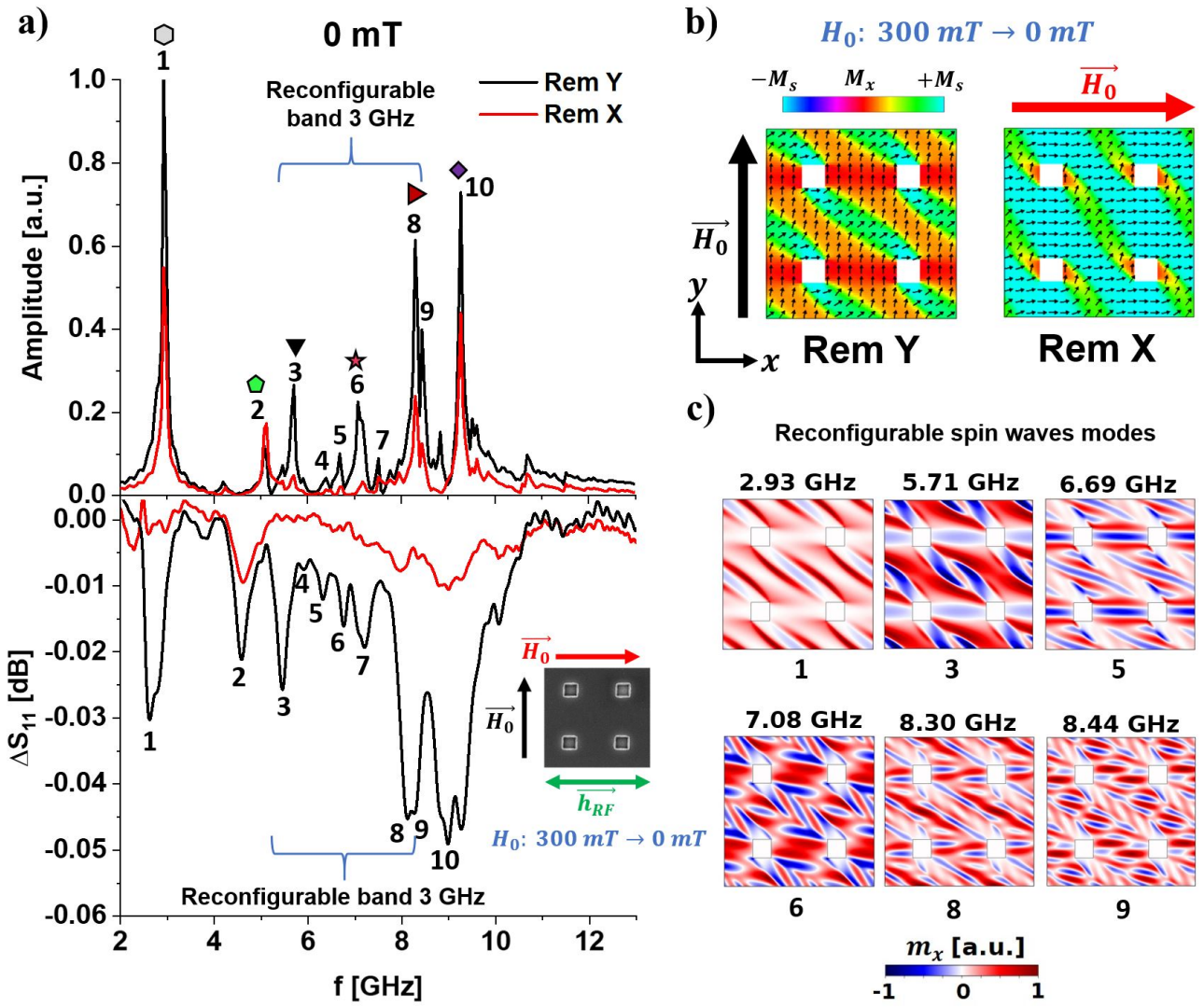

Figure 6.18: a) Plots of the numerical FFT spectra (upper graph) and the measured ΔS_{11} parameters (lower graph) in the Rem Y state (black line) and in the Rem X state (red line) at remanence $\mu_0 H_0 = 0$ mT. The amplitude in the FFT spectra is normalized according to the maximum amplitude reached. The relevant spin wave modes are indexed with numbers and/or colored symbols. The colored symbols are the same as those in Figure 6.11. b) Equilibrium magnetic configurations Rem Y and Rem X at remanence. The colorbar is color coded according to the x-component value of the magnetization M_x. c) Temporal snapshots of the simulated dynamic m_x spatial profiles for some indexed reconfigurable spin wave modes in a). The m_x component of each mode is normalized according to its own maximum amplitude.

The results are shown in Figure 6.18 a) with the measured ΔS_{11} (lower graph) and calculated FFT (upper graph) spectra performed on the M_z component in the case of these two remanent states. Figure 6.18 b) shows the Rem X and Y remanent states. The different absorption peaks with a relevant amplitude in the Rem Y state are indexed with numbers. On the FFT spectrum, we indexed the spin wave modes with the colored symbols used in section 6.2.1. The simulation and the experimental results are in good agreement even if we observe frequency shifts from -180 to 500 MHz depending

on the spin wave mode. It is to be noted that in the VNA-FMR measurements, the first mode is far from being as intense as expected from the simulations. In the Rem Y state, one major observation is that the amplitudes of the absorption peaks are very low, about a factor 10, as compared to the case of the quasi-saturated magnetic configurations (Figure 6.15). This results from the non-uniformity of the magnetization at remanence. The $45°$ domains couple to the pumping field less efficiently as only the projected M_y component couples to $\vec{h}_{RF}$). This leads to a decrease in the signal amplitude. The larger frequency linewidths of the absorption peaks may also contribute to the low measured amplitude.

Now, dealing with the microwave response in the Rem X state, one can observe in the FFT spectra that many FFT peaks are nonetheless strongly attenuated even with the presence of the $45°$ domains in the remanent configuration. This strong attenuation of these spin wave modes occurs more particularly in the frequency range $5.3 - 8.3$ GHz. Despite some differences, this reconfigurable frequency band is retrieved in the VNA-FMR measurements, where the absorption peaks are well attenuated. Some exceptions arise for the modes 1 and 8 which are more attenuated than expected. The spatial profiles of the reconfigurable spin wave modes are shown in Figure 6.18 c) for the Rem Y remanent state. One can observe that these profiles are complex and present different localization of intense precession of the magnetization due to the presence of the $45°$ domains. The mode 1 corresponds to the precession of the magnetization mainly at the boundaries of the $45°$ domains but also to a lesser extent in-between the $45°$ domains in the horizontal channels. The mode 3 seems quite similar to the mode 1 but antinodes appear within the $45°$ domains. The mode 5 presents large precessions along the horizontal rows of antidots and in-between $45°$ domains. These regions are not well excited by the pumping field in the Rem X state as most of the magnetization lies in the x direction. The other higher frequency modes present quantized precessions in the regions inside and in-between the 45° domains. Interestingly, for the modes 8 and 9, the amplitude of the magnetization precession is weak in the domains compared to the regions in-between the domains.

Conclusion

To conclude on the samples $\#2$ and $\#3$, the use of EBL and IBE for the nanostructuration of CMS thin films allowed to achieve reproducible magnetic antidot lattices, whose measured microwave responses are very consistent with the micromagnetic simulations. This validates our approach for the nanostructuration of CMS magnonic crystals. In the particular case of the sample $\#2$, the slight non-orthogonality of the antidot lattice, as detailed in chapter 4 4.3.2.1 seems to have a negligble impact on the measured spin wave mode spectra. Other measurements (not shown here) were conducted on the sample $\#2$ such as with the application of an electrical current to observe its impact on the FMR spectra or with the application of varying amplitudes of power injected in order to observe nonlinear effects. The analysis of the experimental data are still in progress at the moment of writing this manuscript. Besides, measurements in the BVMSW configuration (pumping field collinear to the external field) could also be performed. This kind of measurements could lead to the observation of a periodic variation of the field linewidths of the measured signals with frequency [294–296]. This periodic variation would result from the periodicity of the lattice, in particular due to Bragg conditions [294–296].

In addition, we were able to obtain reconfigurable spin wave modes at remanence in a squared antidot lattice with cubic crystal anisotropy (sample $\#2$). However, the anisotropy constant was not sufficiently large to stabilize a well-defined quasi-uniform state at remanence and the number of reconfigurable modes is limited. For this sample it would have been better to increase the spacing between the antidots to compensate this unexpected lower cubic crystal anisotropy. In the micromagnetic simulations, an antidot size and spacing of 200 nm and 800 nm respectively would have allowed the stabilization of quasi-uniform remanent states. In the sample made for micro-BLS measurements (sample $\#3$), an antidot lattice with these characteristics has been patterned and BLS spectra (not shown here) were found in agreement with the simulations at 100 mT. However strong discrepan-

cies were observed at 7 mT (in the micro-BLS experiments, it was not possible to be exactly at zero bias field due to the remanent field of the electromagnet used) most probably due to the area scanned by the laser spot as the latter was close to the edges of the magnonic crystal (Figure 6.16). Further measurements are expected on this device to observe a correct reconfigurable property at remanence.

Conclusion and Perspectives

The objective of this thesis was to produce reconfigurable magnonic crystals based on squared magnetic antidot lattices. Moreover, our objective was that these systems operate at zero field (i.e. remanence) since this opens the way for microwave components operating without the presence of permanent magnets. In order to achieve this goal and to optimize the reconfigurable aspect, we explored the possibility of taking advantage of the cubic crystal anisotropy present in $\mathrm{Co_2MnSi}$ Heusler alloy thin films.

First, we showed via micromagnetic simulations that spin wave modes could be excited or not by a microwave field when the remanent equilibrium state in the magnonic crystal is modified by an external field pulse applied in two different directions perpendicular to each other. In particular, we have shown that for the attenuation amplitudes of the modes to be as large as possible, it is preferable to have the most uniform magnetic equilibrium states possible between the antidots. This is favored by the presence of a material with cubic crystal anisotropy such as $\mathrm{Co_2MnSi}$, notably by orienting the easy magnetic axes with the symmetry axes of the antidot lattice. We have also demonstrated that the number of spin wave modes, the amplitude of their attenuations and their excitation frequencies can be tuned by controlling the dimensions of the antidots and their spacing. In the numerical study that we conducted, a ratio of $1/3$ between the size of the antidot squares and their spacing is optimal. However this ratio will strongly depends on the value of the cubic crystal anisotropy constant and of the saturation magnetization of the material. In addition, with our model material, our numerical study predicts that switching times between two different remanent states of the order of $1\ \mathrm{ns}$ could be reached with pulses of the order of a few mT. Consequently, a magnonic crystal based on a $\mathrm{Co_2MnSi}$ square antidot lattice could be a good candidate for the design of multi-band receiving antennas for example.

We then sought to make such devices. For this, we fabricated $\mathrm{Co_2MnSi}$ Heusler alloy thin films in the laboratory, which were then nanostructured by different methods in order to obtain a magnonic crystal. The targeted antidot dimensions are of the order of a few hundred of nanometers. For this stage, we explored two strategies.

The first consisted in using $\mathrm{Ga^+}$ focused ion beam (FIB) etching. Its experimental study of the spin wave spectrum measured by FM-FMR revealed several limitations. Among these we can mention the importance of shaping the ion beam in order to have the straightest possible flanks on the edges of the antidots. The consideration in our numerical simulations of the dispersion of the geometries and dimensions of the holes over the lattice makes it possible to partially explain the low intensity of the experimental signals and their large field linewidths associated to the different modes. Nevertheless, our analysis seems to show that the main limitation lies in the modification of the magnetic properties of the $\mathrm{Co_2MnSi}$ volumes of a few tens of nanometers long around the antidots. We attribute these damaged magnetic volumes to $\mathrm{Ga^+}$ ion implantation occuring during FIB milling of the antidots. This local modification of the magnetic properties leads to a broadening of the main spin wave modes, but also to the appearance of additional absorption peaks at high frequencies.

The second strategy explored consisted in producing magnonic crystals by e-beam lithography

followed by Ar^+ ion beam etching in an IBE chamber. With this method we obtained antidot lattices whose antidot geometry and dimensions present few dispersions. The fabricated CMS antidot lattice could then be simply modeled in the case of a lattice with ideal squared antidots. Thus, this method turns out to be much more relevant than FIB etching with Ga^+ ions. This technological development work represented a large part of this thesis work since it was necessary to set up all the techniques and tools of e-beam lithography and IBE milling in the environment of the CEMES clean room facility.

Through these studies on the spin wave modes of the fabricated magnonic crystals via these two methods, we have followed the evolution of the spatial profile of the modes according to the more or less uniform character of the magnetization at equilibrium. Thus, we were able to show that in the case of the sample prepared by e-beam lithography and IBE, most of the modes keep the same spatial profile up close to the remanence. However, the profile of the main mode is sensitive to the evolution of the dipolar field between the antidots. Please note that our micromagnetic simulations could be validated through micro-Brillouin Light Scattering experiments performed at the University of Perugia which demonstrated the rather propagative or localized nature of the different simulated modes. In the case of the samples prepared by FIB, the spatial profile of the modes evolves in a much more notable way as a function of the applied field, as the quasi-saturated equilibrium state is reached for relatively intense fields (> 100 mT).

Finally, we were able to observe reconfigurable spin wave modes at remanence in the sample prepared by e-beam lithography and IBE. However, since the value of the cubic crystal anisotropy constant of this sample was lower than expected, the remanent states are not uniform and therefore only a few modes could be attenuated on a frequency band of the order of 3 GHz. Other results that are not discussed in this manuscript have been obtained such as the evolution of the spin wave mode amplitudes as a function of the injected microwave power. An example of such measurements is shown for information in Figure 6.19 a). It can be observed a variation of the ΔS_{11} of certain modes. These results are still under consideration. We also tested the effect of an electrical current on the spin wave spectrum obatined by FM-FMR. As the CMS was proved theoritically and experimentally half-metallic in the literature, we wanted to observe some effects related to spin polarized current on the magnonic spectrum. At this time, no significant effects except Joule heating has been observed.

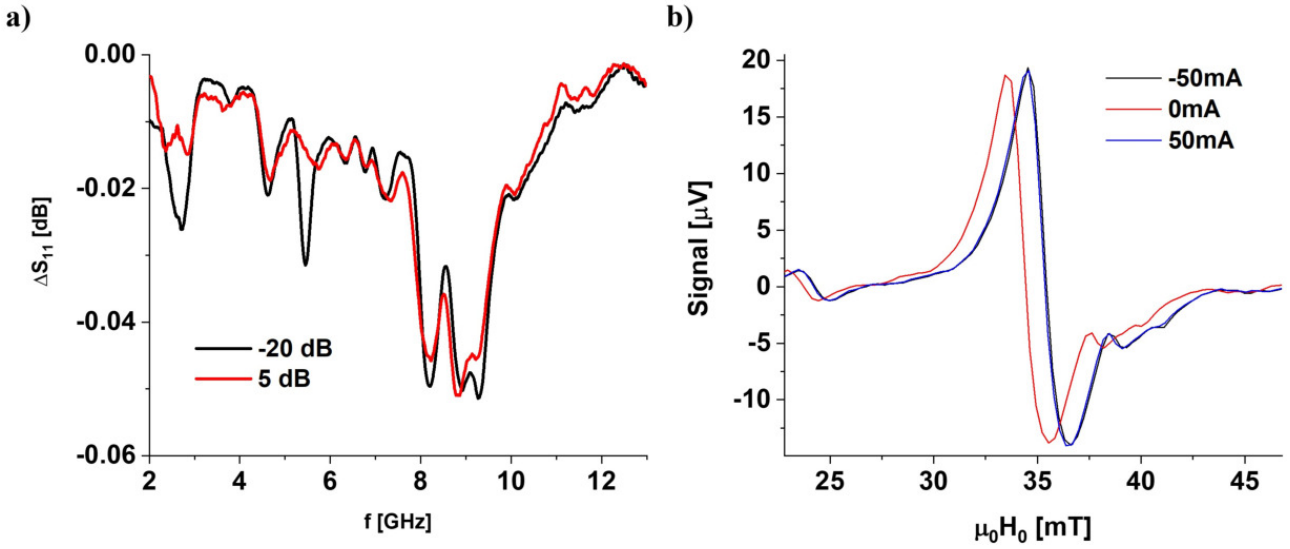

Figure 6.19: a) VNA-FMR ΔS_{11} measurements performed on sample #2 at 0 mT for two different injected powers -20 dB (black line) and 5 dB (red line). b) FM-FMR measurements performed on sample #2 at 7 GHz with an applied electrical current through the MC of -50 mA (black line), 0 mA (red line) and 50 mA (blue line).

Among the perspectives opened up by this thesis work, the possibility of now being able to pro-

duce magnonic crystals based on Heusler alloys paves the way for interesting perspectives. From a purely material point of view, it is interesting to focus on the reconfigurable aspect in other materials exhibiting cubic crystal anisotropy. More precisely, this concerns the optimal combination of cubic crystal anisotropy and saturation magnetization values. Also, it will be important to study the degree of reconfigurability of an antidot lattice according to the geometry of the patterns. Indeed, a lattice of circles or diamonds will not have the same response as a lattice of squares for example. The purpose of this work seeks the realization of microwave systems of multi-band receiver types. Then, the most obvious stage that we did not have time to prospect is obviously the study of the spin wave propagation through these crystals, notably to study the possibility of making reconfigurable microwave filters. Further studies by micro-BLS may be particularly suitable for this type of study for example. The objective could be to observe how the frequency pass bands and forbidden bands can be modulated to the remanence, with always taking advantage of the cubic crystal anisotropy of the material. However, the impact of not only the nanostructuration but also of the finite dimensions of the crystal will have to be studied in detail. This last point is one of the most important for the design and miniaturization of microwave components. Finally, we believe that the strong theoretical spin polarization of the Heusler alloys paves the way for excitation and detection of spin wave modes by spin-orbit coupling via placing for example Pt lines on top of it. As it has been shown for YIG, it is possible to consider amplification effects of spin waves by injection of a spin current in these systems and to have a very local detection of the spin wave propagation by Inverse Spin Hall Effect.

Synthèse en français

6.4 Introduction

6.4.1 Concept de magnonique et de magnétisme dynamique

Dans un matériau magnétique, une perturbation uniforme ou localisée de l'ordre magnétique résulte en la précession collective ou propagative respectivement des moments magnétiques de spin. Lorsque la précession des moments magnétiques est non-uniforme (i.e. déphasée), on parle d'ondes de spin (ou magnons dans le cas d'une description corpusculaire) (figure 6.20), dont le concept a été introduit en 1930 par Bloch [1]. Ces ondes présentent des caractéristiques particulières com-

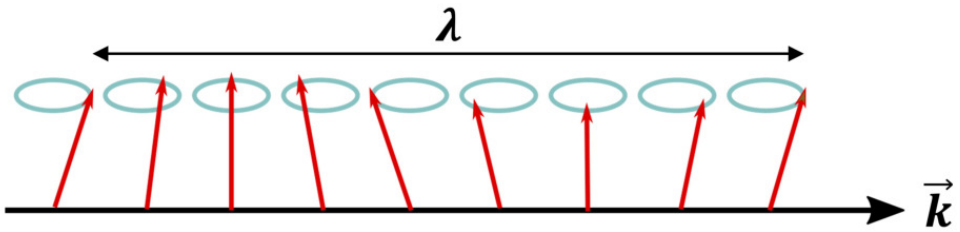

Figure 6.20: Représentation imagée d'une onde de spin

parées aux ondes électromagnétiques dans le vide, qui les rendent particulièrement intéressantes notamment pour la miniaturisation de composants radiofréquences (quelques MHz à la dizaine de THz). Premièrement, leurs longueurs d'ondes sont plusieurs ordres de grandeur inférieurs à celles des ondes électromagnétiques dans le vide et leurs fréquences d'excitation peuvent être modifiées par l'application d'un champ magnétique par exemple. En particulier, leur relation de dispersion $f(k)$ dépend de l'ordre magnétique du matériau, de sa forme ou encore de l'amplitude et direction d'un champ magnétique appliqué par rapport à sa direction de propagation. De ce fait, la propagation d'ondes de spin peut ainsi être anisotrope ou isotrope.

Le domaine de la magnonique consiste en l'étude de l'émission, propagation et détection des ondes de spin. D'intenses recherches portent sur ce sujet depuis une vingtaine d'années avec pour objectif de développer de nouveaux composants électroniques qui pourraient être moins énergivores et plus polyvalents. Pour donner quelques exemples, il a été démontré en laboratoire que le contrôle de l'amplitude et/ou de la phase des ondes de spin peuvent permettre de réaliser des composants logiques tels que le transistor à magnon [2], des composants radiofréquences (filtres radiofréquences, lignes à retard de phase, déphaseurs, circulateurs, multiplexeurs ... [3]), ou encore pour les technologies de communication 5G [4–7]. La magnonique embrasse ainsi un fort potentiel, que ce soit fondamental ou appliqué, au travers de la promesse de miniaturisation, de large bande de fréquence utilisable et de faible consommation d'énergie. Également il est à noter que les ondes de spin sont porteurs d'un courant de spin, analogue à un courant électronique mais sans effet Joule. La combi-

naison de matériau magnétique avec des matériaux à fort couplage spin-orbite ouvre notamment la voie au développement de composants basse énergie, de faibles dimensions et multifonctionnels. Ce domaine de recherche émergeant est appelé « spin-orbitronique » et est actuellement en plein essor. Toutes ces recherches sur la magnonique et la spin-orbitronique sont motivées par le besoin d'aller au-delà des technologies CMOS actuelles. Dans ce contexte, en 2021, les dispositifs à ondes de spin ont été mentionnés comme une alternative crédible aux technologies CMOS par « the International Roadmap for Devices and Systems (IRDS) » [8]. Par exemple, des guides d'ondes magnoniques aux dimensions proches de celles de transistors CMOS actuels, 50 nm, ont été produit [9].

6.4.2 Concept des cristaux magnoniques

Dans le cadre de cette thèse, nous nous sommes intéressés en particulier à un type de dispositif magnonique appelé cristal magnonique. Un cristal magnonique est un matériau magnétique dont les propriétés magnétiques ont été modifiées périodiquement et artificiellement. La propagation des ondes de spin dans ces systèmes magnétiques peut être décrite par les lois établies et formalisées par C. Kittel en 1929 concernant la propagation d'ondes dans des systèmes périodiques, qui par ailleurs constituent depuis les fondements de la physique du solide [10]. Une propriété importante et unique de ces structures périodiques est que la propagation d'ondes dans ces milieux ne peut avoir lieu que dans des bandes de fréquences bien spécifiques. En effet, pour des longueurs d'ondes correspondant à un multiple de la périodicité du réseau, les ondes subissent de multiples réflexions de Bragg, générant ainsi des bandes d'énergie interdites à la propagation.

Les cristaux magnoniques permettent ainsi l'émergence d'une multitude de méthodes innovantes afin de contrôler et moduler les ondes de spin pour des applications d'opérations logiques ou de traitement du signal. Ces derniers constituent ainsi la contrepartie magnétique des cristaux photoniques qui sont apparus en 1987 [11, 12] et qui permettent notamment de guider et/ou piéger des ondes électromagnétiques pour produire par exemple des circuits intégrés optiques et des cellules solaire photovoltaïques plus efficientes [13]. Bien que les structures périodiques magnétiques soient apparues avant dans les années 1970 [14], ce n'est que dans les années 2000 que le concept de cristal magnonique émerge réellement [15, 16] grâce en particulier à la maîtrise des techniques de nanofabrication et de dépôts de couches ultra-minces. Comparé aux autres cristaux artificiels (photoniques, phononiques...), les cristaux magnoniques offrent un avantage majeur : leur structure de bande n'est pas seulement dépendante de la périodicité du cristal, mais également de la configuration magnétique ou de l'application d'un champ magnétique externe. Ce degré de liberté additionnel les différencie fortement des cristaux photoniques. Pour aller plus loin dans l'ingénierie de bande, de nombreuses stratégies, autres que l'application d'un champ magnétique, ont été explorées dans la littérature, notamment en variant la géométrie des centres réflecteurs du cristal magnonique tel que l'épaisseur, la largeur ou le nombre de couches magnétiques [17, 18], l'arrangement périodique de disques magnétiques [19, 20] ou de trous dans une couche mince [21–23], mais également en modulant les constantes magnétiques au travers de l'incorporation périodique d'un autre matériau magnétique [24, 25] ou par implantation ionique [26] dans la couche mince magnétique.

6.4.3 Applications magnoniques reconfigurables à la rémanence

Les cristaux magnoniques présentent ainsi une riche diversité d'applications, et dans le cadre de cette thèse, nous nous sommes en particulier intéressés aux propriétés d'absorption radiofréquence (RF) et de filtrage [23, 27, 28]. En particulier, notre principal objectif a été d'obtenir un système modèle pouvant fonctionner sans champ magnétique appliqué, i.e. à la rémanence, et présentant des bandes

d'absorption RF pouvant être modifiées à la demande. Ce type de composant est appelé reconfigurable. Ces systèmes fonctionnant à la rémanence permettent d'éviter l'utilisation d'aimants permanents pour maintenir une aimantation uniforme du système magnétique pour assurer sa fonctionnalité. Actuellement, la majorité des dispositifs magnoniques et des cristaux magnoniques présents dans la littérature fonctionne avec un champ magnétique de saturation selon une direction particulière. Le fait de retirer l'utilisation d'aimants permanents va non seulement résoudre les problèmes de champs rayonnés par ces derniers lorsque présents dans des circuits intégrés, mais également peut répondre aux problèmes écologiques et économiques quant à la fourniture de terres rares pour ces aimants permanents et dont le marché est contrôlé par seulement quelques pays.

La reconfigurabilité du dispositif s'obtient généralement en changeant le système entre différents états magnétiques offrant différentes réponses RF. Bien que cette thématique présente un fort potentiel applicatif, peu d'études existent dans la littérature sur ce sujet. Parmi les travaux présents, on peut notamment mentionner ceux utilisant des réseaux de nanopillers [29, 30], des nanostructures elliptiques avec deux matériaux magnétiques différents [31], de nanofils couplés par interaction dipolaire [32–34]. Cependant, la majorité de ces travaux requièrent des schémas d'initialisation complexes avec de forts champs magnétiques appliqués. Parmi ces travaux, la voie la plus prometteuse consiste en l'utilisation de l'anisotropie de forme de nanostructures avec une forme rhomboédrique et dimensions spécifiques. Ces nanostructures permettent en particulier la stabilisation d'états magnétiques quasi-uniformes selon l'axe long ou court de la nanostructure au travers de l'application d'une impulsion de champ magnétique de l'ordre de la quelques dizaines de mT [35]. De cette manière, un décalage en fréquence de l'ordre de 400-600 MHz suivant les configurations utilisées a été obtenu [36, 37]. En combinant plusieurs couches magnétiques et non-magnétiques (par exemple NiFe/Cr/NiFe) dans le même type de nanostructures, les auteurs ont pu augmenter le décalage en fréquence entre 1-5 GHz dans la gamme 3-15 GHz suivant le nombre de couches et leur arrangement [38–40]. Pour aller plus loin, ils ont par ailleurs démontré la possibilité de propager des ondes de spin à la rémanence via des guides d'ondes droits ou courbés formés par un arrangement en chaîne de ces même nanostructures, cela a permis en particulier d'obtenir une fonction "d'interrupteur à ondes de spin" [41].

6.4.4 Réseaux périodiques 2D de trous (Magnetic antidot lattice)

Dans cette thèse, nous avons cherché à réaliser un cristal magnonique reconfigurable à la rémanence à partir d'une géométrie périodique simple et largement étudiée dans la littérature : un réseau périodique de trous dans une couche mince (magnetic antidot lattice en anglais). Sur les dix dernières années, un large nombre de publications s'est focalisé sur la détermination des modes d'ondes de spin dans ce type de cristal magnonique ainsi que sur l'observation de bandes de fréquence interdites à la propagation des ondes de spin. Des applications autres que pour la magnonique ont été également étudiées telle que via la production de mémoires de stockage à forte densité [42, 43] ou de capteurs de nanoparticules [44].

Dans les réseaux périodiques de trous, la présence des trous induit la quantification des ondes de spin et une modulation périodique du champ magnétique interne. Cette inhomogénéité périodique du champ interne agit comme des centres de diffusions qui permettront de générer des bandes de fréquences interdites et permises pour les ondes de spin se propageant dans un tel milieu. Pour aider à la description des modes d'ondes de spin quantifiés et confinés dans ces cristaux magnoniques, nous utilisons les termes schématisés dans la figure 6.21. Les canaux horizontaux correspondent aux canaux horizontaux étendus entre deux lignes de trous, tandis que les lignes horizontales de trous se trouvent entre deux canaux horizontaux.

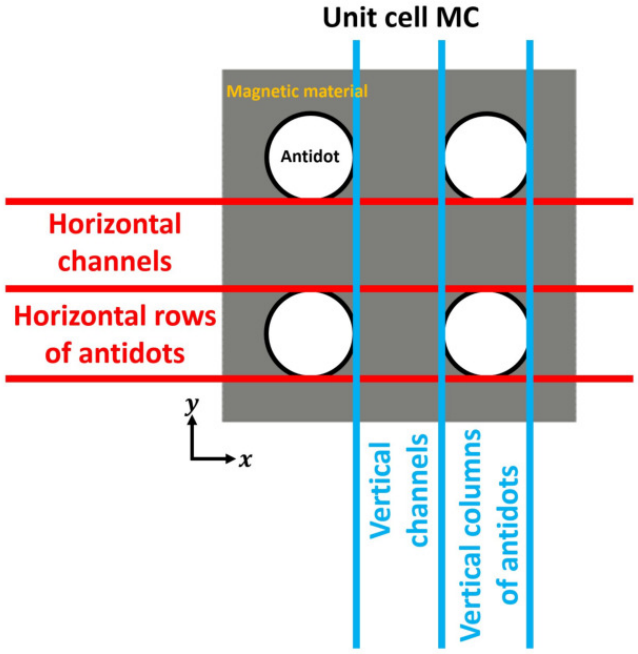

Figure 6.21: Schéma de la cellule unitaire d'un réseau périodique de trous montrant les différents termes utilisés pour identifier des régions spécifiques de la structure.

6.4.5 Utilisation des propriétés matériaux dans la quête de reconfigurabilité

Afin d'obtenir des fonctionnalités reconfigurables à la rémanence avec ces réseaux de trous, nous avons opté pour une approche peu explorée pour le moment dans la magnonique. Cela consiste à tirer parti des propriétés magnétiques intrinsèques au matériau, et dans notre cas particulier, celle de l'anisotropie magnéto-cristalline cubique de certains. Peu de travaux de recherche ont exploré les propriétés intrinsèques au matériau magnétique afin de réaliser des composants RF à la rémanence. On peut néanmoins remarquer le cas de couches épaisses de ferrites tel que le bismuth hexaferrite qui possède une forte anisotropie magnéto-cristalline [45]. Ce type de dispositif est actuellement commercialisé [46], cependant en raison de leur grande épaisseur et dimensions (de l'ordre du mm), ces derniers sont ainsi difficiles à nanostructurer, limitant ainsi leur miniaturisation.

En ce qui concerne les couches minces magnétiques, la plupart des études sur les cristaux magnoniques ou sur la magnonique de manière générale sont principalement basées sur du YIG (Yttrium Iron Garnet) ou sur du Py (Permalloy, NiFe). Le YIG est un matériau ferrimagnétique isolant possédant le coeffient d'amortissement le plus bas, de l'ordre de 3.10^{-5} [47], ce qui permet de propager des ondes de spin sur de très longues distances, de l'ordre du mm dans le cas de films épais (autour du μm) [7]. Néanmois, son aimantation à saturation est faible (autour de 0.17 T), ce qui limite grandement son utilisation dans la gamme RF (quelques centaines de MHz lorsqu'on est proche de la rémanence). Toutes les démonstrations d'opérations logiques mentionnées plus haut ont été menées avec du YIG. Cependant, pour être compatible avec les technologies CMOS existantes, ce dernier doit pouvoir croître dans sa forme cristalline sur des substrats de silicium, ce qui pour le moment est compliqué technologiquement même si de grands progrès ont été atteints ces dernières années [48]. Le permalloy, quant à lui, est un matériau ferromagnétique métallique très largement utilisé dans la littérature en raison de sa facilité de déposition et nanostructuration [7]. Son aimantation à saturation est relativement élevée (~ 1 T) mais son coefficient d'amortissement est bien plus élevé que celui du YIG (de l'ordre de 6.10^{-3} [7]). De ce fait, la distance que peut parcourir les ondes de spin dans ce matériau est largement réduite à quelques microns seulement.

En conséquence, nous proposons dans cette thèse d'étudier la possibilité de fabriquer des réseaux périodiques de trous à partir d'une couche mince d'alliages d'Heusler Co_2MnSi (CMS) [49, 50]. Ce

matériau a été notamment étudié au CEMES pendant plusieurs années [51–53]. Dans le cadre de ce travail, l'avantage majeur de ce matériau par rapport au YIG ou au Py est son anisotropie magnéto-cristalline cubique, qui peut atteindre quelques dizaines de mT [52, 53]. Il est à noter que peu de recherches ont jusqu'à présent étudié des guides d'ondes à base d'alliages d'Heusler [54–57, 59], et encore moins portant sur les cristaux magnoniques d'alliages d'Heusler [49, 50]. Par rapport au YIG et au Py, le $\mathrm{Co_2MnSi}$ présente d'autres avantages. Son aimantation à saturation est de l'ordre de $1.3\ \mathrm{T}$, ce qui permet d'obtenir des fréquences de travail supérieures à $1\ \mathrm{GHz}$ à la rémanence [52, 53]. Dans le cas des cristaux magnoniques, cela pourrait également augmenter la largeur des bandes interdites en fréquence [60, 61]. Ce matériau est également demi-métallique (polarisation de spin supérieur à $90\ \%$), ce qui résulte en un faible coefficient d'amortissement entre 1.10^{-3} [53, 64] et 4.10^{-4} [54, 65]. Enfin, sa température de Curie est autour de $985\ \mathrm{K}$ [66] offrant ainsi une stabilité thermique correcte en tant que composant. Un tel matériau permet d'envisager le développement de dispositifs combinant magnonique, spintronique et spin-orbitronique [67, 68]. Néanmoins, son principal désavantage concerne sa fabrication. Généralement, ce matériau est déposé sur des substrats de MgO (001) afin d'assurer une croissance épitaxiale, ce qui pourrait limiter sa compatibilité avec les dispositifs micro-électroniques existants. Néanmoins de récentes recherches ont prouvé la possibilité de faire croître du $\mathrm{Co_2MnSi}$ polycristallin sur des substrats de verre sans observer un changement drastique de la polarisation de spin et du coefficient d'amortissement (de l'ordre de $1.5.10^{-3}$) [64]. Un tel résultat offre la possibilité d'envisager de déposer du $\mathrm{Co_2MnSi}$ de bonne qualité sur des substrats de silicium permettant ainsi de le rendre compatible pour des applications industrielles.

6.5 Micro-nanofabrication de cristaux magnoniques à base d'alliages d'Heusler $\mathrm{Co_2MnSi}$

6.5.1 Caractérisation des couches minces d'alliages d'Heusler $\mathrm{Co_2MnSi}$

Initialement notre objectif était d'obtenir des couches minces de $\mathrm{Co_2MnSi}$ *avec une épaisseur de 30-40 nm cristallisées dans la phase* $L2_1$*. Malheureusement, après le confinement lié au COVID en 2020, notre sputtering a depuis présenté des pannes majeures quelques semaines après le début de notre campagne de croissance. Au moment de la rédaction de ce manuscrit, le sputtering est toujours en panne. En conséquence, très peu de couches minces de* $\mathrm{Co_2MnSi}$ *ont pu être déposées et nous n'avons pas pu optimiser les conditions de croissance.*

Des mesures FM-FMR (mesures de la puissance absorbée par le système magnétique en modulant en champ, scan en champ à fréquence fixe) ont été réalisées sur les couches minces de CMS cappées avec du MgO afin de déterminer ses propriétés magnétiques. Les résultats présentés ci-dessous suggèrent que nos films minces ne possèdent pas qu'une seule phase cristalline comme attendu et de faibles variations des paramètres magnétiques (M_s, H_k, α) ont été observées d'un échantillon à l'autre. Dans cette partie, nous montrons un exemple typique des propriétés magnétiques mesurées sur un lot d'échantillons qui ont été utilisés pour la nanostructuration en cristaux magnoniques.

Les mesures ont été faites en appliquant un champ magnétique $\vec{H_0}$ suivant l'axe de facile aimantation et suivant l'axe de difficile aimantation. En raison des axes cristallographiques du CMS à 45° par rapport au substrat MgO et de la négativité de la constante d'anisotropie K_c, les axes de facile aimantation du CMS sont parallèles aux bords du substrat de MgO tandis que les axes de difficile aimantation sont suivant les diagonales du substrat. Lors des mesures, la fréquence du courant RF injecté dans la microstrip est fixe et le champ magnétique $\mu_0 H_0$ dans le plan est balayé de 0 à $300\ \mathrm{mT}$. Les signaux mesurés correspondant à des dérivées de Lorentzienne ($\propto dP/dH$) n'étaient pas symétriques.

Nous attribuons cette asymétrie au fait que nos échantillons ne sont pas parfaitement cristallisés dans une seule phase cristalline. Comme mentionné plus haut, de tels films minces n'auraient pas été utilisés en temps normal pour réaliser les cristaux magnoniques car ils n'ont pas pu être optimisés. Par ailleurs, nous n'avons pas réalisé d'analyses structurales complètes et chronophages telles que HRTEM-STAADF, diffraction aux rayons X pour différentes longueurs d'ondes, combinés à des mesures FMR en angle comme réalisés dans la thèse de I. Abdallah [111]. Nous nous sommes appuyés sur les précédents travaux de notre groupe de recherche qui étudie ces matériaux depuis une dizaine d'années. Au vue des précédents travaux de notre groupe, nous supposons ainsi que nos échantillons possèdent des grains cristallisés de faibles dimensions dans la phase $B2$ incorporés dans une large matrice de phase cristalline $L2_1$ [111]. En conséquence, nous considérons qu'on a une phase majoritaire (très probablement $L2_1$) et une phase minoritaire (très probablement $B2$) dans nos échantillons de CMS avec des propriétés magnétiques très semblables.

Malgré les deux pics mélangés, nous avons pu extraire la valeur du champ de résonance H_r pour chaque fréquence en ajustant l'équation (3.5) avec les pics de résonance. Sur la figure 6.22 a), nous avons tracé $f(H_r)$ pour les directions de facile et difficile aimantation avec des points colorés pour les deux phases cristallines. La valeur du champ d'anisotropie cubique H_k correspond au point

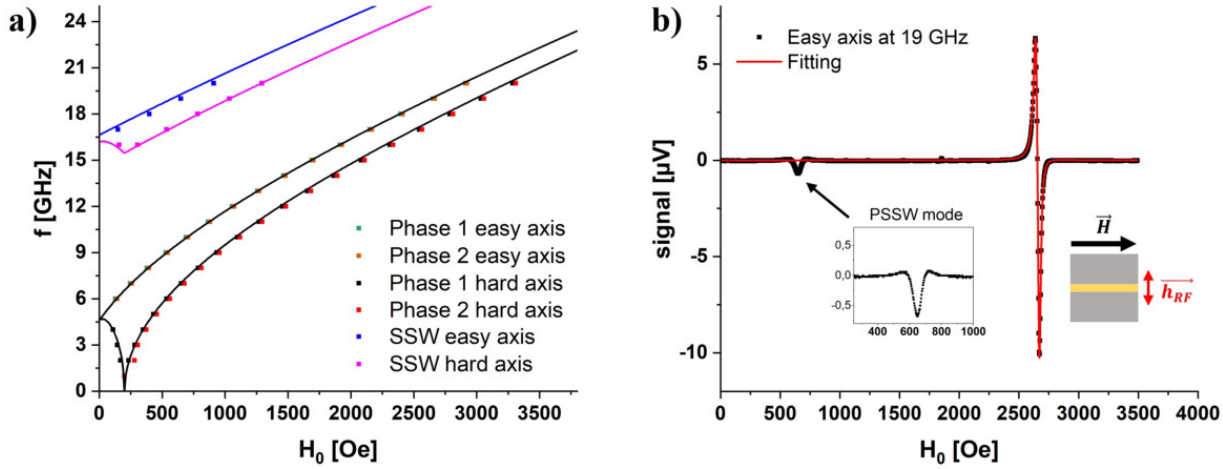

Figure 6.22: a) Evolution de la fréquence de résonance f en fonction du champ magnétique H_0 appliqué suivant un axe de facile aimantation (points verts phase majoritaire, points oranges phases minoritaire) et de difficile aimantation (points noirs phase majoritaire, points rouges phase minoritaire). Les points de mesures concernant le mode en épaisseur PSSW sont également montrés en bleu pour l'axe facile et en rose pour l'axe difficile . b) Exemple de signal FM-FMR mesuré à 19 GHz. La ligne rouge correspond à l'ajustement des points de mesures en noir. Dans l'encart, nous montrons le pic de résonance correspondant au premier mode en épaisseur PSSW.

d'inflexion (à $f = 0$ GHz) lorsque $\vec{H}_0$ est appliqué suivant l'axe difficile. Ces courbes $f(H_r)$ sont ajustées avec l'équation Smit-Belger pour les axes facile et difficile, correspondant aux lignes sur la figure 6.22 a), ce qui permet alors de déterminer le facteur gyromagnétique γ et l'aimantation à saturation M_s. La constante d'échange peut ensuite être obtenue à partir du premier mode en épaisseur PSSW pouvant être mesuré à haute fréquence et bas champ comme montré dans l'encart de la figure 6.22 b). Les constantes magnétiques ainsi déterminées sont résumées dans la table 6.3. Ces résultats sont proches de ceux obtenus lors des précédents travaux de I. Abdallah [53, 111], sauf en ce qui concerne le champ d'anisotropie cubique dont la valeur est inférieure à celle attendue (de l'ordre de 30 mT).

En traçant l'évolution de la largeur des pics de résonance en champ en fonction de la fréquence $\Delta H(f)$, il est possible de déterminer le coefficient d'amortissement de Gilbert α en ajustant la courbe de l'équation (1.97). Cependant, en raison de la proximité des pics associés aux deux phases majoritaire et minoritaire, le traitement de ces mesures fut difficile résultant en des barres d'erreurs im-

Aimantation à saturation $\mu_0 M_s$ **[T]**	**Champ d'anisotropie cubique** $\mu_0 H_k$ **[mT]**	**Constante d'anisotropie cubique** K_{c1} **[J m^{-3}]**	**Facteur gyromagnétique** $\frac{\gamma}{2\pi}$ **[GHz T^{-1}]**	**Constante d'échange** A **[pJ m^{-1}]**
1.28	20	-10186	28.8	21.5

Table 6.3: Paramètres magnétiques obtenus à partir des ajustements des courbes $f(H_r)$.

portantes. La valeur de α extraite est approximativement 2.10^{-3}. La contribution extrinsèque ΔH_0 déterminée est relativement élevée (de l'ordre de 20 Oe), ce qui reflète la "mauvaise" cristallinité de nos échantillons.

6.5.2 Micro/Nanostructuration des cristaux magnoniques à base de couches minces Co_2MnSi

Il existe différentes techniques de nanostructuration afin de réaliser des réseaux périodiques de trous (dimensions inférieures au micron) dans des couches minces. Les principales techniques utilisées dans la littérature sont la gravure FIB (Focused Ion Beam) [219–222], la lithographie optique "deep ultraviolet" et lift-off [22, 223, 224], la lithographie électronique (EBL) et gravure ionique (Ion Beam etching, IBE) [49, 225], EBL et lift-off [226] ou encore via l'utilisation de membranes poreuses [227]. Cette partie présente les étapes de micro/nanofabrication qui ont été développées au CEMES afin de produire les cristaux magnoniques de CMS. Ces travaux ont représenté une part majeure des développements expérimentaux que j'ai mené durant cette thèse. Nous rappelons brièvement les contraintes que nous nous sommes imposés pour la fabrication de nos échantillons :

- Nous avons choisi de faire des réseaux dont les trous sont de forme carrée et possédant des dimensions réalisables, i.e. suffisamment larges pour que cela puisse être fait de manière systématique avec des techniques de nanostructuration standard mais tout en étant suffisamment de petites dimensions afin d'observer des effets significatifs sur les ondes de spin (création de bandes de fréquence interdites, effets reconfigurables). Dans la littérature, il existe de nombreux travaux numériques sur des cristaux magnoniques dont les motifs ont des dimensions de l'ordre de quelques nm, ce qui permet d'observer de larges bandes de fréquences interdites de quelques GHz, mais sans études experimentales associées en raison du grand défi technologique que nécessite la réalisation d'aussi petites dimensions. En conséquence, nous avons choisi des dimensions des trous carrés s entre 100 et 300 nm avec un espacement d tel que $s \leq d \leq 3s$.

- Le réseau périodique de trous doit s'étendre sur une surface du CMS suffisamment large afin de pouvoir considérer notre cristal magnonique comme 2D quasi-infini. Cela dépend notamment de la taille des motifs et de leur espacement. Nous avons considéré qu'il nous fallait au moins 50 périodes a ($a = s + d$). De plus, nous souhaitions mesurer ces cristaux magnoniques avec des micro-antennes larges d'une dizaine de microns afin d'être dans des conditions proches d'une excitation uniforme (FMR). Nous avons donc cherché à réaliser des réseaux de trous s'étendant sur quelques dizaines de microns (limité par les champs de vue en FIB et EBL).

Pour réaliser les réseaux périodiques de trous dans des couches minces de CMS, nous avons utilisé des techniques de gravure sèche. Lorsque je suis arrivée au laboratoire, la lithographie électronique n'était pas encore opérationnelle. Par conséquent, dans un premier temps, nous avons commencé par faire les motifs par gravure FIB avec des ions Ga^+. Cette technique a l'avantage d'une écriture

directe des motifs mais présente certaines limites pour atteindre nos objectifs, ce que nous verrons dans la section 6.7.1. Par conséquent, en parallèle j'ai travaillé au développement de la lithographie électronique et équipements de lift-off au CEMES afin de produire des réseaux de trous par gravure ionique Ar^+ au travers d'un masque de résine électrosensible. La principale difficulté que nous avons rencontrée provenait de la gravure lente du Co_2MnSi. Cela a nécessité des tests de différentes résines électrosensibles afin de déterminer celle qui tiendrait le temps nécessaire pour graver 45 à 50 nm d'épaisseur de nos couches minces. De plus, le bâti de gravure IBE que nous utilisons au laboratoire n'est pas un bâti commercial mais un prototype, ce qui a également requis des travaux de développement.

6.5.2.1 Gravure FIB des réseaux périodiques de trous dans des couches minces de Co_2MnSi

La gravure FIB permet une micro/nanostructuration directe sans masque des motifs sur un substrat. Dans cette thèse, nous avons utilisé le FEI Helios Nanolab 600i dual-beam FIB-SEM [233, 234], qui est donc équipé à la fois d'un microscope électronique à balayage (SEM) pour de l'imagerie et d'une colonne FIB aux ions Ga^+ pour de l'imagerie, gravure et dépôt de couches.

Lorsque le faisceau Ga^+ impacte la surface de l'échantillon, plusieurs phénomènes physiques se produisent en plus de la gravure ionique, tels que la génération d'électrons secondaires, l'implantation d'ions Ga^+ et l'amorphisation/recristallisation du matériau [235]. Selon l'énergie des ions Ga^+ définie par la haute tension appliquée, les couches endommagées vont s'étendre plus ou moins profondément. Afin de pourvoir éjecter la matière de manière efficiente, nous avons appliqué une haute tension de 30 kV, ce qui permet par la même occasion d'obtenir une taille de spot du faisceau ionique très faible [231].

La qualité et la résolution de la gravure FIB sont principalement limitées par deux effets. Le premier est la redéposition d'atomes éjectés. La seconde limite concerne l'implantation d'ions Ga^+ dans le matériau. Ces ions peuvent interagir chimiquement avec les atomes du matériau gravé et potentiellement modifier les propriétés physiques (mécanique, électrique, magnétique, optique) du matériau. L'implantation va apparaître sur un faible volume autour de la zone gravée de l'échantillon.

Les méthodes de balayage du faisceau ionique et les paramètres d'exposition peuvent aider à réduire l'impact de ces problèmes. Pour réaliser les différents trous, il est possible de travailler en mode série ou parallèle. En mode série, un trou est entièrement gravé avant de passer à un autre trou. Cela implique que le faisceau reste un certain temps sur la zone à gravée, ce qui peut augmenter les effets de redéposition. En mode parallèle, le faisceau ionique réalise une passe de gravure (faible temps de gravure) sur chaque motif de tout le réseau. Pour graver entièrement les motifs, de multiples passes successives sur chacun des motifs sont réalisées jusqu'à gravure complète de tous les trous. Le mode parallèle est généralement utilisé pour réduire la redéposition [236]. Pour le balayage du faisceau sur le motif pour faire un trou, on a de même les modes de balayage une seule passe et multi-passes analogues aux modes série et parallèle mais pour le motif d'un seul trou.

Pour obtenir la meilleure résolution et donc les meilleurs motifs, idéalement il serait préférable de travailler avec la taille de spot du faisceau ionique la plus petite possible (diaphragme et donc le courant le plus petit possible). Cependant, ce n'est pas toujours pertinent de se placer dans ces conditions lorsque l'on souhaite graver de nombreux motifs couvrant une large surface de l'échantillon car cela risque d'augmenter fortement le temps total de gravure, générant ainsi des problèmes de désalignement des trous les uns par rapport aux autres en raison de dérives mécaniques et électroniques au cours du temps. En conséquence, un compromis doit être fait entre les paramètres expérimentaux pour optimiser le rendu des motifs gravés et le temps total de gravure.

Réseaux périodiques de trous gravés par FIB

L'utilisation du FIB au CEMES est très limitée en raison d'un nombre conséquent d'utilisateurs. Malgré de nombreux tests pour optimiser la gravure des réseaux de trous, le temps limité (maximum 8h de gravure) et le peu de sessions de travail obtenues nous a obligé à faire un compromis sur la qualité des motifs gravés. Un exemple est donné à la figure 6.23 où l'on peut voir la différence entre les stratégie de gravures parallèles (a)) et série (b)) sur ces images SEM. Pour ce test, nous avons

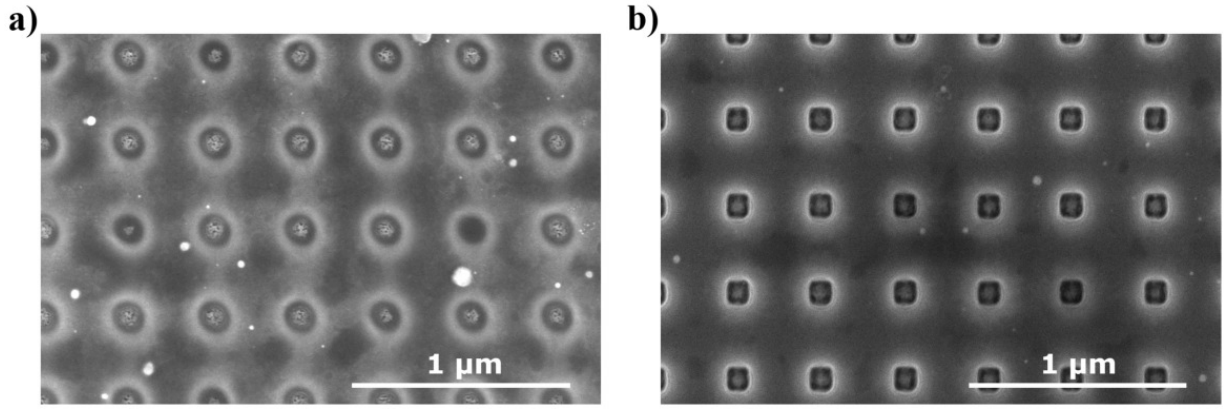

Figure 6.23: Images SEM de réseaux de trous carrés de Co_2MnSi ($40\ \mu m \times 40\ \mu m$) dont la taille des trous est 100 nm et l'espacement entre les trous 300 nm gravés par FIB avec a) une stratégie parallèle multi-passes et b) une stratégie série multi-passes.

gravé un réseau de trous s'étendant sur une surface de $40\ \mu m \times 40\ \mu m$ dont les trous ont une taille latérale de 100 nm et d'espacement bord à bord entre les trous de 300 nm. Les conditions expérimentales sont résumées dans la table 6.4. Il est évident qu'en mode parallèle (figure 6.23 a)) nous n'avons

Haute tension [kV]	**Champ de vue** [μm^2]	**Courant** [pA]	**Taille théorique de spot du faisceau ionique** [nm]
30	100×100	70	21

Table 6.4: Conditions expérimentales FIB

pas trouvé les conditions de gravure correctes pour obtenir des trous carrés gravés. Par contre, au vue de l'image SEM de la figure 6.23 b), la stratégie série multi-passes permet d'obtenir des trous carrés assez bien définis. Par conséquent, nous avons choisi de travailler avec cette procédure de gravure. Il est cependant à noter que le temps nécessaire pour graver un tel réseau en entier avec cette stratégie était de 8 heures contre 1 heure dans le cas de la stratégie parallèle. Par conséquent, les contraintes d'accès au FIB ont ainsi limité les dimensions latérales du réseaux de trous à $40 - 50\ \mu m$ pour des trous carrés de 100 nm espacés de 300 nm.

On peut remarquer sur l'image SEM de la figure 6.23 b) la présence d'un halo blanc autour des trous et la forme arrondie des sommet des motifs carrés. Ce phénomène a été observé quelque soit la taille des trous (jusqu'à 300 nm) et l'espacement entre les trous. En particulier, les trous présentent une forme en cuve (flancs non droits mais incurvés) lorsqu'on les observe avec un angle de vue de 52° et en cross-section. Une cause possible pour cette géométrie en cuve serait la forme conique du faisceau ionique et le fait que nous avons focalisé le faisceau sur la surface de l'échantillon.

En plus des imperfections géométriques obtenues, les mesures FMR de la section 6.7.1 démontreront également que l'implantation d'ions Ga^+ sur les flancs des trous induit une forte modification des propriétés magnétiques du CMS dans ces zones, ce qui sera au détriment de la possibilité de réaliser un cristal magnonique reconfigurable. Par conséquent, nous n'avons pas entrepris plus de développement sur cette technique de nanostructuration. A la place, nous avons développé une autre méthode pour atteindre nos objectifs.

6.5.2.2 Combinaison de lithographie électronique et gravure ionique pour la nanofabrication des réseaux périodiques de trous de Co_2MnSi

Contrairement à la technique FIB présentée précédemment, la combinaison d'EBL et gravure ionique n'est donc pas une approche d'écriture directe des motifs du fait qu'elle requiert plusieurs étapes de fabrication. Dans un premier temps, on transfère les motifs à graver dans un masque de résine. Dans un second temps, on transfère les motifs dans l'échantillon en gravant par IBE au travers du masque. Pour cette étape, l'échantillon est généralement placé dans une chambre IBE permettant de graver pleine plaque avec des ions inertes Ar^+. Il existe plusieurs stratégies pour réaliser le masque de gravure (résines, masques métalliques). Dans cette thèse, nous avons opté pour un masque de résine électrosensible. Les différentes étapes pour la nanofabrication des réseaux de trous sont illustrées dans la figure 6.24. Tout d'abord, la résine est déposée sur la surface de l'échantillon avec une tournette (spin-coater) et recuite. La lithographie électronique est ensuite opérée pour définir les motifs dans la résine (masque). Après développement (révélation des motifs), l'échantillon est soumis à la gravure ionique afin de transférer les motifs dans l'échantillon tandis que le reste de l'échantillon est protégé de la gravure par le masque de résine. Enfin, l'échantillon est placé dans un solvant afin de retirer la résine.

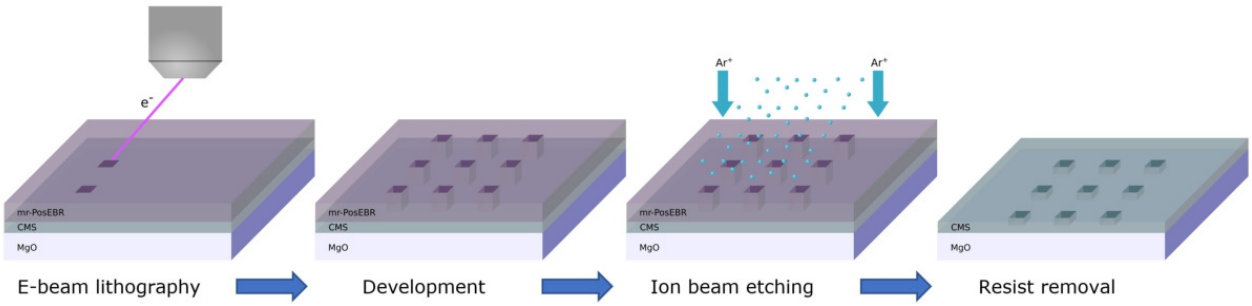

Figure 6.24: Schéma du procédé combinant lithographie électronique et gravure IBE pour la nanofabrication de réseaux de trous périodiques dans une couche mince de CMS.

La lithographie électronique consiste à utiliser un faisceau d'électrons focalisés pour écrire des motifs prédéfinis par l'utilisateur sur une résine électrosensible. L'irradiation au faisceau électronique change la solubilité de la résine exposée dans un développeur (solvant) approprié. Cette technique offre une très grande résolution en raison de la faible longueur d'onde des électrons (de l'ordre du picomètre voire moins) et de sa petite taille de spot, permettant ainsi de réaliser notamment des motifs de lignes de dimensions inférieures à $10\ \mathrm{nm}$ [244]. Dans cette thèse nous avons travaillé sur le microscope électronique ZEISS SEM équipé d'un module de lithographie électronique ELPHY Multibeam Raith de la salle blanche du CEMES. Des tests ont été également réalisés avec le microscope électronique JEOL SEM et module EBL ELPHY Quantum Raith à l'AIME (LPCNO, INSA Toulouse).

Réseaux périodiques de trous gravés par EBL+IBE

La principale difficulté de cette approche a été de trouver les conditions d'opérations afin d'obtenir les réseaux de trous avec les spécifications désirées. En particulier, il a fallu trouver une résine électrosensible qui puisse être suffisamment résistante pour tenir l'étape de gravure IBE tout en étant facilement retirable après des conditions de gravure rudes. Généralement, les résines négatives telles que HSQ [248] ou ma-N2400 [252] sont utilisées pour les procédés de gravure en raison de leur forte résistance à la gravure. Ce type de résine est ainsi très utile pour faire des réseaux de nanopoints (nanodots en anglais) mais pas pour des réseaux de trous. Dans ce cas, nous avons plutôt opté pour

des résines positives qui se dissolvent dans le développeur lorsqu'exposées au faisceau électronique. Contrairement aux procédés de lift-off qui requièrent préférentiellement un profil de résine "en casquette" (undercut en anglais), pour des procédés impliquant de la gravure, il est préférable un profil de résine avec des flancs ouverts droits afin d'assurer des flancs droits gravés dans la couche mince sous-jacente. De ce fait, nous avons testé deux résines en particulier : PMMA 950, en raison de son extrême résolution pouvant être inférieure à $10\ \mathrm{nm}$ et sa facilité à être retirée (acétone), et mr-PosEBR de Micro Resist Technology GmbH [253, 254]. Après de nombreux tests sur les conditions d'EBL et de gravure, nous n'avons pas pu réaliser des réseaux de trous correctes avec la PMMA en raison de sa faible résistance à la gravure (bords des trous rugueux, formes carrés inhomogènes) et de sa très grande difficulté à être retirée après gravure (réticulation de la résine lors de la gravure ionique). Par conséquent, nous nous sommes par la suite focalisés sur la résine mr-PosEBR durant la seconde année de mon doctorat. Cette résine acrylate est fortement sensible aux électrons et particulièrement appropriée pour la gravure en raison de sa forte résistance à la gravure sèche. Cette résine n'avait jamais été utilisée au laboratoire, nous avons donc développé tous les procédés permettant des conditions expérimentales optimales. Les principaux paramètres optimaux pour la réalisation de nos réseaux de trous sont indiqués dans la troisième colonne de la table 6.5. Avec cette résine, nous avons rencontré princi-

	Conditions process 1	**Conditions process 2**	**Conditions process 3**
Résines	mr-PosEBR 0.1	mr-PosEBR 0.3	mr-PosEBR 0.3
Vitesse tournette [rpm]	1500	4000	4000
Epaisseur résine [nm]	≈ 150	≈ 330	≈ 330
Température pré-recuit [$^\circ\mathrm{C}$]	150	150	150
Temps pré-recuit [min]	2	1	1
Haute tension [kV]	20	20	30
Courant [pA]	40	40	40
Focus sur marques proches	No	Yes	Yes
Dose surfacique [$\mu C.\mathrm{cm}^{-2}$]	75	224	224
Développeur	mr-Dev800 (amyl acetate)	mr-Dev800 (amyl acetate)	mr-Dev800 (amyl acetate)
Temps de développement [s]	60	60	60
Haute tension IBE [V]	1000	1000	1000
Pression IBE [mbar]	$\approx 3.3.10^{-3}$	$\approx 3.3.10^{-3}$	$\approx 3.3.10^{-3}$
Courant IBE [mA]	14	14	14
Temps de gravure [min]	7	8	8
Solvant remover	ultrasonic bath SVC-14 45°	ultrasonic bath SVC-14 45°	ultrasonic bath SVC-14 45°

Table 6.5: Table des principaux paramètres de trois procédés utilisés pour fabriquer les réseaux de trous dans des couches minces de CMS d'épaisseur $45 - 50\ \mathrm{nm}$.

palement un problème lié aux effets de proximité (les électrons du faisceau incident sont diffusés dans la résine et l'échantillon sous-jacent et peuvent exposer lors de leurs parcours des zones de résines adjacentes non désirées pouvant impliquer une distorsion des motifs une fois révélés). Pour réduire au maximum ces effets, nous avons principalement décidé de travailler avec une résine épaisse ($300\ \mathrm{nm}$) pour compenser l'érosion plus rapide de la résine proche des motifs au détriment de la résolution de nos motifs (cela devient plus compliqué de faire motifs de $100\ \mathrm{nm}$), et d'appliquer le maximum de

haute tension possible avec notre microscope électronique soit 30 kV. Des images de réseaux de trous obtenus avec le procédé 3 de la table 6.5 sont montrés dans la figure 6.25. On peut remarquer sur ces

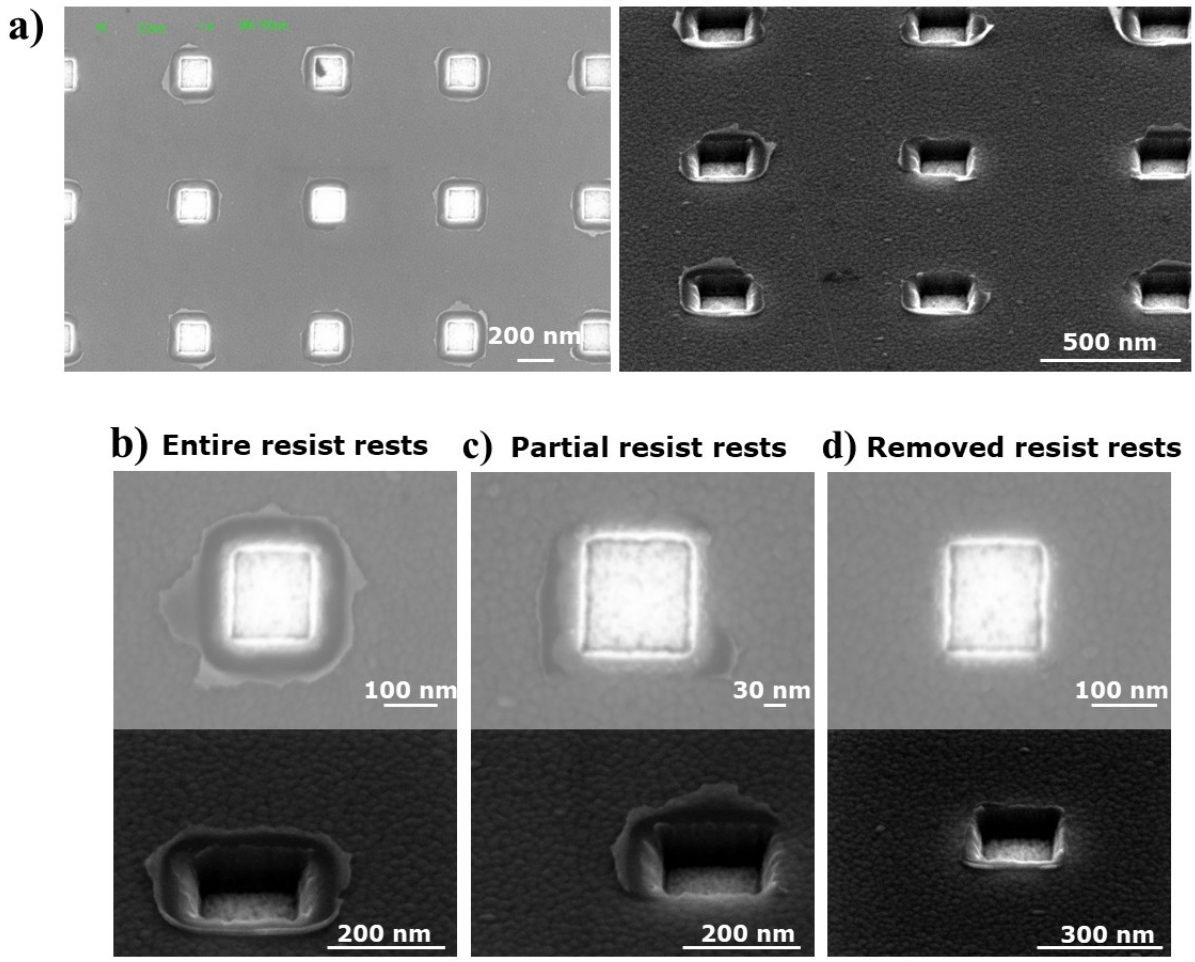

Figure 6.25: Images SEM de face et tiltées (52°) de l'échantillon avec a) plusieurs trous dans la couche de CMS (taille latérale 200 nm), avec des trous particuliers comportant b) des restes de résines complets attachés au trou, c) des restes de résines partiellement enlevés et d) sans restes de résines.

images que la taille (200 nm) et la forme carrée des trous sont respectées et on observe également la présence d'un résidu autour des trous qui par endroit est partiellement, voire entièrement enlevé et à d'autres entièrement présent autour des trous. Nous ne savons pas exactement ce que sont ces résidus, cela pourrait être de la résine ou/et du redépôt. Nous pensons plutôt que ce sont des restes de résine mais nous ne pouvons pas le prouver totalement. Plusieurs tests ont été menés pour réduire ces résidus, mais nous ne sommes pas parvenus à un enlèvement complet de ces résidus.

Nous avons également testé la réalisation de différentes tailles de trous, 300, 200 et 100 nm, avec pour espacements respectivement 900, 600, 300 nm comme montré dans la figure 6.26. On constate ainsi que pour des trous carrés de 300 et 200 nm, les tailles et formes sont respectées avec des flancs droits. Par contre, concernant les trous de dimensions 100 nm, on voit très bien les résidus de résine restants. Il devient alors difficile de savoir si dans ce cas la couche de CMS a été suffisamment gravée.

Par conséquent, nous avons réussi à obtenir des réseaux périodiques de trous carrés correctes dans des couches minces de CMS d'épaisseurs $45 - 50$ nm jusqu'à des dimensions de trous de 200 nm.

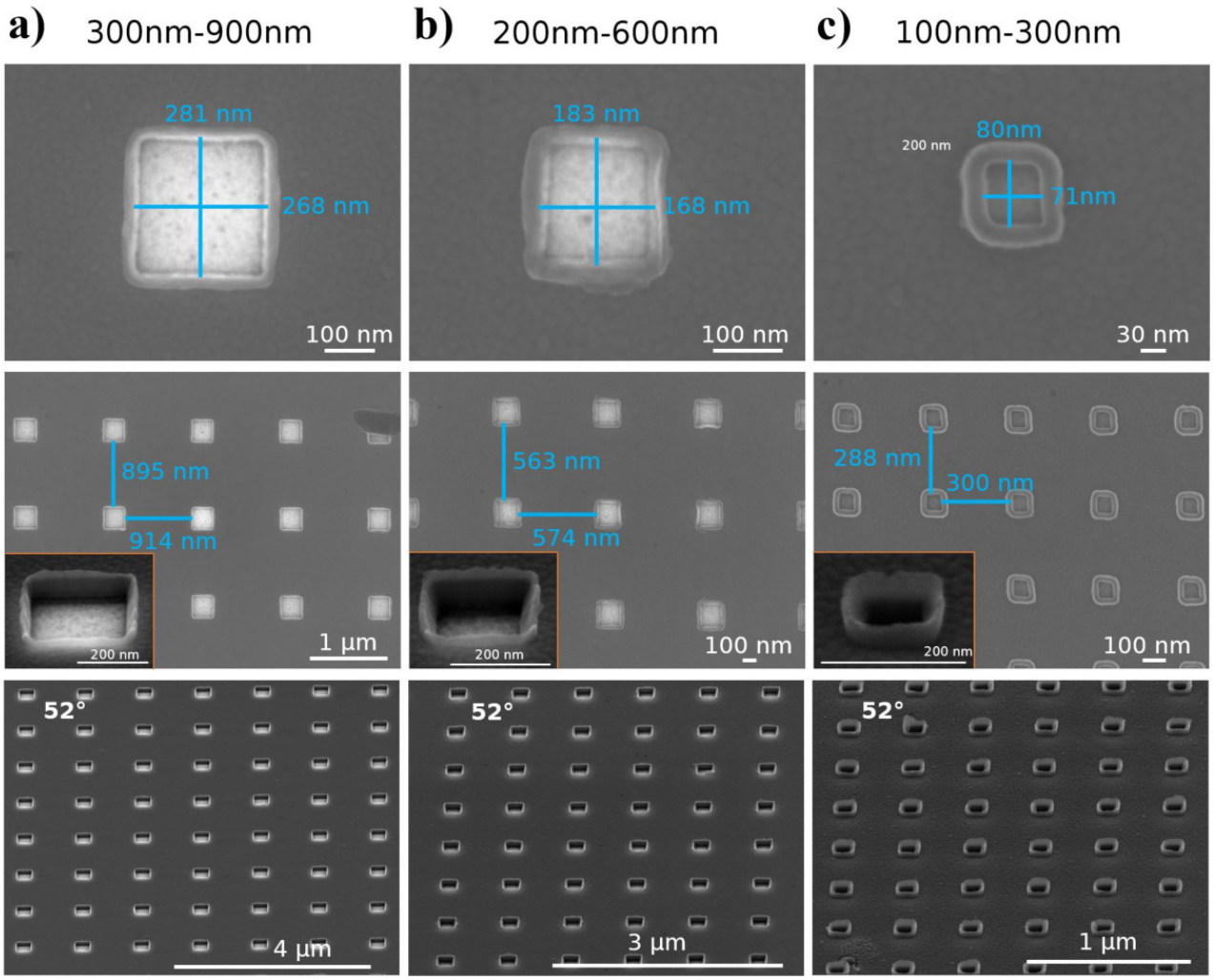

Figure 6.26: Images SEM à différents grandissements et pour un angle de vue de $52°$ de réseaux de trous de CMS de forme carrée pour trois combinaisons de taille de trou et d'espacement a) 300 nm et 900 nm, b) 200 nm et 600 nm et c) 100 nm et 300 nm respectivement. Dans les encarts sont montrés des images SEM tiltées d'un trou de taille correspondante.

6.5.3 Dispositifs de cristaux magnoniques complets

Afin de mesurer ces cristaux magnoniques de CMS avec des micro-antennes, d'autres étapes de micro-fabrication sont nécessaires. Une fois le cristal magnonique fait, il faut l'isoler du reste de la couche mince de CMS en gravant le CMS tout autour du cristal magnonique sur une surface pouvant comporter la micro-antenne et éventuellement des contacts électriques (cas de l'échantillon $\#2$). Ensuite, on dépose une couche de passivation sur le cristal magnonique et la zone gravée tout autour avec 200 nm de Si_3N_4. Enfin on fait une lithographie laser puis lift-off de Ti (10 nm), Cu (200 nm), Au (30 nm) pour réaliser la micro-antenne.
Trois échantillons ont été fabriqués et étudiés : l'échantillon $\#1$ comporte un réseau périodique de trous carrés de 100 nm et de périodicité 400 nm gravés par FIB et une micro-antenne pour des mesures FMR ; l'échantillon $\#2$ comporte un réseau périodique de trous carrés de taille 200 nm et espacement 600 nm gravés par EBL+IBE, des contacts électriques et une micro-antenne pour des mesures FMR ; l'échantillon $\#3$ comporte 6 dispositifs de cristal magnonique de CMS avec différentes tailles de trous et espacements gravés par EBL+IBE et des micro-antennes pour des mesures micro-BLS. Chaque échantillon sera présenté dans les parties suivantes concernant les mesures.

6.6 Etats dynamiques reconfigurables dans les cristaux magnoniques de Co_2MnSi à la rémanence : une étude numérique

Comme abordé dans la section 6.4.2, nous proposons d'utiliser des cristaux magnoniques d'alliages d'Heusler Co_2MnSi pour développer des opérations radiofréquences reconfigurables à la rémanence. Pour réaliser cet objectif, nous avons choisi des réseaux periodiques de trous (magnetic antidot lattices) comme cristaux magnoniques et dans cette section nous démontrons de manière numérique la possibilité d'allumer/éteindre plusieurs modes d'ondes de spin dans un dispositif fonctionnant sans champ magnétique de saturation. Des simulations micromagnétiques ont été réalisées avec Mumax3 [191] et OOMMF afin de calculer les états magnétiques rémanents de réseaux périodiques de trous de CMS ainsi que leurs réponses radiofréquences. Nous avons utilisé des conditions périodiques 2D (PBC Periodic Boundary Conditions en anglais) afin de simuler un cristal magnonique infini tout en réduisant la taille du système magnétique simulé (ce qui permet de gagner en rapidité de calcul). En effet, avec l'application de conditions PBC 2D, il suffit de simuler une cellule unitaire du cristal magnonique composée de quatre trous carrés arrangés dans un réseau carré comme montré dans la figure 6.27. La taille des trous et leur espacement bord à bord sont respectivement s et d. Les dimen-

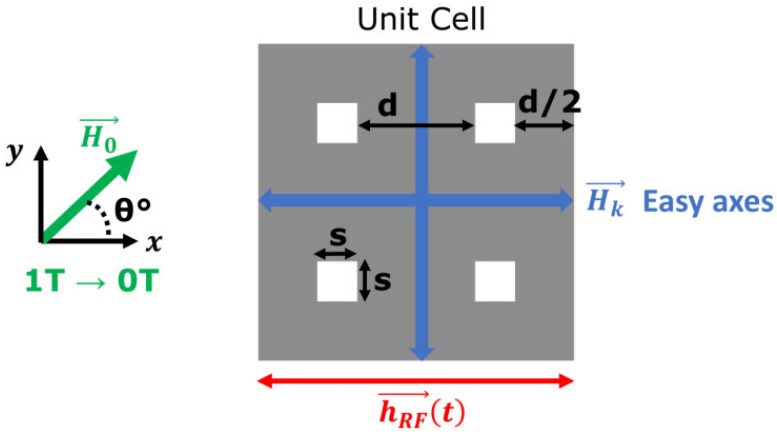

Figure 6.27: Représentation schématisée de la cellule unitaire simulée du cristal magnonique de Co_2MnSi.

sions latérales de la cellule unitaire sont $2s + 2d$. Les axes de symétrie du réseau carré sont orientés suivant les axes x et y.

Les paramètres magnétiques du CMS utilisés pour les simulations sont : l'aimantation à saturation $M_s = 1003.10^3$ A m^{-1}, la constante d'échange $A = 18.10^{-12}$ J m^{-1}, la constante d'anisotropie magnéto-cristalline $K_{c1} = -17.10^3$ J m^{-3} ($\mu_0 H_k \approx 35$ mT) et le facteur gyromagnétique $\gamma = 29$ GHz T^{-1}. Ces valeurs sont similaires à celles obtenues expérimentalement lors de précédents travaux de mon groupe de recherche [53]. Les directions cristallines des axes de facile aimantation sont orientées suivant les directions x et y ($K_{c1} < 0$). La cellule unitaire est discrétisée avec des celulles cubiques de dimensions $5 \times 5 \times 5$ nm^3, ces dernières sont inférieures à la longueur d'échange $\Lambda_{ex} \approx 5.4$ nm. Le coefficient d'amortissement a été fixé à 1.10^{-3}, en accord avec les précédents travaux [53] et les valeurs rapportées récemment dans la littérature [64, 65, 264]. L'épaisseur de la couche mince est 20 nm, ce qui est suffisamment fin pour considérer une aimantation uniforme le long de l'épaisseur.

Simulations des états statiques rémanents

Premièrement on calcule les états magnétiques rémanents à l'équilibre. A partir d'une orientation aléatoire des moments magnétiques du système, on applique un champ magnétique $\mu_0 H_0$ de 1 T afin de saturer les moments magnétiques $\vec{M}$ dans sa direction. $\vec{H}_0$ forme un angle θ avec l'axe x comme

montré sur la figure 6.27. Ensuite, l'amplitude de $\vec{H}_0$ est progressivement diminuée jusqu'à 0 T par pas de champs de 0.01 T. A chaque pas de champ, l'énergie du système magnétique est minimisée. L'état rémanent ainsi obtenu constitue le point de départ pour le calcul des modes dynamiques.

Simulations dynamiques

Nous avons appliqué un champ magnétique uniforme dynamique sous la forme d'une impulsion temporelle en sinus cardinal suivant la direction x. L'amplitude de l'impulsion était de 1 mT, ce qui est suffisamment faible pour assurer un régime linéaire de précession de l'aimantation, et la fréquence de coupure est $f_c = 30$GHz. Les valeurs de l'aimantation en chaque cellule spatiale du système simulé $\vec{M}(t, x, y, z)$ sont enregistrées toutes les 10 ps. La réponse radiofréquence est obtenue à partir de la transformée de Fourier (FFT Fast Fourier Transform) de la composante dynamique en z de l'aimantation moyennée sur l'ensemble de la cellule unitaire, $m_z(t)$.

Le profil spatial de chaque mode d'ondes de spin est obtenu en réalisant d'abord une FFT sur $m_x(t)$ en chaque cellule spatiale du système puis en appliquant une transformée de Fourier inverse (IFFT) à la fréquence du mode d'ondes de spin à visualiser. Le profil spatial correspond au "cliché" (snapshot) temporel pour lequel on a calculé le maximum d'amplitude moyennée sur toutes les cellules spatiales.

Recherche d'états rémanents reconfigurables

Comme mentionné dans la section 6.4.2, nous recherchons des états rémanents clairement distincts à l'équilibre lorsqu'on applique un champ magnétique d'initialisation suivant la direction x ou y. Cela est nécessaire afin d'obtenir des réponses radiofréquences du dispositif différentes pour un champ radiofréquence uniforme (appliqué suivant x par exemple), ce qui constitue la base de la reconfigurabilité. Egalement, nous cherchions à obtenir des états rémanents les plus uniformes possibles magnétiquement. Nous voulions aussi garder un espacement entre les trous suffisamment faible afin d'avoir des bandes de fréquences interdites suffisamment larges, et les dimensions des trous doivent être réalisables via des techniques de nanostructuration standards comme discutées dans la section 6.5.2. Enfin, nous nous sommes concentrés sur une excitation uniforme car nous souhaitions réaliser un dispositif dont les dimensions sont bien plus petites que la longueur d'onde d'ondes radiofréquences dans le vide.

Pour atteindre ces objectifs, nous avons testé plusieurs configurations de tailles de trous s et d'espacements d. Nous avons obtenu des opérations reconfigurables pertinentes à la rémanence pour un rapport d'aspect $s/d \leq 1/3$.

6.6.1 Réponses radiofréquences de différents états rémanents

Stabilisation d'états rémanents différents

Nous présentons des résultats pour un cristal magnonique avec des tailles de trous $s = 300$ nm et d'espacement $d = 900$ nm. Dans la figure 6.28 a), quatre états rémanents ont pu être obtenu suivant la direction d'application du champ d'initialisation $\vec{H}_0$ par rapport à l'axe x. Parmi ces quatres configurations, les configurations A1 ($\theta = 0°$) et A4 ($\theta = 90°$) présentent une aimantation quasi-uniforme alignée selon la direction du champ d'initialisation H_0, i.e. suivant x ou y respectivement. Ces états rémanents sont très semblables à des états saturés, à l'exception de la présence de petits domaines magnétiques apparaissant proches des bords des trous, que l'on nomme dans ce manuscrit domaines de bords. Les configurations A1 et A4 sont stabilisées pour $0° \leq \theta \leq 40°$ et $50° \leq \theta \leq 90°$ respectivement. Ces états rémanents résultent de la compétition entre le champ démagnétisant induit par

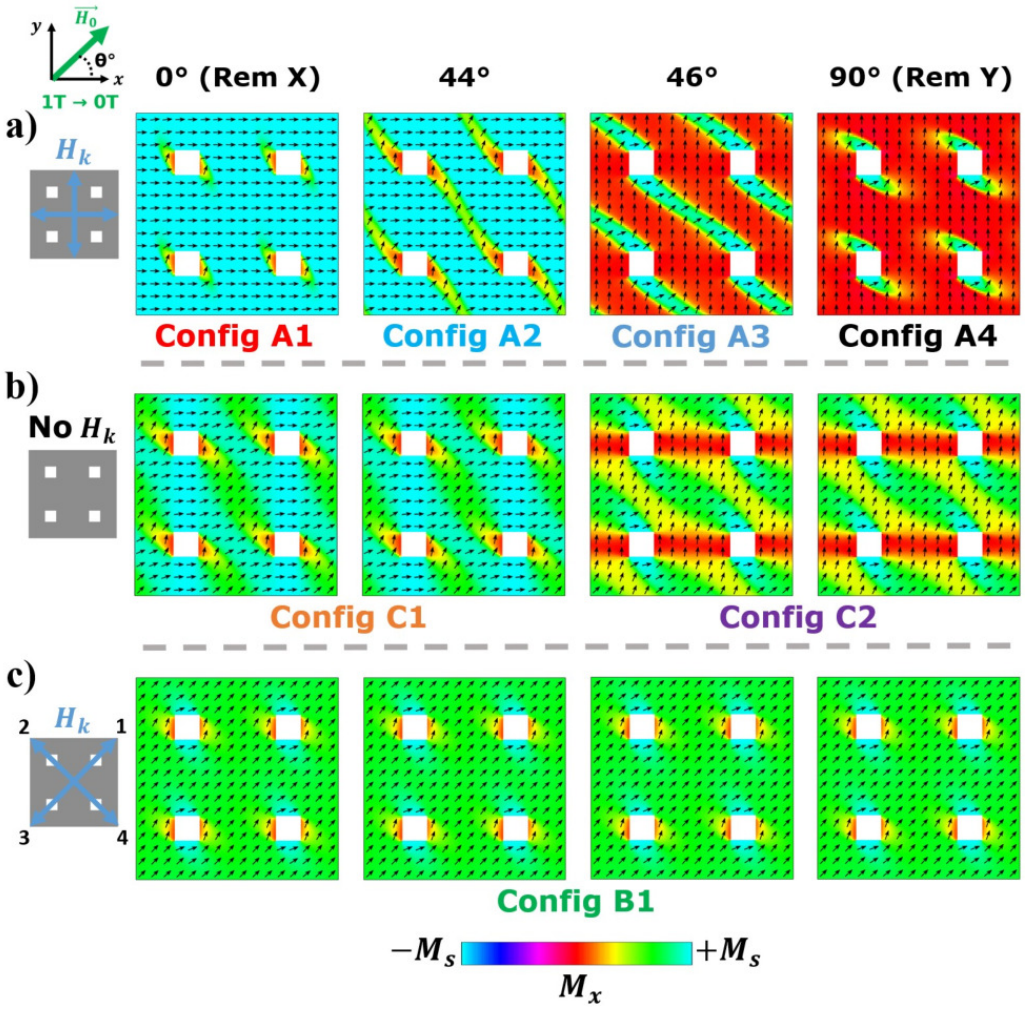

Figure 6.28: Etats rémanents simulés d'un réseau périodique de trous carrés 2D de Co_2MnSi avec $s = 300$ nm et $d = 900$ nm en fonction de l'angle θ entre le champ d'initialisation H_0 et l'axe x dans le cas a) d'axes de facile aimantation (anisotropie cubique) alignés selon les axes de symétrie du réseau de trous, b) d'un même système sans anisotropie cubique ($H_k = 0$), c) d'axes d'anisotropie cubique (axes faciles) tournés de $45°$ par rapport aux axes de symétrie du réseau de trous.

la présence des trous (anisotropie de forme), l'anisotropie cristalline cubique du CMS, l'interaction d'échange et la direction du champ d'initialisation H_0. La symétrie du réseau carré de trous induit une anisotropie planaire quadruple (four-fold en anglais) qui favorise un alignement de l'aimantation suivant les diagonales du réseau [162, 265, 266]. Dans le cas des configurations A1 et A4, l'amplitude de l'anisotropie cubique du CMS et du champ d'initialisation H_0 surpasse l'anisotropie de forme induite par le réseau, ce qui mène à la quasi-uniformité de ces états rémanents.

Afin de démontrer l'intérêt d'utiliser des matériaux magnétiques avec une forte anisotropie cubique, nous avons comparé ces résultats avec ceux obtenu avec le même système magnétique (même réseau de trous, même propiétés magnétiques que le CMS) mais sans anisotropie cubique ($K_{c1} = 0$ J m^{-3}). Les états rémanents sont montrés dans la figure 6.28 b). Les deux états rémanents nommés C1 et C2 sont observés pour $0° \leq \theta \leq 45°$ et $45° \leq \theta \leq 90°$ respectivement. Ces deux états rémanents sont fortement non uniformes quelque soit la direction de $\vec{H}_0$. Dans ce cas, l'anisotropie de forme du réseau joue un rôle majeur et induit de multiples domaines magnétiques orientés en "zigzag" [49, 265].

Réponses radiofréquences ajustables à la rémanence

Lorsqu'excités de manière uniforme par une impulsion RF, $\vec{h}_{RF}$, appliquée selon l'axe x comme

illustrée à la figure 6.27, ces différents états magnétiques offrent différentes réponses RF. La réponse RF de l'état rémanent A1 (courbe rouge) et celle de l'état rémanent A4 (courbe noir) sont montrées dans la figure 6.29 a). Plusieurs modes d'ondes de spin (fréquences pour lesquelles on observe

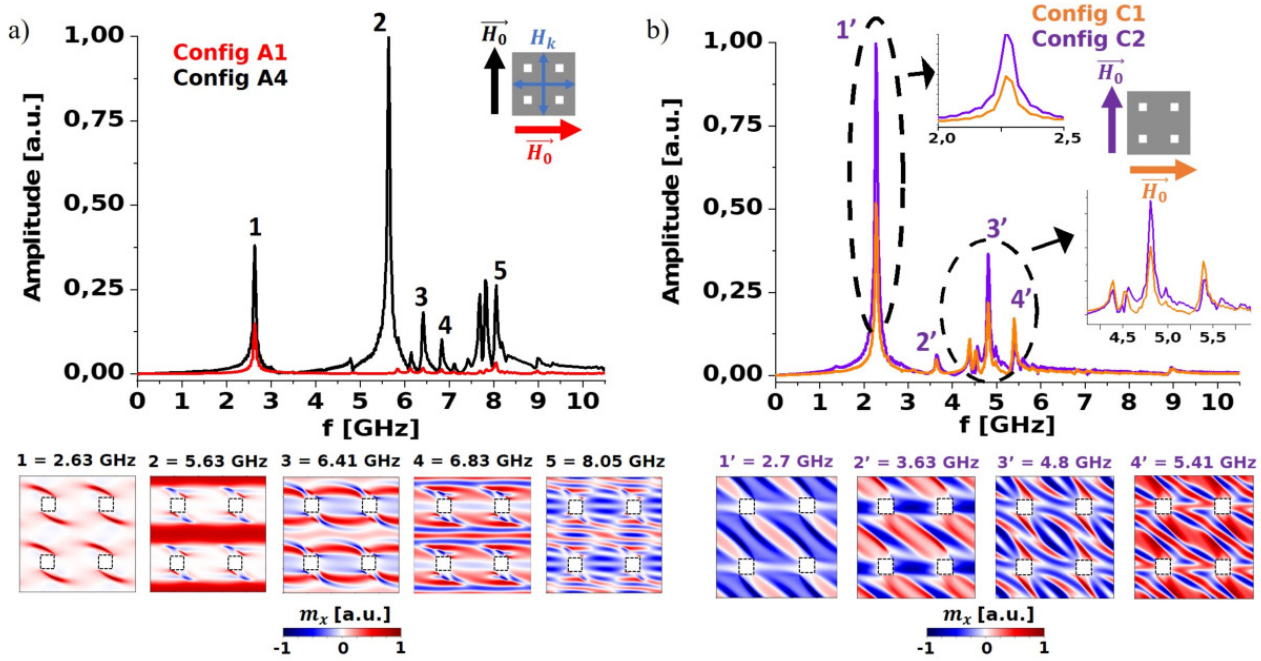

Figure 6.29: Spectres d'amplitude FFT pour différents états magnétiques rémanents présentés dans la figure 6.28 : dans le cas a) d'un cristal magnonique de CMS avec anisotropie cubique dont les axes sont alignés suivant x et y avec les états rémanents A4 et A1, et b) du même cristal magnonique mais sans anisotropie cubique avec les états rémanents C2 et C1. Sous chacun des deux spectres FFT, des clichés temporels du profil spatial de la composante dynamique $m_x(t)$ pour des modes d'ondes de spin particuliers indexés par des chiffres sur les spectres FFT sont montrés. Les amplitudes des modes en fréquence ont été normalisées par rapport au pic d'amplitude le plus intense. L'amplitude de précession des modes d'ondes de spin dans les profils spatiaux est normalisée par rapport à leur propre maximum d'amplitude pour une meilleure visualisation.

des pics avec des amplitudes assez importantes) sont visibles jusqu'à 10 GHz et les principaux sont indexés par des chiffres. Les profils spatiaux des modes d'ondes de spin excités dans le réseau périodique de trous de CMS dans la configuration A4 sont montrés sous le spectre FFT avec des clichés de la composante dynamique m_x pour les fréquences indexées.

En passant de la configuration A4 à A1, on peut observer que la majorité des modes d'ondes de spin sont fortement atténués. En particulier, le mode 2 est quasiment complètement éteint. De telles différences résultent de la quasi-uniformité de l'aimantation des deux états rémanents. En effet, dans la configuration A1, la majorité de l'aimantation est alignée suivant la direction du champ de pompage $\vec{h}_{RF}$, empêchant ainsi son couplage de manière directe et efficace avec l'aimantation. Dans les expériences FMR, la réponse RF d'un système magnétique est souvent mesurée en terme de puissance RF absorbée. Par conséquent, nous avons choisi de quantifier l'atténuation des différents modes comme la variation de puissance de la composante dynamique m_z que l'on peut calculer en dB avec $20\log_{10}(m_z^{A1}/m_z^{A4})$ avec m_z^{A1} (m_z^{A4}) la composante dynamique en z de l'aimantation de l'état rémanent $A1$ ($A4$). Une très forte atténuation de -40 dB est atteinte concernant le second mode. En regardant le profil spatial de ce mode, ce dernière possède de fortes amplitudes de précession dans les canaux horizontaux. Ces canaux horizontaux sont majoritairement alignés suivant x (même direction que le champ de pompage $\vec{h}_{RF}$) dans la configuration A1 impliquant une forte extinction de ces modes dans cette configuration. Les modes 3, 4 et 5 sont atténués entre -16 dB et -20 dB. Enfin, le mode 1 n'est atténué que de -8 dB. Contrairement aux autres modes excités, ce mode précesse uniquement dans les domaines de bords. Comme l'aimantation de ces modes n'est pas complètement orientée vers

la direction du champ de pompage même dans la configuration A1, ces domaines peuvent toujours présenter une valeur non-nulle de la composante moyennée m_y qui peut toujours se coupler à $\vec{h}_{RF}$.

En conséquence, en appliquant un champ d'initialisation suivant deux directions différentes particulières, il est possible d'obtenir deux réponses radiofréquences différentes à la rémanence avec un même cristal magnonique de CMS. Cette différence se traduit dans l'extinction de modes d'ondes de spin, qui est une fonctionnalité analogue à un interrupteur, permettant ainsi des opérations reconfigurables fonctionnant à la rémanence.

Pour démontrer que le caractère reconfigurable à la rémanence est possible grâce à la forte anisotropie magnéto-cristalline du CMS, les réponses RF des configurations C1 et C2 sont montrées dans la figure 6.29 b). Lorsqu'on observe les profils spatiaux des principaux modes d'ondes de spin dans la configuration C2, ces derniers présentent tous une forte précession de l'aimantation dans les domaines orientés à $45°$. La configuration magnétique en zigzag des états rémanents C1 et C2 implique qu'il y aura toujours un domaine magnétique qui pourra se coupler au champ de pompage. De ce fait, l'atténuation maximale est faible et vaut seulement -6 dB pour le mode 1' ce qui est bien inférieur comparé aux valeurs d'atténuation obtenues dans le cas avec anisotropie cubique.

Ces résultats ont été obtenus pour une taille de trous et d'espacement spécifiques. Des variations de ces deux paramètres peut détruire ou améliorer les propriétés reconfigurables.

6.6.2 Influence du ratio d'aspect taille/espacement des trous

Variation des tailles de trous s avec un rapport d'aspect fixe $s/d = 1/3$

En diminuant la taille des trous, on va pouvoir déplacer les modes d'ondes de spin excités vers de plus hautes fréquences. Nous avons également remarqué que les états rémanents étaient moins uniformes en diminuant la taille des trous, car les domaines de bords s'étendent plus vers le centre de la cellule unitaire du réseau en raison de l'augmentation de la contribution de l'interaction d'échange.

6.6.3 Performances de commutation

Pour aller plus loin dans la démonstration de l'intérêt d'un tel dispositif pour des opérations RF reconfigurables, nous avons étudié deux paramètres cruciaux à la facilité d'utilisation pour de potentiels applications : le minimum d'amplitude du champ d'initialisation $\vec{H}_0$ et le temps minimum requis pour commuter d'un état rémanent à un autre. Dans le contexte actuel de diminution de la consommation d'énergie, ces deux paramètres sont particulièrement importants.

Nous avons testé les performances de commutation de notre cristal magnonique pour un ratio d'aspect $s/d = 1/3$ et différentes tailles de trous $s = 300, 200, 100, 50$ nm. Afin de se comparer aux travaux publiés traitant de ces problèmes sur d'autres systèmes magnoniques [269–271], nous avons suivi la même méthodologie comme décrite dans ces travaux pionniers [270]. Nous avons testé la transition d'un état rémanent Rem Y ($\vec{H}_0$ suivant y, analogue à l'état A4) et d'un état rémanent Rem X ($\vec{H}_0$ suivant x, analogue à l'état A1) avec une impulsion de champ magnétique d'amplitude P et de durée 1 ns appliquée suivant l'axe x. Les résultats sont montrés dans la figure 6.30. Quelque soit la taille des trous, le temps de commutation atteint approximativement 1 ns. L'amplitude de champ nécessaire pour déclencher la commutation est de quelques mT, de 6 mT dans le cas d'une taille de trous de $s = 300$ nm et cela peut diminuer jusqu'à 3.5 mT avec des trous de $s = 50$ nm. Nos amplitudes d'impulsion de champ sont inférieures d'un ordre de grandeur par rapport aux résultats obtenus dans d'autres travaux avec des nanostructures de permalloy [269–271].

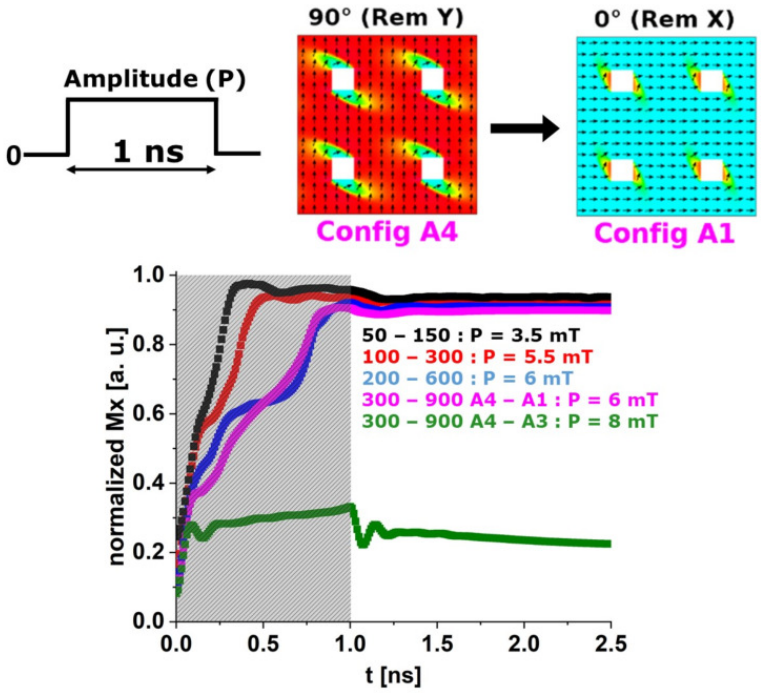

Figure 6.30: Simulations des temps de commutation (de Rem Y vers Rem X) pour différentes tailles de trous s et de ratio d'aspect fixe $s/d = 1/3$. L'impulsion de champ magnétique d'amplitude P et de durée 1 ns a été appliquée suivant l'axe x sauf dans le cas de la transition de l'état rémanent A4 vers l'état rémanent A3 (courbe verte) où $\vec{H}_0$ est appliqué à $45°$ de x. Les courbes noire, rouge, bleue et rose correspondent aux cas $s = 50, 100, 200, 300$ nm respectivement.

6.7 Impact des techniques de nanostructuration sur les propriétés des cristaux magnoniques de Co_2MnSi

6.7.1 Influence de la gravure FIB Ga^+ sur les modes d'ondes de spin dans un cristal magnonique de Co_2MnSi

Le cristal magnonique de CMS du dispositif $\#1$ a été fait par FIB. Le réseau périodique de trous couvre une surface de 47×47 μm^2 et, la taille et la distance centre à centre des trous sont respectivement $s = 100$ nm et $a = 400$ nm. Des images SEM du cristal magnonique sont montrées dans la figure 6.31. Comme discuté plus haut, les trous présentent une forme carrée avec des sommets arrondis et des flancs incurvés ressemblant à une cuve. A la surface du CMS, la taille des trous est de 200 nm tandis que dans le creux des trous, elle est de 140 nm. Les axes de symétrie du réseau de trous sont alignés avec les axes de facile aimantation du CMS. La micro-antenne a été déposée de telle manière que son axe long est parallèle aux bords du réseau afin d'assurer une configuration MSSW lorsque le champ magnétique est appliqué selon la longueur de la micro-antenne.

Des mesures FM-FMR ont été réalisées sur cet échantillon. La fréquence d'excitation est fixe tandis que le champ magnétique appliqué est balayé de 350 à 0 mT avec des pas de 0.3 mT. Cette mesure est ensuite répétée pour chaque fréquence d'excitation, de 1 à 18 GHz avec des pas de 0.5 GHz.

Mesures FM-FMR

L'évolution de l'absorption radiofréquence en fonction de la fréquence d'excitation f et du champ magnétique appliqué H_0 est montrée dans la figure 6.32. On observe une large bande d'absorption

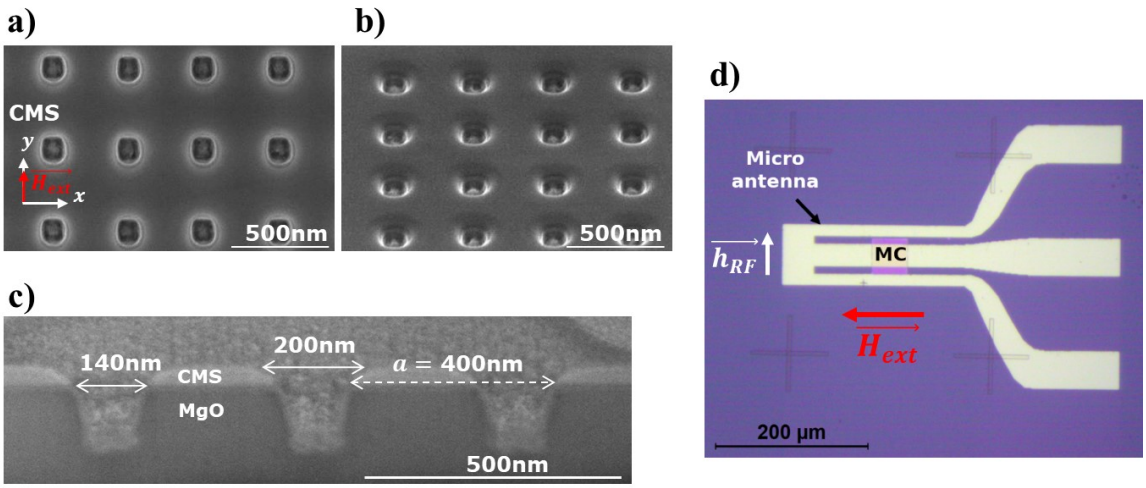

Figure 6.31: Images SEM de a) la vue de dessus, b) la vue tiltée à 52° et c) la vue en coupe transversale (cross-section en anglais) du réseau de trous de CMS gravés par FIB (échantillon #1). d) Image optique de la micro-antenne au-dessus du cristal magnonique de CMS.

dans laquelle peu de pics de résonance peuvent être distingués. Un mode se démarque particulièrement des autres à haute fréquence. Un exemple de mesure est donné à 9 GHz dans l'encart de la figure. La présence de plusieurs pics de résonance est indiquée par des flèches. Ces résonances correspondent à l'excitation de modes d'ondes de spin quantifiés et confinés dans le réseau périodique de trou. Ces pics de résonances sont difficilement individuellement discernables du fait qu'ils soient larges et qu'ils se superposent. Le pic le plus intense apparaissant au plus bas champ (i.e. haute fréquence) a la largeur pic à pic la plus faible (≈ 2 mT) alors que cela peut atteindre 13 mT pour les autres modes. Une telle largeur de raie résulte en de faibles amplitudes.

Modélisation numérique des trous gravés par FIB

Pour expliquer ces mesures, des simulations micromagnétiques ont été menées avec MuMax3. En raison de la forme complexe des trous observés dans la figure 6.31, nous avons testé plusieurs géométries telles que carré, circulaire, circulaire avec les sommets arrondis et la forme en cuve. La forme en cuve est la plus proche géométrie déduite des images SEM. Les simulations portaient sur une cellule unitaire du réseau de trou en utlisant des conditions périodiques 2D pour se placer dans le cas d'un réseau infini. Le système est discrétisé avec des cellules spatiales de $5 \times 5 \times 5$ nm^3. Les paramètres magnétiques utilisés pour les simulations sont indiqués dans la table 6.6. Les états

Aimantation à saturation M_s [T]	Champ d'anisotropie cubique H_k [mT]	Constante d'anisotropie cubique K_{c1} [J m^{-3}]	Facteur gyromagnétique $\frac{\gamma}{2\pi}$ [GHz T^{-1}]	Constante d'échange A [pJ m^{-1}]	Coefficient d'amortissement α
1.28	24	-12223	28.8	20	0.001

Table 6.6: Paramètres magnétiques du CMS utilisés pour les simulations micromagnétiques.

magnétiques statiques et dynamiques sont calculés comme mentionné précédemment. Pour calculer les spectres des modes d'ondes de spin, une FFT est appliquée sur la composante en z du champ rayonné dynamique, $h_{d,z}(t)$, dans un plan localisé à 5 nm de la surface du cristal magnonique. Nous avons utilisé cette approche pour avoir une description qualitative de l'amplitude des signaux FMR attendus pour chaque mode d'ondes de spin excité.

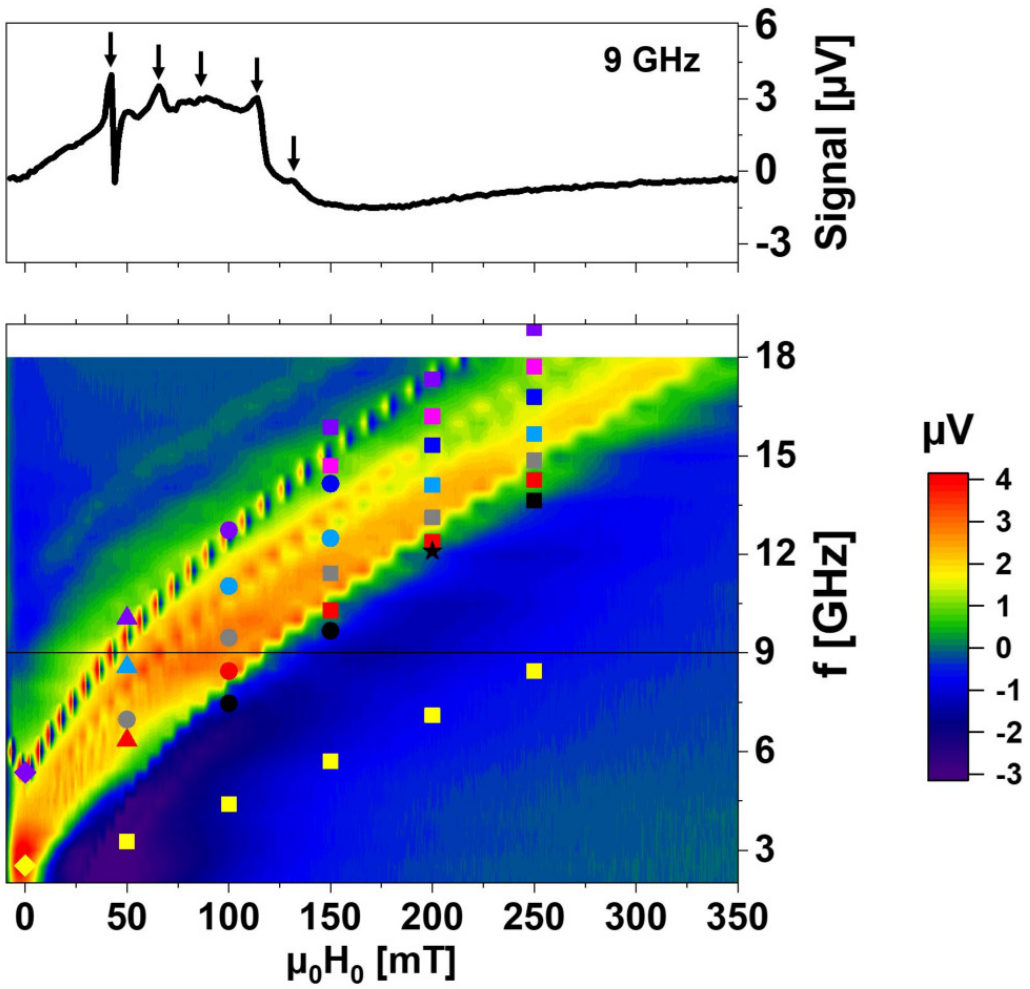

Figure 6.32: Evolution de la puissance radiofréquence absorbée par le cristal magnonique de CMS nanostructuré par FIB (échantillon #1) en fonction du champ magnétique appliqué $\mu_0 H_0$ et de la fréquence d'excitation f. Les amplitudes des signaux FMR sont colorés en fonction de l'échelle de couleur sur la droite. Un exemple de spectre FMR mesuré à 9 GHz est montré au-dessus de la figure principale (ligne noire). Les symboles colorés correspondent aux positions en fréquence des modes d'ondes de spin simulés pour différentes valeurs de champ appliqué. Ces symboles sont les même que ceux de la figure 6.6.

Réponses radiofréquences des différentes géométries de trous

Pour chaque géométrie, nous avons observé que plusieurs modes d'ondes de spin principaux ont leurs fréquences concordant relativement bien avec les mesures expérimentales. La fréquence des différents modes d'ondes de spin dépend fortement de la géométrie des trous, avec des décalages allant jusqu'à 1 GHz suivant le mode concerné. En conséquence, les variations locales de forme et de dimension des trous relativement aux autres sur l'ensemble du réseau peuvent être à l'origine de l'élargissement important des pics de résonance mesurés et de leur superposition. Néanmoins, avec ces géométries de trous, nous n'avons pas été capable de reproduire le mode le plus intense expérimentalement que l'on observe à 17.2 GHz à 200 mT, que ce soit en fréquence ou en amplitude.

Considération de la modification locale des propriétés magnétiques du CMS par gravure FIB Ga^+

Comme abordé dans la section 6.5.2.1, des ions accélérés incidents Ga^+ peuvent induire de multiples collisions d'atomes en cascades dans le cristal de CMS. En plus du désordre atomique, des ions Ga^+ peuvent également s'implanter durant la gravure FIB. Cela pourrait notamment modifier les pro-

priétés électroniques du CMS localement dans les régions proches des trous. Il a été démontré dans la littérature que l'implantation au Ga^+ peut affecter les propriétés magnétiques des couches minces ferromagnétiques au travers d'une aimantation à saturation, de constante d'échange et d'anisotropie cristalline réduites [275–278].

Pour déterminer l'étendue du volume de CMS dégradé autour des trous, des simulations de dommages avec IPROS, un logiciel "fait-maison" Monte-Carlo d'implantation ionique, ont été réalisées par Dr. Alain Claverie de notre équipe de recherche. Nous avons calculé que le plan d'arrêt d'ions incidents Ga^+ d'énergie 30 keV atteint une profondeur de 30 nm dans le CMS et des dommages latéraux s'étendent sur 20 nm tout autour de la trajectoire des ions incidents. Ce volume dégradé autour des trous correspond approximativement à la différence de diamètres des trous à la base (140 nm) et en surface (200 nm). Il est très probable que ces dommages latéraux et implantation ionique varient progressivement du bord interne du trou au volume de CMS, et également de la surface du CMS au travers de son épaisseur [283]. En raison de la complexité d'un tel système, nous avons tenté de le décrire avec un modèle très simple pour les simulations micromagnétiques. Cela consiste à considérer que le volume impacté autour des trous est modifié de manière uniforme. Pour les simulations, nous avons utilisé la géométrie en cuve avec l'ajout d'un volume de diamètre 200 nm encerclant les trous avec des propriétés magnétiques dégradées comme montré dans la figure 6.33 b). Les propriétés magnétiques du volume dégradé autour des trous sont modifiée par un facteur de dommage β de 0.18, après plusieurs variations de β pour ajuster au mieux les mesures. Comme on peut le

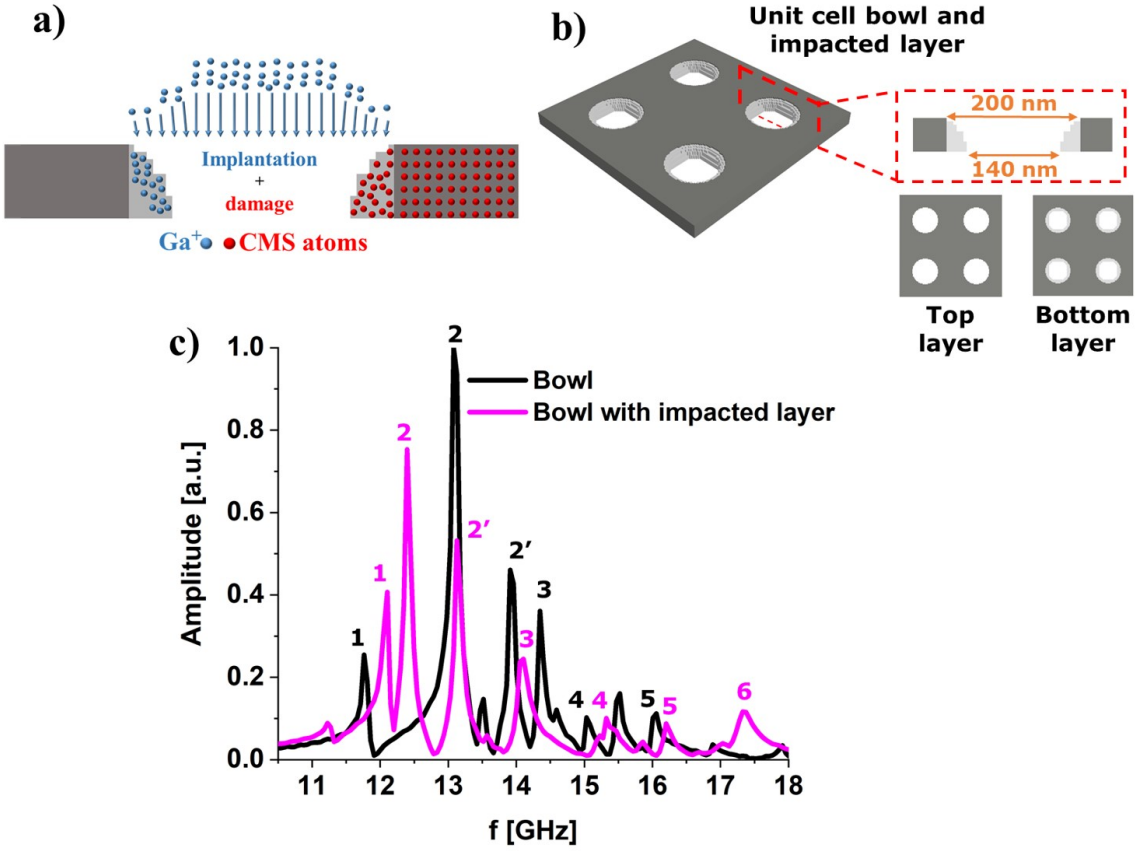

Figure 6.33: a) Schéma du dommage structural latéral et d'implantation Ga^+ induites par la gravure FIB autour des trous. b) Schémas de la cellule unitaire comprenant des trous avec une forme en cuve et un volume magnétique dégradé par FIB encerclant les trous souligné en gris clair. c) Spectres FFT pour une forme de trous en cuve avec pas de volume dégradé (en noir) et avec un volume dégradé (en rose) à $\mu_0 H_0 = 200$ mT et avec $\beta = 0.18$.

voir sur la réponse RF de la nouvelle géométrie, on observe désormais un mode d'ondes de spin à 17.32 GHz avec une amplitude relativement intense, qui peut s'associer au pic de résonance intense à

haute fréquence qui était non expliqué jusqu'à présent.

Nous démontrons ainsi l'importance de considérer à la fois les variations géométriques et magnétiques induites par la gravure FIB afin de reproduire qualitativement et quantitativement la réponse radiofréquence du cristal magnonique sur l'ensemble de la gamme en champ. L'implantation constitue ainsi un obstacle majeur à la réalisation de nos cristaux magnoniques de CMS reconfigurables avec cette technique de nanostructuration.

6.7.2 Etude d'un réseau périodique de trous de Co_2MnSi par lithographie électronique et gravure ionique

L'échantillon #2 comporte un réseau périodique de trous fait par lithographie électronique et gravure IBE, comme détaillé dans la section 6.5.2.2. La taille des trous carrés est de 200 ± 10 nm et l'espacement entre les trous 600 ± 10 nm (périodicité 800 ± 10 nm) comme montré dans les images SEM de la figure 6.34 a) et b). Le réseau de trous couvre une surface de 70×70 μm^2. Sur les

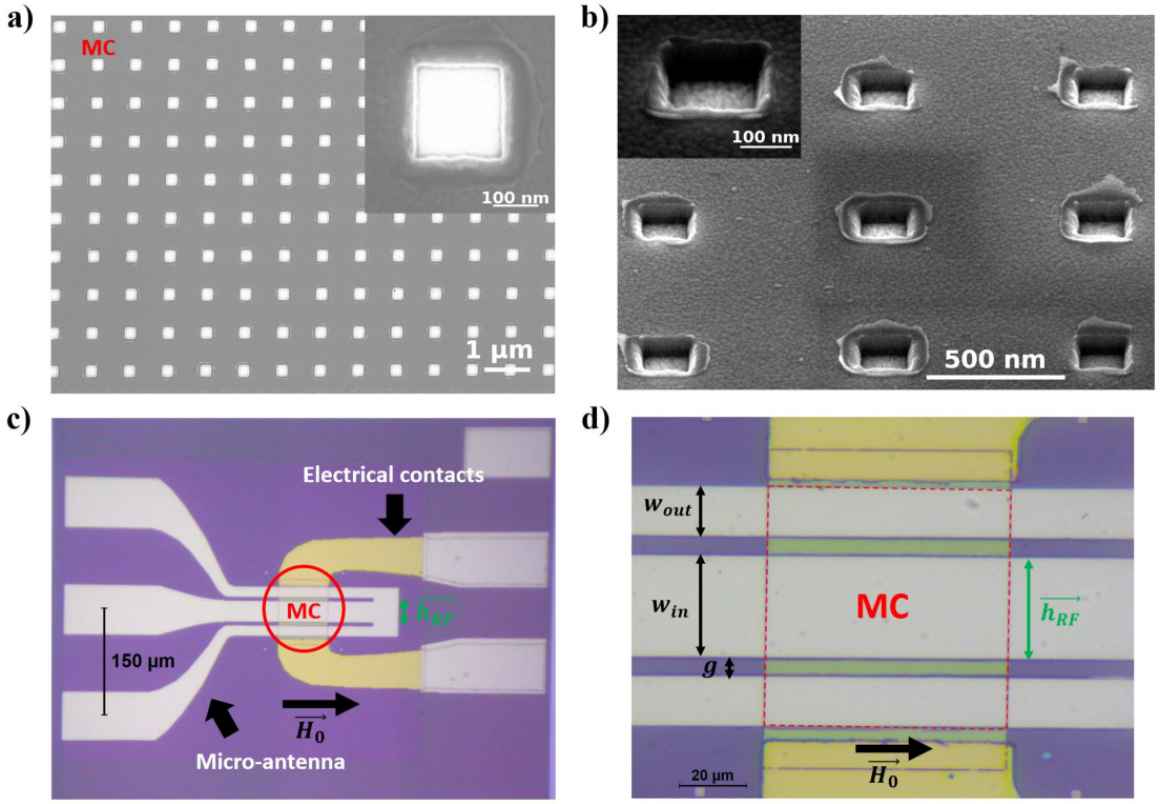

Figure 6.34: Images SEM du réseau périodique de trous de CMS fait par EBL et IBE a) en vue du dessus et b) avec un angle de vue tilté de 52°. Images optiques a) du dispositif complet comprenant le cristal magnonique de CMS avec les contacts électriques et la micro-antenne placée au-dessus, et c) du zoom sur la micro-antenne montrant sa position complète (conducteurs externes compris) sur le cristal magnonique.

images SEM, on peut voir que la forme et la taille des trous sont respectées et que les flancs des trous sont plutôt droits comme souhaité. Quelques résidus de résine et/ou de redépôt sont visibles. Une telle différence de géométrie des trous contraste fortement avec la section précédente, ce qui devrait améliorer significativement les mesures (et c'est le cas comme nous le verrons brièvement plus bas).

Mesures FM-FMR

Des mesures de résonance ferromagnétique modulée en champ (FM-FMR) ont été menées sur cet

échantillon. Les spectres d'absorption radiofréquence $f(H_0)$ sont montrés dans la figure 6.35. Les paramètres magnétiques utilisés pour les simulations micromagnétiques sont résumés dans la table 6.7. Même si la taille des trous de cet échantillon est supérieure à celle de l'échantillon #1 fait au

Aimantation à saturation M_s [T]	**Champ d'anisotropie cubique** H_k [mT]	**Constante d'anisotropie cubique** K_{c1} [J m^{-3}]	**Facteur gyromagnétique** $\frac{\gamma}{2\pi}$ [GHz T^{-1}]	**Constante d'échange** A [pJ m^{-1}]
1.28	20	-10186	28.8	21.5

Table 6.7: Propriétés magnétiques du CMS pour les simulations micromagnétiques du dispositif #2.

FIB, on peut néanmoins remarquer que les pics de résonance des différents modes d'ondes de spin sont très bien résolus pour l'échantillon #2. Cela se voit particulièrement dans l'encart de la figure 6.35 a) montrant le signal FMR mesuré à 11.5 GHz. Huit pics d'absorption sont ainsi clairement identifiés. Les signaux mesurés présentent une plus forte amplitude du fait de la faible largeur de raie en champ des modes. De telles amplitudes et résolution des pics permettent d'observer le "splitting" de différents modes d'ondes de spin avec l'augmentation de H_0. Une partie de ces splittings résulte probablement de la quantification des modes d'ondes de spin danx les canaux du réseau de trous [225, 285]. Il a été démontré que dans des guides d'ondes aimantés perpendiculairement à l'axe long des guides, les conditions finies des guides causent le splitting de modes d'ondes de spin en raison de la formation d'ondes de spin stationnaires le long de la largeur des guides [286]. D'autres splittings peuvent venir d'un champ démagnétisant non-uniforme dû à la présence des trous, ce qui peut également mené à l'excitation de modes d'ondes de spin non uniformes [287]. En-dessous de 10 mT, on entre dans le régime non saturé où les états magnétiques sont moins uniformes impliquant des signaux mesurés plus faibles.

Du fait du bon accord mesures et simulations dans le cas d'un système avec des trous carrés parfaits, nous supposons que l'irradiation aux ions Ar^+ (inerte, faible énergie 1kV) latérale (en surface le CMS était protégé par la résine pendant la gravure ionique) semble moins endommager le CMS à proximité des trous.

Mesures micro-BLS

Pour aller plus loin dans l'analyse de nos cristaux magnoniques de CMS, nous avons comparé nos résultats avec des expériences de micro-BLS (BLS, Brillouin Light Scattering, diffusion Brillouin) sur l'échantillon #3 qui a été fait avec la même technique de nanostructuration que l'échantillon #2 (EBL+IBE). Six cristaux magnoniques ont été réalisés sur un seul substrat (figure 6.36) dont deux d'entre eux ont des réseaux périodiques de trous carrés de taille 200 nm et d'espacement 600 nm. Les mesures micro-BLS ont été réalisées par l'équipe de recherche du Dr. Silvia Tacchi de l'Université de Perugia. L'objectif des mesures micro-BLS est de permettre une imagerie des modes d'ondes de spin se propageant dans des micro-nanostructures avec une résolution spatiale de 300 nm. Cette technique est basée sur la diffusion inélastique des photons par des ondes de spin excitées de manière thermique ou inductive. Un spot laser de résolution 300 nm est focalisé sur le cristal magnonique et les ondes de spin sont excitées par une micro-antenne. L'intensité des mesures en fréquence par micro-BLS pour des champs appliqués de 100 et 50 mT sont montrées dans la figure 6.37 a) et b) respectivement. On peut observer que les résultats expérimentaux et numériques sont en bon accord. Les fréquences des deux modes d'ondes de spin principaux du réseau de trous, le mode 6 (localisé) et le mode 5 (étendu), sont retrouvés dans les spectres micro-BLS.

Le balayage spatial des mesures micro-BLS sur notre échantillon permet de valider encore plus nos simulations micromagnétiques en scannant le profil spatial des ondes de spin correspondant aux pics de résonance détectés. Les mesures micro-BLS ne sont pas résolues en phase mais uniquement

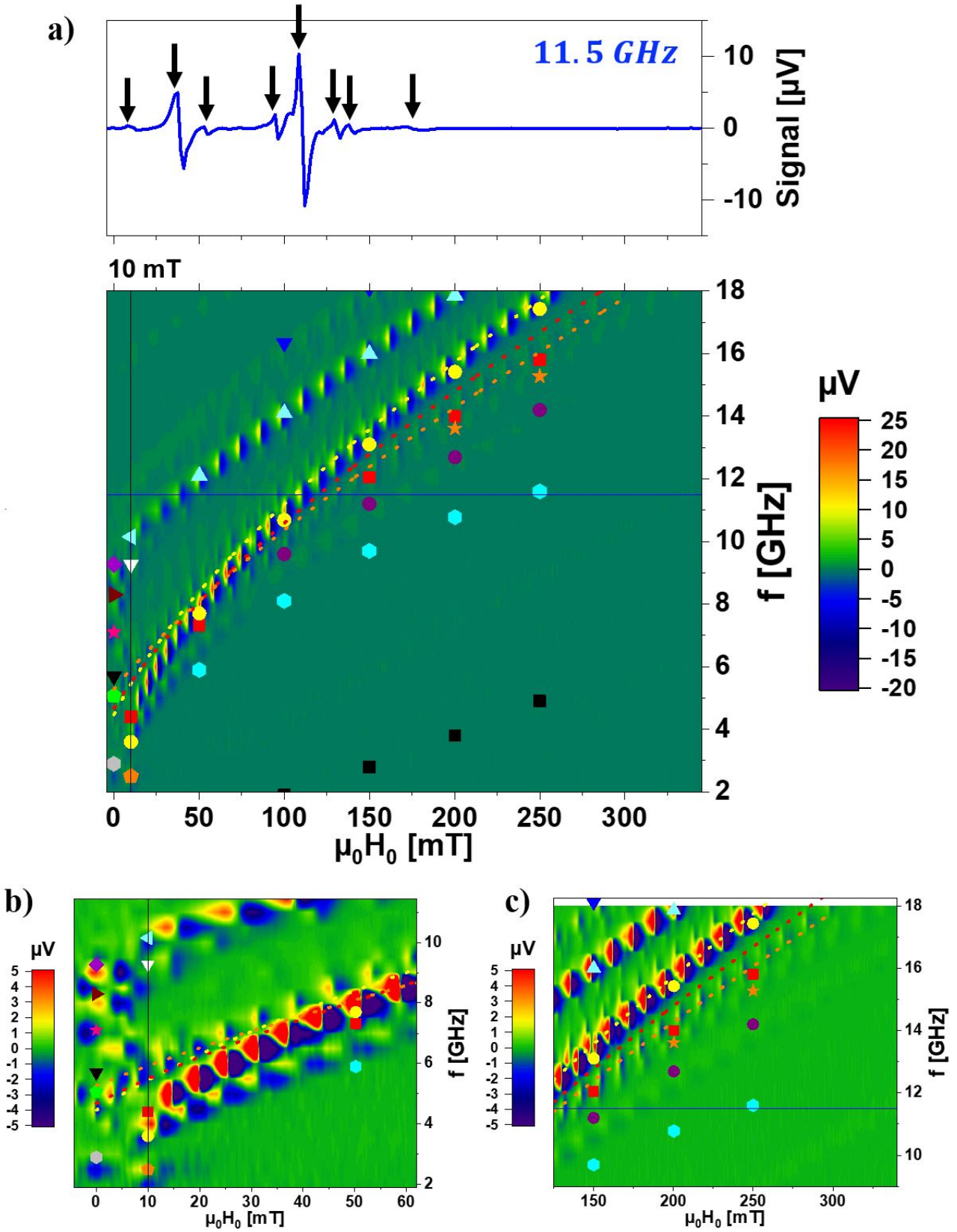

Figure 6.35: a) Evolution de la puissance radiofréquence absorbée par le réseau périodique de trous de CMS nanostructuré par EBL et IBE (dispositf #2) en fonction du champ magnétique appliqué $\mu_0 H_0$ et de la fréquence f. L'amplitude du signal FMR est colorée avec l'échelle de couleur sur la gauche. Un exemple de spectre FMR mesuré à 11.5 GHz est montré au-dessus du graphe principal (ligne bleue). Les symboles colorés correspondent aux positions en fréquence des modes d'ondes de spin simulés pour différentes valeurs de champs. Ces symboles sont les mêmes que ceux de la figure 6.11. b) Graphe zoomé de a) pour $\mu_0 H_0 \leq 60$ mT. c) Graphe zoomé de a) pour $\mu_0 H_0 \geq 125$ mT.

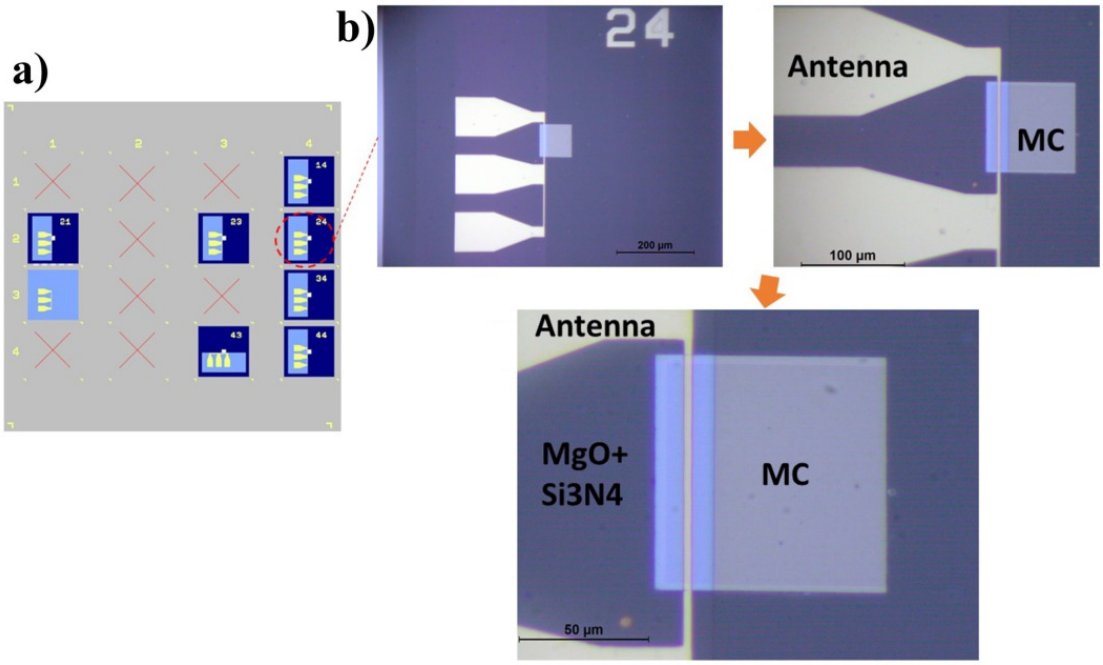

Figure 6.36: Schéma de l'échantillon contenant les différents dispositifs de réseaux de trous de CMS pour des mesures micro-BLS et différentes images optiques zoomées sur l'un des dispositif.

en amplitude de précession. Ainsi, l'information importante de ce type de mesures est d'observer la localisation spatiale des modes. Ces balayages en amplitude de précession sont montrés dans les encarts de la figure. On retrouve bien les profils spatiaux simulés des modes étendu et localisé. En effet, pour le mode à 10.4 GHz à 100 mT, le maximum d'amplitude de précession est continu et se situe le long des canaux horizontaux, comme attendu pour un mode étendu. Concernant le mode à 13.70 GHz, le maximum d'amplitude de précession apparaît de manière discontinue (saccadée) entre les lignes horizontales de trous, ressemblant ainsi à un mode localisé. Ces mesures confirment ainsi les modes d'ondes de spin étendu et localisé prédits numériquement.

6.7.3 Démonstration expérimentale d'une propriété reconfigurable à la rémanence avec un cristal magnonique de Co_2MnSi

Dans la section 6.6, nous avons démontré par le biais de simulations micromagnétiques la possibilité de stabiliser des états magnétiques quasi-uniformes à la rémanence dans des réseaux périodiques de trous de Co_2MnSi avec des tailles de trous, espacements et propriétés magnétiques spécifiques. Le paramètre clé pour obtenir des états rémanents quasi-uniformes est une assez forte anisotropie cubique dont les axes de faciles aimantation sont orientés suivant les axes de symétrie du réseau (axes x et y). En appliquant un champ d'initialisation $\vec{H}_0$ suivant l'axe x, on peut stabiliser un état rémanent uniformément aimanté suivant l'axe x (Rem X) ou suivant l'axe y (Rem Y) lorsque $\vec{H}_0$ est appliqué suivant y. Par conséquent, en appliquant un champ de pompage $\vec{h}_{RF}$ suivant l'axe x de manière uniforme sur le dispositif, deux réponses RF peuvent alors être obtenues à la rémanence, correspondant ainsi à une opération reconfigurable.

Pour l'échantillon $\#2$, l'anisotropie cubique est suffisamment forte pour stabiliser une aimantation quasi-uniforme jusqu'à 10 mT mais pas jusqu'à la rémanence. Bien que l'état rémanent de cet échantillon n'est pas idéal du fait qu'il présente des domaines à $45°$ dans le centre de la cellule unitaire du réseau, cet état rémanent semble être moins non-uniforme que celui observé dans la section 6.6 pour une anisotropie cubique nulle ($K_{c1} = 0$). Nous avons donc tenté l'expérience pour observer la

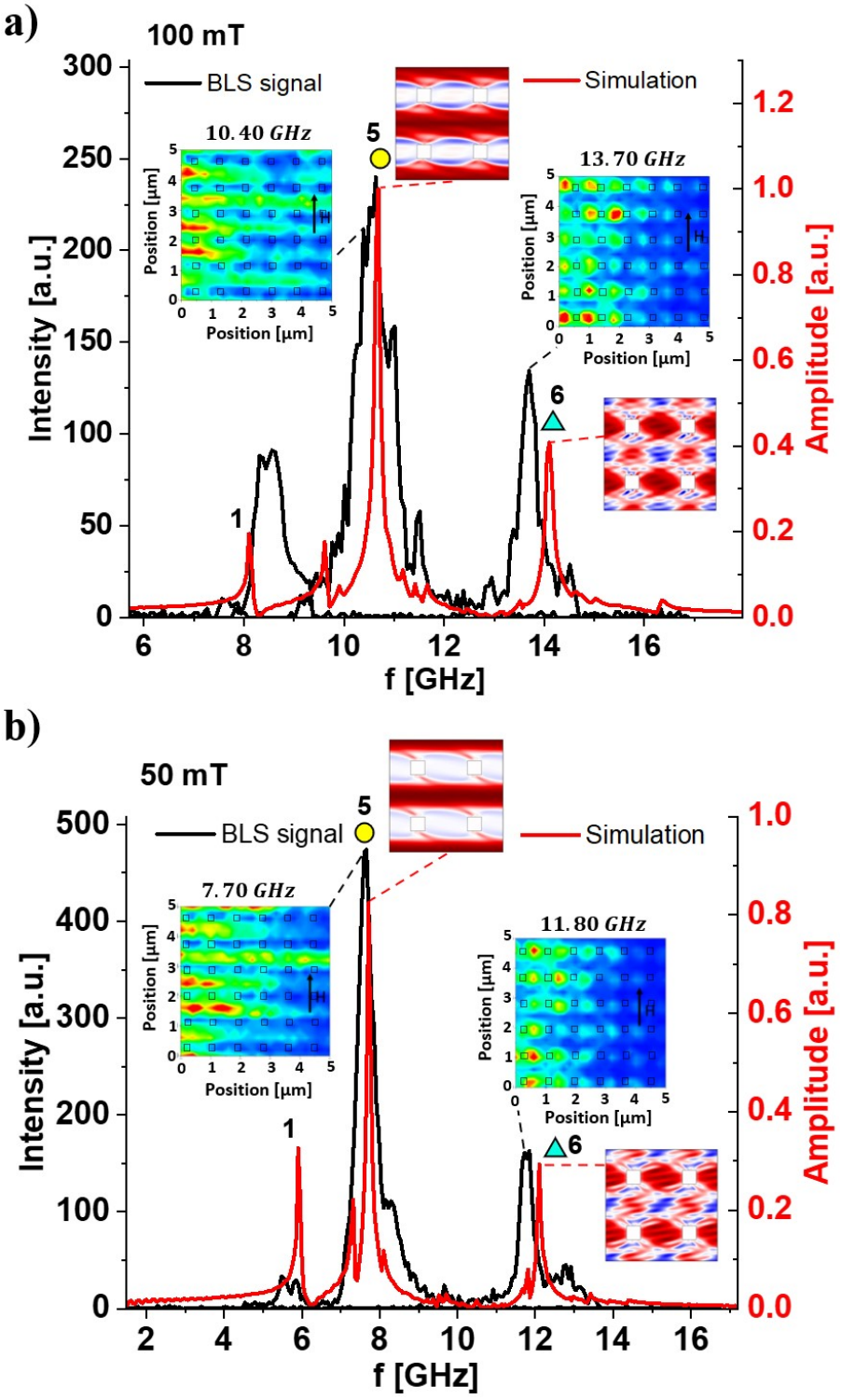

Figure 6.37: Spectres d'intensité micro-BLS pour les champs magnétiques appliqués a) 100 mT et b) 50 mT. Encarts des colormaps 2D spatiales de l'amplitude des deux principaux modes d'ondes de spin propagatifs (mode étendu indexé avec un cercle jaune et mode localisé indexé avec un triangle cyan) sont montrés dans a) et b). Par comparaison, les profils spatiaux simulés des deux modes d'ondes de spin principaux sont également montrés.

reconfigurabilité à la rémanence.

Les mesures ont été réalisées à l'analyseur de réseaux VNA-FMR (mesures en balayant en fréquence à champ fixe, VNA Vector Network Analyser). Les résultats sont montrés dans la figure 6.38 a) avec les variations du paramètre mesuré ΔS_{11} et des spectres FFT simulés.

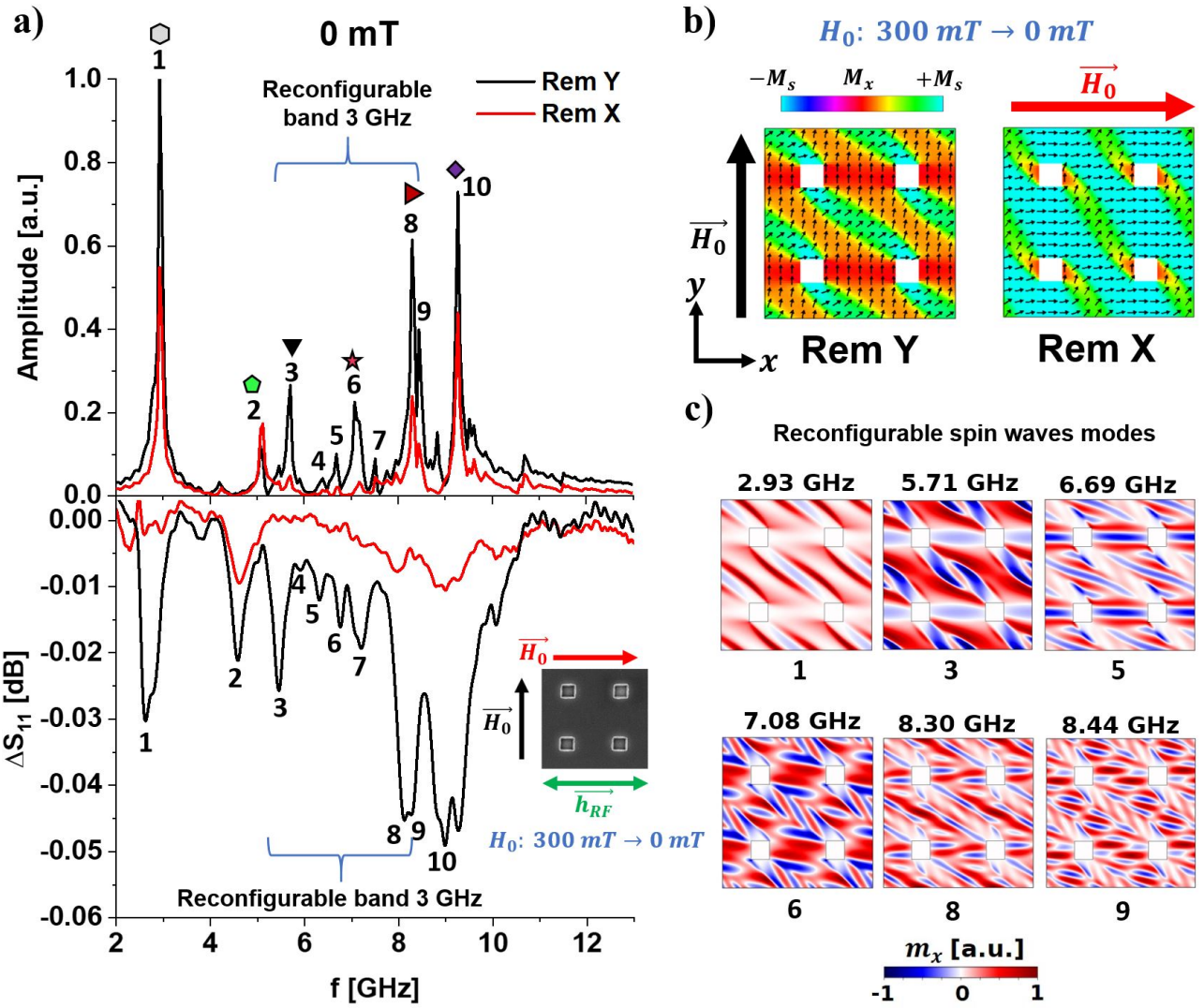

Figure 6.38: a) Graphes des spectres FFT numériques (en haut) et les paramètres ΔS_{11} mesurés (en bas) dans l'état Rem Y (ligne noire) et dans l'état Rem X (ligne rouge) à la rémanence $\mu_0 H_0 = 0$ mT. b) Etats magnétiques d'équilibre Rem Y et Rem X à la rémanence. c) Clichés temporels des profils spatiaux de la composante dynamique simulée m_x pour différents modes d'ondes de spin reconfigurables.

Les simulations et les résultats expérimentaux sont en bon accord même si l'on observe des décalages en fréquence de -180 à 500 MHz suivant le mode d'ondes de spin considéré. Une première observation est que les pics d'absorption mesurés sont faibles, par un facteur de 10, comparés aux précédentes mesures dans le régime quasi-saturé. Cela provient de la non-uniformité de l'aimantation à la rémanence puisque les domaines à $45°$ se couplent moins efficacement au champ de pompage impliquant ainsi une baisse d'amplitude du signal. De plus, l'observation de large pics de résonance en fréquence contribue également à leur faible amplitude.

En ce qui concerne la réponse de l'état Rem X, on peut observer une bonne atténuation de certains modes, en particulier dans la gamme de fréquence $5.3 - 8.3$ GHz.

6.8 Conclusion et perspectives

L'objectif de cette thèse était de produire des cristaux magnoniques reconfigurables à la rémanence à partir de réseaux périodiques de trous carrés. Cela ouvre la voie à la réalisation de composants magnoniques RF fonctionnant sans aimants permanents. Afin d'atteindre cet objectif, nous avons tirer partie de la forte anisotropie magnéto-cristalline cubique de l'alliage d'Heusler $\mathrm{Co_2MnSi}$.

Nous avons dans un premier temps démontré par des simulations micromagnétiques la possibilité d'exciter ou non des modes d'ondes de spin suivant l'état rémanent stabilisé par l'application d'une impulsion de champ magnétique dans deux directions différentes. Pour cela, il est important d'obtenir des états magnétiques rémanents quasi-uniformes pour une reconfigurabilité efficace. La quasi-uniformité est favorisée par une forte anisotropie cubique du CMS qui vient contre-balancer l'anisotropie de forme induite par la présence des trous. Notre modèle permet également d'obtenir des temps de commutation entre deux états rémanents de l'ordre de la nanoseconde s'inscrivant dans une démarche d'opérations ultra-rapides avec une impulsion de champ de l'ordre de quelques mT. Par conséquent, les réseaux périodiques de trous carrés de CMS constituent de bons candidats pour le design d'antennes réceptrices multi-bandes par exemple.

Une fois le potentiel numérique étudié, nous avons cherché à le démontrer expérimentalement. Pour ce faire, il fallait déposer puis nanostructurer les couches minces de CMS. Nous avons développé deux techniques de nanostructuration pour obtenir des trous dans la gamme $300 - 100\ \mathrm{nm}$: la gravure FIB et une combinaison de la lithographie électronique et de la gravure IBE. La gravure FIB n'a pas permis d'obtenir des réseaux de trous respectant les spécifications au vue des défauts géométriques des trous et de l'implantation ionique autour des trous. Par contre, la lithographie électronique combinée à la gravure IBE a permis d'obtenir des trous avec les bonnes dimensions, formes et des flancs droits. Les simulations micromagnétiques sur une géométrie parfaite des réseaux de trous carrés sont en très bon accord avec les mesures d'absorption des modes d'ondes de spin par le cristal magnonique ainsi fabriqué. D'autres types de mesures, VNA-FMR et micro-BLS, ont également confirmé l'excellent accord entre les simulations et les mesures. Un tel échantillon nous a permis de mesurer une opération reconfigurable malgré une anisotropie cubique plus faible que prévue.

Parmi les perspectives ouvertes à ce travail de thèse, il y a la possibilité de propager des ondes de spin dans ces cristaux et notamment d'observer du filtrage fréquentiel à la rémanence. D'autres perspectives concernent l'améliorations de l'aspect reconfigurable via la recherche de nouveaux designs de cristal magnonique.

Bibliography

[1] F. Bloch, "Zur Theorie des Ferromagnetismus", Zeitschrift für Physik **61**, Number: 3, 206–219 (1930).

[2] A. V. Chumak, A. A. Serga, and B. Hillebrands, "Magnon transistor for all-magnon data processing", Nature Communications **5**, Number: 1 Publisher: Nature Publishing Group, 4700 (2014).

[3] V. G. Harris, "Modern microwave ferrites", IEEE Transactions on Magnetics **48**, Number: 3 Conference Name: IEEE Transactions on Magnetics, 1075–1104 (2012).

[4] J. M. Owens, J. H. Collins, and R. L. Carter, "System applications of magnetostatic wave devices", Circuits, Systems and Signal Processing **4**, Number: 1, 317–334 (1985).

[5] J. Adam, "Analog signal processing with microwave magnetics", Proceedings of the IEEE **76**, Number: 2 Conference Name: Proceedings of the IEEE, 159–170 (1988).

[6] V. V. Kruglyak, S. O. Demokritov, and D. Grundler, "Magnonics", Journal of Physics D: Applied Physics **43**, Number: 26 Publisher: IOP Publishing, 264001 (2010).

[7] A. V. Chumak, A. A. Serga, and B. Hillebrands, "Magnonic crystals for data processing", Journal of Physics D: Applied Physics **50**, Number: 24 Publisher: IOP Publishing, 244001 (2017).

[8] *IRDS™ 2021: beyond CMOS - IEEE IRDS™*, https://irds.ieee.org/images/files/pdf/2021/2021IRDS_BC.pdf.

[9] B. Heinz, T. Brächer, M. Schneider, Q. Wang, B. Lägel, A. M. Friedel, D. Breitbach, S. Steinert, T. Meyer, M. Kewenig, C. Dubs, P. Pirro, and A. V. Chumak, "Propagation of spin-wave packets in individual nanosized yttrium iron garnet magnonic conduits", Nano Letters **20**, Number: 6 Publisher: American Chemical Society, 4220–4227 (2020).

[10] C. Kittel, *Introduction to solid state physics*, 8th Edition (John Wiley & Sons, Hoboken, NJ, Nov. 11, 2004), 704 pages.

[11] E. Yablonovitch, "Inhibited spontaneous emission in solid-state physics and electronics", Physical Review Letters **58**, Number: 20 Publisher: American Physical Society, 2059–2062 (1987).

[12] S. John, "Strong localization of photons in certain disordered dielectric superlattices", Physical Review Letters **58**, Number: 23 Publisher: American Physical Society, 2486–2489 (1987).

[13] S. John, "Why trap light?", Nature Materials **11**, Number: 12 Publisher: Nature Publishing Group, 997–999 (2012).

[14] C. G. Sykes, J. D. Adam, and J. H. Collins, "Magnetostatic wave propagation in a periodic structure", Applied Physics Letters **29**, Publisher: American Institute of Physics, 388–391 (1976).

[15] Y. V. Gulyaev and A. A. Nikitov, "Magnonic crystals and spin waves in periodic structures", Doklady Physics **46**, Number: 10, 687–689 (2001).

[16] H. Puszkarski and M. Krawczyk, "Magnonic crystals — the magnetic counterpart of photonic crystals", Solid State Phenomena **94**, Conference Name: Interfacial Effects and Novel Properties of Nanomaterials ISBN: 9783908450801 Publisher: Trans Tech Publications Ltd, 125–134 (2003).

[17] A. V. Chumak, A. A. Serga, B. Hillebrands, and M. P. Kostylev, "Scattering of backward spin waves in a one-dimensional magnonic crystal", Applied Physics Letters **93**, Number: 2 Publisher: American Institute of Physics, 022508 (2008).

[18] A. V. Chumak, P. Pirro, A. A. Serga, M. P. Kostylev, R. L. Stamps, H. Schultheiss, K. Vogt, S. J. Hermsdoerfer, B. Laegel, P. A. Beck, and B. Hillebrands, "Spin-wave propagation in a microstructured magnonic crystal", Applied Physics Letters **95**, Number: 26 Publisher: American Institute of Physics, 262508 (2009).

[19] J. O. Vasseur, L. Dobrzynski, B. Djafari-Rouhani, and H. Puszkarski, "Magnon band structure of periodic composites", Physical Review B **54**, Publisher: American Physical Society, 1043–1049 (1996).

[20] R. Zivieri, F. Montoncello, L. Giovannini, F. Nizzoli, S. Tacchi, M. Madami, G. Gubbiotti, G. Carlotti, and A. O. Adeyeye, "Collective spin modes in chains of dipolarly interacting rectangular magnetic dots", Physical Review B **83**, Publisher: American Physical Society, 054431 (2011).

[21] R. Mandal, P. Laha, K. Das, S. Saha, S. Barman, A. K. Raychaudhuri, and A. Barman, "Effects of antidot shape on the spin wave spectra of two-dimensional ni80fe20 antidot lattices", Applied Physics Letters **103**, Number: 26 Publisher: American Institute of Physics, 262410 (2013).

[22] M. Zelent, N. Tahir, R. Gieniusz, J. W. Kłos, T. Wojciechowski, U. Guzowska, A. Maziewski, J. Ding, A. O. Adeyeye, and M. Krawczyk, "Geometrical complexity of the antidots unit cell effect on the spin wave excitations spectra", Journal of Physics D: Applied Physics **50**, Number: 18 Publisher: IOP Publishing, 185003 (2017).

[23] J. W. Kłos, D. Kumar, M. Krawczyk, and A. Barman, "Magnonic band engineering by intrinsic and extrinsic mirror symmetry breaking in antidot spin-wave waveguides", Scientific Reports **3**, Number: 1 Publisher: Nature Publishing Group, 2444 (2013).

[24] S. Choudhury, S. Saha, R. Mandal, S. Barman, Y. Otani, and A. Barman, "Shape- and interface-induced control of spin dynamics of two-dimensional bicomponent magnonic crystals", ACS Applied Materials & Interfaces **8**, Number: 28 Publisher: American Chemical Society, 18339–18346 (2016).

[25] F. S. Ma, H. S. Lim, Z. K. Wang, S. N. Piramanayagam, S. C. Ng, and M. H. Kuok, "Micromagnetic study of spin wave propagation in bicomponent magnonic crystal waveguides", Applied Physics Letters **98**, Number: 15 Publisher: American Institute of Physics, 153107 (2011).

[26] B. Obry, P. Pirro, T. Brächer, A. V. Chumak, J. Osten, F. Ciubotaru, A. A. Serga, J. Fassbender, and B. Hillebrands, "A micro-structured ion-implanted magnonic crystal", Applied Physics Letters **102**, Number: 20 Publisher: American Institute of Physics, 202403 (2013).

[27] Q. Wang, Z. Zhong, L. Jin, X. Tang, F. Bai, H. Zhang, and G. S. D. Beach, "Design of nanostrip magnonic crystal waveguides with a single magnonic band gap", Journal of Magnetism and Magnetic Materials **340**, 23–26 (2013).

[28] E. K. Semenova and D. V. Berkov, "Spin wave propagation through an antidot lattice and a concept of a tunable magnonic filter", Journal of Applied Physics **114**, Number: 1 Publisher: American Institute of Physics, 013905 (2013).

[29] R. Verba, G. Melkov, V. Tiberkevich, and A. Slavin, "Fast switching of a ground state of a reconfigurable array of magnetic nano-dots", Applied Physics Letters **100**, Number: 19 Publisher: American Institute of PhysicsAIP, 192412 (2012).

[30] R. Verba, G. Melkov, V. Tiberkevich, and A. Slavin, "Collective spin-wave excitations in a two-dimensional array of coupled magnetic nanodots", Physical Review B **85**, Number: 1 Publisher: American Physical Society, 014427 (2012).

[31] G. Gubbiotti, P. Malagò, S. Fin, S. Tacchi, L. Giovannini, D. Bisero, M. Madami, G. Carlotti, J. Ding, A. O. Adeyeye, and R. Zivieri, "Magnetic normal modes of bicomponent permalloy/cobalt structures in the parallel and antiparallel ground state", Physical Review B **90**, Number: 2 Publisher: American Physical Society, 024419 (2014).

[32] G. Gubbiotti, H. T. Nguyen, R. Hiramatsu, S. Tacchi, M. G. Cottam, and T. Ono, "Resonant spin-wave modes in trilayered magnetic nanowires studied in the parallel and antiparallel ground state", Journal of Magnetism and Magnetic Materials **384**, 45–48 (2015).

[33] J. Topp, D. Heitmann, M. P. Kostylev, and D. Grundler, "Making a reconfigurable artificial crystal by ordering bistable magnetic nanowires", Physical Review Letters **104**, Number: 20 Publisher: American Physical Society, 207205 (2010).

[34] J. Ding, M. Kostylev, and A. O. Adeyeye, "Realization of a mesoscopic reprogrammable magnetic logic based on a nanoscale reconfigurable magnonic crystal", Applied Physics Letters **100**, Number: 7 Publisher: American Institute of Physics, 073114 (2012).

[35] A. Haldar and A. O. Adeyeye, "Reconfigurable and self-biased magnonic metamaterials", Journal of Applied Physics **128**, Number: 24 Publisher: American Institute of Physics, 240902 (2020).

[36] A. Haldar and A. O. Adeyeye, "Deterministic control of magnetization dynamics in reconfigurable nanomagnetic networks for logic applications", ACS Nano **10**, Number: 1 Publisher: American Chemical Society, 1690–1698 (2016).

[37] A. Haldar and A. O. Adeyeye, "Artificial metamaterials for reprogrammable magnetic and microwave properties", Applied Physics Letters **108**, Number: 2 Publisher: AIP Publishing LLCAIP Publishing, 022405 (2016).

[38] C. Tian and A. O. Adeyeye, "Bias-free tunability of microwave properties in multilayer rhomboid shaped nanomagnets", Applied Physics Letters **111**, Number: 15 Publisher: American Institute of Physics, 152404 (2017).

[39] C. Tian and A. O. Adeyeye, "Tunable microwave properties of rhomboid shaped nanomagnet pairs", Applied Physics Letters **111**, Number: 26 Publisher: AIP Publishing LLC AIP Publishing, 262402 (2017).

[40] K. Begari and A. Haldar, "Bias-free giant tunability of microwave properties in multilayer rhomboid nanomagnets", Journal of Physics D: Applied Physics **51**, Number: 27 Publisher: IOP Publishing, 275004 (2018).

[41] A. Haldar, D. Kumar, and A. O. Adeyeye, "A reconfigurable waveguide for energy-efficient transmission and local manipulation of information in a nanomagnetic device", Nature Nanotechnology **11**, Number: 5 Publisher: Nature Publishing Group, 437–443 (2016).

[42] L. Torres, L. Lopez-Diaz, and O. Alejos, "Micromagnetic analysis of recording processes in periodic antidot arrays: interaction between adjacent bits", Journal of Applied Physics **87**, Number: 9 Publisher: American Institute of Physics, 5645–5647 (2000).

[43] S. K. Abbas, M. Saleem, S. Naseem, S. Riaz, and S. Atiq, "Synthesis of ni80fe20 permalloy antidots for high storage ferroelectric memories", Materials Letters **271**, 127852 (2020).

[44] P. J. Metaxas, M. Sushruth, R. A. Begley, J. Ding, R. C. Woodward, I. S. Maksymov, M. Albert, W. Wang, H. Fangohr, A. O. Adeyeye, and M. Kostylev, "Sensing magnetic nanoparticles using nano-confined ferromagnetic resonances in a magnonic crystal", Applied Physics Letters **106**, Number: 23 Publisher: American Institute of Physics, 232406 (2015).

[45] V. G. Harris and A. S. Sokolov, "The self-biased circulator: ferrite materials design and process considerations", Journal of Superconductivity and Novel Magnetism **32**, Number: 1, 97–108 (2019).

[46] *RF and microwave circulators and isolators. small, light weight, and surface mount.* (Aug. 19, 2022) https://www.mtmgx.com/rf-microwave-smt-circulators-isolators/ (visited on 08/19/2022).

[47] M. Sparks, *Ferromagnetic-relaxation theory* (McGraw-Hill, Jan. 1, 1964), 227 pages.

[48] A. Barman, G. Gubbiotti, S. Ladak, A. O. Adeyeye, M. Krawczyk, J. Gräfe, C. Adelmann, S. Cotofana, A. Naeemi, V. I. Vasyuchka, B. Hillebrands, S. A. Nikitov, H. Yu, D. Grundler, A. V. Sadovnikov, A. A. Grachev, S. E. Sheshukova, J.-Y. Duquesne, M. Marangolo, G. Csaba, W. Porod, V. E. Demidov, S. Urazhdin, S. O. Demokritov, E. Albisetti, D. Petti, R. Bertacco, H. Schultheiss, V. V. Kruglyak, V. D. Poimanov, S. Sahoo, J. Sinha, H. Yang, M. Münzenberg, T. Moriyama, S. Mizukami, P. Landeros, R. A. Gallardo, G. Carlotti, J.-V. Kim, R. L. Stamps, R. E. Camley, B. Rana, Y. Otani, W. Yu, T. Yu, G. E. W. Bauer, C. Back, G. S. Uhrig, O. V. Dobrovolskiy, B. Budinska, H. Qin, S. v. Dijken, A. V. Chumak, A. Khitun, D. E. Nikonov, I. A. Young, B. W. Zingsem, and M. Winklhofer, "The 2021 magnonics roadmap", Journal of Physics: Condensed Matter **33**, Number: 41 Publisher: IOP Publishing, 413001 (2021).

[49] S. Mallick, S. Mondal, T. Seki, S. Sahoo, T. Forrest, F. Maccherozzi, Z. Wen, S. Barman, A. Barman, K. Takanashi, and S. Bedanta, "Tunability of domain structure and magnonic spectra in antidot arrays of heusler alloy", Physical Review Applied **12**, Number: 1 Publisher: American Physical Society, 014043 (2019).

[50] M. Langer, K. Wagner, T. Sebastian, R. Hübner, J. Grenzer, Y. Wang, T. Kubota, T. Schneider, S. Stienen, K. Lenz, H. Schultheiß, J. Lindner, K. Takanashi, R. E. Arias, and J. Fassbender, "Parameter-free determination of the exchange constant in thin films using magnonic patterning", Applied Physics Letters **108**, Number: 10 Publisher: American Institute of Physics, 102402 (2016).

[51] G. Ortiz, A. García-García, N. Biziere, F. Boust, J. F. Bobo, and E. Snoeck, "Growth, structural, and magnetic characterization of epitaxial co2mnsi films deposited on MgO and cr seed layers", Journal of Applied Physics **113**, Publisher: American Institute of Physics, 043921 (2013).

[52] I. Abdallah, N. Ratel-Ramond, C. Magen, B. Pecassou, R. Cours, A. Arnoult, M. Respaud, J. F. Bobo, G. BenAssayag, E. Snoeck, and N. Biziere, "Structural and magnetic properties of he+ irradiated co2mnsi heusler alloys", Materials Research Express **3**, Number: 4 Publisher: IOP Publishing, 046101 (2016).

[53] I. Abdallah, B. Pradines, N. Ratel-Ramond, G. BenAssayag, R. Arras, L. Calmels, J. F. Bobo, E. Snoeck, and N. Biziere, "Evolution of magnetic properties and damping coefficient of co2mnsi heusler alloy with mn/si and co/mn atomic disorder", Journal of Physics D: Applied Physics **50**, Number: 3 Publisher: IOP Publishing, 035003 (2016).

[54] T. Stückler, C. Liu, H. Yu, F. Heimbach, J. Chen, J. Hu, S. Tu, M. S. Alam, J. Zhang, Y. Zhang, I. L. Farrell, C. Emeny, S. Granville, Z.-M. Liao, D. Yu, and W. Zhao, "Spin wave propagation detected over 100 um in half-metallic heusler alloy co2mnsi", Journal of Magnetism and Magnetic Materials, Perspectives on magnon spintronics **450**, 13–17 (2018).

[55] T. Sebastian, Y. Ohdaira, T. Kubota, P. Pirro, T. Brächer, K. Vogt, A. A. Serga, H. Naganuma, M. Oogane, Y. Ando, and B. Hillebrands, "Low-damping spin-wave propagation in a micro-structured co2mn0.6fe0.4si heusler waveguide", Applied Physics Letters **100**, Number: 11 Publisher: American Institute of Physics, 112402 (2012).

[56] T. Stückler, C. Liu, T. Liu, H. Yu, F. Heimbach, J. Chen, J. Hu, S. Tu, Y. Zhang, S. Granville, M. Wu, Z.-M. Liao, D. Yu, and W. Zhao, "Ultrabroadband spin-wave propagation in co2mn0.6fe0.4si thin films", Physical Review B **96**, 144430 (2017).

[57] S. Wang, J. Ding, X. Guan, M. B. Jungfleisch, Z. Zhang, X. Wang, W. Gu, Y. Zhu, J. E. Pearson, X. Cheng, A. Hoffmann, and X. Miao, "Linear and nonlinear spin-wave dynamics in ultralow-damping microstructured co2feal heusler waveguide", Applied Physics Letters **113**, Number: 23 Publisher: American Institute of Physics, 232404 (2018).

[58] T. Sebastian, T. Brächer, P. Pirro, A. A. Serga, B. Hillebrands, T. Kubota, H. Naganuma, M. Oogane, and Y. Ando, "Nonlinear emission of spin-wave caustics from an edge mode of a microstructured co2mn0.6fe0.4si waveguide", Physical Review Letters **110**, Number: 6 Publisher: American Physical Society, 067201 (2013).

[59] P. Pirro, T. Sebastian, T. Brächer, A. A. Serga, T. Kubota, H. Naganuma, M. Oogane, Y. Ando, and B. Hillebrands, "Non-gilbert-damping mechanism in a ferromagnetic heusler compound probed by nonlinear spin dynamics", Physical Review Letters **113**, Number: 22 Publisher: American Physical Society, 227601 (2014).

[60] R. Zivieri, S. Tacchi, F. Montoncello, L. Giovannini, F. Nizzoli, M. Madami, G. Gubbiotti, G. Carlotti, S. Neusser, G. Duerr, and D. Grundler, "Bragg diffraction of spin waves from a two-dimensional antidot lattice", Physical Review B **85**, 012403 (2012).

[61] M. Krawczyk and H. Puszkarski, "Plane-wave theory of three-dimensional magnonic crystals", Physical Review B **77**, Number: 5 Publisher: American Physical Society, 054437 (2008).

[62] M. Jourdan, J. Minár, J. Braun, A. Kronenberg, S. Chadov, B. Balke, A. Gloskovskii, M. Kolbe, H. J. Elmers, G. Schönhense, H. Ebert, C. Felser, and M. Kläui, "Direct observation of half-metallicity in the heusler compound co2mnsi", Nature Communications **5**, Number: 1 Publisher: Nature Publishing Group, 3974 (2014).

[63] S. Andrieu, A. Neggache, T. Hauet, T. Devolder, A. Hallal, M. Chshiev, A. M. Bataille, P. Le Fèvre, and F. Bertran, "Direct evidence for minority spin gap in the co2mnsi heusler compound", Physical Review B **93**, 094417 (2016).

[64] C. Guillemard, S. Petit-Watelot, J.-C. Rojas-Sánchez, J. Hohlfeld, J. Ghanbaja, A. Bataille, P. Le Fèvre, F. Bertran, and S. Andrieu, "Polycrystalline co2mn-based heusler thin films with high spin polarization and low magnetic damping", Applied Physics Letters **115**, Number: 17 Publisher: American Institute of Physics, 172401 (2019).

[65] C. Guillemard, S. Petit-Watelot, L. Pasquier, D. Pierre, J. Ghanbaja, J.-C. Rojas-Sánchez, A. Bataille, J. Rault, P. Le Fèvre, F. Bertran, and S. Andrieu, "Ultralow magnetic damping in co 2 mn -based heusler compounds: promising materials for spintronics", Physical Review Applied **11**, 064009 (2019).

[66] P. J. Brown, K. U. Neumann, P. J. Webster, and K. R. A. Ziebeck, "The magnetization distributions in some heusler alloys proposed as half-metallic ferromagnets", Journal of Physics: Condensed Matter **12**, Number: 8 Publisher: IOP Publishing, 1827–1835 (2000).

[67] A. V. Chumak, V. I. Vasyuchka, A. A. Serga, and B. Hillebrands, "Magnon spintronics", Nature Physics **11**, Number: 6 Publisher: Nature Publishing Group, 453–461 (2015).

[68] V. E. Demidov, S. Urazhdin, A. Anane, V. Cros, and S. O. Demokritov, "Spin–orbit-torque magnonics", Journal of Applied Physics **127**, Number: 17 Publisher: American Institute of Physics, 170901 (2020).

[69] B. D. Cullity and C. D. Graham, *Introduction to magnetic materials*, 2nd edition (Wiley-IEEE Press, Piscataway, NJ, Dec. 10, 2008), 568 pages.

[70] D. D. Stancil and A. Prabhakar, *Spin waves: theory and applications*, Softcover reprint of hardcover 1st ed. 2009 édition (Springer, New York, NY, Nov. 5, 2010), 372 pages.

[71] M. Coey, *Magnetism and magnetic materials* (CAMBRIDGE UNIVERSITY PRESS, Apr. 26, 2010).

[72] D. D. Stancil, *Theory of magnetostatic waves*, Softcover reprint of the original 1st ed. 1993 edition (Springer, Dec. 16, 2011), 225 pages.

[73] W. Heisenberg, "Zur theorie des ferromagnetismus", Zeitschrift fur Physik **49**, ADS Bibcode: 1928ZPhy...49..619H, 619–636 (1928).

[74] J. E. Miltat and M. J. Donahue, "Numerical micromagnetics: finite difference methods", in *Handbook of magnetism and advanced magnetic materials* (John Wiley & Sons, Ltd, 2007).

[75] A. Hubert and R. Schäfer, *Magnetic domains: the analysis of magnetic microstructures*, 1st ed. 1998. Corr. 3rd printing 2008 édition (Springer-Verlag Berlin and Heidelberg GmbH & Co. K, Berlin, Oct. 22, 2008), 696 pages.

[76] L. Exl, D. Suess, and T. Schrefl, "Micromagnetism", in *Handbook of magnetism and magnetic materials*, edited by M. Coey and S. Parkin (Springer International Publishing, Cham, 2020), pages 1–44.

[77] A. Aharoni, *Introduction to the theory of ferromagnetism*, 2nd édition (Clarendon Press, Oxford, Aug. 9, 2001), 332 pages.

[78] J. H. van Vleck, "On the anisotropy of cubic ferromagnetic crystals", Physical Review **52**, Publisher: American Physical Society, 1178–1198 (1937).

[79] L. Landau and E. Lifshitz, "3 - on the theory of the dispersion of magnetic permeability in ferromagnetic bodiesreprinted from physikalische zeitschrift der sowjetunion 8, part 2, 153, 1935.", in *Perspectives in theoretical physics*, edited by L. P. Pitaevski (Pergamon, Amsterdam, Jan. 1, 1992), pages 51–65.

[80] A. G. Gurevich and G. A. Melkov, *Magnetization oscillations and waves*, 1st edition (CRC Press, Boca Raton, Nov. 30, 1996), 464 pages.

[81] T. Gilbert, "A phenomenological theory of damping in ferromagnetic materials", IEEE Transactions on Magnetics **40**, Conference Name: IEEE Transactions on Magnetics, 3443–3449 (2004).

[82] P. W. Anderson and H. Suhl, "Instability in the motion of ferromagnets at high microwave power levels", Physical Review **100**, Publisher: American Physical Society, 1788–1789 (1955).

[83] H. Suhl, "The theory of ferromagnetic resonance at high signal powers", Journal of Physics and Chemistry of Solids **1**, 209–227 (1957).

[84] D. Polder, "On the theory of ferromagnetic resonance", Physica **15**, 253–255 (1949).

[85] J. H. E. Griffiths, "Anomalous high-frequency resistance of ferromagnetic metals", Nature **158**, Number: 4019 Publisher: Nature Publishing Group, 670–671 (1946).

[86] C. Kittel, "On the theory of ferromagnetic resonance absorption", Physical Review **73**, Publisher: American Physical Society, 155–161 (1948).

[87] J. Smit and H. G. Beljers, "Ferromagnetic resonance absorption in $BaFe_{12}o_{19}$, a highly anisotropic crystal", Philips Res. Rep. **10**, 113–130 (1955).

[88] H. Suhl, "Ferromagnetic resonance in nickel ferrite between one and two kilomegacycles", Physical Review **97**, Publisher: American Physical Society, 555–557 (1955).

[89] L. Baselgia, M. Warden, F. Waldner, S. L. Hutton, J. E. Drumheller, Y. Q. He, P. E. Wigen, and M. Maryško, "Derivation of the resonance frequency from the free energy of ferromagnets", Physical Review B **38**, Publisher: American Physical Society, 2237–2242 (1988).

[90] J. R. Macdonald, "Ferromagnetic resonance and the internal field in ferromagnetic materials", Proceedings of the Physical Society. Section A **64**, Publisher: IOP Publishing, 968–983 (1951).

[91] B. A. Kalinikos, M. P. Kostylev, N. V. Kozhus, and A. N. Slavin, "The dipole-exchange spin wave spectrum for anisotropic ferromagnetic films with mixed exchange boundary conditions", Journal of Physics: Condensed Matter **2**, 9861–9877 (1990).

[92] L. R. Walker, "Magnetostatic modes in ferromagnetic resonance", Physical Review **105**, Publisher: American Physical Society, 390–399 (1957).

[93] R. W. Damon and H. Van De Vaart, "Propagation of magnetostatic spin waves at microwave frequencies in a normally-magnetized disk", Journal of Applied Physics **36**, Publisher: American Institute of Physics, 3453–3459 (1965).

[94] B. A. Kalinikos, "Excitation of propagating spin waves in ferromagnetic films", IEE Proceedings H (Microwaves, Optics and Antennas) **127**, Publisher: IET Digital Library, 4–10 (1980).

[95] R. W. Damon and J. R. Eshbach, "Magnetostatic modes of a ferromagnet slab", Journal of Physics and Chemistry of Solids **19**, 308–320 (1961).

[96] G. T. Rado and J. R. Weertman, "Spin-wave resonance in a ferromagnetic metal", Journal of Physics and Chemistry of Solids **11**, 315–333 (1959).

[97] B. A. Kalinikos and A. N. Slavin, "Theory of dipole-exchange spin wave spectrum for ferromagnetic films with mixed exchange boundary conditions", Journal of Physics C: Solid State Physics **19**, Publisher: IOP Publishing, 7013–7033 (1986).

[98] K. Y. Guslienko, S. O. Demokritov, B. Hillebrands, and A. N. Slavin, "Effective dipolar boundary conditions for dynamic magnetization in thin magnetic stripes", Physical Review B **66**, Publisher: American Physical Society, 132402 (2002).

[99] J. Jorzick, C. Krämer, S. O. Demokritov, B. Hillebrands, B. Bartenlian, C. Chappert, D. Decanini, F. Rousseaux, E. Cambril, E. So/ndergard, M. Bailleul, C. Fermon, and A. N. Slavin, "Spin wave quantization in laterally confined magnetic structures (invited)", Journal of Applied Physics **89**, Publisher: American Institute of Physics, 7091–7095 (2001).

[100] Q. Wang, B. Heinz, R. Verba, M. Kewenig, P. Pirro, M. Schneider, T. Meyer, B. Lägel, C. Dubs, T. Brächer, and A. V. Chumak, "Spin pinning and spin-wave dispersion in nanoscopic ferromagnetic waveguides", Physical Review Letters **122**, Publisher: American Physical Society, 247202 (2019).

[101] K. Y. Guslienko and A. N. Slavin, "Boundary conditions for magnetization in magnetic nanoelements", Physical Review B **72**, 014463 (2005).

[102] A. Mahmoud, F. Ciubotaru, F. Vanderveken, A. V. Chumak, S. Hamdioui, C. Adelmann, and S. Cotofana, "Introduction to spin wave computing", Journal of Applied Physics **128**, Number: 16 Publisher: American Institute of Physics, 161101 (2020).

[103] A. Haldar and A. O. Adeyeye, "Functional magnetic waveguides for magnonics", Applied Physics Letters **119**, 060501 (2021).

[104] M. P. Kostylev, G. Gubbiotti, J.-G. Hu, G. Carlotti, T. Ono, and R. L. Stamps, "Dipole-exchange propagating spin-wave modes in metallic ferromagnetic stripes", Physical Review B **76**, Publisher: American Physical Society, 054422 (2007).

[105] M. Belmeguenai, H. Tuzcuoglu, M. S. Gabor, T. Petrisor, C. Tiusan, D. Berling, F. Zighem, T. Chauveau, S. M. Chérif, and P. Moch, "Co${}_{2}$FeAl thin films grown on MgO substrates: correlation between static, dynamic, and structural properties", Physical Review B **87**, Publisher: American Physical Society, 184431 (2013).

[106] V. Kamberský, "On the landau–lifshitz relaxation in ferromagnetic metals", Canadian Journal of Physics **48**, Publisher: NRC Research Press, 2906–2911 (1970).

[107] V. Kamberský, "Dissipative boundary conditions for ferromagnetic resonance equations", Czechoslovak Journal of Physics B **23**, 627–635 (1973).

[108] V. Kamberský, "FMR linewidth and disorder in metals", Czechoslovak Journal of Physics B **34**, 1111–1124 (1984).

[109] V. Kamberský, "Spin-orbital gilbert damping in common magnetic metals", Physical Review B **76**, Publisher: American Physical Society, 134416 (2007).

[110] K. Gilmore, Y. U. Idzerda, and M. D. Stiles, "Spin-orbit precession damping in transition metal ferromagnets (invited)", Journal of Applied Physics **103**, Publisher: American Institute of Physics, 07D303 (2008).

[111] I. Abdallah, "Spin dynamics and structural modifications of co2mnsi heusler alloys by helium ions irradiation", PhD thesis (2016).

[112] K. Zakeri, J. Lindner, I. Barsukov, R. Meckenstock, M. Farle, U. von Hörsten, H. Wende, W. Keune, J. Rocker, S. S. Kalarickal, K. Lenz, W. Kuch, K. Baberschke, and Z. Frait, "Spin dynamics in ferromagnets: gilbert damping and two-magnon scattering", Physical Review B **76**, Publisher: American Physical Society, 104416 (2007).

[113] M. Krawczyk and D. Grundler, "Review and prospects of magnonic crystals and devices with reprogrammable band structure", Journal of Physics: Condensed Matter **26**, Number: 12 Publisher: IOP Publishing, 123202 (2014).

[114] C. Elachi, "Waves in active and passive periodic structures: a review", Proceedings of the IEEE **64**, Number: 12 Conference Name: Proceedings of the IEEE, 1666–1698 (1976).

[115] F. Bloch, "Über die Quantenmechanik der Elektronen in Kristallgittern", Zeitschrift für Physik **52**, Number: 7, 555–600 (1929).

[116] J. D. Joannopoulos, S. G. Johnson, J. N. Winn, and R. D. Meade, *Photonic crystals: molding the flow of light - second edition*, 2nd edition (Princeton University Press, Princeton, Mar. 2, 2008), 304 pages.

[117] J.-M. Lourtioz, H. Benisty, V. Berger, J.-M. Gerard, D. Maystre, A. Tchelnokov, D. Pagnoux, and P. d. Fornel, *Photonic crystals: towards nanoscale photonic devices*, 2nd ed. 2008 édition (Springer-Verlag Berlin and Heidelberg GmbH & Co. K, Berlin, May 20, 2008), 514 pages.

[118] M. Notomi, "Theory of light propagation in strongly modulated photonic crystals: refraction-like behavior in the vicinity of the photonic band gap", Physical Review B **62**, Publisher: American Physical Society, 10696–10705 (2000).

[119] E. Cubukcu, K. Aydin, E. Ozbay, S. Foteinopoulou, and C. M. Soukoulis, "Negative refraction by photonic crystals", Nature **423**, Number: 6940 Publisher: Nature Publishing Group, 604–605 (2003).

[120] P. V. Parimi, W. T. Lu, P. Vodo, and S. Sridhar, "Imaging by flat lens using negative refraction", Nature **426**, Number: 6965 Publisher: Nature Publishing Group, 404–404 (2003).

[121] A. Berrier, M. Mulot, M. Swillo, M. Qiu, L. Thylén, A. Talneau, and S. Anand, "Negative refraction at infrared wavelengths in a two-dimensional photonic crystal", Physical Review Letters **93**, Publisher: American Physical Society, 073902 (2004).

[122] C. Croënne, E. J. S. Lee, H. Hu, and J. H. Page, "Band gaps in phononic crystals: generation mechanisms and interaction effects", AIP Advances **1**, Publisher: American Institute of Physics, 041401 (2011).

[123] H. Gao, W. Zhou, and T. W. Odom, "Plasmonic crystals: a platform to catalog resonances from ultraviolet to near-infrared wavelengths in a plasmonic library", Advanced Functional Materials **20**, _eprint: https://onlinelibrary.wiley.com/doi/pdf/10.1002/adfm.200901623, 529–539 (2010).

[124] S. A. Nikitov, P. Tailhades, and C. S. Tsai, "Spin waves in periodic magnetic structures—magnonic crystals", Journal of Magnetism and Magnetic Materials **236**, 320–330 (2001).

[125] G. Gubbiotti, S. Tacchi, G. Carlotti, N. Singh, S. Goolaup, A. O. Adeyeye, and M. Kostylev, "Collective spin modes in monodimensional magnonic crystals consisting of dipolarly coupled nanowires", Applied Physics Letters **90**, Publisher: American Institute of Physics, 092503 (2007).

[126] M. Mruczkiewicz, M. Krawczyk, V. K. Sakharov, Y. V. Khivintsev, Y. A. Filimonov, and S. A. Nikitov, "Standing spin waves in magnonic crystals", Journal of Applied Physics **113**, Publisher: American Institute of Physics, 093908 (2013).

[127] F. S. Ma, H. S. Lim, V. L. Zhang, Z. K. Wang, S. N. Piramanayagam, S. C. Ng, and M. H. Kuok, "Band structures of exchange spin waves in one-dimensional bi-component magnonic crystals", Journal of Applied Physics **111**, Publisher: American Institute of Physics, 064326 (2012).

[128] F. Ciubotaru, A. V. Chumak, N. Y. Grigoryeva, A. A. Serga, and B. Hillebrands, "Magnonic band gap design by the edge modulation of micro-sized waveguides", Journal of Physics D: Applied Physics **45**, Publisher: IOP Publishing, 255002 (2012).

[129] S.-K. Kim, K.-S. Lee, and D.-S. Han, "A gigahertz-range spin-wave filter composed of width-modulated nanostrip magnonic-crystal waveguides", Applied Physics Letters **95**, Publisher: American Institute of Physics, 082507 (2009).

[130] A. V. Chumak, T. Neumann, A. A. Serga, B. Hillebrands, and M. P. Kostylev, "A current-controlled, dynamic magnonic crystal", Journal of Physics D: Applied Physics **42**, 205005 (2009).

[131] T. Schwarze, R. Huber, G. Duerr, and D. Grundler, "Complete band gaps for magnetostatic forward volume waves in a two-dimensional magnonic crystal", Physical Review B **85**, Publisher: American Physical Society, 134448 (2012).

[132] M. Langer, R. A. Gallardo, T. Schneider, S. Stienen, A. Roldán-Molina, Y. Yuan, K. Lenz, J. Lindner, P. Landeros, and J. Fassbender, "Spin-wave modes in transition from a thin film to a full magnonic crystal", Physical Review B **99**, Publisher: American Physical Society, 024426 (2019).

[133] G. Gubbiotti, M. Kostylev, S. Tacchi, M. Madami, G. Carlotti, J. Ding, A. O. Adeyeye, F. Zighem, A. A. Stashkevich, E. Ivanov, and S. Samarin, "Collective spin waves on a nanowire array with step-modulated thickness", Journal of Physics D: Applied Physics **47**, Publisher: IOP Publishing, 105003 (2014).

[134] A. V. Chumak, A. A. Serga, S. Wolff, B. Hillebrands, and M. P. Kostylev, "Scattering of surface and volume spin waves in a magnonic crystal", Applied Physics Letters **94**, Publisher: American Institute of Physics, 172511 (2009).

[135] Y. Zhu, K. H. Chi, and C. S. Tsai, "Magnonic crystals-based tunable microwave phase shifters", Applied Physics Letters **105**, Publisher: American Institute of Physics, 022411 (2014).

[136] A. V. Chumak, V. S. Tiberkevich, A. D. Karenowska, A. A. Serga, J. F. Gregg, A. N. Slavin, and B. Hillebrands, "All-linear time reversal by a dynamic artificial crystal", Nature Communications **1**, Number: 1 Publisher: Nature Publishing Group, 141 (2010).

[137] A. B. Ustinov, A. V. Drozdovskii, and B. A. Kalinikos, "Multifunctional nonlinear magnonic devices for microwave signal processing", Applied Physics Letters **96**, Publisher: American Institute of Physics, 142513 (2010).

[138] M. Inoue, A. Baryshev, H. Takagi, P. B. Lim, K. Hatafuku, J. Noda, and K. Togo, "Investigating the use of magnonic crystals as extremely sensitive magnetic field sensors at room temperature", Applied Physics Letters **98**, Publisher: American Institute of Physics, 132511 (2011).

[139] A. A. Nikitin, A. B. Ustinov, A. A. Semenov, A. V. Chumak, A. A. Serga, V. I. Vasyuchka, E. Lähderanta, B. A. Kalinikos, and B. Hillebrands, "A spin-wave logic gate based on a width-modulated dynamic magnonic crystal", Applied Physics Letters **106**, Publisher: American Institute of Physics, 102405 (2015).

[140] A. Khitun, M. Bao, and K. L. Wang, "Magnonic logic circuits", Journal of Physics D: Applied Physics **43**, Number: 26 Publisher: IOP Publishing, 264005 (2010).

[141] G. Gubbiotti, S. Tacchi, M. Madami, G. Carlotti, A. O. Adeyeye, and M. Kostylev, "Brillouin light scattering studies of planar metallic magnonic crystals", Journal of Physics D: Applied Physics **43**, 264003 (2010).

[142] A. V. Chumak, A. A. Serga, S. Wolff, B. Hillebrands, and M. P. Kostylev, "Design and optimization of one-dimensional ferrite-film based magnonic crystals", Journal of Applied Physics **105**, Publisher: American Institute of Physics, 083906 (2009).

[143] F. S. Ma, H. S. Lim, Z. K. Wang, S. N. Piramanayagam, S. C. Ng, and M. H. Kuok, "Effect of interrow magnetic coupling on band structures of 2-d magnonic crystal waveguides", IEEE Transactions on Magnetics **47**, Conference Name: IEEE Transactions on Magnetics, 2689–2692 (2011).

[144] M. L. Sokolovskyy and M. Krawczyk, "The magnetostatic modes in planar one-dimensional magnonic crystals with nanoscale sizes", Journal of Nanoparticle Research **13**, 6085–6091 (2011).

[145] G. Gubbiotti, S. Tacchi, M. Madami, G. Carlotti, S. Jain, A. O. Adeyeye, and M. P. Kostylev, "Collective spin waves in a bicomponent two-dimensional magnonic crystal", Applied Physics Letters **100**, Publisher: American Institute of Physics, 162407 (2012).

[146] S. Tacchi, G. Gubbiotti, M. Madami, and G. Carlotti, "Brillouin light scattering studies of 2d magnonic crystals", Journal of Physics: Condensed Matter **29**, Publisher: IOP Publishing, 073001 (2016).

[147] J. Ding and A. O. Adeyeye, "Binary ferromagnetic nanostructures: fabrication, static and dynamic properties", Advanced Functional Materials **23**, _eprint: https://onlinelibrary.wiley.com/doi/pdf/10.1684–1691 (2013).

[148] Z. K. Wang, V. L. Zhang, H. S. Lim, S. C. Ng, M. H. Kuok, S. Jain, and A. O. Adeyeye, "Observation of frequency band gaps in a one-dimensional nanostructured magnonic crystal", Applied Physics Letters **94**, Publisher: American Institute of Physics, 083112 (2009).

[149] J. W. Kłos, D. Kumar, M. Krawczyk, and A. Barman, "Influence of structural changes in a periodic antidot waveguide on the spin-wave spectra", Physical Review B **89**, Publisher: American Physical Society, 014406 (2014).

[150] S. Neusser, B. Botters, and D. Grundler, "Localization, confinement, and field-controlled propagation of spin waves in ${\text{ni}}_{80}{\text{fe}}_{20}$ antidot lattices", Physical Review B **78**, Publisher: American Physical Society, 054406 (2008).

[151] K.-S. Lee, D.-S. Han, and S.-K. Kim, "Physical origin and generic control of magnonic band gaps of dipole-exchange spin waves in width-modulated nanostrip waveguides", Physical Review Letters **102**, Publisher: American Physical Society, 127202 (2009).

[152] J. Rychły, P. Gruszecki, M. Mruczkiewicz, J. W. Kłos, S. Mamica, and M. Krawczyk, "Magnonic crystals—prospective structures for shaping spin waves in nanoscale", Low Temperature Physics **41**, Publisher: American Institute of Physics, 745–759 (2015).

[153] S. L. Vysotskii, S. A. Nikitov, and Y. A. Filimonov, "Magnetostatic spin waves in two-dimensional periodic structures (magnetophoton crystals)", Journal of Experimental and Theoretical Physics **101**, 547–553 (2005).

[154] S. Neusser and D. Grundler, "Magnonics: spin waves on the nanoscale", Advanced Materials **21**, _eprint: https://onlinelibrary.wiley.com/doi/pdf/10.1002/adma.200900809, 2927–2932 (2009).

[155] R. Zivieri, "Chapter three - metamaterial properties of one-dimensional and two-dimensional magnonic crystals", in *Solid state physics*, Vol. 63, edited by R. E. Camley and R. L. Stamps (Academic Press, Jan. 1, 2012), pages 151–216.

[156] S. Tacchi, P. Gruszecki, M. Madami, G. Carlotti, J. W. Kłos, M. Krawczyk, A. Adeyeye, and G. Gubbiotti, "Universal dependence of the spin wave band structure on the geometrical characteristics of two-dimensional magnonic crystals", Scientific Reports **5**, Number: 1 Publisher: Nature Publishing Group, 10367 (2015).

[157] M. J. Pechan, C. Yu, R. L. Compton, J. P. Park, and P. A. Crowell, "Direct measurement of spatially localized ferromagnetic-resonance modes in an antidot lattice (invited)", Journal of Applied Physics **97**, Publisher: American Institute of Physics, 10J903 (2005).

[158] M. Kostylev, G. Gubbiotti, G. Carlotti, G. Socino, S. Tacchi, C. Wang, N. Singh, A. O. Adeyeye, and R. L. Stamps, "Propagating volume and localized spin wave modes on a lattice of circular magnetic antidots", Journal of Applied Physics **103**, Publisher: American Institute of Physics, 07C507 (2008).

[159] C. Bayer, J. Jorzick, B. Hillebrands, S. O. Demokritov, R. Kouba, R. Bozinoski, A. N. Slavin, K. Y. Guslienko, D. V. Berkov, N. L. Gorn, and M. P. Kostylev, "Spin-wave excitations in finite rectangular elements of ${\mathrm{ni}}_{80}{\mathrm{fe}}_{20}$", Physical Review B **72**, Publisher: American Physical Society, 064427 (2005).

[160] S. Tacchi, M. Madami, G. Gubbiotti, G. Carlotti, A. O. Adeyeye, S. Neusser, B. Botters, and D. Grundler, "Magnetic normal modes in squared antidot array with circular holes: a combined brillouin light scattering and broadband ferromagnetic resonance study", IEEE Transactions on Magnetics **46**, Conference Name: IEEE Transactions on Magnetics, 172–178 (2010).

[161] S. Neusser, G. Duerr, H. G. Bauer, S. Tacchi, M. Madami, G. Woltersdorf, G. Gubbiotti, C. H. Back, and D. Grundler, "Anisotropic propagation and damping of spin waves in a nanopatterned antidot lattice", Physical Review Letters **105**, Publisher: American Physical Society, 067208 (2010).

[162] S. Tacchi, M. Madami, G. Gubbiotti, G. Carlotti, A. O. Adeyeye, S. Neusser, B. Botters, and D. Grundler, "Angular dependence of magnetic normal modes in NiFe antidot lattices with different lattice symmetry", IEEE Transactions on Magnetics **46**, Conference Name: IEEE Transactions on Magnetics, 1440–1443 (2010).

[163] V. V. Kruglyak, P. S. Keatley, A. Neudert, R. J. Hicken, J. R. Childress, and J. A. Katine, "Imaging collective magnonic modes in 2d arrays of magnetic nanoelements", Physical Review Letters **104**, Publisher: American Physical Society, 027201 (2010).

[164] A. Manzin, R. Ferrero, and M. Vicentini, "Application of magnonic crystals in magnetic bead detection", Nanomaterials **12**, Number: 19 Publisher: Multidisciplinary Digital Publishing Institute, 3278 (2022).

[165] N. Kumar and A. Prabhakar, "Resonant spin wave excitations in a magnonic crystal cavity", Journal of Magnetism and Magnetic Materials, Perspectives on magnon spintronics **450**, 46–50 (2018).

[166] J. Ding, M. Kostylev, and A. O. Adeyeye, "Magnetic hysteresis of dynamic response of one-dimensional magnonic crystals consisting of homogenous and alternating width nanowires observed with broadband ferromagnetic resonance", Physical Review B **84**, Publisher: American Physical Society, 054425 (2011).

[167] S. Tacchi, M. Madami, G. Gubbiotti, G. Carlotti, S. Goolaup, A. O. Adeyeye, N. Singh, and M. P. Kostylev, "Analysis of collective spin-wave modes at different points within the hysteresis loop of a one-dimensional magnonic crystal comprising alternative-width nanostripes", Physical Review B **82**, Publisher: American Physical Society, 184408 (2010).

[168] R. Verba, V. Tiberkevich, E. Bankowski, T. Meitzler, G. Melkov, and A. Slavin, "Conditions for the spin wave nonreciprocity in an array of dipolarly coupled magnetic nanopillars", Applied Physics Letters **103**, Publisher: American Institute of Physics, 082407 (2013).

[169] M. C. Onbasli, A. Kehlberger, D. H. Kim, G. Jakob, M. Kläui, A. V. Chumak, B. Hillebrands, and C. A. Ross, "Pulsed laser deposition of epitaxial yttrium iron garnet films with low gilbert damping and bulk-like magnetization", APL Materials **2**, Publisher: American Institute of Physics, 106102 (2014).

[170] C. Hauser, T. Richter, N. Homonnay, C. Eisenschmidt, M. Qaid, H. Deniz, D. Hesse, M. Sawicki, S. G. Ebbinghaus, and G. Schmidt, "Yttrium iron garnet thin films with very low damping obtained by recrystallization of amorphous material", Scientific Reports **6**, Number: 1 Publisher: Nature Publishing Group, 20827 (2016).

[171] Y. Zhang, J. Xie, L. Deng, and L. Bi, "Growth of phase pure yttrium iron garnet thin films on silicon: the effect of substrate and postdeposition annealing temperatures", IEEE Transactions on Magnetics **51**, Conference Name: IEEE Transactions on Magnetics, 1–4 (2015).

[172] R. Xiang, L. Chen, S. Zhang, H. Li, J. Du, Y. W. Du, and R. H. Liu, "Electrical generation and detection of spin waves in polycrystalline YIG/pt grown on silicon wafers", Materials Research Express **7**, Publisher: IOP Publishing, 046105 (2020).

[173] A. Delgado, Y. Guerra, E. Padrón-Hernández, and R. Peña-Garcia, "Combining the sol gel method and spin coating to obtain YIG films with low FMR linewidth on silicon (100) substrate", Materials Research Express **5**, Publisher: IOP Publishing, 026419 (2018).

[174] S. Trudel, O. Gaier, J. Hamrle, and B. Hillebrands, "Magnetic anisotropy, exchange and damping in cobalt-based full-heusler compounds: an experimental review", Journal of Physics D: Applied Physics **43**, 193001 (2010).

[175] R. A. de Groot, F. M. Mueller, P. G. v. Engen, and K. H. J. Buschow, "New class of materials: half-metallic ferromagnets", Physical Review Letters **50**, Publisher: American Physical Society, 2024–2027 (1983).

[176] S. Tsunegi, Y. Sakuraba, M. Oogane, N. D. Telling, L. R. Shelford, E. Arenholz, G. v. d. Laan, R. J. Hicken, K. Takanashi, and Y. Ando, "Tunnel magnetoresistance in epitaxially grown magnetic tunnel junctions using heusler alloy electrode and MgO barrier", Journal of Physics D: Applied Physics **42**, 195004 (2009).

[177] R. Fetzer, S. Ouardi, Y. Honda, H.-x. Liu, S. Chadov, B. Balke, S. Ueda, M. Suzuki, T. Uemura, M. Yamamoto, M. Aeschlimann, M. Cinchetti, G. H. Fecher, and C. Felser, "Spin-resolved low-energy and hard x-ray photoelectron spectroscopy of off-stoichiometric co2mnsi heusler thin films exhibiting a record TMR", Journal of Physics D: Applied Physics **48**, Publisher: IOP Publishing, 164002 (2015).

[178] B. Heinrich, D. Fraitová, and V. Kamberský, "The influence of s-d exchange on relaxation of magnons in metals", physica status solidi (b) **23**, _eprint: https://onlinelibrary.wiley.com/doi/pdf/10.1002/p 501–507 (1967).

[179] B. Pradines, R. Arras, I. Abdallah, N. Biziere, and L. Calmels, "First-principles calculation of the effects of partial alloy disorder on the static and dynamic magnetic properties of ${\mathrm{co}}_{2}\mathrm{MnSi}$", Physical Review B **95**, Publisher: American Physical Society, 094425 (2017).

[180] G. Ortiz, "Elaboration et étude des propriétés physiques de couches minces monocristallines d'alliage de heusler à faible amortissement magnétique pour composants hyperfréquences", PhD thesis (2013).

[181] B. Pradines, "Electronic structure and static and dynamic magnetic properties of partly disordered bulk Heusler alloys and all-Heusler hétérostructures", PhD thesis (Université Toulouse 3 Paul Sabatier, Nov. 3, 2017).

[182] P. J. Webster, "Magnetic and chemical order in heusler alloys containing cobalt and manganese", Journal of Physics and Chemistry of Solids **32**, 1221–1231 (1971).

[183] S. Picozzi, A. Continenza, and A. J. Freeman, "Role of structural defects on the half-metallic character of ${\mathrm{co}}_{2}\mathrm{MnGe}$ and ${\mathrm{co}}_{2}\mathrm{MnSi}$ heusler alloys", Physical Review B **69**, Publisher: American Physical Society, 094423 (2004).

[184] S. Picozzi, A. Continenza, and A. J. Freeman, "${\mathrm{co}}_{2}\mathrm{mn}x$ $(x=\mathrm{si},$ ge, sn) heusler compounds: an ab initio study of their structural, electronic, and magnetic properties at zero and elevated pressure", Physical Review B **66**, Publisher: American Physical Society, 094421 (2002).

[185] A. Rajanikanth, Y. K. Takahashi, and K. Hono, "Spin polarization of co2mnge and co2mnsi thin films with a2 and l21 structures", Journal of Applied Physics **101**, Publisher: American Institute of Physics, 023901 (2007).

[186] G. Grigaliūnaitė-Vonsevičienė, B. Vengalis, A. Maneikis, and R. Juškėnas, "Magnetic and electrical properties of postannealed co2mnsi heusler alloy films", Applied Nanoscience **10**, 2229–2237 (2020).

[187] F. Yang, W. Li, J. Li, H. Chen, D. Liu, X. Chen, and C. Yang, "The microstructure and magnetic properties of co2mnsi thin films deposited on si substrate", Journal of Alloys and Compounds **723**, 188–191 (2017).

[188] H. Wu, P. Kratzer, and M. Scheffler, "First-principles study of thin magnetic transition-metal silicide films on si(001)", Physical Review B **72**, Publisher: American Physical Society, 144425 (2005).

[189] D. Kumar and A. O. Adeyeye, "Techniques in micromagnetic simulation and analysis", Journal of Physics D: Applied Physics **50**, Publisher: IOP Publishing, 343001 (2017).

[190] M. J. Donahue, "OOMMF user's guide, version 1.0", NIST, Last Modified: 2018-11-10T10:11-05:00 Publisher: Michael J. Donahue (1999).

[191] A. Vansteenkiste, J. Leliaert, M. Dvornik, M. Helsen, F. Garcia-Sanchez, and B. Van Waeyenberge, "The design and verification of MuMax3", AIP Advances **4**, Publisher: American Institute of Physics, 107133 (2014).

[192] K. M. Lebecki, M. J. Donahue, and M. W. Gutowski, "Periodic boundary conditions for demagnetization interactions in micromagnetic simulations", Journal of Physics D: Applied Physics **41**, 175005 (2008).

[193] W. Wang, C. Mu, B. Zhang, Q. Liu, J. Wang, and D. Xue, "Two-dimensional periodic boundary conditions for demagnetization interactions in micromagnetics", Computational Materials Science **49**, 84–87 (2010).

[194] A. Vansteenkiste and B. Van de Wiele, "MuMax: a new high-performance micromagnetic simulation tool", Journal of Magnetism and Magnetic Materials **323**, 2585–2591 (2011).

[195] L. Exl, S. Bance, F. Reichel, T. Schrefl, H. Peter Stimming, and N. J. Mauser, "LaBonte's method revisited: an effective steepest descent method for micromagnetic energy minimization", Journal of Applied Physics **115**, Publisher: American Institute of Physics, 17D118 (2014).

[196] G. Venkat, D. Kumar, M. Franchin, O. Dmytriiev, M. Mruczkiewicz, H. Fangohr, A. Barman, M. Krawczyk, and A. Prabhakar, "Proposal for a standard micromagnetic problem: spin wave dispersion in a magnonic waveguide", IEEE Transactions on Magnetics **49**, Conference Name: IEEE Transactions on Magnetics, 524–529 (2013).

[197] D. Kumar, O. Dmytriiev, S. Ponraj, and A. Barman, "Numerical calculation of spin wave dispersions in magnetic nanostructures", Journal of Physics D: Applied Physics **45**, Publisher: IOP Publishing, 015001 (2011).

[198] E. Montoya, T. McKinnon, A. Zamani, E. Girt, and B. Heinrich, "Broadband ferromagnetic resonance system and methods for ultrathin magnetic films", Journal of Magnetism and Magnetic Materials **356**, 12–20 (2014).

[199] I. S. Maksymov and M. Kostylev, "Broadband stripline ferromagnetic resonance spectroscopy of ferromagnetic films, multilayers and nanostructures", Physica E: Low-dimensional Systems and Nanostructures **69**, 253–293 (2015).

[200] M. Bailleul, "Propagation et confinement d'ondes de spin dans les microstructures magnétiques", These de doctorat (Palaiseau, Ecole polytechnique, Jan. 1, 2002).

[201] R. Garg, I. Bahl, and M. Bozzi, *Microstrip lines and slotlines, third edition*, 3rd edition (Artech House, Boston, Mass., May 1, 2013), 560 pages.

[202] C. Wen, "Coplanar waveguide: a surface strip transmission line suitable for nonreciprocal gyromagnetic device applications", IEEE Transactions on Microwave Theory and Techniques **17**, Conference Name: IEEE Transactions on Microwave Theory and Techniques, 1087–1090 (1969).

[203] D. M. Pozar, *Microwave engineering*, 4th Edition (John Wiley & Sons, Hoboken, NJ, Dec. 23, 2011), 752 pages.

[204] V. Vlaminck, "Décalage doppler d'ondes de spin induit par un courant électrique", These de doctorat (Strasbourg 1, Jan. 1, 2008).

[205] R. Lassalle-Balier, "Spin wave propagation and interferometry", These de doctorat (Paris 6, Jan. 1, 2011).

[206] N. Biziere, "Détection de radiofréquences par des composants magnéto-résistifs", These de doctorat (Paris 11, Jan. 1, 2007).

[207] *AWR TX-line*, https://www.cadence.com/ko_KR/home/tools/system-analysis/rf-microwave-design/awr-tx-line.html (visited on 01/26/2023).

[208] V. Vlaminck and M. Bailleul, "Spin-wave transduction at the submicrometer scale: experiment and modeling", Physical Review B **81**, Number: 1 Publisher: American Physical Society, 014425 (2010).

[209] T. Schwarze, "Spin waves in 2d and 3d magnonic crystals: from nanostructured ferromagnetic materials to chiral helimagnets", PhD thesis (2013).

[210] G. Counil, "Perméamétrie hyperfréquence de couches minces magnétiques", PhD thesis (2005), 1 vol. (154 p.)

[211] C. Bilzer, "Microwave susceptibility of thin ferromagnetic films:
metrology and insight into magnetization dynamics", PhD thesis (Université Paris Sud - Paris XI, Nov. 30, 2007).

[212] T. J. Silva, C. S. Lee, T. M. Crawford, and C. T. Rogers, "Inductive measurement of ultrafast magnetization dynamics in thin-film permalloy", Journal of Applied Physics **85**, Publisher: American Institute of Physics, 7849–7862 (1999).

[213] S. S. Kalarickal, P. Krivosik, M. Wu, C. E. Patton, M. L. Schneider, P. Kabos, T. J. Silva, and J. P. Nibarger, "Ferromagnetic resonance linewidth in metallic thin films: comparison of measurement methods", Journal of Applied Physics **99**, Publisher: American Institute of Physics, 093909 (2006).

[214] A. Technologies, *Agilent network analyser basics* ().

[215] O. Gaier, J. Hamrle, S. J. Hermsdoerfer, H. Schultheiß, B. Hillebrands, Y. Sakuraba, M. Oogane, and Y. Ando, "Influence of the l21 ordering degree on the magnetic properties of co2mnsi heusler films", Journal of Applied Physics **103**, Publisher: American Institute of Physics, 103910 (2008).

[216] O. Gaier, J. Hamrle, S. Trudel, B. Hillebrands, H. Schneider, and G. Jakob, "Exchange stiffness in the co2fesi heusler compound", Journal of Physics D: Applied Physics **42**, 232001 (2009).

[217] H. Pandey, P. C. Joshi, R. P. Pant, R. Prasad, S. Auluck, and R. C. Budhani, "Evolution of ferromagnetic and spin-wave resonances with crystalline order in thin films of full-heusler alloy co2mnsi", Journal of Applied Physics **111**, Publisher: American Institute of Physics, 023912 (2012).

[218] M. Belmeguenai, F. Zighem, D. Faurie, H. Tuzcuoglu, S.-M. Chérif, P. Moch, K. Westerholt, and W. Seiler, "Structural and magnetic properties of co2mnsi thin films", physica status solidi (a) **209**, _eprint: https://onlinelibrary.wiley.com/doi/pdf/10.1002/pssa.201228039, 1328–1333 (2012).

[219] H. Ulrichs, B. Lenk, and M. Münzenberg, "Magnonic spin-wave modes in CoFeB antidot lattices", Applied Physics Letters **97**, Publisher: American Institute of Physics, 092506 (2010).

[220] S. Neusser, B. Botters, M. Becherer, D. Schmitt-Landsiedel, and D. Grundler, "Spin-wave localization between nearest and next-nearest neighboring holes in an antidot lattice", Applied Physics Letters **93**, Publisher: American Institute of Physics, 122501 (2008).

[221] N. Porwal, A. De, S. Mondal, K. Dutta, S. Choudhury, J. Sinha, A. Barman, and P. K. Datta, "Observation of angle-dependent mode conversion and mode hopping in 2d annular antidot lattice", Scientific Reports **9**, Number: 1 Publisher: Nature Publishing Group, 12138 (2019).

[222] S. Neusser, G. Duerr, S. Tacchi, M. Madami, M. L. Sokolovskyy, G. Gubbiotti, M. Krawczyk, and D. Grundler, "Magnonic minibands in antidot lattices with large spin-wave propagation velocities", Physical Review B **84**, Publisher: American Physical Society, 094454 (2011).

[223] G. Gubbiotti, F. Montoncello, S. Tacchi, M. Madami, G. Carlotti, L. Giovannini, J. Ding, and A. O. Adeyeye, "Angle-resolved spin wave band diagrams of square antidot lattices studied by brillouin light scattering", Applied Physics Letters **106**, Publisher: American Institute of Physics, 262406 (2015).

[224] R. Zivieri, P. Malagò, L. Giovannini, S. Tacchi, G. Gubbiotti, and A. O. Adeyeye, "Soft magnonic modes in two-dimensional permalloy antidot lattices", Journal of Physics: Condensed Matter **25**, Publisher: IOP Publishing, 336002 (2013).

[225] R. Mandal, S. Barman, S. Saha, Y. Otani, and A. Barman, "Tunable spin wave spectra in two-dimensional ni80fe20 antidot lattices with varying lattice symmetry", Journal of Applied Physics **118**, Publisher: American Institute of Physics, 053910 (2015).

[226] M. Yu, L. Malkinski, L. Spinu, W. Zhou, and S. Whittenburg, "Size dependence of static and dynamic magnetic properties in nanoscale square permalloy antidot arrays", Journal of Applied Physics **101**, Publisher: American Institute of Physics, 09F501 (2007).

[227] S. Martens, O. Albrecht, K. Nielsch, and D. Görlitz, "Local modes and two magnon scattering in ordered permalloy antidot arrays", Journal of Applied Physics **105**, Publisher: American Institute of Physics, 07C113 (2009).

[228] N. Yao, editor, *Focused ion beam systems: basics and applications* (Cambridge University Press, Cambridge, 2007).

[229] B. Schmidt and K. Wetzig, *Ion beams in materials processing and analysis* (Springer, Vienna, 2013).

[230] J. Gierak, "Focused ion beam technology and ultimate applications", Semiconductor Science and Technology **24**, 043001 (2009).

[231] M. Urbánek, V. Uhlíř, P. Bábor, E. Kolíbalová, T. Hrnčíř, J. Spousta, and T. Šikola, "Focused ion beam fabrication of spintronic nanostructures: an optimization of the milling process", Nanotechnology **21**, 145304 (2010).

[232] J. Orloff, L. Swanson, and M. Utlaut, *High resolution focused ion beams: fib and its applications : the physics of liquid metal ion sources and ion optics and their application to focused ion beam technology*, 2003e édition (Kluwer Academic/Plenum Publishers, New York, Oct. 31, 2002), 304 pages.

[233] *FIB SEM | Focused Ion Beam Scanning Electron Microscopes - FR*, https://www.thermofisher.com/fr/fr/home/electron-microscopy/products/dualbeam-fib-sem-microscopes.html (visited on 11/15/2022).

[234] *Nanoscale Prototyping - FR*, https://www.thermofisher.com/fr/fr/home/materials-science/nanoprototyping.html (visited on 11/15/2022).

[235] S. Reyntjens and R. Puers, "A review of focused ion beam applications in microsystem technology", Journal of Micromechanics and Microengineering **11**, 287 (2001).

[236] O. Wilhelmi, S. Reyntjens, C. Mitterbauer, L. Roussel, D. J. Stokes, and D. H. W. Hubert, "Rapid prototyping of nanostructured materials with a focused ion beam", Japanese Journal of Applied Physics **47**, Publisher: IOP Publishing, 5010 (2008).

[237] *FIB SEM | NanoBuilder Software - FR*, https://www.thermofisher.com/fr/fr/home/electron-microscopy/products/software-em-3d-vis/nanobuilder-software.html (visited on 11/15/2022).

[238] J. Renaud, "Application des faisceaux d'ions focalisés à la création de centres NV du diamant. caractérisation de ces faisceaux d'ions issus d'une source plasma.", PhD thesis (2019).

[239] D. A. Dahl, "Simion for the personal computer in reflection", International Journal of Mass Spectrometry **200**, 3–25 (2000).

[240] T. Jung, L. Kreiner, C. Pauly, F. Mücklich, A. M. Edmonds, M. Markham, and C. Becher, "Reproducible fabrication and characterization of diamond membranes for photonic crystal cavities", physica status solidi (a) **213**, _eprint: https://onlinelibrary.wiley.com/doi/pdf/10.1002/pssa.20160065 3254–3264 (2016).

[241] A. Joshi-Imre and S. Bauerdick, "Direct-write ion beam lithography", Journal of Nanotechnology **2014**, Publisher: Hindawi, e170415 (2014).

[242] M. S. M. Saifullah, "Sub-10 nm direct patterning of oxides using an electron beam — a review", COSMOS **05**, Publisher: World Scientific Publishing Co., 1–21 (2009).

[243] M. M. Greve and B. Holst, "Optimization of an electron beam lithography instrument for fast, large area writing at 10kV acceleration voltage", Journal of Vacuum Science & Technology B **31**, Publisher: American Vacuum Society, 043202 (2013).

[244] W. (Hu, K. Sarveswaran, M. Lieberman, and G. H. Bernstein, "Sub-10 nm electron beam lithography using cold development of poly(methylmethacrylate)", Journal of Vacuum Science & Technology B: Microelectronics and Nanometer Structures Processing, Measurement, and Phenomena **22**, Publisher: American Institute of Physics, 1711–1716 (2004).

[245] J. Nabity, L. A. Compbell, M. Zhu, and W. Zhou, "E-beam nanolithography integrated with scanning electron microscope", in *Scanning microscopy for nanotechnology: techniques and applications*, edited by W. Zhou and Z. L. Wang (Springer, New York, NY, 2007), pages 120–151.

[246] M. A. Mohammad, M. Muhammad, S. K. Dew, and M. Stepanova, "Fundamentals of electron beam exposure and development", in *Nanofabrication: techniques and principles*, edited by M. Stepanova and S. Dew (Springer, Vienna, 2012), pages 11–41.

[247] A. S. Gangnaik, Y. M. Georgiev, and J. D. Holmes, "New generation electron beam resists: a review", Chemistry of Materials **29**, Publisher: American Chemical Society, 1898–1917 (2017).

[248] A. E. Grigorescu and C. W. Hagen, "Resists for sub-20-nm electron beam lithography with a focus on HSQ: state of the art", Nanotechnology **20**, 292001 (2009).

[249] T. H. P. Chang, "Proximity effect in electron-beam lithography", Journal of Vacuum Science and Technology **12**, Publisher: American Vacuum Society, 1271–1275 (1975).

[250] *Proximity effect correction | electron dose*, https://raith.com/, https://raith.com/technology/nanofabrication-software/proximity-effect-correction/ (visited on 11/22/2022).

[251] M. BRONSGEEST, *Ultracompact ultralow power ECR technology*, POLYGON PHYSICS, (Nov. 7, 2016) https://polygonphysics.com/technology/ultracompact-ecr-technology/ (visited on 02/02/2023).

[252] W. Yue, Z. Wang, Y. Yang, L. Chen, A. Syed, K. Wong, and X. Wang, "Electron-beam lithography of gold nanostructures for surface-enhanced raman scattering", Journal of Micromechanics and Microengineering **22**, Publisher: IOP Publishing, 125007 (2012).

[253] S. Pfirrmann, A. Voigt, A. Kolander, G. Grützner, O. Lohse, I. Harder, and V. A. Guzenko, "Towards a novel positive tone resist mr-PosEBR for high resolution electron-beam lithography", Microelectronic Engineering, Micro- and Nanopatterning 2015 **155**, 67–73 (2016).

[254] R. Fallica, D. Kazazis, R. Kirchner, A. Voigt, I. Mochi, H. Schift, and Y. Ekinci, "Lithographic performance of ZEP520a and mr-PosEBR resists exposed by electron beam and extreme ultraviolet lithography", Journal of Vacuum Science & Technology B **35**, Publisher: American Vacuum Society, 061603 (2017).

[255] T. B. Borzenko, Y. I. Koval, and V. A. Kudryashov, "Ion beam etching mechanism of PMMA based resists by noble gas ions", Microelectronic Engineering **23**, 337–340 (1994).

[256] Y. Koval, T. Borzenko, and S. Dubonos, "Use of polymethylmethacrylate for pattern transfer by ion beam etching: improvement of etching homogeneity and patterning quality", Journal of Vacuum Science & Technology B: Microelectronics and Nanometer Structures Processing, Measurement, and Phenomena **21**, Publisher: American Institute of Physics, 2217–2219 (2003).

[257] S. Wolff, B. Lägel, and S. Trellenkamp, "Incident angle dependent damage of PMMA during ar+-ion beam etching", Microelectronic Engineering, The 35th International Conference on Micro- and Nano-Engineering (MNE) **87**, 1444–1446 (2010).

[258] Y. Koval, "Mechanism of etching and surface relief development of PMMA under low-energy ion bombardment", Journal of Vacuum Science & Technology B: Microelectronics and Nanometer Structures Processing, Measurement, and Phenomena **22**, Publisher: American Institute of Physics, 843–851 (2004).

[259] G. S. Oehrlein, R. J. Phaneuf, and D. B. Graves, "Plasma-polymer interactions: a review of progress in understanding polymer resist mask durability during plasma etching for nanoscale fabrication", Journal of Vacuum Science & Technology B **29**, Publisher: American Vacuum Society, 010801 (2011).

[260] *Remover PG – microresist*, https://www.microresist.de/en/produkt/remover-pg/ (visited on 11/23/2022).

[261] *SVC-14 – microresist*, https://www.microresist.de/en/produkt/svc-14/ (visited on 11/23/2022).

[262] *E-beam resist AR-p 6200 series (CSAR 62)*, Allresist EN, https://www.allresist.com/portfolio-item/e-beam-resist-ar-p-6200-series-csar-62/ (visited on 11/22/2022).

[263] S. Mantion and N. Biziere, "Cubic anisotropy for a reconfigurable magnonic crystal based on co 2 mn si heusler alloy", Physical Review Applied **17**, 044054 (2022).

[264] C. Guillemard, S. Petit-Watelot, T. Devolder, L. Pasquier, P. Boulet, S. Migot, J. Ghanbaja, F. Bertran, and S. Andrieu, "Issues in growing heusler compounds in thin films for spintronic applications", Journal of Applied Physics **128**, Publisher: American Institute of Physics, 241102 (2020).

[265] C. T. Yu, H. Jiang, L. Shen, P. J. Flanders, and G. J. Mankey, "The magnetic anisotropy and domain structure of permalloy antidot arrays", Journal of Applied Physics **87**, Publisher: American Institute of Physics, 6322–6324 (2000).

[266] C. C. Wang, A. O. Adeyeye, and N. Singh, "Magnetic antidot nanostructures: effect of lattice geometry", Nanotechnology **17**, 1629 (2006).

[267] B. Hillebrands and K. Ounadjela, *Spin dynamics in confined magnetic structures i*, Google-Books-ID: Ky0TBwAAQBAJ (Springer Science & Business Media, July 1, 2003), 363 pages.

[268] F. Groß, M. Zelent, A. Gangwar, S. Mamica, P. Gruszecki, M. Werner, G. Schütz, M. Weigand, E. J. Goering, C. H. Back, M. Krawczyk, and J. Gräfe, "Phase resolved observation of spin wave modes in antidot lattices", Applied Physics Letters **118**, Publisher: American Institute of Physics, 232403 (2021).

[269] K. Begari and A. Haldar, "Reconfigurable microwave properties in c-, l- and s-shaped nanomagnets", Journal of Physics D: Applied Physics **52**, Publisher: IOP Publishing, 335003 (2019).

[270] K. Begari and A. Haldar, "Reconfigurable microwave properties of zigzag magnetic nanowires", Journal of Physics D: Applied Physics **53**, Publisher: IOP Publishing, 455005 (2020).

[271] K. Begari and A. Haldar, "Reconfigurable microwave properties in trapezoid-shaped nanomagnets without bias magnetic field", Journal of Magnetism and Magnetic Materials **540**, 168431 (2021).

[272] S. Mantion and N. Biziere, "Influence of ga + milling on the spin waves modes in a co 2 MnSi heusler magnonic crystal", Journal of Applied Physics **131**, 113905 (2022).

[273] R. Mandal, S. Saha, D. Kumar, S. Barman, S. Pal, K. Das, A. K. Raychaudhuri, Y. Fukuma, Y. Otani, and A. Barman, "Optically induced tunable magnetization dynamics in nanoscale co antidot lattices", ACS Nano **6**, Publisher: American Chemical Society, 3397–3403 (2012).

[274] O. Gaier, J. Hamrle, B. Hillebrands, M. Kallmayer, P. Pörsch, G. Schönhense, H. J. Elmers, J. Fassbender, A. Gloskovskii, C. A. Jenkins, C. Felser, E. Ikenaga, Y. Sakuraba, S. Tsunegi, M. Oogane, and Y. Ando, "Improvement of structural, electronic, and magnetic properties of co2mnsi thin films by he+ irradiation", Applied Physics Letters **94**, Publisher: American Institute of Physics, 152508 (2009).

[275] J. Hamrle, S. Blomeier, O. Gaier, B. Hillebrands, H. Schneider, G. Jakob, B. Reuscher, A. Brodyanski, M. Kopnarski, K. Postava, and C. Felser, "Ion beam induced modification of exchange interaction and spin–orbit coupling in the co2fesi heusler compound", Journal of Physics D: Applied Physics **40**, 1558 (2007).

[276] S. Pal, J. W. Klos, K. Das, O. Hellwig, P. Gruszecki, M. Krawczyk, and A. Barman, "Optically induced spin wave dynamics in [co/pd]8 antidot lattices with perpendicular magnetic anisotropy", Applied Physics Letters **105**, Publisher: American Institute of Physics, 162408 (2014).

[277] J. M. Shaw, S. E. Russek, T. Thomson, M. J. Donahue, B. D. Terris, O. Hellwig, E. Dobisz, and M. L. Schneider, "Reversal mechanisms in perpendicularly magnetized nanostructures", Physical Review B **78**, Publisher: American Physical Society, 024414 (2008).

[278] R. Hyndman, P. Warin, J. Gierak, J. Ferré, J. N. Chapman, J. P. Jamet, V. Mathet, and C. Chappert, "Modification of co/pt multilayers by gallium irradiation—part 1: the effect on structural and magnetic properties", Journal of Applied Physics **90**, Publisher: American Institute of Physics, 3843–3849 (2001).

[279] M. Urbánek, L. Flajšman, V. Křižáková, J. Gloss, M. Horký, M. Schmid, and P. Varga, "Research update: focused ion beam direct writing of magnetic patterns with controlled structural and magnetic properties", APL Materials **6**, Publisher: American Institute of Physics, 060701 (2018).

[280] I. Utke, P. Hoffmann, and J. Melngailis, "Gas-assisted focused electron beam and ion beam processing and fabrication", Journal of Vacuum Science & Technology B: Microelectronics and Nanometer Structures Processing, Measurement, and Phenomena **26**, Publisher: American Institute of Physics, 1197–1276 (2008).

[281] C. Castán-Guerrero, J. Herrero-Albillos, J. Bartolomé, F. Bartolomé, L. A. Rodríguez, C. Magén, F. Kronast, P. Gawronski, O. Chubykalo-Fesenko, K. J. Merazzo, P. Vavassori, P. Strichovanec, J. Sesé, and L. M. García, "Magnetic antidot to dot crossover in co and py nanopatterned thin films", Physical Review B **89**, Publisher: American Physical Society, 144405 (2014).

[282] L. A. Rodríguez, C. Magén, E. Snoeck, C. Gatel, C. Castán-Guerrero, J. Sesé, L. M. García, J. Herrero-Albillos, J. Bartolomé, F. Bartolomé, and M. R. Ibarra, "High-resolution imaging of remanent state and magnetization reversal of superdomain structures in high-density cobalt antidot arrays", Nanotechnology **25**, Publisher: IOP Publishing, 385703 (2014).

[283] R. D. McMichael and B. B. Maranville, "Edge saturation fields and dynamic edge modes in ideal and nonideal magnetic film edges", Physical Review B **74**, Publisher: American Physical Society, 024424 (2006).

[284] D. H. Y. Tse, S. J. Steinmuller, T. Trypiniotis, D. Anderson, G. A. C. Jones, J. A. C. Bland, and C. H. W. Barnes, "Static and dynamic magnetic properties of ${\text{ni}}_{80}{\text{fe}}_{20}$ square antidot arrays", Physical Review B **79**, Publisher: American Physical Society, 054426 (2009).

[285] S. McPhail, C. M. Gürtler, J. M. Shilton, N. J. Curson, and J. A. C. Bland, "Coupling of spin-wave modes in extended ferromagnetic thin film antidot arrays", Physical Review B **72**, Publisher: American Physical Society, 094414 (2005).

[286] C. Mathieu, J. Jorzick, A. Frank, S. O. Demokritov, A. N. Slavin, B. Hillebrands, B. Bartenlian, C. Chappert, D. Decanini, F. Rousseaux, and E. Cambril, "Lateral quantization of spin waves in micron size magnetic wires", Physical Review Letters **81**, Publisher: American Physical Society, 3968–3971 (1998).

[287] O. N. Martyanov, V. F. Yudanov, R. N. Lee, S. A. Nepijko, H. J. Elmers, R. Hertel, C. M. Schneider, and G. Schönhense, "Ferromagnetic resonance study of thin film antidot arrays: experiment and micromagnetic simulations", Physical Review B **75**, Publisher: American Physical Society, 174429 (2007).

[288] S. Neusser, H. G. Bauer, G. Duerr, R. Huber, S. Mamica, G. Woltersdorf, M. Krawczyk, C. H. Back, and D. Grundler, "Tunable metamaterial response of a ni${}_{80}$fe${}_{20}$ antidot lattice for spin waves", Physical Review B **84**, Publisher: American Physical Society, 184411 (2011).

[289] C.-L. Hu, R. Magaraggia, H.-Y. Yuan, C. S. Chang, M. Kostylev, D. Tripathy, A. O. Adeyeye, and R. L. Stamps, "Field tunable localization of spin waves in antidot arrays", Applied Physics Letters **98**, Publisher: American Institute of Physics, 262508 (2011).

[290] R. Zivieri, "Critical phenomena in ferromagnetic antidot lattices", AIP Advances **6**, Publisher: American Institute of Physics, 055709 (2016).

[291] F. J. T. Goncalves, G. W. Paterson, R. L. Stamps, S. O'Reilly, R. Bowman, G. Gubbiotti, and D. S. Schmool, "Competing anisotropies in exchange-biased nanostructured thin films", Physical Review B **94**, Publisher: American Physical Society, 054417 (2016).

[292] S. O. Demokritov and V. E. Demidov, "Micro-brillouin light scattering spectroscopy of magnetic nanostructures", IEEE Transactions on Magnetics **44**, Conference Name: IEEE Transactions on Magnetics, 6–12 (2008).

[293] G. Gubbiotti, G. Carlotti, M. Madami, S. Tacchi, P. Vavassori, and G. Socino, "Setup of a new brillouin light scattering apparatus with submicrometric lateral resolution and its application to the study of spin modes in nanomagnets", Journal of Applied Physics **105**, Publisher: American Institute of Physics, 07D521 (2009).

[294] P. Landeros and D. L. Mills, "Spin waves in periodically perturbed films", Physical Review B **85**, Publisher: American Physical Society, 054424 (2012).

[295] I. Barsukov, F. M. Römer, R. Meckenstock, K. Lenz, J. Lindner, S. Hemken to Krax, A. Banholzer, M. Körner, J. Grebing, J. Fassbender, and M. Farle, "Frequency dependence of spin relaxation in periodic systems", Physical Review B **84**, Publisher: American Physical Society, 140410 (2011).

[296] R. A. Gallardo, A. Banholzer, K. Wagner, M. Körner, K. Lenz, M. Farle, J. Lindner, J. Fassbender, and P. Landeros, "Splitting of spin-wave modes in thin films with arrays of periodic perturbations: theory and experiment", New Journal of Physics **16**, Publisher: IOP Publishing, 023015 (2014).

Étude de cristaux magnoniques reconfigurables à base d'alliages d'Heusler Co_2MnSi

Les ondes de spin sont des excitations élémentaires de matériaux magnétiques consistant en une précession déphasée des moments magnétiques du matériau. Tout comme une onde électromagnétique, les ondes de spin peuvent transmettre des informations. Ces ondes présentent plusieurs caractéristiques attractives par rapport aux ondes électromagnétiques pour la miniaturisation de composants radiofréquences (dans la gamme de quelques MHz à la dizaine de THz). Notamment, leurs longueurs d'ondes sont plusieurs ordres de grandeurs inférieures à celles des ondes électromagnétiques dans le vide et leurs fréquences peuvent être modifiées par l'application d'un champ magnétique. Un cristal magnonique est un matériau magnétique dont les propriétés magnétiques sont modulées de manière périodique et artificielle. A l'instar des photons dans un cristal photonique, les ondes de spin diffusent et interfèrent au travers du cristal magnonique générant ainsi des bandes de fréquences permises et d'autres interdites à la propagation. Suivant le design des cristaux magnoniques, diverses applications sont possibles tels que des filtres à ondes de spin, des portes logiques, mémoires non volatiles. Actuellement, la majorité des cristaux magnoniques présents dans la littérature fonctionne avec l'application d'un champ magnétique de saturation, ce qui nécessite l'utilisation d'aimants permanents. Cela limite l'incorporation de ces dispositifs magnoniques dans des circuits intégrés. Ainsi l'objectif principal de cette thèse consiste à obtenir un système modèle de cristal magnonique présentant des bandes radiofréquences reconfigurables, c'est-à-dire pouvant être modifiées à dessein, à champ magnétique nul (rémanence).
Dans ce contexte, les couches minces d'alliages d'Heusler Co_2MnSi (CMS) constituent des candidats prometteurs pour des applications magnoniques en raison de leur forte aimantation à saturation, de leur faible coefficient d'amortissement et de leur forte anisotropie magnéto-cristalline cubique (proche de 30 mT). En particulier, nous avons démontré dans un premier temps de manière numérique que la forte anisotropie cubique du CMS permet la stabilisation d'états magnétiques quasi-uniformes à la rémanence dans un système modèle de cristal magnonique : un réseau périodique de trous carrés de tailles 300-50 nm et de périodicité le triple de la taille des trous au minimum. Suivant la direction du champ d'initialisation, différents états magnétiques rémanents peuvent être obtenus. Lorsque soumis à un champ de pompage radiofréquence, ces différents états offrent alors différentes réponses radiofréquences. Nous montrons également comment la taille des trous et leur espacement influe sur le nombre et la fréquence des modes reconfigurables. Nous avons par la suite fabriqué et mesuré des cristaux magnoniques de CMS. La nanostructuration du CMS a été réalisée via deux techniques différentes : gravure Focused Ion Beam (FIB) et une combinaison de lithographie électronique et gravure Ion Beam Etching (IBE). Tout d'abord, un cristal magnonique de CMS avec des trous carrés de 140 nm et de périodicité 400 nm a été réalisé par FIB. En mesurant sa réponse radiofréquence par des mesures inductives via une micro-antenne et en réalisant des simulations micromagnétiques, nous avons montré la nécessité de prendre en compte les imperfections géométriques et la dégradation des propriétés magnétiques du matériau induites lors de la nanostructuration au FIB pour comprendre les mesures. Afin de s'affranchir de ces désavantages, un dispositif similaire à celui du FIB a été fait par combinaison de lithographie électronique et gravure IBE. Des modes d'ondes de spin bien distincts ont alors pu être observés, ce qui nous a permis de mesurer la reconfigurabilité à la rémanence prédite numériquement. Ce travail ouvre ainsi la voie à la réalisation de dispositifs magnoniques radiofréquences reconfigurables pour des opérations logiques ou de filtrages d'ondes de spin à la rémanence.

Study of reconfigurable Co_2MnSi Heusler based magnonic crystals

Spin waves are elementary excitations within magnetic materials consisting of a phase-shifted precession of the magnetic moments of the material. Analog to an electromagnetic wave, spin waves can transmit information. These waves present several attractive characteristics compared to electromagnetic waves for the miniaturization of microwave components (in the range of a few MHz to ten THz). In particular, their wavelengths are several orders of magnitude shorter than those of electromagnetic waves in vacuum and their frequencies can be modified by the application of a magnetic field. A magnonic crystal is a magnetic material whose magnetic properties are periodically and artificially modulated. Analog to photons in a photonic crystal, spin waves scatter and interfere through the magnonic crystal generating allowed frequency bands and frequency band gaps where their propagation is forbidden. Depending on the design of the magnonic crystals, various applications are possible such as spin wave filters, logic gates, non volatile memories. Currently, the majority of magnonic crystals present in the literature operate with the application of a saturation magnetic field, which requires the use of permanent magnets. This limits the incorporation of these magnonic devices in integrated circuits. The main objective of this thesis is to obtain a model system of magnonic crystal with reconfigurable frequency bands, i.e. which can be modified on purpose, at zero magnetic field (remanence).
In this context, thin films of Heusler Co_2MnSi alloys (CMS) are promising candidates for magnonic applications due to their strong saturation magnetization, low damping coefficient and high cubic magneto-crystalline anisotropy (close to 30 mT). In particular, we have first demonstrated numerically that the strong cubic anisotropy of CMS allows the stabilization of quasi-uniform magnetic states at remanence in a model magnonic crystal system: a periodic array of square holes of sizes 300-50 nm and periodicity at least three times the hole size. Depending on the direction of an initialization field, different remanent magnetic states can be obtained. When subjected to a microwave pumping field, these different states offer different microwave responses. We also show how the size of the holes and their spacing affect the number and frequency of reconfigurable modes. We then fabricated and measured CMS magnonic crystals. The nanostructuring of the CMS was achieved via two different techniques: Focused Ion Beam Etching (FIB) and a combination of electron beam lithography and Ion Beam Etching (IBE). First, a CMS magnonic crystal with 140 nm square holes and 400 nm periodicity has been made by FIB. By measuring its microwave response by inductive measurements with a micro-antenna and by performing micromagnetic simulations, we have shown the necessity to take into account the geometrical imperfections and the degradation of the magnetic properties of the material induced by the FIB nanostructuring to understand the measurements. In order to overcome these disadvantages, a device similar to the FIB one has been made this time by combining electron beam lithography and IBE etching. Well distinct spin wave modes could then be observed, which allowed us to measure the reconfigurability at remanence numerically predicted. This work paves the way to the realization of reconfigurable microwave magnonic devices for logic operations or spin waves filtering applications at remanence.